Understanding Biofilms: Plasma Polymer Coatings to Prevent Biofilm Formation and Understanding the Chemical Pathway to Their Formation by Spectroscopy

Amy R. Crisp

This dissertation is submitted for the degree of Doctor of Philosophy

May 2024

School of Engineering

Declaration

This thesis is my original work and has not been submitted for another degree at this or any other university. The work does not contain, to the best of my knowledge, any material published by someone else except when acknowledged in the text. Work within this thesis was made possible through a series of collaborative projects and all work contributed by another researcher has been explicitly indicated as such. The primary collaborators involved in this study include:

- Professor Gordon Ramage from Glasgow University (UK) where a series of standard microbiology testing was conducted on all species utilised in this work, to supplement information provided with spectroscopy.

- Professor James Bradley and Dr Stephane Simon from the University of Liverpool (UK) who aided in the production of 12-crown-4 plasma polymer coatings which were transferred to myself at Lancaster University for materials analysis.

- Tony Simula, the CEO at TekCyte® and the adjoining research team at the University of South Australia (AUS) who provided the protocol and advice to successfully produce HPG coatings at Lancaster. The known coating HPG was rigorously analysed across a range of substrate materials, as part of this PhD.

Publications

Research displayed in this thesis has been or will soon be published in the following academic publications:

A.R. Crisp, B. Short, L. Rowan, G. Ramage, I.U.R. Rehman, R.D. Short and C. Williams. Investigating the chemical pathway to the formation of a single biofilm using infrared spectroscopy. *Biofilm*. **2023**, 30 (6), 100141, doi: 10.1016/j.bioflm.2023.100141.

E. Moore, A.J. Robson, A.R. Crisp, M.P. Cockshell, R. Ganesan, N. Robinson, S. Al-Bataineh, V. Nankivell, A.L.S. Burzava, M. Tondl, G. Benveniste, J.W. Finnie, P.J. Psaltis, H.J. Griesser, C.A. Bursill, N.H. Voelcker, L. Martocq, A. Quadrelli, S.P. Jarvis, C. Williams, G. Ramage, I.U.R. Rehman, T. Simula, C.S. Bonder and R.D. Short. Study of the structure of hyperbranched polyglycerol coatings and their anti-biofouling and anti-thrombotic applications. *Advanced Healthcare Materials*, **2024**, e2401545, doi: 10.1002/adhm.202401545.

Presentations

Oral presentations

"Methods to understand and prevent biofilm progression", A.R.Crisp, I.U.R. Rehman, D. Cheneler, R.D. Short, C. Williams, A. Robson, GISMO+ seminar, 9th June 2022, online.

"The potential of spectroscopy to diagnose biofilm infection", A.R.Crisp, I.U.R. Rehman, C. Williams, G. Ramage, Microbiology department talk given at Royal Lancaster Infirmary and Furness General Hospital, Feb 2023, in person.

"Preventing central venous catheter biofilm infection using a HPG coating", A.R. Crisp, R. Short, A. Robson, T. Simula, A. Quadrelli, L. Martocq, NBIC showcase: Supporting collaboration for impact in biofilm research, 17th May 2023, University of Nottingham.

"Understanding the formation pathway of biofilms with infrared spectroscopy", A.R.Crisp, I.U.R. Rehman, D. Cheneler, R.D. Short, C. Williams, A. Robson, Biosci Network symposium, 13th July 2023, Lancaster University.

Poster presentations

"Polyethylene oxide coatings towards the prevention of biofilm development", A.R.Crisp, I.U.R. Rehman, D. Cheneler, R.D. Short, C. Williams, A. Robson, 9th International Conference on Plasma Medicine, 26th-1st July 2022, Utrecht, Netherlands.

"Fourier-transform infrared spectroscopy to distinguish between planktonic and biofilm samples", A.R.Crisp, I.U.R. Rehman, D. Cheneler, R.D. Short, C. Williams, A. Robson, EuroBiofilms, 31st-3rd September 2022, Palma, Mallorca.

"Understanding and preventing biofilm infections", A.R.Crisp, I.U.R. Rehman, D. Cheneler, R.D. Short, C. Williams, A. Robson, Postgraduate research conference, held each year 2021-2023, Lancaster University.

Abstract

Biofilm is the name of microbial communities, where microorganisms irreversibly adhere to each other and a surface, whilst encompassed by a complex extracellular matrix. Biofilms are ubiquitous throughout the world, but in the healthcare system they pose a significant threat, particularly in the infection risk of blood contacting materials. Once an infection progresses to a biofilm, there are limited effective treatment options to completely eradicate them. A substantial issue in clinical management is identifying when the microbes in an infection have switched from a planktonic to a biofilm phenotype. Despite efforts to develop new treatments, due to the adaptable nature of microorganisms and the mounting antimicrobial resistance crisis, prevention is the best option to combat biofilm infection mortality. A proposed solution is to treat all blood contacting materials with an anti-biofouling coating. In this research project, both biofilm diagnostics and coatings to prevent biofilm growth have been investigated.

Vibrational spectroscopy can reveal the precise chemical composition of natural materials, whilst remaining non-destructive and requiring minimal sample preparation. FTIR has been successfully applied in this work to identify chemical markers of intact bacterial (*S. epidermidis*) and fungal (*C. albicans*) biofilms, and for the first time FTIR has chemically defined the timeframe for irreversible attachment to a substrate. This foundational study provides a baseline to support FTIR for implementation in clinical diagnosis to identify infection maturity, informing treatment options.

Plasma polymerisation has been utilised to produce and initiate anti-biofouling coatings on a diverse range of clinically relevant materials. In this research, the aim was to maximise ethylene oxide content on a given surface, naturally increasing the hydrophilicity to reduce protein adsorption. Firstly, the γ-regime (high pressure and low power) was applied to crown ether monomer, to optimise the functional group retention and results show the new polymer coating approached the ethylene oxide retention observed in an industry standard coating. In an adjoining study, the ultra-thin industrial hyperbranched polyglycerol coating has been rigorously monitored across 7 different materials, including clinically relevant nitinol stents. Vitally, results are presented for the novel application of ion-milling X-ray photoelectron spectroscopy, after a protein adsorption test, indicating HPG can prevent protein penetration

within the coating structure. Further evidence for HPG having high non-biofouling capability was revealed in biofilm exposure testing that used vibrational spectroscopy to define the timepoint of biofilm initiation. While further work is required to produce an optimal crown ether plasma polymer coating, HPG should soon be suitable for clinical trial.

Acknowledgments

Firstly, I would like to offer my sincere gratitude to my amazing supervisory team who gave me the opportunity to complete this PhD work and made this multidisciplinary research project possible. Thank you very much Professor Ihtesham Rehman, Dr David Cheneler, Professor Robert Short, Professor Craig Williams and Dr Lorna Ashton for the continuous support and guidance you provided as well as the additional opportunities I have been fortunate to receive.

I would also like to thank Dr Alex Robson who was extremely generous with his time guiding the plasma polymerisation and XPS work throughout the project. Thank you to Dr Samuel Jarvis for his additional support and access to the XPS. Thank you to all of the additional technical staff in the Engineering, Physics and Chemistry departments at Lancaster University who contributed to the production of various pieces of equipment that were instrumental in the plasma polymer coatings study. Thank you to all of the microbiology team at the Royal Lancaster Infirmary who provided two days of basic microbiology training. Thank you as well to Dr Carlos Meza Ramirez who provided training on microorganism sample preparation for FTIR analysis.

I would also like to take this opportunity to thank all of the people involved in the collaborative studies that have contributed to this project. The research team at Glasgow university, led by Professor Ramage, including Mark Butcher and Jontana Allkja were instrumental in the collection of standard microbiological characterisation data. I was also afforded the brilliant opportunity to travel to their university and receive additional training in fluorescence microscopy. The HPG project would also not have been possible without the researchers at TekCyte® and UniSA, Dr. Eli Moore and Dr Sameer Al-bataineh, in particular. Thank you as well to Alessio Quadrelli at Lancaster who aided in the AFM analysis of HPG coatings and Laurine Martocq at Lancaster who completed TFAA derivatisation on HPG.

I am also appreciative of the industrial funding that was provided by Greater Innovation for Smarter Materials Optimisation (GISMO) which made this research project possible. Through this collective of researchers, I am also thankful for the multiple opportunities to work with small companies based across the North West, as well as for the opportunity to share my research throughout their network.

A big thank you to my friends and family who have provided unwavering support throughout my PhD journey. Thank you to my parents Mr Mark and Mrs Gaynor Crisp who have supported me throughout my entire educational journey. Thank you also to my in-laws Mr Andrew and Mrs Ruth Salthouse. Finally, I would like to thank my partner Tom who has always offered support and encouragement throughout this PhD, and particularly in the process of writing the thesis. This work would truly not have been possible without you.

Contents

Abbreviations

AFM	Atomic Force Microscopy
AMP	Antimicrobial Peptide
AMR	Antimicrobial Resistance
ATR	Attenuated Total Reflectance
BHI	Brain Heart Infusion
CaF_2	Calcium Fluoride
CBA	Columbia horse Blood Agar
CCD	Charged Couple Device
CFU	Colony Forming Unit
CPS	Counts Per Second
CRBSI	Catheter Related Blood Stream Infection
CV	Crystal Violet
CVC	Central Venous Catheter
E_B	Binding Energy
ECM	Extracellular Matrix
EPS	Extracellular Polymeric Substances
FISH	Fluorescence in Situ Hybridisation
FTIR	Fourier Transform Infrared Spectroscopy
FWHM	Full Width at Half-Maximum
GCIS	Gas Cluster Ion Source
HCA	Hierarchical Cluster Analysis

HGT	Horizontal Gene Transfer
HPG	Hyperbranched Polyglycerol
KE	Kinetic Energy
LDA	Linear Discriminant Analysis
LU	Lancaster University
MVA	Multivariate Analysis
NB	Nutrient Broth
NN	Neural Network
NO	Nitric Oxide
PBS	Phosphate Buffer Saline
PCA	Principal Component Analysis
PEG	Poly (ethylene glycol)
PEO	Poly (ethylene oxide)
PLS	Partial Least Squares
PP	Plasma Polymerisation
PS	Polystyrene substrate
PTFE	Polytetrafluoroethylene substrate
QS	Quorum Sensing
RF	Radiofrequency
RLI	Royal Lancaster Infirmary
RMS	Raman Microspectroscopy
RPMI	Roswell Park Memorial Institute
RS	Raman Spectroscopy

RSF	Relative Sensitivity Factor
SDS	Sodium Dodecyl Sulphate
SEM	Scanning Electron Microscopy
Si	Silicon substrate
SVM	Support Vector Machine
TEMPO	2,2,6,6-tetramethyl-1-piperidinyloxy
TFAA	Trifluoracetic Anhydride
TiSi	Titanium-Silicon substrate
TSB	Tryptic Soy Broth
UHV	Ultra-high Vacuum
UniSA	University of South Australia
WCA	Water Contact Angle
XPS	X-ray Photoelectron Spectroscopy
YPD	Yeast extract Peptone Dextrose

List of Figures

List of Tables

Chapter 1. Introduction and Literature Review

1.1 Research Motivation and Aims

Microorganisms favour community development rather than existing as single cells due to the protection this offers against environmental stressors.[1] Once irreversibly attached to a surface, microorganisms will coordinate the production of extracellular polymeric substances (EPS) and at this stage the community is defined as a biofilm. Whilst the general pathway to biofilm formation is widely accepted, there is a lack in understanding of the chemical changes which accompany the phenotypic switch from individual cells (planktonic) to a biofilm.[2]

Biofilms are ubiquitous throughout the natural world but their detrimental impact is amplified in the healthcare sector. Biofilms cannot be easily treated or removed, as a result of the extracellular matrix (ECM), comprised of proteins, EPS, nucleic acids and lipids, which provides protection to the cells.[3] The development of treatment options for biofilm derived infections is not viable and the most appropriate solution is to promote biofilm prevention. Microorganism colonisation of medical devices, namely implantable equipment such as catheters, is a regular clinical occurrence and an increasing issue. If allowed to progress inside wounds, biofilms will lead to chronic infection. Due to communication mechanisms established in the ECM and the community structure which incorporates dormant cells, biofilms contribute significantly to the issue of antimicrobial resistance (AMR). As such non-fouling novel coating technologies are an intense source of research to improve the longevity of medical devices and prevent the initial microbial colonisation which precedes biofilm development.

The hypothesis addressed in this thesis was that vibrational spectroscopy could be used to chemically evaluate intact biofilms and the information yielded should then be useful to inform the production of anti-biofouling coatings. The project to investigate this hypothesis involved the simultaneous exploration of biofilm formation, alongside the development and testing of novel thin film antibiofouling coatings. The key objectives outlined at the inception of the project were:

- Spectroscopically define a biofilm and identify biomarkers associated with the beginning stage of biofilm formation, for a single live model
- Utilise vibrational spectroscopy to monitor the development of a live, single biofilm from initial surface attachment to maturity, across multiple microorganisms
- Explore polyethylene oxide (PEO)-like thin film coatings to reduce biomolecule adsorption to the surface, including the development of novel plasma polymer coatings and comparative work with an established industrial gold standard coating
- Design and build a purpose-built plasma polymer reactor to exert control over the surface and permit maximum non-fouling characteristics to be obtained in the coating
- Determine the realistic viability of both the new and industrial coatings against biofilm formation

Each of these objectives was addressed throughout the project and this thesis explores the results across four chapters. **Figure 1.1** provides a summary of how the chapters of this thesis link together and correspond to the study objectives. **Chapter 2** details the exploration of a single bacterial biofilm with vibrational spectroscopy. Significantly, this chapter highlights the novel Fourier-Transform Infrared (FTIR) spectroscopic protocol to track the initiation and proliferation of a single biofilm, as well as identifying the chemical signature found to associate with the switch from planktonic to biofilm forming cells. **Chapter 3** builds upon these findings by applying the same FTIR monitoring protocol firstly to a fungal biofilm model, exposing the same biomarker region is changed upon biofilm formation for both a bacterial and a fungal species. This chapter then explores the application of FTIR to monitor a multispecies biofilm model. In **Chapter 4**, the focus of the research presented moves from biofilm understanding to biofilm prevention. In this chapter, the development of several PEO-like plasma polymer

coatings is detailed, leading to the production of a novel surface coating with 60% C-O dominance. Moreover, this chapter presents the original and rigorous materials analysis of hyperbranched polyglycerol (HPG), an existing industry gold standard PEO-like coating. Finally, **Chapter 5** details the anti-biofouling experiments conducted on all non-fouling coatings to determine the realistic potential and relevance to clinical implementation. This chapter includes the first depth profiling analysis of HPG, following protein exposure, which reveals that the coating prevents protein molecules from entering and becoming trapped within the coating structure. This successful finding was also reflected in further biofilm exposure testing, to show that HPG reliably resists biofilm development compared to the uncoated substrate material.

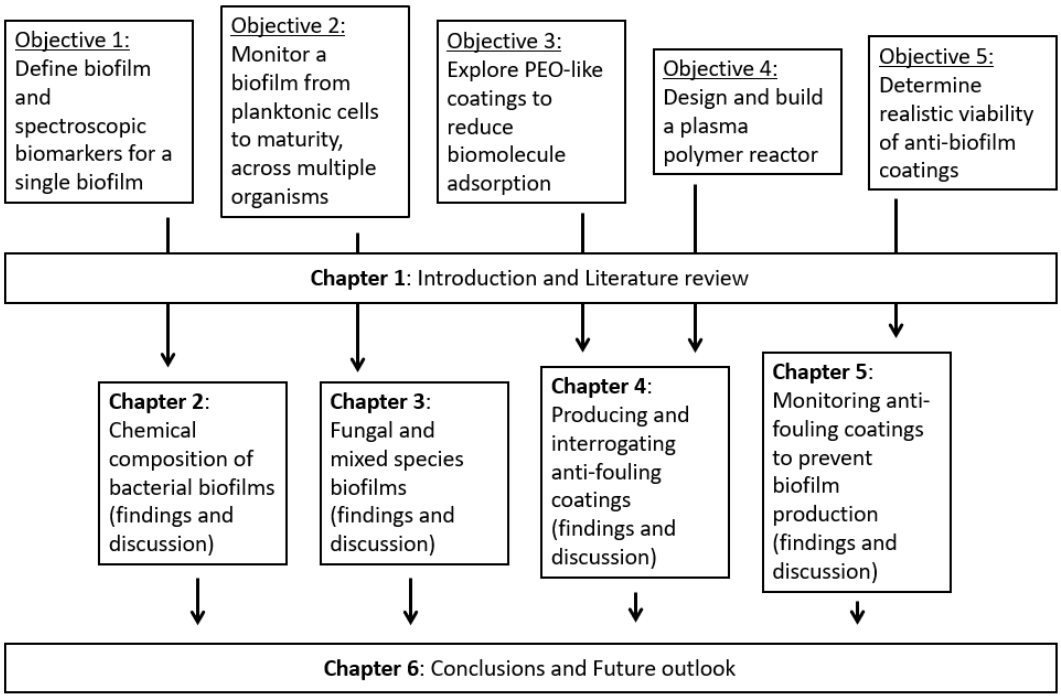

Figure 1.1 Diagrammatic summary of how the 5 key research objectives outlined at the beginning of this project have been investigated and addressed in this thesis.

This interdisciplinary study aims to combine explorative vibrational spectroscopy for understanding biofilms, alongside novel materials development for anti-biofouling coating production. This unique project brings together two of the key research themes within the area of infection investigation. It is standard practice to segregate different themes of research and

within biofilm studies, often the microbiology teams focused on understanding the microorganisms have little to no communication with materials scientists aiming to prevent microbial colonisation. Within this piece of work the two themes have been investigated simultaneously in the hope that it will ignite conversations between experts in the field.

1.2 Biofilms

1.2.1 What is a biofilm?

The term microorganism defines bacteria, viruses, fungi, algae and protozoa. Bacteria are characterised as prokaryotic microorganisms meaning the cells contain unenclosed genetic material, unlike eukaryotic cells which feature a defined nucleus. Bacteria exist in every environment on the planet, yet the link between bacterial species and disease was not highlighted until the 19th century.[4,5] It is however important to recognise that pathogenic bacteria only represent a small proportion of the known bacterial species; many species do not cause disease and are essential for life to exist on Earth. Pathogens have resulted in devasting consequences throughout human history, only improving with the discovery of antibiotics, beginning with penicillin in 1928.[6] Bacteria can be classed as gram-positive or gram-negative. Gram-positive species, such as *Streptococcus* and *Staphylococcus*, have a large amount of peptidoglycan in the cell wall; a substance uncommon inside the human body, leading to an immune response when the bacteria enter the system.[7] These species of bacteria exist harmlessly at the skin barrier. On the other hand, gram-negative bacteria, such as *E. Coli* and *P. Aeruginosa*, lack peptidoglycan in the cell wall and often have an outer capsule preventing recognition of foreign antigens in the human immune response system.[7] The latter type of bacteria prevent the immune system from recognising and targeting them, which can lead to more life-threatening infection. Fungus is also ubiquitous across the natural world, but pathogenic infections in the human body can be deadly; *Candida* species are the fourth most common cause of blood stream infections.[8] Whilst some species of *Candida* (i.e. *C. glabrata* or *C. krusei*) do not interact with the human body, *C. albicans* is the primary strain responsible for infection (termed candidiasis).[8,9] *C. albicans* is found to harmlessly exist in the oral cavity and

in gastrointestinal organs, but when these microorganisms grow uncontrollably they pose a risk to human health; the organisms are highly adaptable moving between different morphologies (yeast cells, hyphae and biofilms) that advantageously prevent cell removal and treatment.

Biofilms are the aggregated form of microorganisms, as oppose to single cells, referred to as planktonic. Biofilms form on any surface, hence research surrounding biofilm development is relevant across a myriad of industries, from food contamination to healthcare.[5,10–12] Briefly recognised in the 17th century in the form of dental plaque, the term 'biofilm' was not coined until 1978, when the prominent connection to disease and inhibiting antimicrobial efforts, was recognised.[13,14] When planktonic microorganisms individually adhere to a surface, they form the so-called biofilm.[1] Once adhering to a surface, the cells become embedded within an ECM, allowing intercellular communication networks to be established.[13] Tightly packed communities of microorganisms permit genes to be shared, allowing community protein synthesis and growth.[10,15,16] Due to the cooperative nature of cells within a biofilm microenvironment, all cells are benefitted by protection from adverse environmental conditions. Biofilms are arguably the most resilient form of life on Earth and are able to populate any surface.[13] Consequently, biofilms are particularly problematic in healthcare settings, whether they colonise on medical equipment or directly in the wound bed.[17]

The process of biofilm progression is significant due to the multistep pathway, consisting of reversible and irreversible stages, but has been hotly debated throughout this area of research. **Figure 1.2** displays the up-to-date depiction of the biofilm life-cycle as described by Sauer and Bjarnsholt.[18] The process begins with a single cell which can reversibly adhere to a surface, once within close proximity. This can be through a mechanical attachment, for instance via the flagella; or, through a surface interaction such as a weak Van der Waals force or hydrophobic interactions.[19–22] There are a range of examples of bacteria without flagella which can participate in surface attachment.[23] This alludes to the presence of external elements such as proteins which encourage surface interaction. In terms of *Candida*, fungal cells undergo a morphological change between the planktonic and biofilm developmental stages; during early surface attachment the cells form hyphae which densely populate the area in what is termed the filamentous stage.[8,24] The most optimal surfaces for biofilm attachment are rough and hydrophobic.[10] Once single cells have interacted with a surface, cells from the surrounding

environment will move, forming a monolayer across the surface. This leads to the production of EPS, forming the matrix to encompass the microorganisms.[25] From this point, the microorganisms are irreversibly adhering to the surface and each other.[26] Exponential growth to a multilayer commences, paving the way to communication pathways and nutrient channel establishment; biofilms experience a coordinated growth.[20] At this point the biofilm would be considered 'mature', often characterised by a three-dimensional morphology. Following maturation, biofilms can adopt other microbes within the local environment.[10,26] The colony can also now detach from the surface in sections to recolonise in the surrounding environment.[27] The process can continue indefinitely, if left untreated.

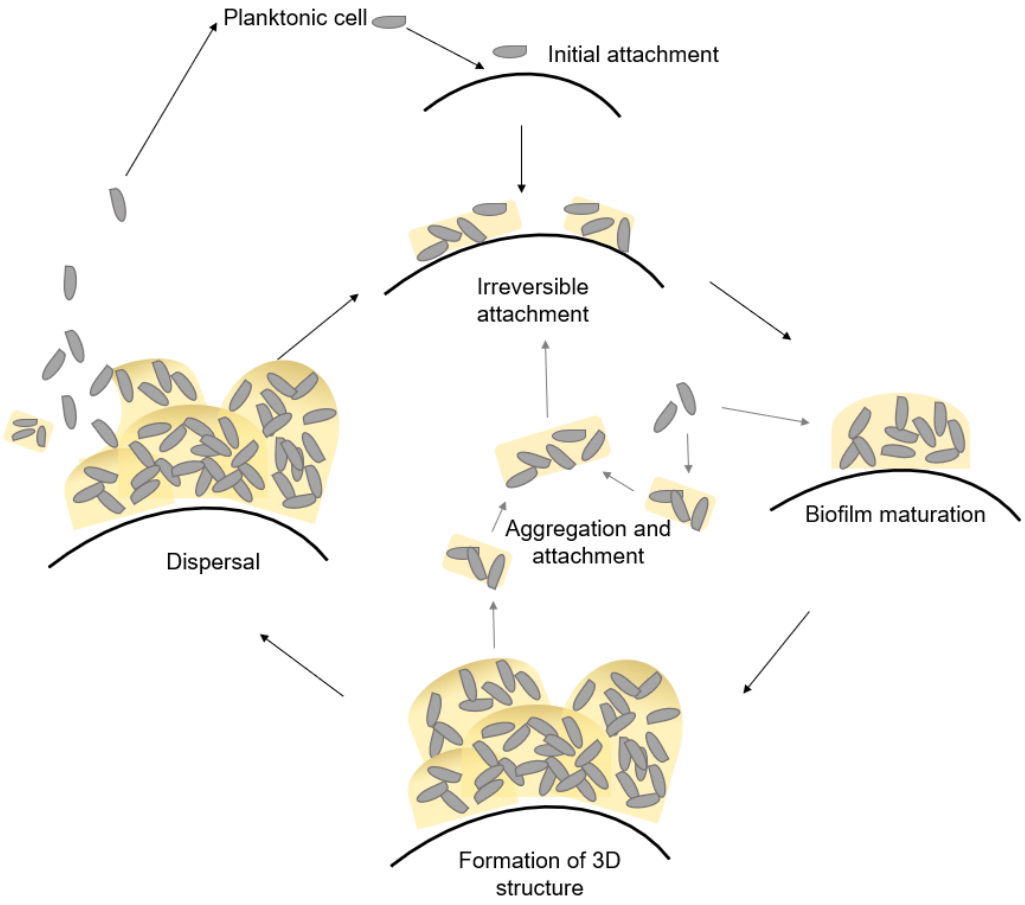

Figure 1.2 Formation pathway following initial attachment of planktonic microorganism cells to a surface, through to production of EPS and biofilm maturation, culminating in a diverse multi-layer structure capable of dispersing and reattachment. Reproduced from Sauer (CC license 5853590048259).[18]

Prior to the start of biofilm formation, the surface must be primed for development.[28] Organic and inorganic materials from the bulk liquid adjacent to the surface will migrate and adsorb, modifying the surface in preparation for bacterial attachment.[29] Due to the wide variety of microorganisms potentially within the vicinity of a target surface, the conditioning layer is dependent on those contributing species. Thus, the constitution of molecules forming the conditioning layer will differ greatly depending on the bacteria present and the immediate environment. Despite conflicting opinions on this layer, the general consensus is that the presence of proteins, such as albumin, gelatine and fibrinogen, on the surface favour bacterial attachment.[23] Further to this point, debridement as a mode to remove biofilm from a surface, theoretically leaves a "footprint" of the microorganisms, which arguably then have a role in subsequent biofilm development.[23]

1.2.2 Biofilm Communication Mechanisms

Briefly negating the wider issue of AMR, biofilms have their own mechanisms in place permitting the resistance of antimicrobial agent treatment.[30] The EPS matrix surrounding the biofilm is a protective barrier to the local environment.[25] Limited antibiotic penetration within this matrix has been demonstrated by the Stewart group.[17] In part this could be explained by the existence of efflux pumps within the biofilm structure. An efflux pump is a widely known active transporter system and while they are located within the cell membrane of individual microorganisms, the efflux pump could play an essential role in biofilm formation.[31] Additionally the inclusion of efflux pumps in the biofilm system should promote the removal of toxins, including antibiotics.[10,32] Similarly, the Sharma group investigated the penetration of certain antibiotics on *S. aureus* and also reported that the matrix prevented penetration, in part explaining this strains resilience to treatment.[33] Further to this point, the EPS has shown to prevent dehydration of the biofilm and other methods of biofilm destruction.[34]

There are instances where antibiotic molecules can penetrate the outer cells.[25,35,36] Often biofilms are arranged such that the core cells are physiologically dormant and surrounded by the 'working' cells, where the nutrient channels exist and primary communications occur.[37]

The existence of these “persister cells” results from the lack of oxygen at the centre of the biofilms meaning antibiotics that penetrate and effect the working microorganisms, leave the internal cells unharmed because antibiotics rely on cellular activity to generate a response.[12,38] Therefore, there exists the argument that these antibiotics only worsen the target infection because the harmed outer cells provide nutrients for the surviving cells to continue growth and expansion. Furthermore, using antibiotics, without removing all cells, contributes significantly to AMR. When discussing biofilm dispersal, this can either be passive or active (**Figure 1.3**): passive dispersal is the use of an external force to remove the biofilm as a complete entity. The risk with this method in scenarios such as the wound bed, is that any cells left behind will be able to form further colonies. Whereas, active dispersal is the application of chemicals to disrupt the biofilm and prevent the ECM from reforming.[39] Both methods strive to prevent biofilm regrowth and progression, but when a biofilm has already formed, it is extremely challenging to removal all microbe signatures; this is the issue at the root of chronic infection. It is clear that a complete disruption of the biofilm must occur to prevent regrowth.

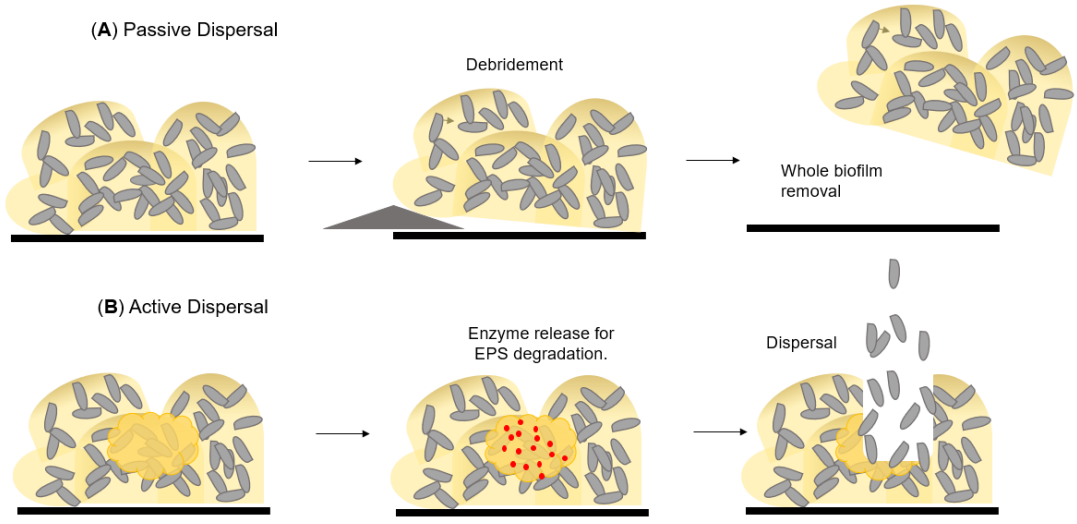

Figure 1.3: Schematic to illustrate the two primary modes of biofilm dispersal from a surface (e.g. the wound bed). (**A**) passive focuses on whole removal of the biofilm via a process such as debridement; (**B**) active biofilm dispersal is the chemical disruption of the ECM to release planktonic cells, hopefully permitting more successful treatment with antimicrobials. Adapted from Fleming (open access article distributed under (CC BY) license).[39]

Another key consideration within biofilms, is the cell-to-cell communication.[40] The use of signalling mechanisms to control gene expression and coordinate behaviour is called quorum sensing (QS).[41] Extensive research has been completed around this communication mechanism.[1,41] QS is defined as density dependent and relies on the detection and production of signalling molecules, “autoinducers”, to coordinate a community response.[42,43] An important question for investigation is the point at which the bacterial density exceeds the threshold to QS.[44]

1.2.3 Antimicrobial Resistance

Pathogenic microbes pose an increasing threat to human health as the resistance to antimicrobial drugs progresses. There are a worryingly high amount of species that are becoming resistant to multiple antimicrobials.[45] Although this resistance is arguably a natural Darwinian-style response, the overuse of such medications has progressed the issue rapidly.[46] Around 50% of the antibiotics prescribed throughout the world are unnecessary.[46] The issue of resistance is exemplified by biofilms, which permit the existence of pathogens, in a protective environment, where intercellular communication is enhanced.

AMR is a natural occurrence, accelerated by human misuse of infection treatment.[47] Resistance can be acquired in two ways: cells can experience mutations in the chromosomes relating to antibiotic response; or, genes relating to resistance can be exchanged between cells via horizontal gene transfer (HGT).[45,48] The worldwide death toll resulting from AMR was 700,000 pa in 2014, and this is projected to reach over 10 million pa, by 2050, overtaking the current number of cancer related mortalities.[49] Currently, we remain reliant on antimicrobial treatments without a sufficient focus on preventing infection.[50] As microbial species and strains grow resistant to treatment, there must be a decision on the direction of antimicrobial research. Although, drug discovery remains prominent, the issue of AMR still exists. Eventually, AMR would render any new drugs obsolete. Hence, this is the time to focus research efforts on infection prevention, as well as rapid infection diagnostics.

HGT is enabled in both bacteria and fungi by the close proximity of individual microorganisms within the same colony.[51] The frequency of HGT occurring has been reported as higher in biofilm communities compared to genetic transfers between planktonic cells.[30] There are three modes of HGT available in biofilms. Briefly, transduction where bacteriophages collect and transport DNA sections between bacteria; transformation where cells can collect free DNA from the ECM; and, conjugation, where the exchange of plasmids between two cells is facilitated by the pili.[46,47,51] Conjugation is the mechanism most often associated with gene transfers relating to AMR. These plasmid transfers are conceivably influenced by the overuse of antibiotics, exerting pressure on the microorganisms to survive.[52] The early investigations by Hausner and Wuertz demonstrated low nutrient environments within biofilms do not diminish the ability to participate in HGT, strengthening the concept that biofilms are driving the urgency of the issue of AMR.[53]

1.2.4 Infections and Common Pathogens

Medical devices are instruments used in the routine treatment of patients for a diverse array of ailments. Devices such as catheters are essential and the most widely recognized example. Although these items are accepted by the general public, the challenges posed by introducing these foreign body items into the human body is seldom considered. Central venous catheters (CVCs) frequently result in catheter related blood stream infections (CRBSIs), which are complex to treat, and mean that these pieces of equipment have a limited lifespan. With all catheters the equipment can either be changed regularly, at a financial cost, or if infection seeds on the devices there are potentially lethal consequences for the patient.[54] This is a growing epidemic; there are 250,000-400,000 cases of CRBSIs each year, reported in the US and the National Biofilm Innovation Centre reported in 2019 that up to $387 bn is spent globally as a result of this.[55,56]

The most common way that CVCs become infected is because the device is pushed through the skin barrier, where strains such as *S. epidermidis* harmlessly exist. But when the *Staphylococcus* enters the blood stream, the catheter can be colonized and in extreme cases

this will end in a biofilm forming.[57] But as highlighted by the Ramage group “there is more to wounds than bacteria”.[58] Fungal disease causes upwards of 2 million infections worldwide each year and *Candida* is in the top 5 for contributing species which are responsible for over 90% of the associated deaths.[59] In the management of chronic wounds, fungi can be a large contributor to the total biomass of an infection site owing to the fact that the cells physically occupy more space than bacterial cells.[58] Fungal-bacterial biofilms are advantageous colonies which have been reported as a significant driver of resistance to antimicrobial treatment. These multispecies systems are established such that the fungi form a base layer on which the bacteria colonise, improving the cumulative growth of each species.[58,60] One of the most frequently reported interkingdom infections from medical devices situated in the urinary tract, wounds and blood stream are derived from *S. epidermidis* and *C. albicans*.[61,62] The combination of these microorganisms may enhance virulence and biofilm development, particularly on indwelling catheters.[61] In one investigation by the Douglas group results revealed that the EPS produced by a strain of *Staphylococcus* was able to prevent anti-fungal drug penetration into the biofilm, removing any interactions with *Candida*.[63]

The clinical impact of CVC infection is three-fold: the overall patient prognosis is worsened; treatment options are limited; and this will ultimately mean an increase in length of hospital stay (which has personal and financial implications). This impact is intensified when the CVC infection is a mature biofilm, causing an exponential increase in mortality rate because biofilm infections are 1000 times less susceptible to antimicrobial therapies.[64] A popular solution to this is coating all blood contacting materials with a non-fouling material which work by minimizing non-specific protein binding to prevent initial microorganism attachment.[65,66]

1.3 Existing Methods to Analyse Biofilms

As explored in preceding sections, biofilms pose a growing level of threat within the healthcare sector; approximately 65% of microbial infections are contributed to by biofilm-forming cells.[67] In order to reduce the amount of infections and increase the survival rate from those that do develop a biofilm infection, diagnostic techniques must be improved. Ideally, an interdisciplinary

approach should be taken to explore the mechanisms of pathogenic biofilm production as well as to enhance the speed and accuracy of detection.[68] The mode of biofilm diagnosis from medical device infections is inconsistent, with a variety of methods in use globally.[67] Implantable medical device infections can only be diagnosed following surgical extraction of the item, followed by microorganism culture onto agar plates.[2] This lack of a standard clinical test to identify biofilms is in part attributed to the reduced metabolic activity of cells, preventing culture leading to the production of false negative results, as the biomass is underestimated.[69,70] Moreover, more metabolically active microorganism strains will grow faster in clinical isolates and therefore their presence will be overrepresented. There is also a lack of understanding about the chemical composition of biofilms, meaning specific biomarkers are not commonly known.[2]

Currently, infection diagnosis is rooted in culture plate assay and microscopy which have remained in place since the 1980s.[71,72] While colony counting (where colony forming units, CFUs, are measured) gravely underestimates biomass, viability staining, also referred to as Live/Dead staining, is a popularly adopted approach used in conjunction to yield qualitative and quantitative information for cells cultured from an infection site.[67] The uptake of different dyes can be used as a quantitative measure of biofilm growth under different environmental conditions.[73] Concisely, Live/Dead staining utilises two dyes (propidium iodide, red and SYTO9, green) which can enter cells (healthy cells penetrated by SYTO9 and damaged cells affected by propidium iodide).[74] One of many comparative studies into the application of viability staining used multispecies biofilms from oral plaque to demonstrate that when solely colony counting, only the microbes capable of cell division at a rate above the threshold for colony formation, in a laboratory culture media, will be counted.[74] On the other hand, the more rapid Live/Dead staining protocol defined total counts and overall cell viability in a single step.[74] Generally Live/Dead staining is a more reliable technique because it shows a higher cell count for the same sample compared to colony counting. This is not to suggest that viability staining can be used as a sole diagnostic method either; cultivation and colony counting should be used in conjunction with staining. Live/Dead staining was more recently shown by the Ivask group to underestimate viability due to the presence of eDNA in adherent biofilm cells that can potentially enhance the uptake of propidium iodide. Their study argued that the preferential uptake of the

red dye means that biofilm samples are regularly classified as unviable when compared to planktonic samples which have a higher degree of green dye uptake.[75]

High resolution microscopy is an emergent branch of diagnostic techniques that are being explored in research currently. Microscopic methods facilitate the whole analysis of the biofilm structure, not only permitting detection but also visualising the colonies on the surface to which they are naturally adhering to.[76] Although these clinical methods have been refined and standardised, they are unable to definitively differentiate between the two phenotypes, planktonic and biofilm.[77] Further issues within these methods are the reliance on chemical labelling and dehydration of the sample before analysis. This not only requires additional time before a diagnosis can be acquired, but it also changes the fundamental chemical signatures of the sample.[78,79] Despite this Scanning Electron Microscopy (SEM) is one method that has been pioneered to visualise the 3D microenvironment.[76,80,81] As well as diagnosing biofilm derived infections, there is still a lack of understanding about the chemical composition of biofilms as well as detail about the environment dependency of the EPS relating to the effects of AMR factors. The Holden group utilised Environmental SEM to maintain some biofilm sample hydration in an effort to monitor the microorganisms in situ, however if the ECM is not pre-processed at all the low electron density prevents visualisation.[76] More recently, Atmospheric SEM was reported to visualise the finer details of a bacterial biofilm structure in aqueous conditions, including the interaction of the ECM between the bacteria and the substrate surface.[82] In spite of this achievement, the sample was chemically labelled and only samples below 2-3 μm thickness could be seen on the sampling surface. The promising diagnostic method favoured within this stream of research, above SEM, in the European Society of Clinical Microbiology and Infectious Diseases guidelines for biofilm infection diagnosis was fluorescence in situ hybridisation (FISH).[83] FISH effectively combines standard culture, microscopy and biochemical identification by treating samples with fluorescently labelled oligonucleotides.[70] This method can preserve the 3D microenvironment. [84]

In the all methods outlined above, with the exception of some microscopy applications, samples undergo pre-processing, increasing time for infection treatment, during which the patient's condition may worsen.[77] A rapid diagnostic solution is required where samples can be collected and analysed in the same day, to both determine which microorganism is causing

an infection and whether the phenotype of the microbe has switched from planktonic to biofilm forming. The emergent optimisation of spectroscopy as a diagnostic protocol, could allow a more targeted approach to antimicrobial use.[46,45]

1.4 Spectroscopy to Evaluate Biofilm Infection

In clinical practice, multiple microorganisms contribute to interkingdom biofilms. These biofilms are dependent on the species forming them and the environment in which they grow.[13] It would be beneficial if cultures could be visualised, directly from patient samples. Infection could be quickly targeted with a specific treatment therapy. It would be more effective and could be life-saving if the correct treatments were applied promptly. Moreover the unnecessary use of antibiotics is contributing to AMR; a targeted approach to prescription is needed to slow the deterioration of current treatment options.[85] One of the key aims addressed in this thesis is to explore the applicability of vibrational spectroscopy to analyse biofilms.

1.4.1 Principals of Vibrational Spectroscopy

Light can be viewed in two ways, either as described by particle theory or wave theory. In the case of spectroscopy, it is useful to think about photons (or individual light particles) coming into contact with your materials. When light interacts with a molecule there are a couple of possible affects that can happen (visualised in **Figure 1.4**). Firstly, the photons can pass through the material without being absorbed or reflected so that the emitted photon energy remains the same as the energy of the incoming photon; this is referred to as transmission. Under certain conditions, the photons could be absorbed by the sample, the energy of which can result in a transition between two vibration and rotational modes. The final action that photons can take is ‘scattering’.[86] When incoming photons interact with a molecule, they can cause a disturbance to the electron cloud around the atoms which places the molecule into a temporary virtual state. In the majority of cases, the affected bond will return to its previous

state, scattering a photon with the same energy. But it is possible for the bond to end up in a different energy state, which will allow an inelastic scattering to occur (the implication of scattering is further discussed in **Section 1.4.2**).

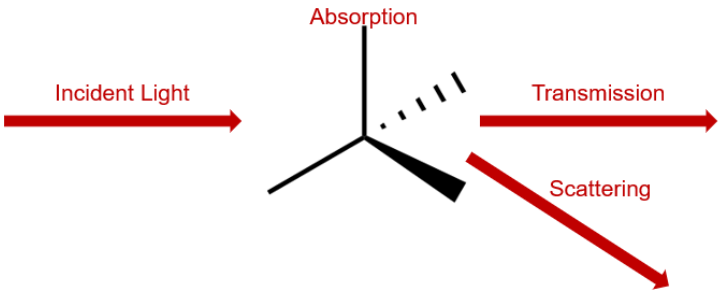

Figure 1.4 Illustration of the 4 processes that can occur when light interacts with a material. The incoming photon can be reflected off or transmitted through the material at the same wavelength. The energy of the photon can be absorbed, raising energy levels of the materials constituent elements. Photons can also be scattered at a different energy to that which they enter the material.

Measuring the energy associated with photons interacting with matter is the basis of spectroscopy. In vibrational spectroscopy the basic principle is that electromagnetic light will pass through a sample allowing absorption, transmission or scattering of the photons. These photons are collected by a detector, presenting results in a spectrum. Vibrational spectroscopy is comprised of infrared and Raman Spectroscopy (RS). FTIR uses the absorption and transmission of photons, whereas RS measures the effect of scattered light.

This branch of spectroscopy quantitatively and qualitatively monitors the effect of radiation on the vibrational modes of different functional groups in the sample.[87] RS and FTIR are complimentary, rather than providing the same information, and an important point of difference between the two vibrational techniques is that RS quantifies relative frequencies at which radiation is scattered in a sample, whereas FTIR defines an absolute frequency where energy has been absorbed.[88] When radiation interacts with a molecular bond a vibration can be induced. If this vibration results in a change in dipole moment, the bond is ‘IR active’ and will be measured in FTIR. The energy of the incoming radiation relates specifically to each chemical bond and a peak will appear in the FTIR spectrum at the specific wavelength.

Similarly, a bond is 'Raman active' if at the specific radiation wavelength, the vibration causes a change in polarisability.[89] The intensity of peaks in these spectra relate to the amount of change to the dipole moment or polarisability. **Figure 1.5** summarises the plausible vibrations, two stretching and two bending modes, for a simple CO_2 molecule. For a centrosymmetric molecule, a bond that is IR active will not be Raman active and vice versa. This simple rule does become complex in molecules without a centre of symmetry, where there can be both strong or weak IR and Raman changes for the same bond. Hence, the two vibrational techniques are often considered as complimentary to one another. While FTIR is able to pinpoint asymmetric polar bonding modes like O-H, RS can distinguish between symmetrical non-polar vibrational modes like C-C and C=C.[88] Essentially polar compounds are less identifiable in RS because of the contrast in electronegativity of the bonded atoms. This is beneficial when considering water, which contains strongly IR absorbing O-H bonds; in FTIR water signals overwhelm the spectrum but in RS water can be used as a solvent because it will not be detected.[88] In the application of vibrational spectroscopy to biomolecules, the individual vibrations of individual bonds are not specifically defined, rather regions of the spectra are assigned to whole molecules/groups of a specific bond i.e. lipids, proteins and nucleic acids that all vibrate at different wavelengths and so appear in different regions of the resultant spectrum. Types of vibrations are denoted separately: ν - stretch, δ - bend, s - symmetric, as - asymmetric.[87] Specific examples and relevant wavenumbers for RS and FTIR are given in the proceeding **sections 1.4.2** and **1.4.3**.

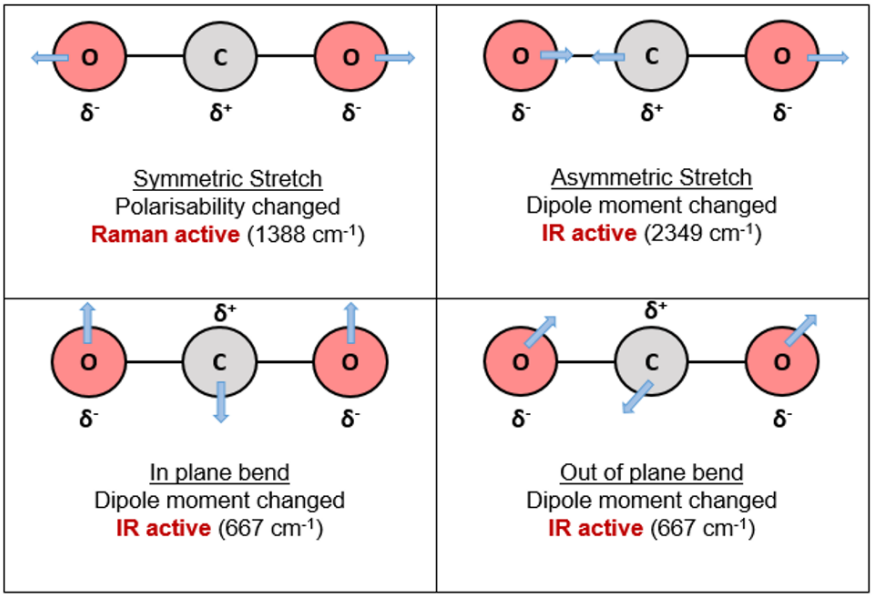

Figure 1.5 Illustration of the vibrational modes, symmetric/asymmetric stretch and bending, exhibited by a simple CO_2 molecule.

In terms of practical application, both techniques afford good sensitivity and have low limits of detection, with Raman frequently evidenced for single cell analytical work. Both methods are can also be non-destructive (there is the possibility of photodamage where lasers are used) and require no additional solvents or chemical agents, making them ideal for biological sample analysis.[87] RS does have the additional advantage of few sample preparation steps and sample constraints, whereas in FTIR sample thickness and uniformity can influence the success of analysis. On the other hand, RS instruments are expensive while FTIR has become relatively inexpensive to run meaning it arguably has a higher viability when considering clinical implementation, especially as a universal method that could be applied in lower income countries.

1.4.2 Raman Spectroscopy

Raman scattering is one type of scattering that happens when light interacts with a molecule.[86,90] Although scattering is fairly common, the scattered light often has the same

energy as the incident light, which is called 'Rayleigh scattering'.[91] Raman scattering is the rarer process whereby the scattered light has a different energy, only occurring for approximately one photon in every 10^6-10^8.[86] When Raman scattering occurs, it will induce nuclear motion allowing photons to scatter at different frequencies (an inelastic process).[86] Raman scattering is split into two varieties: Stokes (energy transfer from the photon to the molecule) and anti-Stokes (energy transfer from the molecule to the photon).[86] RS is the vibrational technique which relies on the target molecule experiencing a change in polarizability to produce a Raman signal.[86] The spectra produced will act as a unique signature for the analyte.[92] **Figure 1.6** depicts the key instruments required for the collection of a Raman spectrum. RS commences with the irradiation of a sample with a laser source; the typical range of acceptable laser wavelengths is 1064-450 nm.[93] The sample will then give a Stokes response, in most cases, because the majority of analysis occurs on samples in their vibrational ground state. An anti-Stokes response would occur if the analysis was in an elevated vibrational state and through laser exposure and scattering the sample is placed in it's ground state; this would result in a scattered photon with more energy compared to the incoming photons. This goes through various filters to remove the more common and less important Rayleigh scattered light. The photons will next move towards the grating system in the Raman spectrometer which disperse the light onto the detector.[94] A Charged Coupled Device (CCD), the most common detector available, will allow each frequency of light to be collected separately to construct the spectrum.[94–96] Each pixel is representing a portion of the spectrum.[97]

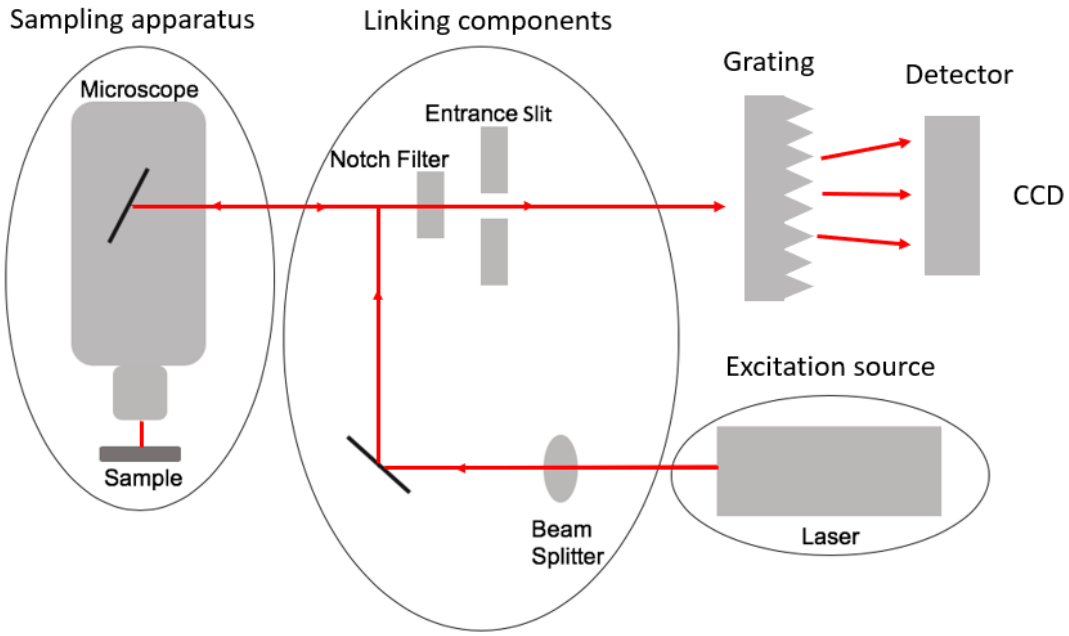

Figure 1.6 Key components required for RS include the laser source, sample apparatus, linking component and detector.

RS, though a highly important analytical tool, experiences various issues. Firstly, the excitation laser must be selected such that the power does not result in the photodegradation of the sample.[98] However, the power cannot be heavily reduced as the Raman signal will be meaninglessly small. The presence of fluorescence also causes issues in the spectra, as it increases background noise, making it more challenging to decipher the real Raman signals. This signal to noise ratio is arguably the largest influence on the conditions used for a Raman analysis.[99]

RS has been extensively explored and exploited throughout the last century, resulting in different variations of the original technique. Raman Microspectroscopy (RMS), the coupling of standard RS with confocal microscopy, allows the laser to focus onto the analyte to enhance resolution.[100,101] RMS is advantageous due to its non-destructive nature, providing the laser and conditions are carefully selected.[102] There is no requirement for pre-processing or labelling of samples, and results can be retaken to ensure reproducibility.[98] For these reasons, RMS is often applied to biological analytes. RMS also allows imaging in the z-plane, therefore three-dimensional images can be produced that provide chemically rich information.[103] Individual cell

components can be separated and visualised, as reported by the Ashton group.[103] This is achievable because each component within a cell will result in a different peak, for example nucleic acids typically peak around 780-800 cm^{-1}.[103,104] This technique is a crucial improvement upon standard microscopy techniques for all cell analysis, including for microorganisms, because it can lower the cost of generating a wide range of detail with a quicker analysis time.[85] Due to the chemical specificity obtained from biological analytes, RMS analysis is slowly becoming an established technique for the examination of microbial cells. Generally, different microbes can be distinguished by small variations in the cell wall composition which produce distinctive Raman signals.[85] Individual bacterial species, like all analytes under Raman analysis, produce unique signatures in the resultant spectra (example given in **Figure 1.7**). The peak assignments for various cell components are available within the literature.[105] Intuitively, many researchers have applied RS to study microorganisms in different ways. For instance the Park group studied the successful removal of bacterial cells with antibiotics.[106] It has recently become clear that RS is capable of differentiating between bacterial samples at the strain level in centrifuged sputum samples.[107] In comparative studies, the Donose group examined electrochemically-active biofilms to distinguish between the various regions and attempt to highlight colony communication mechanisms.[108] Some recent work has progressed from this to the exploration of biofilm development.[109,110] One study by the Lu group even began to highlight the biomarkers associated with the different stages of biofilm development.[111]

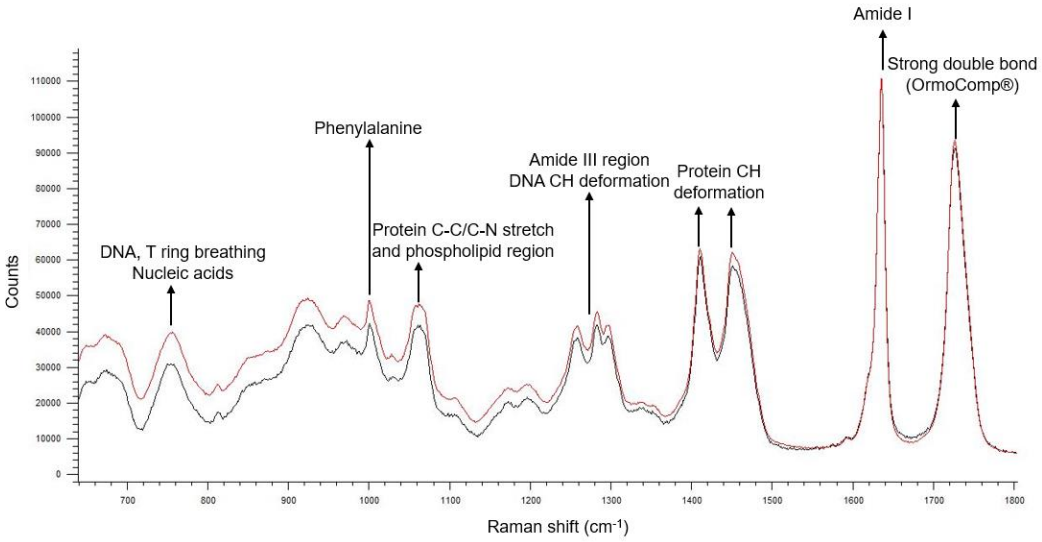

Figure 1.7 Example of Raman spectrum showing a potential peak distribution found in bacterial samples. Spectrum produced during work presented in **Chapter 2, section 2.3.2.1**. The two spectra relate to a *S. epidermidis* biofilm (red) and the polymer scaffold OrmoComp (black).

Although reports exist in this area, the use of RMS to elucidate biofilm diversity has not be extensively exploited. While research is more prominent for microbes in general terms, the work rarely extends to biofilms. Various gaps exist such as the development of biofilms on different surfaces and the potential chemical differences this induces. Using RMS for two and three-dimensional analysis of biofilms would allow current assumptions regarding the formation pathway to be evidenced. From the collection of single spectra, three-dimensional images could be visualised of a biofilm colony. Advancing from here, work could move to live-cell mapping of the whole growth cycle; the biomarkers associated with the irreversible stage of biofilm development need to be found to progress understanding.

In reality, biofilms are formed from various microorganisms and each biofilm is not only dependent on the species forming it but also the environment in which it grows.[13] It would be beneficial if cultures could be visualised, directly from patient samples, with RS, speeding up the application of targeted treatment therapies. Moreover the unnecessary use of antibiotics used as an interim solution whilst a diagnosis if formed, is contributing to AMR; we require a targeted approach to prescription to slow the deterioration of our current treatment options.[85]

1.4.3 Fourier-Transform Infrared Spectroscopy

FTIR is a slightly less well-researched spectroscopy for the non-destructive analysis of biological analytes. It has been shown that repeated analysis of the same biofilm does not disrupt the ECM or damage the encased microorganisms.[112] Infrared spectroscopy is the process by which a sample is exposed to IR light from a blackbody source and the interaction of that light with the sample is measured, as visualised in **Figure 1.8**. The process was revolutionised with the invention of the Michelson interferometer. This interferometer works by having the incoming light divided by a beam splitter with one wave going to a static mirror and the second wave going to a moving mirror; this alters the path length difference between the two beams of light. Constructive or destructive interference of the beams will occur because of the moving mirror, producing the interferogram (where wavelengths are given as cosine values). The interaction of the combined beam with the sample is measured; this can either be in a transmission set up where the beam moves through the sample to the detector or in attenuated total reflectance (ATR)-FTIR, the wave moves through the surface of the sample and is reflected back towards the detector. The interferogram, a plot of intensity and wavelength as a function of time, is then computed using Fourier Transformation to gain a spectrum displaying the intensity plotted against wavelength.[113] The mid-infrared region is classically applied for the FTIR analysis of microorganisms, meaning the wavenumbers focused on are 4000 – 400 cm^{-1}.[114] Peak positions relate to the specific bond vibrations (C=O, CH_2, CH_3, C-O-C and O-P-O) that belong to proteins, phospholipids, amino acids and carbohydrates in biological samples.[115] FTIR spectra from microorganism samples are highly complex with adsorptions in almost all spectral regions. FTIR spectroscopy is in routine application for analysis of natural materials.[116] Recently, spectroscopy has emerged as a major tool for biomedical applications and has made significant progress in the field of clinical evaluation.[117]

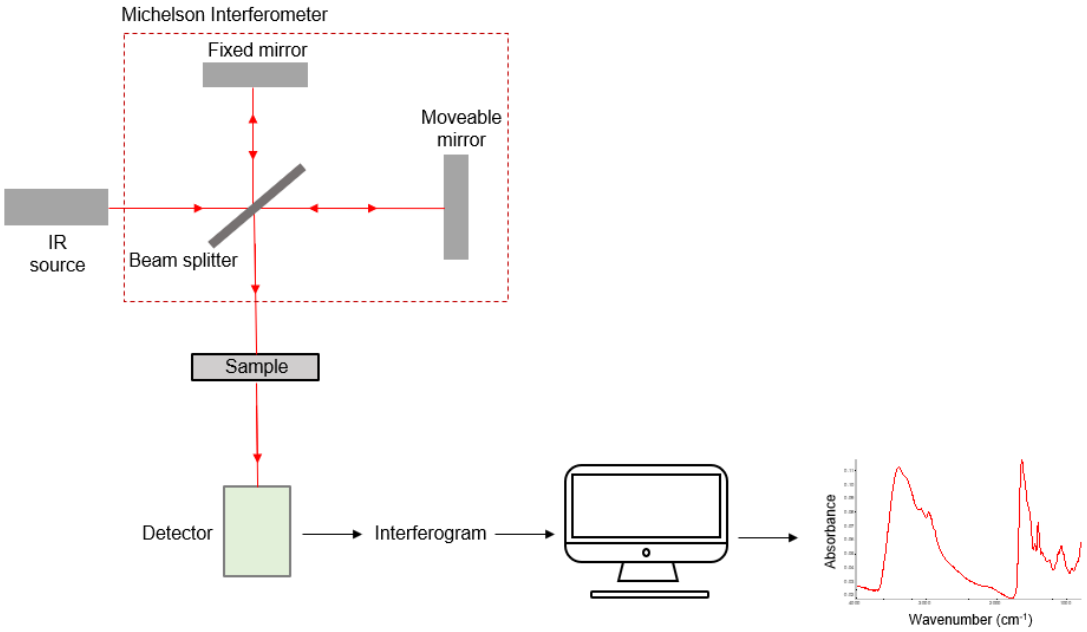

Figure 1.8 Spectrometer components used in the collection of FTIR analyses, including the laser source, sample apparatus, detector.

The use of FTIR to classify microorganisms took off in the late 20th century.[113,118] **Figure 1.9** displays an example of the spectra which are produced by biofilms, split into the three main wavenumber sections. The lipid region reflects hydration; water content will broaden this region. In the protein region shifting indicates change to chemical composition of the protein structures of the microorganisms. Finally, alterations between samples in the DNA region will usually be co-incident with protein deformations because all proteins are derived from these amino acids. One of the first FTIR studies, conducted by Flemming gave evidence to the hypothesis that spectroscopy could be used to denote chemical signature discrepancies between microbe samples at the strain level.[119,120] Since this, research topics have extended to encompass a wide range of microorganisms and the biofilms they form, incorporating live cell monitoring and investigating environmental impact on biofilm composition.[121–123] Furthermore there have been studies that interrogate the processes by which sessile cells adhere to different surfaces and the preferred conformation different species adopt.[124] The key issue with this use of spectroscopy in biological modelling experiments, is the influence that culture media can have on the spectra. All constituents of the sample composition will be included in the final recording, therefore background chemical signatures from the media will be visible. Only spectra for

samples of the same basic constitution (microorganism strain and culture media), produced under the same culture conditions (temperature, growth container, aerobic/anaerobic), should be directly compared.[125] FTIR can be used as a sole analytical tool, though it is often applied in conjunction with standard microbiological practices to validate the findings. In one set of experiments the Yantorno group used FTIR to characterise bacteria, complementing their findings about *B. pertussis* biofilm growth, using the spectroscopy.[126] Although the amount of research dedicated to optimising FTIR for biological sample analysis is increasing, there is a gap in reports for the live analysis of a single biofilm. If this could be achieved, it would conceivably garner understanding about the chemical biomarkers which indicate the shift from the planktonic to biofilm state. Ideally a chemical marker should be found for the irreversible attachment of microbial cells to a surface. By defining the chemical changes that occur during this phenotypic switch, strategies to prevent or delay biofilm maturation on medical devices could be improved.

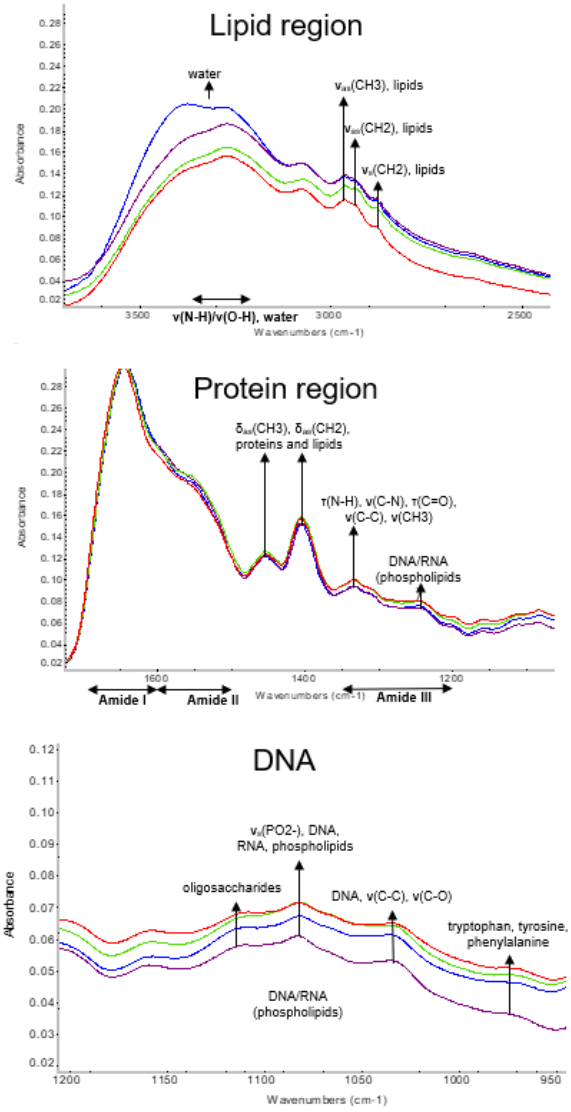

Figure 1.9 Example of FTIR spectra showing a potential peak distribution found in bacterial samples as a biofilm develops. Spectra produced during work presented in **Chapter 2**. The spectra displayed were recorded at 4 different timepoints (24 hr, 48 hr, 72 hr and 96 hr) during biofilm development.

1.4.4 Multivariate Analysis

When collecting vibrational spectra for multiple sets of data, for example biofilm and planktonic samples, it is beneficial for differences in those spectra to be quantified. Whilst in some cases an obvious difference in the peak distribution will be visible, more often different wavelength contributions are subtle across a range of absorption wavenumbers. In order to deduce all

contributions to these spectral differences, mathematical and computational approaches can be used.[127] Chemometrics is the name given to the process of applying multivariate analysis (MVA) to chemistry and biology. MVA permits large data sets, consisting of more than one variable, to be processed simultaneously, with the ultimate aim to evaluate the relationship between each of the variables. Hence, chemometrics are vital when considering spectroscopy where data sets are made up of thousands of variables (i.e. FTIR typically considers wavenumbers from 800 to 4000 cm^{-1} and each wavenumber is a potential separate variable where a measurement is recorded).[128] To use MVA, first vibrational spectroscopic data should be pre-processed such that noise and fluorescence are minimised, cosmic rays are removed in RS; spectra are often normalised and baseline corrected as well to ensure only sample components are considered as significant variance factors between spectra, rather than any influence that may come from the background. By then applying an MVA method, whole data sets can be explored to reveal patterns which are then visualised to either solely provide quantitative evidence of spectral differences or as a prelude to building a classification model where new data can continually be categorised.[128,129]

MVA methods can be separated into two categories: unsupervised and supervised. Unsupervised means that data is inputted into the method without labelling, which is helpful when searching for minor variations between data sets. These methods are most often used before inputting the data into supervised MVA methods. Supervised methods are classed as such because all inputted data is labelled (i.e. 'biofilm' data set and 'planktonic' data set). This approach begins with a training data set to establish the key patterns within the spectra. The model can then be used as a prediction method where new data (i.e. new spectra that have not previously been run in the MVA method) are compared to the model data set and the computational model will assign a label. The accuracy of this prediction is then considered to define the success of the MVA model.[128] These processes can be run on a range of computational software, the most popularly selected are Python, MATLAB, Unscrambler and SIMCA.[87]

Examples of MVA methods that are frequently used in conjunction with vibrational spectroscopy are principal component analysis (PCA), linear discriminant analysis (LDA), hierarchical cluster analysis (HCA), partial least squares (PLS), support vector machines (SVM)

and neural networks (NN).[87,128,130] PCA is the most widely applied tool throughout spectroscopy, especially when used in conjunction with LDA.[129] PCA is an unsupervised method that reduces the dimensionality of data and establishes the degree of variation without minimising it. By comparing all of the spectra to one another after this process, clusters can be formed, grouping together spectra by similarities.[130] In PCA, there is a score plot, illustrating the number of differences found, and loadings plots which demonstrate the peaks that contribute to the differences between the spectra. By assigning the peaks in the loadings plots, the cause of the variance between spectra can be defined. The supervised method LDA can then use the scores results from PCA as the input variables to classify labelled data.[88] Two other MVA approaches frequently applied to microorganism investigations with spectroscopy are: HCA which similarly to PCA is a clustering method where spectra are continuously compared to one another with the outcome of a plotted hierarchy, as the name suggested; and, NNs are a sophisticated machine learning approach which are self-trained, supervised classification systems.[130]

Chemometric usage has become standard practice in the analysis of microorganisms with vibrational spectroscopy, in recent years. Brito and Lourenço exemplified the usefulness of PCA-LDA methods to reveal a complete separation of FTIR spectra between different microorganisms including *Bacillus*, *Candida*, *Staphylococcus* and *Pseudomonas*. Their effective use of PCA reduced the data sets such that the relevant variables could be used to classify the spectra. In computing subsequent LDA, their model correctly predicted the microorganisms with a 94% accuracy.[131] Even more specifically, Tata and collaborators were able to discriminate at the strain level for isolates of *Legionella* taken from various water samples. Once again, PCA-LDA was used to first classify and then predict which water samples contained different strains of the *Legionella* with an overall sensitivity of between 94-99%.[132] In terms of biofilm analysis, the Mahajan group conducted a study using multi-excitation RS to differentiate between *S. aureus* and *P. aeruginosa* from cystic fibrosis patient sputum samples. This group again used PCA first to cluster the spectra by the species and strain of microorganism, before using the machine learning technique SVM to classify spectra, showing a 99.75% accuracy.[107] The application of chemometrics for biological sample analysis has even recently been tested to aid in SARS-CoV-2 diagnosis in the food supply chain, by the Conte-Junior group.[133] This group applied a variation of PLS, PLS-discriminant analysis to achieve

almost 100% detection sensitivity. It should be noted that although all of the example studies given report an MVA method accuracy of above 90%, these approaches have principally been used in pilot studies, as such the samples used are often highly concentrated and arguably do not correctly model realistic samples. For instance, the Mahajan group used artificial sputum samples where the bacteria were in a 1:1 ratio with the other sputum constituents.[107]

1.5 Polymer Coatings for Anti-biofouling Surfaces

Medical device colonization and subsequent infection are a big problem for indwelling blood contacting materials. As stated earlier (**section 1.2.4**) CVC infections, particularly where a biofilm is involved, have a huge impact on patient mortality because of the reduced effect of antimicrobial therapies on biofilms.[64] Reducing the time taken to diagnose the infection, as explored in **section 1.4,** is beneficial but the ultimate solution is to prevent colonization on the devices to begin with. A popular solution is to coat all blood contacting equipment with a non-fouling material that will work to minimise non-specific protein binding, preventing initial microorganism attachment.[65,66] Coating technology has historically included organic and inorganic materials as well as biological compounds.[134–137] A popular approach for medical device non-fouling coating innovation is the implementation of PEO to reduce biomolecule adsorption.[138] The most famous example of a PEO coating, already seen in clinical practice is polyethylene glycol (PEG), which boasts high biocompatibility and crucially prevents protein adsorption.[139] Unfortunately PEG is not thermally stable and it suffers from oxidative degradation, both of which ultimately increase protein adhesion.[139] In addition to this, PEG is not universally applicable.[140] Thus new PEO coating options need to be explored and there is an extensive list of ways this can be done, but only two plasma based methods will be explored in this thesis.

1.5.1 Plasma Polymerisation

1.5.1.1 What is Plasma?

Plasma is the term used to describe a naturally occurring or laboratory produced, completely or partially ionised gas that is electrically neutral.[141] It typically consists of molecules, atoms, ions, electrons and radicals, as well as metastable species and energetic photons (UV). Natural examples of plasma formation include lightening, stars and the aurora borealis.[142] To produce a plasma in the laboratory, several methods can be used but general requirements include a power source to provide a current (alternating or direct) through a gas (which can be something as simple as air), between two electrodes (**Figure 1.10**). Radiofrequency (RF) is one of the most common generators used because it is noted to produce more stable plasma.[142,143] To create a plasma an initial ionisation must occur between the electrodes; random ionisation constantly occurs from the interactions of background cosmic radiation. When an electric field is applied, electrons will be accelerated by the electric field and the field direction will change with an alternating current. Electrons then impact with any present gaseous species; inelastic collisions transfer energy into other forms than momentum. If sufficient energy is transferred by inelastic collision, further free electrons are generated, which eventually triggers an electron avalanche; this is the basis of a plasma. A glow, the most distinct feature of a plasma, is produced by inelastic collisions, raising atoms/molecules to excited states (and relaxation of electrons to lower energy levels results in the emission of a photon). Due to greater electron mobility, surfaces in contact with the plasma (including the electrodes) become negatively charged with respect to the bulk of the plasma. This creates a sheath, which is depleted of electrons.[144] Whilst plasma can be struck at atmospheric pressure or in a vacuum, the latter is the focal point of work given in **Chapter 4** of this thesis. A further feature of the reduced pressure (vacuum) plasmas is that the electron temperature is much greater than in the bulk plasma (atoms, molecules, ions etc). In a glow discharge a thermal equilibrium between the electrons, ions and neutral species is not maintained; the temperature of electrons often sits ~60,000 K as oppose to 300-500 K for all other species in the consortium.[141]

The outcome of generating highly reactive species near a surface is seen in the modification of materials which are placed within the plasma. The bombardment of the surface by electrons, ions or excited chemical components can influence the character of previously inert materials.[143] Surface modifications include, but are not limited to: etching (i.e. removal of surface contaminants); pre-treatment to introduce surface radicals (i.e. as a pre-cursor to surface grafting); or, the deposition of thin films.[145]

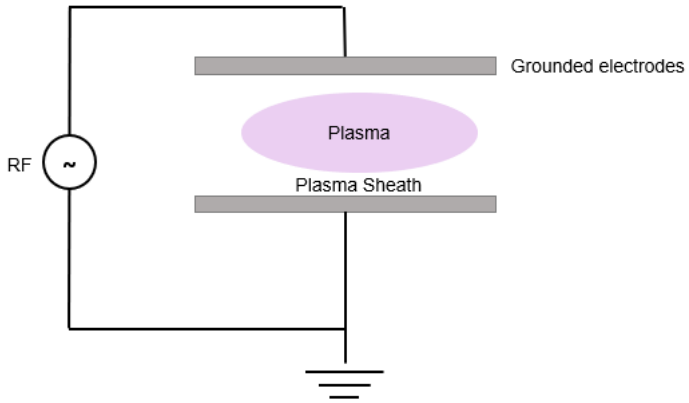

Figure 1.10 Schematic of the basic set up required to produce a plasma glow discharge in the laboratory.

1.5.1.2 How are Plasma Polymers Deposited?

In cold plasma (where only the electrons are at a high temperature), polymerisation can be mediated where the plasma source produces a discharge of a chosen monomer.[146] Plasma polymers, in spite of the name, are not molecularly comparable to conventional polymers, as depicted in **Figure 1.11**, in place of repeating units of the monomer structure, a plasma polymer is formed from a highly dense, cross-linked array of molecules.[147] When a monomer is activated by plasma the molecules partake in fragmentation and rearrangement reactions creating reactive species which near a surface can initiate polymerisation.[148] Plasma polymerisation (PP) can proceed at near ambient temperatures where the electrons continue to break covalent bonds in the monomer gas.[144] The active fragments can then combine at a provided substrate

surface, forming the cross linked structure.[149] PP permits this deposition on most materials irrespective of form (sheet, fibre, textile etc).[150,151] This is a technique that has been in use since the 1960s, with some processes scaled up to a commercial level. A low RF power with the monomer is used to maximise retainment of the functionality associated with the original material, as evidenced later within this thesis (**Chapter 4**).[150,152]

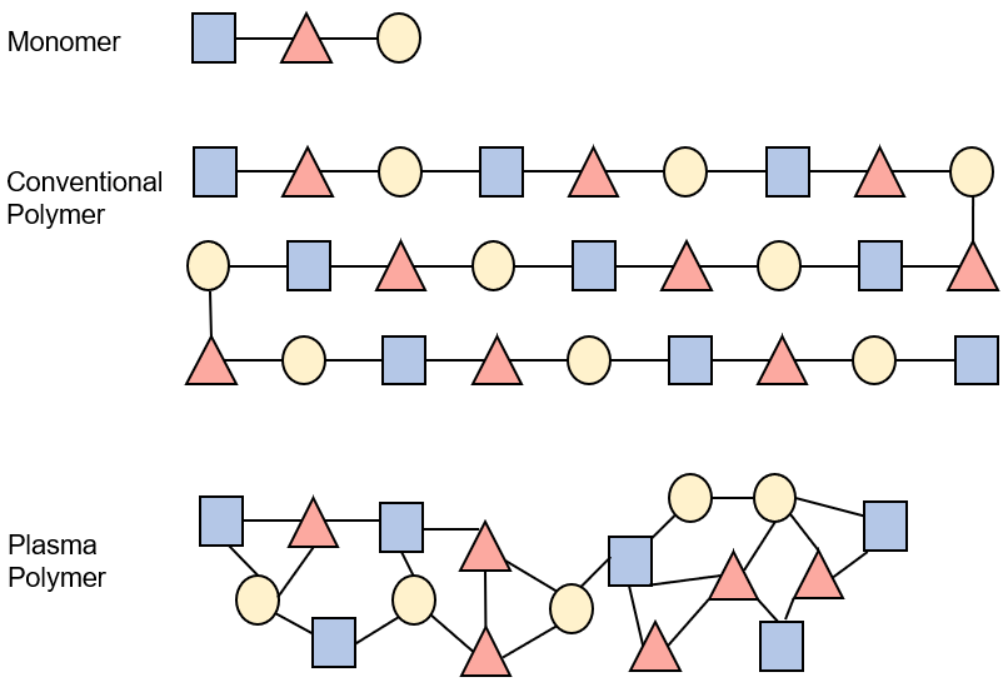

Figure 1.11 Illustration of the key difference between molecule arrangement in conventional and plasma polymers, based on the same starting material (monomer). Reproduced from Thiry (CC license 5853631065309).[147]

The advantages of using PP to form a thin-film coating results from the facile production process. It can often be a solvent-free one-step reaction, carried out at ambient temperature.[150] Once the films are deposited onto a chosen surface it will be dry, making it desirable for a variety of uses.[146] Hence, one area that this technique has found prominence, is for the generation of non-fouling surfaces, for medical applications.

A consistent issue within the field of PP is the translation of results between different reactor set-ups.[151] PP can be divided into two groups: i) plasma-state polymerisation, which

relies on vacuum deposition; and, ii) plasma-induced polymerisation.[141] Work throughout this project to produce a novel thin film coating will rely on the former. Also explored within the project is a material investigation of an existing industrial anti-biofouling coating, that is produced using plasma-induced polymerisation (**section 1.5.2**). Reactor chambers are typically built as required, and so, often comprise various features, specified by each research team. The basic requirements for a chamber (outlined in **Figure 1.12**) are that it is sealable to allow the introduction of monomer as a volatile liquid or gas; and, there must be a method of initiating and maintaining the plasma.[150] To coat a surface, with a functionalised plasma polymer, it must also be possible for the chamber to be placed under vacuum conditions.[146] The chamber should be connected with a continuous or pulsed excitation source.[150]

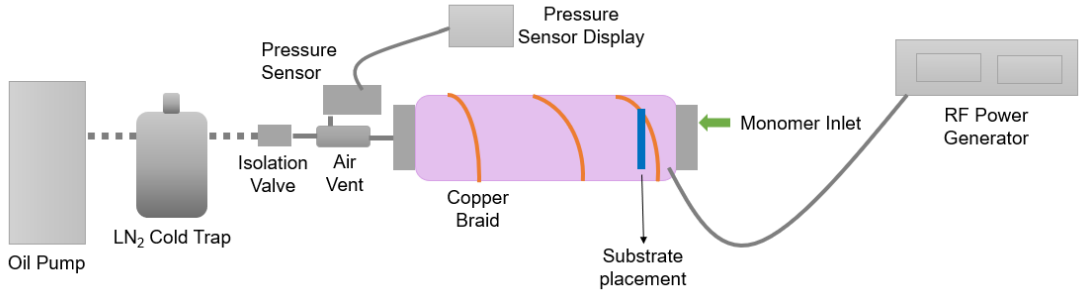

Figure 1.12 Single barrel plasma reactor composed of a glass barrel wrapped in copper braid, connected to a vacuum pump, to maintain low pressure. A RF generator is connected to the copper braid, to allow ignition of plasma. By connecting a monomer solution to the inlet valve and reducing the system pressure, the liquid can be vaporised and upon ignition of a plasma, deposition and polymerisation will occur on a given substrate material.

The process of PP progresses from initiation of the plasma, to propagation (forming a polymeric chain) and then termination (to close the chain).[153] A benefit of this coating procedure is the control that can be yielded over the surface chemistry and particularly in the functional retention from the starting material, which can be used to promote surface hydrophilicity and prevent biofouling. The collisions of the reactive plasma species can be controlled by varying the pressure of the monomer vapour inside the chamber, and the amount of RF power used to

ignite the plasma. The pressure will influence the collisional behaviour of the reactive species; at high pressures (greater than 10 Pa) the glow discharge will be condensed around the electrode (γ-mode) whereas at lower pressures (α-mode) the plasma will occupy the whole space of the reactor barrel. At these lower pressures the electrons are able to move freely around the chamber, obtaining energy from the RF field such that the plasma can be maintained through inelastic collisions; this ultimately means that the deposition process cannot easily be controlled.[154] Power can also exact influence over the polymer surface, by minimising the RF power, or even pulsing it (periodically switching the plasma on and off), which increases the functional group retention. The γ-regime is the name given to systems that operate at high monomer pressure and low RF power, simultaneously, to maximise functional retention in the coating.[155]

1.5.1.3 Monomers to Produce Ideal Anti-Biofouling PP Coatings

Almost any material that can be vaporised could be used as a pre-cursor for PP and many monomers will yield a functionalised plasma polymer, which can be formed directly on the surface of medical devices to prevent biofilm formation.[156] To prevent a biofilm, active dispersal methods must be enforced in the early stages of colonisation i.e. before EPS are produced by the planktonic microorganisms.[26] This can be achieved in a single step by employing monomers in PP with antimicrobial functionality. Some studies apply a two-stage method, first depositing a plasma polymer surface, then affixing an additional antibacterial molecule.[152] An early example of the one-step method, produced by the Prakash group, applied a nitric oxide (NO) coating where NO was released by the coating as an enzymatic gas to prevent bacterial colonisation.[156] NO is a popular example of an anti-microbial group for inclusion in plasma polymer thin-film coatings, because it is reported to work against a wide variety of bacteria.[157–159]. Dispersal of biofilms in the early stage of development has been reported to occur with NO at concentrations as low as 20 μM.[160,161] The common use of NO is due to the chemicals natural presence within bacteria as a biological mediator. Consequently, it is accepted that chemical products containing NO are able to diffuse within a biofilm matrix to affect the cells directly.[156,162]

In addition to NO, other chemicals have been explored in the context of plasma polymer coatings, for example rhamnolipids.[39] These glycolipids, similarly to NO, are already present within the matrix of biofilms. When the level of rhamnolipids is maintained, the biofilm will be stable, therefore, coatings disperse biofilms by incorporating excess levels.[39]

In contrast to the Prakash group, Michl and colleagues reported the application of chlorinated organic monomers to generate a polymer coating.[152] They concluded that a Cl/C ratio of greater than 1.5 will prevent a biofilm for 24 hours, on medical implant surfaces.[152] Following this work, the group progressed onto preventing colonisation of bacteria on equipment with nitrogen-based plasmas.[163] In these coatings, the incorporation of antimicrobial peptides (AMPs) was unsuccessfully explored, as another method to actively disperse biofilms.[163] It was reported that the application of these AMP coatings was nonoptimal for biofilm growth rather than wholly preventative. From the work with AMPs, Michl and colleagues, have recently been looking at chronic wounds and using plasma polymers to encourage the dispersal of established pre-formed biofilms.[164] In this study the stable radical 2,2,6,6-tetramethyl-1-piperidinyloxy (TEMPO), an NO molecule, was used.[164] TEMPO has been demonstrated in PP by various groups.[164] Like many NO coating examples, it is conceivable that the cell-signalling within the biofilm is interrupted by contact with the TEMPO surface.

Importantly, as will be investigated throughout this thesis, plasma polymer coatings that increase the C-O moiety of a surface, have particularly good non-fouling character because they are capable of resisting biomolecule adsorptions.[165–167] PEO-like surfaces are non-fouling because of the increased surface hydrophilicity afforded which prevents the displacement of proteins with pre-adsorbed water, minimising the occurrence of conditioning films.[138] Ethanol is the simplest example of a starting monomer to produce PEO-like coatings in PP reactions.[168,169] The simple, linear structure forms a range of fragments following plasma ignition, including ethylene, acetylene, water and hydrogen molecules, as reported by the Vasilev group following an extensive mass spectrometry investigation into ethanol plasma. Importantly this group also discovered that high power plasmas, which force a higher degree of fragmentation, were linked with a reduction in oxygen functionalisation of the deposits.[168] Earlier examples of PEO-like monomers used to successfully form plasma coatings were tetraglyme and triethylene glycol monoallylether.[170,171] The latter of these monomers was vaporised and the ignition power was

kept low to maximise ethylene oxide retention (determined via X-ray photoelectron spectroscopy), whilst pulsing the plasma. More recently, cyclic PEO monomers (dioxane, 12-crown-4, 15-crown-5) have been trialled in a pulsing regime by the Timmons group. The best coating achieved through this work was made from 12-crown-4 at 25 W (plasma on/off time of 0.1/4 ms); this coating was 150 nm thick and withstood stability testing, with little loss to chemical composition, in the form of PBS exposure (37 ℃, 15 days).[172] Similar depositions were attempted by the Ratner group.[173] While the plasma parameters used in these two studies did deposit coatings with dominant C-O features, the experimental conditions used to facilitate the monomer vaporisation were far too extreme to be viable for industrial application of the process; the monomer had to be heated to at least 100 ℃ to allow vapour formation.

1.5.2 Alternative PEO-Like Coatings

Dendritic polymer coatings were first introduced at the close of the 20th Century when the term 'hyperbranched polymer' was coined.[174] HPG is made from a ring opening mechanism of the starting material glycidol (**Figure 1.13**) which can branch out across the target surface to maximise protection against protein adsorption.[175] These coatings can be benefited with multiple functional properties by introducing myriad modifications to the production regime, for a diverse range of applications.[139] For instance applications range from medical device coatings to prevent implant infection and rejection, to drug delivery systems where HPG can be used to prevent nanoparticles from coagulating together, and even expanding outside of the medical field to prevent biofouling in marine environments.[176–178] HPG exhibits excellent long-term stability, positioning it as an ideal anti-fouling coating for medical devices; it has also been tested against industrial sterilisation methods and showed no degradation of surface functionality.[66]

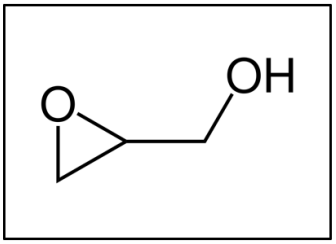

Figure 1.13 Chemical structure of glycidol, the starting material that is polymerised to form HPG.

HPG is easily achieved in a single step mechanism, although many different routes to the formation can be used.[179] Production typically proceeds in one of two ways: graft-to or graft-from regimes. Graft-to indicates the pre-polymerisation of glycidol, followed by the anchoring of the polymer to the substrate surface.[180,181] While the first attempts to graft this polymer used cationic polymerisation, this method proved ineffective when targeting higher molecular weight surface coatings due to chain inactivating side mechanisms.[175] This was rapidly overcome when Sunder introduced the most popular mechanistic route of anion ring opening of the starting monomer, glycidol.[175,182] This group provided the favoured graft-to protocol to effectively produce a hyperbranched coating, under slow monomer addition conditions.[179] Conversely, graft-from protocols require surface activation to promote growth of the polymer directly onto the substrate. In many examples this involves the pre-oxidation of the substrate, made from metallic or plastic materials.[175,179,180] This could happen via a deprotonation of -OH bonds on the substrate surface to initiate the polymerisation reaction, as proposed by Khan and Huck. By deprotonating Si-OH with sodium methoxide, before washing with anhydrous methanol and toluene, then exposing the surface to glycidol this group produced a successful 15 nm coating.[183] Wet chemical methods remain heavily favoured within recent literature, for example the Abu Haija group have explored an Al catalyst and trimethylolpropane initiator with glycidol and achieved a HPG coating evidenced by measuring a low water contact angle (WCA) of between 18-21℃.[184] Besides pure HPG coatings, there are plenty of examples where HPG derivatives have been made, from HPG with terminal thiols grown onto stainless steel to methoxylated HPG grafted onto glass in an anionic ring opening mechanism.[139,185–187]

A facile approach to induce self-initiation of different substrate surfaces to start polymerisation is plasma treatment, as proposed by the Buchmeiser group.[188] This work demonstrated the ability to induce graft-from polymerisation on polystyrene and polyethylene terephthalate by forming a surface oxide layer, without generating chemical waste. Plasma was shown to efficiently induce ion and radical formation at the surface, as explained in **section 1.5.1**, which then promoted polymerisation on contact with glycidol, without the need for further initiating chemicals. The plasma activation time was relatively low (5 min) and exposure to glycidol was 3 hr, at room temp.[188] This work sparked further interest in the potential benefit of plasma which is an attractive option when considering process scalability to coat implantable medical devices en masse.

In several attempts to build upon the earlier plasma activation method, the Terfort group utilised O_2 plasma, with an activation time of 2 minutes on steel, aluminium and silicon, followed by 140℃ incubation for 24 hours in glycidol, yielding a 20 nm HPG coating.[189] But this work did not use pure glycidol, instead a 10 wt% solution of glycidol in N-methyl-2-pyrrolidone was used and consequently it was found, through fluorescence microscopy, that bacterial resistance decreased as the coating thickness dropped below 17 nm.[189] The plasma activation conditions have been optimised by the Moore group where polystyrene (on silicon) was exposed to an air plasma (100 W, 5 minutes) before immediate submersion in glycidol (100℃, 24 hr), providing a coating of 24 nm thickness.[65] This work ultimately revealed the potential for maximising C-O-C content in these HPG coatings, with %C-O reaching 65.3%, as measured by X-ray photoelectron spectroscopy (XPS).[65]

Each previous investigation into HPG formation across the literature has focused on coating a single substrate material; there are few experiments which demonstrate successful coating using a single protocol independent of the substrate. Another issue identified within this area of research is the lack of uniformity in characterisation methods used to identify successful HPG formation. Frequently the WCA is provided as sole evidence for the successful formation of this hydrophilic coating, but this does not reveal anything about the chemical composition of the coating formed by each protocol.[184,187,190,191] It is essential for anti-biofouling coatings to maintain a uniform and pinhole free topography, and this should be proven when new HPG production methods are introduced.

1.5.3 Examining Anti-biofouling Surfaces

The potential for biofilm formation on implantable medical devices has reduced the life span of equipment and led to the overuse of antibiotics in attempt to combat the issue.[192] In recent times polymer coatings have been explored to resolve this because they can be made to prevent microbial colonisation relieving the use of antimicrobials.[193,194] In blood-contacting materials, colonisation can be aided by minimising cell attachment through the prevention of non-specific protein binding.[65,66,195] It is the initial protein adsorption to the surface of an implantable materials that leads to the advantageous development of a conditioning layer to permit device colonisation resulting in complications such as chronic infection.[196] The most common ways to test coatings against biofouling are to expose the surface to different radiolabelled proteins and measure the uptake, or to conduct whole blood contact experiments using fibrinogen as a biomarker for protein adsorption.[172,197]

1.5.4 X-ray Photoelectron Spectroscopy

1.5.4.1 General Principals of XPS

XPS, also called electron spectroscopy for chemical analysis, is a routine technique for surface analysis, particularly in the PP field.[152,163] XPS was first introduced in the 1960s by Siegbahn, and became established for plasma polymer coating analysis in the 1970s, due to the superior sensitivity for the elements present in the top 5-10 nm of a sample.[198,199] The principle of XPS is the irradiation of a sample with X-rays (typically using an Al K_α or Mg K_α source) which photoionise the atoms, molecules and ions present in the sampling area (**Figure 1.14**). Absorption of the photon energy leads to the ejection of a core level electron with varying kinetic energy (KE) that are recorded by an analyser (**Figure 1.15 (A)**).[200] The KE is converted using **equation (1)** to the electron binding energies (E_B) by deducting the KE from the energy of the incoming X-rays (hv) and accounting for the work function of the spectrometer (a constant).

These values relate directly to the element and core level from which they were ejected, and the chemical state of the atom.[201] Spectra are produced such that the number of electrons detected (intensity, measured in counts per second, CPS) is plotted against the binding energy (given in eV). Each element has standard photoemission peaks assigned based on the origin of the ejected core level electrons (1s, 2s, 2p), e.g. C 1s falls at 285 eV and O 1s at 532 eV.[202,203]

$$E_B = hv - KE - \phi_{spec} \quad \textbf{(1)}$$

Another consideration when an electron is ejected from a core level is the 'hole' that remains. The atom is briefly placed in a high energy state and to facilitate relaxation an electron must drop down from a valence level which is energetically reflected by X-ray fluorescence (not seen in XPS spectra) or by the emission of an auger electron (**Figure 1.15 (B)**).[202] The KE of auger electrons (orbitals referred to using K, L, M nomenclature) is distinct from the energy of the ejected electrons.[204] A common example of an auger electron peak is the O 1s KLL peak at 980 eV.

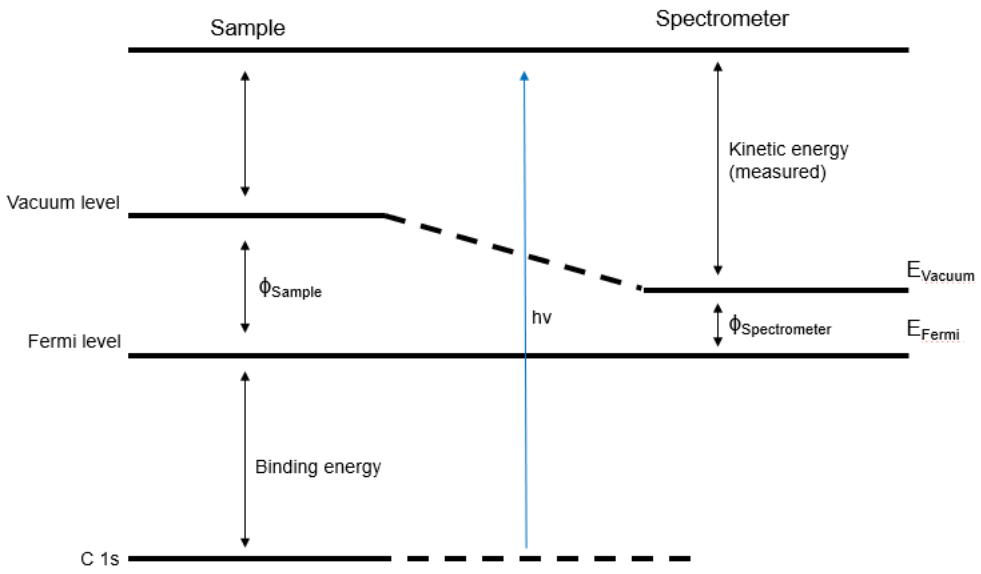

Figure 1.14 Schematic to illustrate that the binding energy of the ejected XPS electron can be calculated by deducting the measured KE and spectrometer work function from the input energy used to eject the electron.

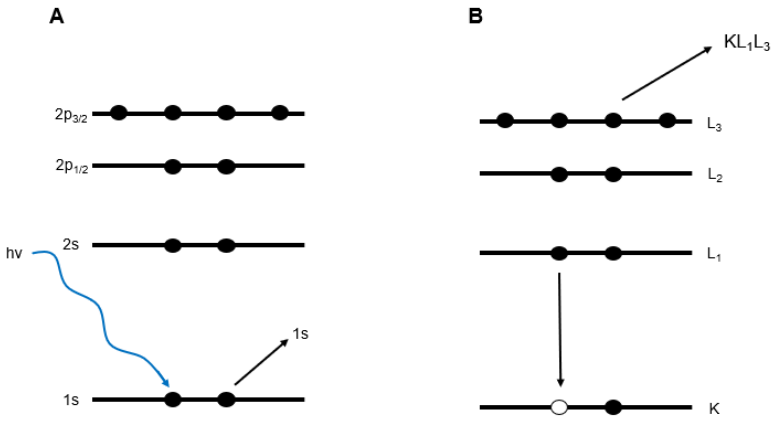

Figure 1.15 Energy levels representing electron ejection of: (**A**) XPS electrons; (**B**) Auger electrons.

1.5.4.2 XPS Instrumentation and The Spectra

XPS requires an ultra-high vacuum (UHV) environment to minimise the chance of the electrons that are ejected from a sample interacting with anything before they reach the detector where the KE is measured. **Figure 1.16** displays a schematic of the basic components that every XPS system is composed from: an X-ray source, sample stage, extraction lenses, analyser and detector.[200] Briefly the electron gun filament is directed to the anode (Al for the Al K_α system used in the work presented in this thesis) generating the X-rays which are directed through a monochromator before interaction with the sample. The maximum anode energy (1486.6 eV for Al) is the variable which controls the electron transitions that are measured, the linewidths and analysis depth (the higher the energy, the deeper into the material).[202] Once the sample has been exposed to the X-rays, the emitted photoelectrons are accelerated through a multichannel detector where electrons are sorted and the energies analysed.

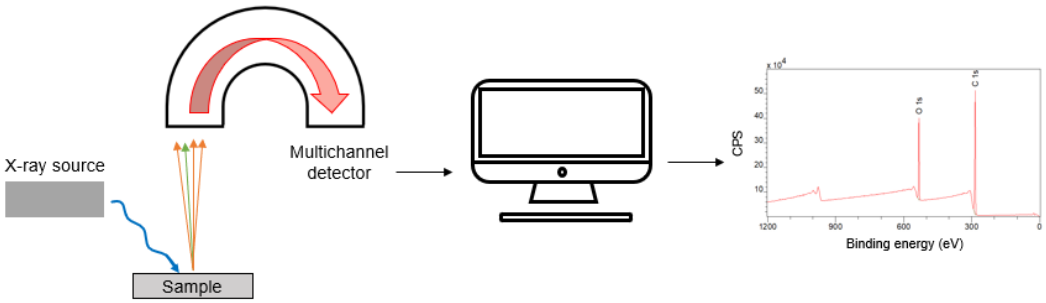

Figure 1.16 Schematic of the basic XPS spectrometer requirements: an X-ray source, sample holder, multichannel detector and computer.

XPS only measures the top 5-10 nm of a surface, despite X-rays penetrating much deeper into the material. **Figure 1.17 (A)** illustrates the different types of electron ejections that are detected in XPS.[202] Electrons that are ejected deeper within the bulk material will experience multiple collisions as they try to leave which causes a loss of energy preventing complete ejection. Some electrons will be ejected from just below the surface level of material and they experience one or two interactions resulting in a slight loss of energy before reaching the detector; these are the most common type of ejections and the degree of this occurrence is reflected in the XPS spectra by an inclined baseline directly leading into the elemental peak (**Figure 1.17 (B)**). The actual XPS photoemission peaks only come from the electrons that are ejected from the top 5-10 nm that lose negligible amounts of energy before detection.

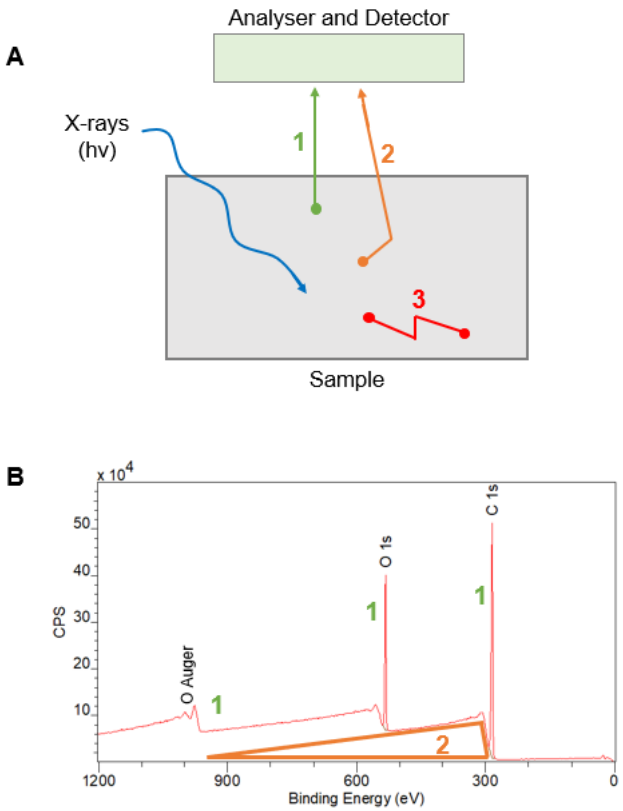

Figure 1.17 (**A**) Illustration of three different types of electron ejection (**1-3**) that occur in a sample following irradiation with X-rays. Electrons ejected by method **1** are reflected as the primary photoemission peaks; electrons ejected by method **2** contribute to the background of the spectrum; electrons generated in method **3** are not seen in the XPS spectrum. (**B**) Example XPS wide scan spectrum revealing C 1s peak at 285 eV, O 1s peak 532 eV and O KLL (auger) peak 980 eV. **1** and **2** are used to denote the two key electron ejections as depicted in part **A**. Reproduced from Stevie. (CC license 5853591427773).[202]

Survey spectra are collected in the first instance which contain the details about elemental composition of the surface, as described in the previous sections. The acquired spectra will require charge correcting to a known reference point with carbon, C 1s, often used (standard binding energy at 285 eV).[200,203] Elemental composition of the sample surface can be determined by comparing the areas of elemental peaks (which directly correlate to concentration of each element). However, as transitions from different elements and different elemental states have different sensitivities, scaling factors, known as relative sensitivity factors (RSFs), must be used to accurately determine the ratio of elemental compositions. In this work the Scofield RSF values in the Casa XPS software were used.

XPS will also elucidate the bonding environments for the atoms measured within the sample. Chemical bonding environment is highly dependent on factors like oxidation state and whether neighbouring atoms are more/less electronegative. These inter-atom interactions change the structure of the valence electrons which has a consequent influence on the core level orbital electrons. This process is chemical shift. Using the C 1s peak as an example, binding energy is increased by having carbon environments where C is bound to more electronegative atoms (i.e. atoms like oxygen draw electron density away from carbon). Therefore, while C-R (R=C or H) has a binding energy of 285 eV, other bonds to carbon result in shifted binding energies: C-N (286 eV), C-O (286.5 eV), C=O (288 eV), O-C=O (289 eV), C-F (>291 eV).

1.5.4.3 XPS Depth Profile Techniques

A valuable application of XPS is in ion milling to elucidate sample composition in the z-axis by irradiating a sample with an ion beam, to remove surface atoms in a step-wise manner.[205,206] Ion milling is importantly able to etch through different organic materials without causing severe structural damage.[205] Historically, monoatomic ion beams were utilised but this inflicted damage to the chemical structure of polymer samples, due to high energy impacts which often limited the ability to analyse the underlying surface; the use of a gas cluster ion source (GCIS, also referred to as gas cluster ion beams) provides lower energy interactions with the atomic surface (illustration of the two ion beams given in **Figure 1.18 (A)**). Although the KE of the cluster is high, the energy is distributed over each atom in the cluster.[207] **Figure 1.18 (B)** visualises the low energy impact cluster ion beams have on a surface. The use of GCISs for surface analysis with secondary ion mass spectrometry is well established and there are many reported cases that use this approach to review organic materials without inducing severe chemical damage.[208] With XPS, the implementation of an ion beam (typically Ar^+) permits the sequential collection of spectra as the sample is milled, to produce a depth profile tracking elemental composition or chemical states as a function of the etching time.[206]

This application of depth profiling is disadvantaged by some issues, such as the preferential sputtering of oxides in metal samples or the chemical reduction of softer organic samples.[206,209,210] Whilst this process has also been hindered by non-uniform sputtering, creating uneven etch craters, which has a knock on effect on depth resolution, recent use of sample rotation has greatly improved results.[206,211] A study by the Alexander group used rotation when depth profiling polystyrene and polyvinylpyrrolidone, revealing incremental rotation of the raster area between each etch and XPS spectral collection, maintained the highest depth resolution.[211]

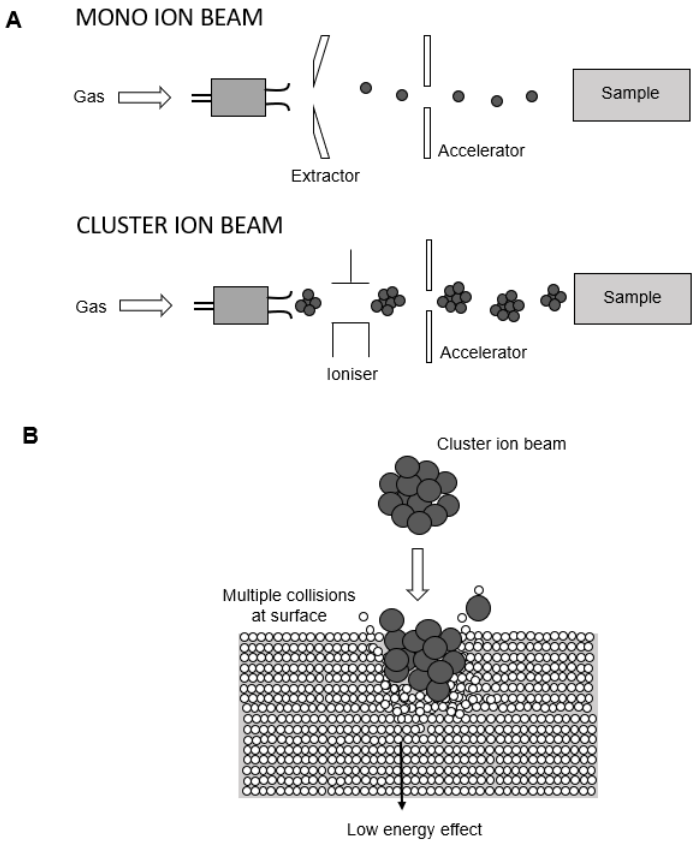

Figure 1.18 (**A**) Illustration of mono ion and cluster ion beams for application in depth profiling XPS, and the basic spectrometer requirements to create these ion beams. (**B**) Visualisation of the advantageous cluster ion beam interaction with a surface to exert minimal damage to underlying atomic layers following surface atom etching. Image redrawn from Yamada. (CC license 5853631295907).[207]

1.6 Outlook

Biofilms exist in all environments and yet they are seldom fully understood. While biofilm existence can be beneficial in some cases, in the healthcare sector, biofilms are a significant threat. In particular the effect of biofilms on CVCs and the resulting infections are vital to the background understanding of this research. While infection as a broad term is considered, the state in which microorganisms live in different infections is not always clear. This is hindered by the understanding of the process of biofilm progression which has been defined, although it is still disputed. To elevate biofilm understanding their chemical composition should be further investigated.

In the currently applied infection diagnostic techniques, samples undergo pre-treatment which not only destroys the integrity of the sample, but also increases the time between diagnosis and treatment. In this thesis, vibrational spectroscopy has been proposed not only as a solution for infection diagnostics, but also as a vital research tool that can be used to analyse biofilm samples without altering the sample chemical composition in any way. In the preliminary study presented, FTIR has been coupled with a PCA-LDA chemometric method to highlight the chemical biomarker for the phenotypic switch between planktonic and biofilm forming microorganisms. Chemometric methods can be useful to reinforce visible spectral differences, as they have been used in this work, but it is recognised that they are more useful when trying to elucidate minor changes.

Despite the clear issue with infection diagnosis and recognising a biofilm infection, in clinical management the equally important issue of infection prevention should simultaneously be considered. AMR is projected to exponentially worsen over the next 25 years and as such, the best option to combat infection mortality as a result of medical instrumentation is exploring preventative tactics. In this thesis the proposed solution is to coat all blood contacting materials with an ultra-thin non-fouling surface. PEO-like surfaces are already well established as non-fouling because of the hydrophilicity that is induced. Therefore, the latter part of this project strove to utilise different variations of plasma technology to develop a clinically viable coating that could easily be applied to all relevant materials.

Chapter 2. Understanding the Chemical Composition of Bacterial Biofilms using Spectroscopy

2.1 Introduction

In this chapter, the application of spectroscopy to understand biofilms will be explored. It was hypothesised that vibrational spectroscopy, namely RS and/or FTIR spectroscopy could be used to diagnose and monitor biofilm progression. Infections become significantly harder to treat once a biofilm has been formed. To improve the prognosis of patients, both with pre-biofilm infections and existing chronic infection, the pathogens and corresponding phenotype causing the issue must be determined rapidly. Current methods of clinical diagnosis are reliant on pre-processing samples by chemically labelling or dehydrating the microorganisms.[77–79] In terms of diagnosis this means the acquisition times to obtain results take more than 24 hours, which has a subsequent impact on viable treatment options. Often general antibiotics will be supplied whilst the diagnostic process is carried out, but this is ultimately contributing to the increasing problem of AMR. Aside from diagnostic practices to detect a biofilm, the development of the generic biofilm is under researched. Methods for biofilm analysis remain rooted in pre-processing which induces chemical change to the microorganisms, preventing longitudinal measurements.

RS and FTIR have been applied in this research alongside routine characterisation methods, to examine the growth of a single biofilm model from individual non-adhering bacterial cells to complex sessile cells. Bacteria has been monitored from 30 minutes incubation to 96 hours to permit the identification of a biomarker for the biofilm phenotype. In the spectra

presented throughout this chapter, there are key changes in the peaks that were identified and these directly correspond to different chemical structures within the samples. Spectral differences were recorded as early as 30 minutes post incubation, with bacterial samples experiencing vast chemical change up to 24 hours incubation. From 24 hours a plateau of biofilm growth and development was seen in this model.

FTIR has non-destructively provided the opportunity to visualise the chemical components of the biofilm microenvironment. As such, the methods presented in this chapter expose the potential of spectroscopy for standard application in clinical practice to diagnose biofilm infection.

2.2 Materials and Methods

2.2.1 Bacteria and General Culture

Staphylococcus epidermidis ATCC 12228 and RP62A (ATCC 35984) were used throughout this work. Initially, the work was done with the ATCC 12228 strain of *S. epidermidis*, because it was readily available at the Royal Lancaster Infirmary (RLI) laboratory, where the primary work for this project was conducted. But it was quickly found that this strain is non-biofilm forming, as confirmed by previous studies within the literature.[81,212] *S. epidermidis* RP62A was kindly provided by the project collaborators at Glasgow University, and has been used as a model throughout the remaining work. Bacteria was stored on beads at -80°C and revived on Columbia CAP Selective agar for 24 hr at 37°C, as needed.

2.2.2 Biofilm Growth Conditions

Culture media (Sigma Aldrich, UK) was used to propagate bacteria, including Nutrient Broth (NB), Brain Heart Infusion (BHI) and Tryptic Soy Broth (TSB). The culture media (3 mL) was

inoculated with a single colony of bacteria and incubated for 24 hr at 37℃. Following media incubation, the bacterial cell density was measured and diluted to $3x10^8$ CFU/mL using the same culture media. The inoculant was then adjusted to $3x10^7$ CFU/mL, again using the same culture media as the initial inoculant. The substrate, either foil, calcium fluoride (CaF_2) slides or CaF_2 disks (Galvoptics, UK) were incubated in the adjusted media (20 mL) for between 30 minutes to 96 hours. Following this incubation period, samples were removed from the solution and placed in an isolated desiccant chamber for 30 minutes to partially dry, allowing the removal of the bulk of hydration. The desiccant chamber was a sealed Perspex box, containing regularly disinfected Perspex shelves with a silica bead tray directly below the sample shelf. In attempt to control the drying process, all samples were consistently placed within the chamber and analysed after 30 minutes. Fluctuations in room temperature and humidity could not be consistently controlled which led to variations in sample hydration. Following the drying period, samples were analysed with FTIR. As a control measure, planktonic samples were analysed in a similar way; bacteria were looped onto clean substrate and isolated in the desiccant chamber for 30 minutes before spectral acquisition. For the preliminary use of RS, samples were explored both dry and in solution. For dry samples, the protocol described above was followed and samples were transported from the RLI lab to Lancaster University (LU). For samples in solution, CaF_2 disks were removed from the culture media and placed in phosphate buffer saline (PBS) for transport to LU.

Following incubation, a swab was collected from all samples which was looped onto a Columbia horse Blood Agar (CBA) plate, as a mode to check for contaminations. Where contaminations were identified, spectroscopic data was not considered in any final results given in this thesis.

2.2.3 Standard Microorganism Characterisation

The standard characterisation of *S. epidermidis* used to supplement the results in this chapter, was completed by Bryn Short, Laurence Rowan and Prof. Gordon Ramage at Glasgow University. The accurate characterisation of the microorganisms was vital to allow comparison

with the complementary spectroscopic results to be obtained, hence this preliminary work was conducted by trained microbiologists. In short, *S. epidermidis* RP62A was revived on Luria Bertani agar (Sigma-Aldrich, UK) for 24 h at 37°C. Bacteria were then propagated in LB broth (Sigma-Aldrich, UK) overnight and washed by centrifugation. Bacterial cells were suspended in PBS and standardised to $1x10^8$ cells/mL before adjustment to $1x10^7$ cells/mL in the relevant culture media (Sigma-Aldrich, UK). Biofilms were grown for up to 96 hours in the culture media on Thermanox coverslips (ThermoFisher, UK) at 37°C. At various time points (30 minutes and 1, 2, 4, 24, 48, 72 and 96 hours) biofilm media was removed and the resultant bacterial samples were incubated with Alamar Blue (ThermoFisher, UK), prepared in biofilm growth media as per the manufacturer's instructions. The fluorescence of the Alamar Blue was measured in a plate reader at excitation/emission wavelengths of 544/590nm. To quantify the biomass, bacteria was removed from solution by sonication in an ultrasonic water bath for 10 minutes before being serially diluted in PBS and plated on LB agar and incubated for 24 hours at 37°C. All data was plotted and analysed using GraphPad Prism (version 9) statistical significance was determined where $P < 0.05$.

After spectroscopic analysis at the RLI, crystal violet (CV) staining was carried out to quickly demonstrate the successful formation of a biofilm. This was done without the aid of a trained microbiologist. Samples were stained with CV for 1 minute, followed by Lugol's iodine staining for a further minute. Samples were washed with water and briefly exposed to acetone for 5-10 seconds before washing again. The final step was to counter stain the samples with neutral red for 2 minutes. After washing the counter stain off the slides, samples were dried and taken for visualisation with x50 oil immersion objective.

2.2.4 Raman Spectroscopy

RS was performed at LU using a confocal Raman system (inVia, Renishaw plc, Wotton-under Edge, UK). Excitation lasers of 532 nm (~60 mW power) and 785 nm (~34 mW power) were utilised. Samples were initially analysed in PBS with a x60 immersion objective. A range of spectral collection conditions and objectives were applied to bacterial samples in PBS and

semi-dried, see **Table 2.1**. Single Raman spectra were normalised and base line corrected, as required, in Wire software (Renishaw plc, Wotton-under Edge, UK). Data was also imported and plotted in MATLAB version R2019b (Mathworks, Natwick, MA, USA).

Table 2.1 RS collection parameters tested to optimise the Raman signal for various bacterial samples.

	Exposure time (s)	**Laser power (%)**	**Accumulations**
In Solution	0.3	50	10
	0.3	100	10
	1	100	20
Dry	1	50	20
	1	100	50

2.2.5 FTIR Spectroscopy

A desktop Summit PRO FTIR spectrometer (Nicolet, Thermo Scientific, UK) with iD1 transmission sampling apparatus was used for all analysis. All data was collected using OMNIC Paradigm™ software (Thermo Scientific, UK). Data acquisition was performed with 4 cm^{-1} resolution, accumulating 64 scans over a spectral range of 4000-800 cm^{-1}. A blank copy of each substrate was taken as a background before each spectrum was acquired. Three locations were analysed on each sample to account for varying biomass distribution across the surface of the substrate. Each sample was repeated in triplicate. To ensure repeatable measurements, under sterile conditions, a stainless-steel sample holder was designed and produced specifically for this work (**Figure 2.1**). The sample holders provided with the instrument are simple reusable cardboard envelopes which are designed to standardise the sample area size that allows IR radiation to pass through the sample. However, for microbiology work, the sample

holder needs to be thoroughly cleaned between spectral collections. The multi-functional purpose made sample holder had an insert on one side to permit accurate measurements of smaller samples (1x1 cm^2), as well as markers on the reverse side to ensure CaF_2 slides were analysed at the same three locations in each experimental repeat.

Figure 2.1 Multi-functional stainless-steel sample holder designed for this project, to allow the consistent analysis of a multitude of different substrate materials after incubation with microorganisms.

Initial data analysis was conducted using OMNIC software. Each spectrum was pre-processed with and automatic baseline correction and where spectra have been overlaid, a min-max normalisation was applied. Unscrambler X (CAMO, Sweden) was then used for multivariate analysis applying PCA and LDA. Each PCA was generated using the fingerprint region and was used to highlight comparisons between the spectral regions with the most significant variance.

2.3 Results and Discussion

2.3.1 Characterising the Bacteria

For this work, *S. epidermidis* RP62A (ATCC 35984) was predominantly selected because it is known to rapidly form a biofilm and is well documented within research where mature biofilms can be visualised after 24 hours of growth.[81] In this project, using the growth parameters given in **Section 2.2.2**, developed biofilms were reported within 4 hours. To validate this, standard

microbiological testing was carried out at Glasgow University, to assess the biofilm growth kinetics of this bacterial strain (**Appendix 2.1**). *S. epidermidis* reliably showed the beginning signs of biofilm development after 30 minutes of incubation. After 1-hour bacteria was reaching between 10^5 and 10^6 CFU/mL and this increased above 10^7 CFU/mL after only 4 hours of incubation. Between 4 and 48 hours, the robust biofilm phenotype was evident, but biomass did not substantially alter. Following 96 hours incubation, the total biomass growing on the substrate rose into the 10^9 CFU/mL range.

2.3.2 Evaluating Planktonic and Biofilm Bacteria

2.3.2.1 Raman Spectroscopy to Analyse Bacteria

The original intention with this PhD project was to utilise RS because it allows in solution, live cell imaging as well as three-dimensional mapping functionalities. To explore the *S. epidermidis* RP62A biofilm with RS, the bacteria was grown onto CaF_2 slides and disks. When viewing bacterial samples in PBS, required to maintain the hydrated structure of the biofilm matrix, the spectra produced contained a high degree of noise (**Figure 2.2 (A)**). Although a couple of peaks were detected, the dominant feature of these spectra was the overwhelming phenylalanine contribution at 1003 cm^{-1} which comes from media solution that the sample was preserved in. It should be noted that when analysing live samples in solution there was visible movement of the microorganism cells away from the path of the laser. This may in part explain the increased difficulty in sampling. In an attempt to improve the Raman peaks observed for the bacteria, samples were monitored after a period of drying, where the bulk of hydration was allowed to evaporate. Dried samples did result in Raman spectra with the expected peak distribution, as shown in **Figure 2.2 (B)**.[105] For bacterial cells the following peaks are expected: DNA, nucleic acids (700-800 cm^{-1}); phenylalanine (1002 cm^{-1}); protein C-C/C-N, phospholipids (1050-1100 cm^{-1}); amide III, DNA C-H (1300-1200 cm^{-1}); protein C-H (1480-1440/1420-1390 cm^{-1}); amide I (1650-1600 cm^{-1}). When using RS, key conclusions about spectral acquisition were identified. Firstly, it was found that the 532 nm laser produced spectra with less interference (noise and

fluorescence) than those produced when using the 785 nm laser. This may be a result of the laser incompatibility at the higher wavelength with the microorganisms cells or the surrounding EPS matrix forming a fluorescence band at 785 nm, masking the useful biofilm features.[85] Furthermore, by increasing laser exposure time from 0.3 s to 2 s and allowing up to 50 accumulations, successful spectra could be produced without visibly damaging the bacteria.

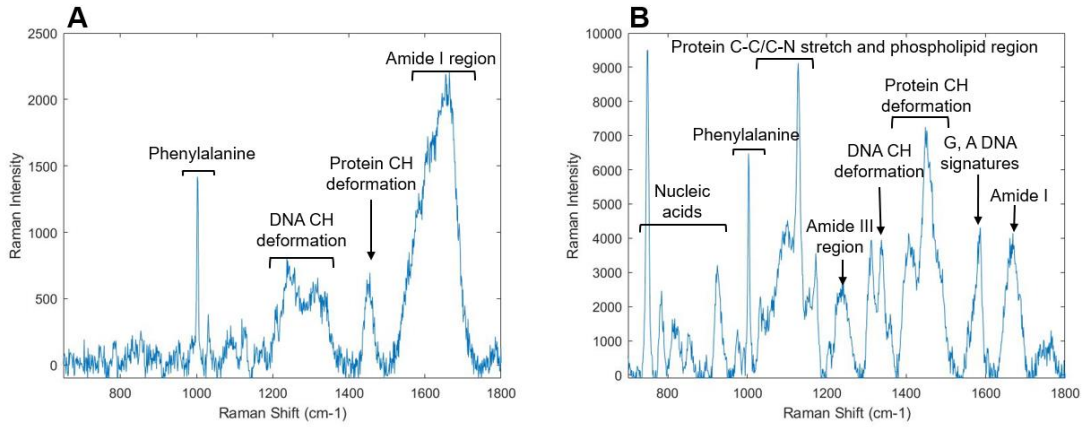

Figure 2.2 Raman spectra for a *S. epidermidis* RP62A biofilm (24 hr incubation) analysed with a 532 nm laser. (**A**) hydrated biofilm monitored in PBS solution; (**B**) dehydrated biofilm monitored in air.

Despite multiple attempts to elucidate the protocol for visualising live bacterial samples, consistent biofilm development was not recorded. The use of RS has been successfully used in previous studies to explore biofilms and particularly to characterise biofilms by strain, rather than monitoring a single developing biofilm, as was the aim of this study. However, these methods generally rely on centrifugation of samples to produce bacterial pellets which are then analysed spectroscopically.[107] In this research project the motivation to use spectroscopy was rooted in the lack of sample preparation required. To make the process clinically viable, samples would ideally be taken from a patient and run directly under spectroscopy. To this end, the focus of this PhD was shifted from RS to FTIR which has been evaluated as a mode to quickly and non-destructively analyse undisturbed biofilm samples.

2.3.2.2 Exploring Different Substrate Materials

Selecting the substrate to grow microorganisms onto is important when planning spectroscopic work. Although the blank substrate background will be subtracted from the sample spectrum, it can cause interference which in some instances will mask valuable analyte peaks. In this FTIR work, biofilm growth was attempted on foil as well as CaF_2 slides (1 mm thick) and disks (2 mm thick). CaF_2 is an ideal substrate material for FTIR because it is 'spectroscopically silent'. Foil does offer a more cost effective alternative and could be an ideal candidate when transitioning this technique to standard clinical practice.[213] Foil and CaF_2 can be examined under the same spectral collection parameters but, whereas in transmission, vertical FTIR sampling can be conducted on the transparent CaF_2 samples, instead ATR-FTIR must be applied when sampling on foil. Despite attempts to monitor bacteria growing on foil for up to 2 weeks of incubation, the substrate was found to cause severe spectral reflectance issues, as seen in **Figure 2.3 (A)**. Reflectance can be exhibited by a distorted baseline at the low wavenumber end of the spectrum (<900 cm^{-1}) and shifted peaks from where they are routinely observed within a sample. Additionally, on foil the growth of the biofilm appears delayed as the amide I and II regions were distinguishable. More severe reflectance issues were recorded when using CaF_2 disks which meant that for each spectrum, peak information was limited to above 1200 cm^{-1} (**Figure 2.3 (B)**). In this case the peak distortions result from the increased thickness of the CaF_2 window in the disks compared to the slides. The increased sample thickness may be preventing all light from transmitting through the material which could lead to detection issues. Hence, throughout this study, CaF_2 slides have been selected as the most practical substrate material for FTIR work to examine the biofilm.

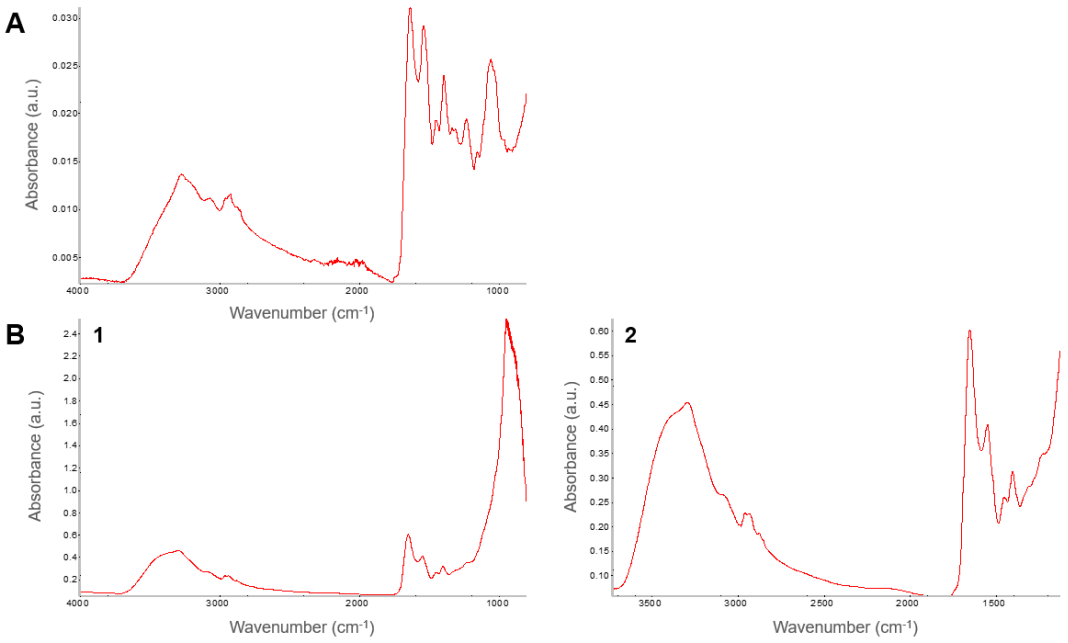

Figure 2.3 FTIR spectra recorded for a mature biofilm, *S. epidermidis* RP62A sample (48 hr growth), highlighting the impact the sample substrate material can have on the resultant spectra, if incompatible materials are chosen. (**A**) Biofilm grown onto aluminium foil. Amide I peak at 1643 cm^{-1}, phospholipid peak centred at 1060 cm^{-1}; (**B**) Biofilm grown onto CaF_2 disks. Spectrum **1** is the raw data produced after sample analysis. Spectrum **2** has been limited to 3600-1200 cm^{-1}, revealing the amide I peak at 1652 cm^{-1}.

To facilitate growth of the bacteria onto the CaF_2 slides, the substrate was placed vertically in the growth media. Whilst this was successful, a gradient of biomass was recorded across the surface of the CaF_2 slide, as depicted in **Figure 2.4**. It is plausible that this is a consequence of the slide being pulled from the culture media, drawing the biomass downwards as each sample was retrieved. Where FTIR spectra have been compared between timepoints, only spectra collected at the same marker point of the slide were considered; marker point 1 was typically selected as an accurate representation of biomass on the surface.

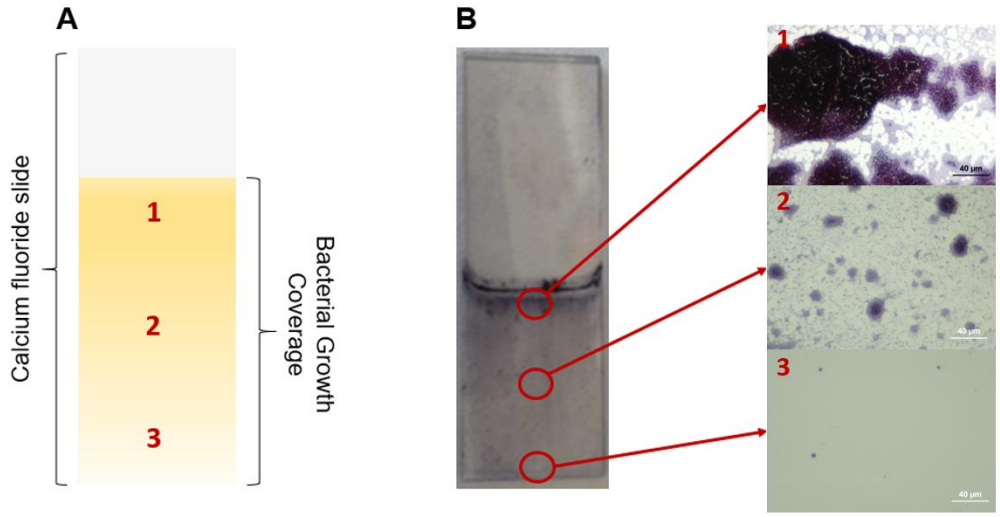

Figure 2.4 (**A**) Illustration of a CaF_2 slide that has been incubated in a culture medium where the lower half of the slide is exposed to the bacteria. The markers 1-3 indicate points at which FTIR spectra were collected, to adequately reflect the difference in biomass across the surface. (**B**) Picture of a CaF_2 slide after 24 hr exposure to *S. epidermidis* RP62A, depicting a mature biofilm. The sample has been stained with CV to visualise the biofilm and distribution of biomass. The microscopy image at marker points 1-3 indicate the reduced biomass towards the base of the CaF_2 slide.

2.3.2.3 Distinguishing Between Planktonic and Biofilm Samples

In standard microbiological testing, it is challenging to distinguish between samples originating from planktonic and sessile microorganisms. **Figure 2.5** depicts specific differences between the FTIR spectrum recorded for planktonic *S. epidermidis* bacteria, compared with the mature biofilm. To achieve a mature biofilm, the bacteria was incubated for 24 hours. From the FTIR spectrum, immediately the lipid region, 3500-2900 cm^{-1} appears to be a differentiating feature. This region of the spectrum is where sample hydration heavily contributes to peak shape because 3700-3000 cm^{-1} is where the O-H stretching vibration mode is presented.[214] The peak centred at 3280 cm^{-1} is visibly broadened in the biofilm sample compared to the planktonic. This was expected because the biofilm is naturally more hydrated than free-floating bacteria due to the EPS that surround the adherent cells.[25] An alternative explanation for this could be the influence of any remaining nutrient growth broth that has been retained within the sample microstructure. The lipid region was the primary cause for employing a standardised sample

semi-drying procedure. Water can overwhelm other components contributing to the FTIR spectrum, so to ensure this disturbance was as consistent as possible, samples were semi-dried. In spite of the semi-drying, all biofilm samples remained consistently broadened in the lipid region, owing strength to the suggestion that this feature results from the presence of the ECM in the samples. To ensure the drying process did not heavily interfere with the results, samples were rehydrated in PBS after FTIR analysis and bacteria was cultured. This also confirms the status of FTIR as a non-destructive analytical technique. Moreover, partial drying rather than total dehydration of the samples was essential to maintain valuable chemical information; dehydration can change the structure of the EPS matrix surrounding the microorganisms.[81] Current clinical practices to identify biofilms often rely on total dehydration, arguably damaging the protein structures within the ECM and the microorganisms. The distribution of peaks in FTIR is reliant on the chemical structures that are exposed to infrared radiation which would be different to the 'natural' biofilm if the sample was first dehydrated. Thus, samples were semi-dried to both prevent overwhelming water signals and ensure the samples represented live biofilms. Unfortunately, in the attempt to standardise water content, natural variation in sample hydration was revealed between experiments. Despite the same growth conditions, each biofilm that grows will have small unique variations which could affect the broadening of the lipid region, due to variable hydration. This meant that peak positions were not largely comparable at the higher wavenumbers, across all data sets considered. It was decided that the lipid region of the spectrum caused too much uncertainty and was not necessary to assess biofilms of differing maturity. The primary analysis was focused on the fingerprint region, 1700-800 cm^{-1}.

The spectral differences observed in **Figure 2.5** in the amide I and II regions at 1700-1500 cm^{-1} are arguably the most valuable when considering defining a biomarker of the biofilm phenotype in *S. epidermidis* RP62A. The ECM is composed of biomolecules such as polysaccharides, proteins, nucleic acids and lipids, by evaluating the relevant regions of the spectrum (the amide regions in particular), the film composition could be determined. Two amide regions are definable in the planktonic sample, but upon biofilm formation these two amide regions merge, leaving a shoulder peak around 1600 cm^{-1}. In addition to this, the average position of the amide I peak shifts from 1653.6 cm^{-1} in the planktonic spectra to 1646.8 cm^{-1} in

the biofilm spectra. Coincident to this are the alterations in the peak region, relating to DNA and RNA structures, 'phospholipid region', at 1085-1060 cm^{-1}, where the centre point of the peak shifts from an average of 1068.6 cm^{-1} in planktonic bacteria spectra to 1082.6 cm^{-1} for the biofilm sample spectrum. Also, there are 2 peaks at 935 and 895 cm^{-1} for planktonic samples which coalesce to a single peak at 919 cm^{-1} when the biofilm has formed. The average peak positions have been generated from 5 separate experiments and the standard deviation of each average was less than 2.2 cm^{-1}.

All of the shifts in peak position, observed in **Figure 2.5** are most likely indicative of chemical differences in the samples being analysed, allowing the conclusion that chemical change occurs as the *S. epidermidis* biofilm forms. Specifically, there is a fundamental change in protein composition that is conducive with the phenotypic switch and ECM formation that is recognised to occur when free-floating cells irreversibly adhere to a surface. Spectroscopy is chemically specific, meaning a shift in peak position indicates a different chemical composition is under inspection. Nonetheless, shifts of 2 cm^{-1} or less have been taken as negligible partly because the resolution of the spectra was 4 cm^{-1} and also there will be natural biological variance between different culture broths.[215,216] If this spectroscopic technique is going to be routinely applied in clinical practice, the error factor needs to be investigated and standardised. An alternative explanation for the downward shift of the amide I peak is the possibility of Mie scattering. Mie scattering is a phenomenon widely reported to occur when the particle size of the analyte is closely matched in size to the wavelength of light being applied. This is reflected in spectra with a 'dispersion artefact' visually seen as a severe decrease in absorbance around the amide I peak.[217] The individual size of the microorganism cells is on a comparative scale to the wavelength of light being applied in this work. As a biofilm develops, the size of the material interacting with the light is changed which will have a consequent influence on any resonant Mie scattering effect. However, comparisons made in this data set do not indicate the derivative-like spectral line shape associated with Mie scattering.

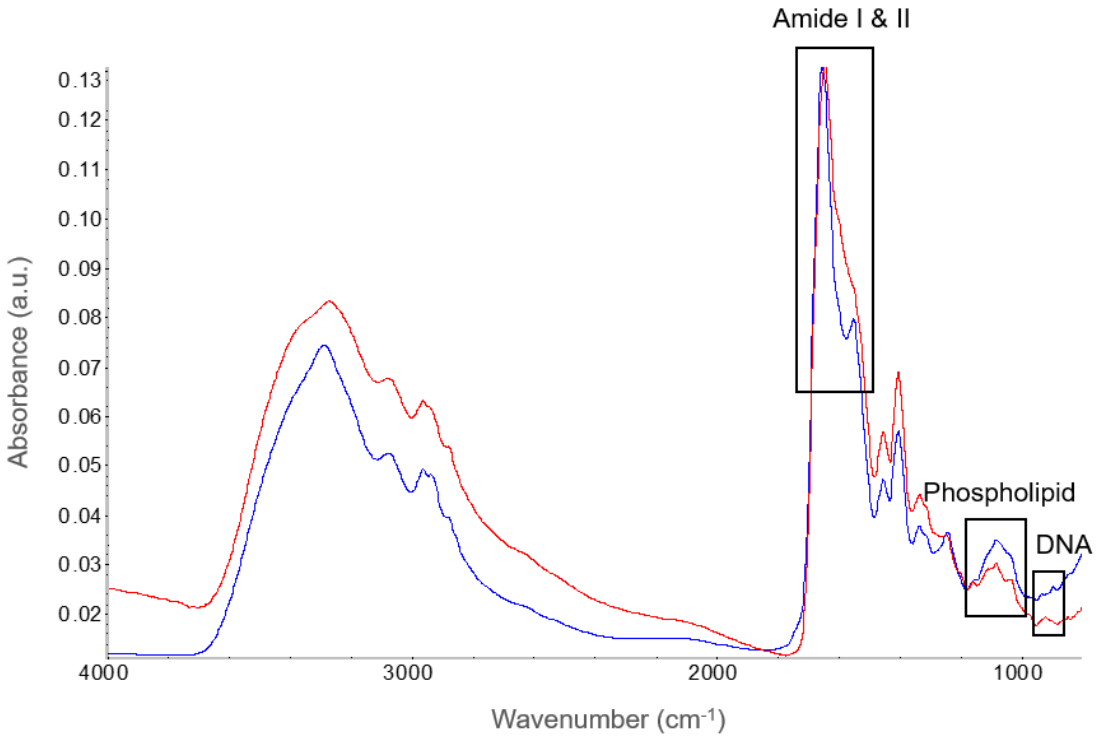

Figure 2.5 Overlaid representative FTIR spectra of *S. epidermidis* RP62A planktonic cells (blue) and 24 hr matured biofilm (red), originating from the same colony. The fingerprint region (1700-800 cm^{-1}) is where the 3 main biomarker peak shifts occur (planktonic to biofilm): amide I (1653.6 to 1646.8 cm^{-1}); phospholipid (1068.6 to 1082.6 cm^{-1}); DNA (935/895 to 919 cm^{-1}).

To quickly confirm the spectral differences between samples of *S. epidermidis* planktonic cells and mature biofilms, MVA techniques were performed on the spectra collected in this preliminary study. PCA is used to highlight the differences between data sets, by separating and quantifying differing spectral regions into sets called principal components, culminating in data points that visibly separate in 2 and 3 dimensions. This was completed on the whole spectrum of the samples, and visualised in 2D, **Figure 2.6 (A)** and in 3D, **Figure 2.6 (B)**. This highlights the clear separation of the planktonic and biofilm data sets. Further PCA data is given in **Appendix 2.2** where the loadings, influence and explained variance plots for the whole spectrum analysis can be found, alongside the PCA for the spectra when limited to only the fingerprint region. This data set was based on 10 repeat spectra and PCA has been quickly used to further visualise spectral differences. To build on this data more results should be collected to improve the accuracy of PCA results. Further to the PCA, LDA was also computed (from inputting the PCA result) to predict which spectra belonged to each data set, planktonic

or biofilm. **Figure 2.7** portrays the result of this method, drawing the conclusion that the FTIR spectra can be predicted to 100% accuracy.

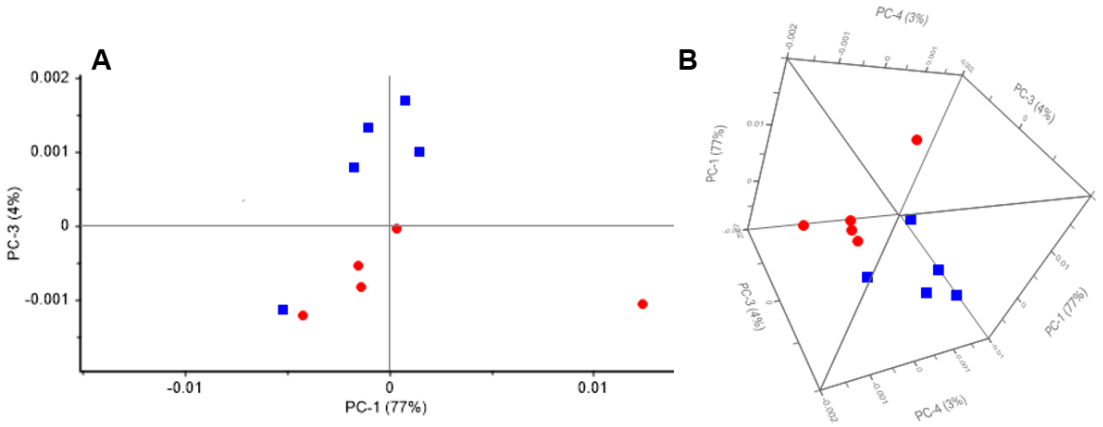

Figure 2.6 PCA scores plot to visualise, in 2D (**A**) and 3D (**B**), the degree of difference between planktonic (blue, square) and biofilm (red, circle) spectra recorded for *S. epidermidis* samples. This PCA utilises 5 experimental results for each sample type.

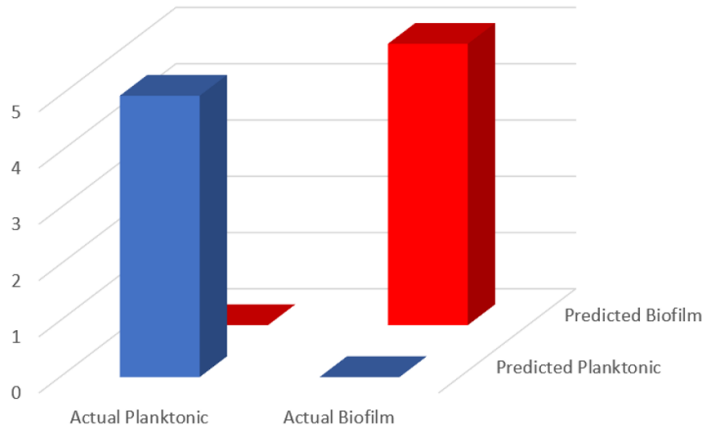

Figure 2.7 Bar plot to represent LDA confusion matrix results, demonstrating the ability of the computational model to correctly predict which group each of the 10 inputted spectra originate from.

2.3.3 Later Stage Biofilms

Late stage biofilms are samples which are allowed to continue growth after a biofilm has formed and developed. For *S. epidermidis* RP62A a biofilm can form within 4 hours and is completely

mature by 24 hours (evidence in **Section 2.3.1** and **2.3.4**). By monitoring chemical changes in mature biofilm samples, as incubation is continued beyond 24 hours, the further establishment of colonies, communication channels and the 3D structure of the EPS matrix could be reflected in the FTIR spectra.

2.3.3.1 Exploring Different Culture Media

Although distinguishing between planktonic and biofilm samples was useful, the primary focus of this work remained whether the progression of a biofilm from early to late development could be spectroscopically tracked. To achieve this, changes in the amide I and II, phospholipid and DNA regions were analysed because these correspond to chemical modifications that happen in biofilm maturation. The 24-hour biofilm model seen in **Section 2.3.2.3** was compared with later stage biofilms, incubated for 48 to 96 hours.

Firstly, to evaluate biofilm growth accurately, the growth media broth was optimised. Three broths were explored: NB, BHI and TSB. From evaluating bacterial growth over three experiments, NB was selected as the best option. BHI caused an issue with inconsistent amide I peak positions and reflectance in the DNA region. TSB was the standard solution recommended by collaborators at Glasgow University. Unfortunately, at the RLI laboratory, limited bacterial growth was reported in TSB. Data to support the conclusions drawn for BHI and TSB are given in **Appendix 2.3**. Whilst NB was chosen as the best growth media available, to add confirmation that the biomarker peak shifts result from biofilm development rather than from the broth, the non-biofilm forming strain of *S. epidermidis,* ATCC 12228, was incubated for 72 hours in NB. **Appendix 2.4** provides the FTIR spectra which show negligible change in the amide I biomarker region, as well as the lack of deformational change in the phospholipid peak region. Biofilm growth was continued in NB and alongside FTIR analysis, **Figure 2.8** displays the microscopy visualisation of planktonic and biofilm cells of various maturity after staining with CV. The change in biomass density between the planktonic (**A**) and 24-hour sample (**B**) is immediately obvious with a large section of dense coverage on the slide. As the incubation was increased to 48 hours (**C**) the density and surface coverage of the biofilm is

increased such that the underlying slide is only partially visible. As the 3D structure of the biofilm further develops for 72 and 96 hours (**D** and **E**), the image is overwhelmed by indistinguishable biomass and the substrate cannot be seen.

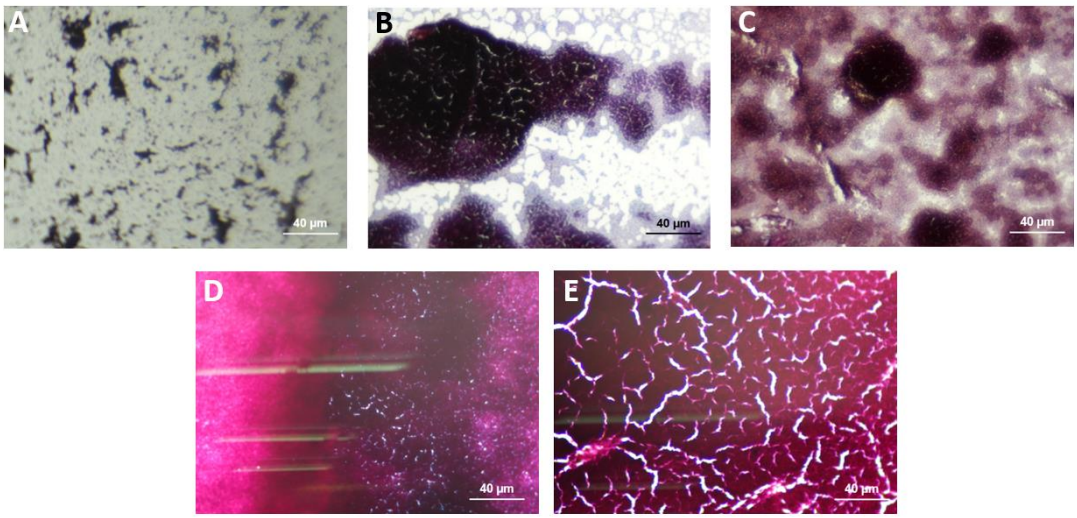

Figure 2.8 Visualised planktonic and biofilm samples under x50 objective in oil. (**A**) planktonic; (**B**) 24 hr sample; (**C**) 48 hr sample; (**D**) 72 hr sample; (**E**) 96 hr sample. All samples stained with CV and counter stained with neutral red dye.

2.3.3.2 Comparing Biofilms after 24 to 96-hour Incubations

Figure 2.9 shows the evident shift between biofilm spectra obtained over 96 hours and the overlaid spectrum for the planktonic bacteria. The broadening of the amide I and II regions is the clearest identifying feature of the spectra with the two regions only remaining distinct in the planktonic sample, permitting the characterisation of the biofilm phenotype. As the biofilm matures, the protein composition is expected to change with the inception and development of the ECM which in turn should cause differing FTIR spectra. However, between the samples incubated for 24 to 96 hours the amide I peak only shifts by 1 cm^{-1}, which is below the decided limit of 2 cm^{-1} indicating the changes between biofilm samples after 24 hours incubation are inconsequential. This suggests that the *S. epidermidis* RP62A biofilm has already matured, hence different chemical signatures are not identifiable. This result was consistently obtained

in repeated experiments. **Table 2.2** states the specific peak assignments related to **Figure 2.9**, for planktonic samples compared to biofilm samples incubated from 24 to 96 hours. The previously decided upon biomarker regions (amide I and phospholipid) are highlighted, with the exclusion of the DNA region which was found to suffer distortions, from spectral reflection, conceivably due to variable biomass on the surface. When minimal peak shifting is recorded, it indicates a small amount of change in the chemical signatures of the biofilm. This could suggest that the biofilm experiences limited growth and development after 24 hours. Or, it could suggest that while the biofilm continues to grow into a 3D structure, there are not any new protein compositional changes to detect.

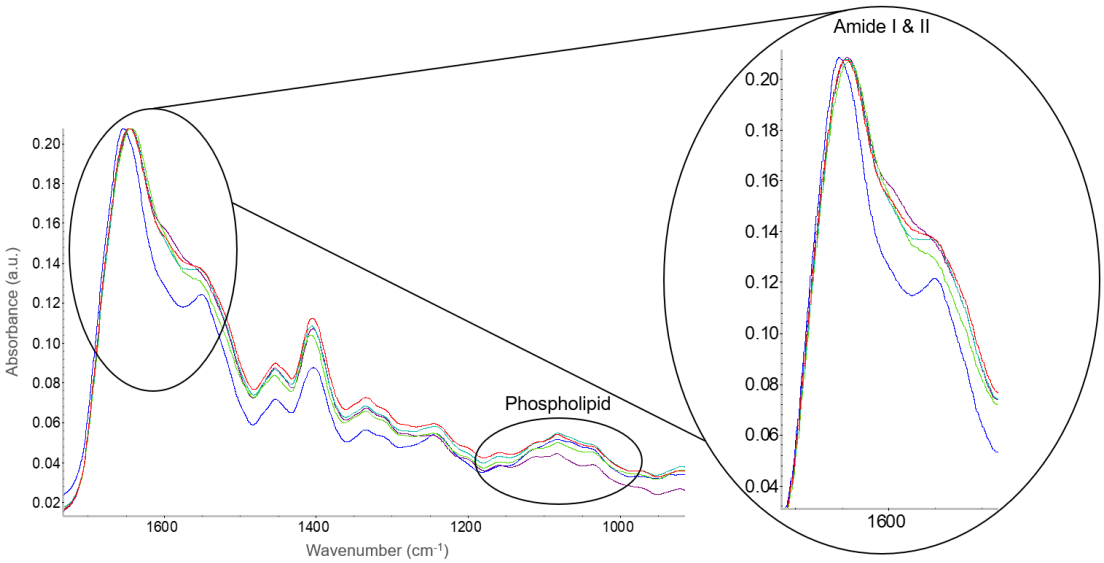

Figure 2.9 FTIR spectra, restricted to the fingerprint region, for *S. epidermidis* RP62A planktonic sample (blue) plotted against biofilm samples grown onto CaF_2 slides in a single broth solution during incubation periods of: 24 hrs (purple), 48 hrs (green), 72 hrs (teal) and 96 hrs (red).

Table 2.2 Complete peak analysis (cm^{-1}) comparing the fingerprint region of planktonic and mature biofilm samples for the spectra shown in **Figure 2.9**. The specific peak positions highlight the lack of peak shifting after 24 hrs incubation as well as the small peak shifts that originate from the natural biological variance factor.

Peak assignment (cm^{-1})	**Plank.**	**24 hr**	**48 hr**	**72 hr**	**96 hr**
Amide I	1653	1644	1644	1645	1645
δ_{as} (CH_3), δ_{as} (CH_2), proteins and lipids.	1453	1454	1454	1454	1453
δ_s (CH_3), δ_s (CH_2), proteins and lipids.	1403	1404	1406	1405	1404
Amide III	1334	1333	1334	1334	1334
ν_5 (PO_2^-), DNA, RNA, phospholipids	1062	1083	1082	1081	1082

To prove the similarities visible in the late stage biofilm data sets, PCA was employed once again as a quick tool to determine any significant differences between the timepoints. From the scores plot displayed in **Figure 2.10** there is subtle separation between the 24, 48- and 72-hour samples, but as the 96-hour samples are included, the data becomes completely overlapped. This may confirm that it is challenging to detect differences in biofilms once the structure has fully matured. It is known from bacterial characterisation that maturation occurs before 24 hours incubation, as explained in **Section 2.3.1**. The early stage of biofilm development is where substantial chemical changes are likely to occur.

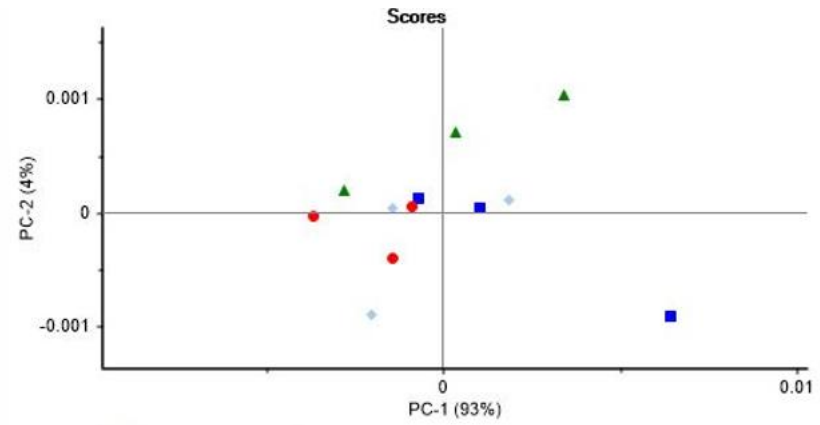

Figure 2.10 PCA 2D score plot showing the differences in biofilm data sets for samples incubated for: 24 hr (square), 48 hr (circle), 72 hr (triangle) and 96 hr (rhombus).

2.3.4 Early Stage Biofilms

As stated *S. epidermidis* (RP62A) develops a biofilm within 4 hours of incubation. The increase in biomass between 1- and 4-hours of incubation which plateaus between 4 hours to 24 hours incubation has been shown and this suggests that most of the changes relating to early biofilm development, attachment and micro-colony formation occur in the first 4 hours of incubation of CaF_2 slides in NB.

Figure 2.11 overlays the FTIR spectra collected for samples from 30 minutes to 4 hours post-incubation, alongside a planktonic sample spectrum. The amide I and II regions are immediately discernible. The amide I region visibly moves to lower wavenumbers as the biofilm forms: planktonic (1652 cm^{-1}), 30 minutes (1648 cm^{-1}), 1 hour (1647 cm^{-1}), 2 hours (1646 cm^{-1}) and 4 hours (1644 cm^{-1}). The characteristic 7-10 cm^{-1} wavenumber shift associated with the phenotypic switch from planktonic to biofilm cells is complete by 4 hours of incubation. This was reproducible across three experiments (**Appendix 2.5**) with the standard deviation remaining below 2 cm^{-1}. Simultaneous to this observation, the amide II region merges into one broad peak with the amide I region. The peak at 1550 cm^{-1}, is only completely distinct in the planktonic sample, before gradually converging with the adjacent amide peak, denoting a fundamental alteration to the protein structure of the sample under inspection.[119] The amide I region chemically derives from C=O stretching modes whereas, amide II is where the N-H bend and

stretch modes appear. These regions result from amino acids in the sample.[119] Amide II specifically relates to the secondary protein structure, so this data could be indicative of the change as the bacteria irreversibly attach to the surface of the CaF_2 slide and the EPS production commences. Despite the gradual decrease and change in the amide I and II regions, there is an immediate shift in the phospholipid peak shape. The peak at 1062 cm^{-1} in the planktonic sample, moves to 1080 cm^{-1} in all subsequent incubated samples, potentially making it a signal for the early surface attachment of bacteria.

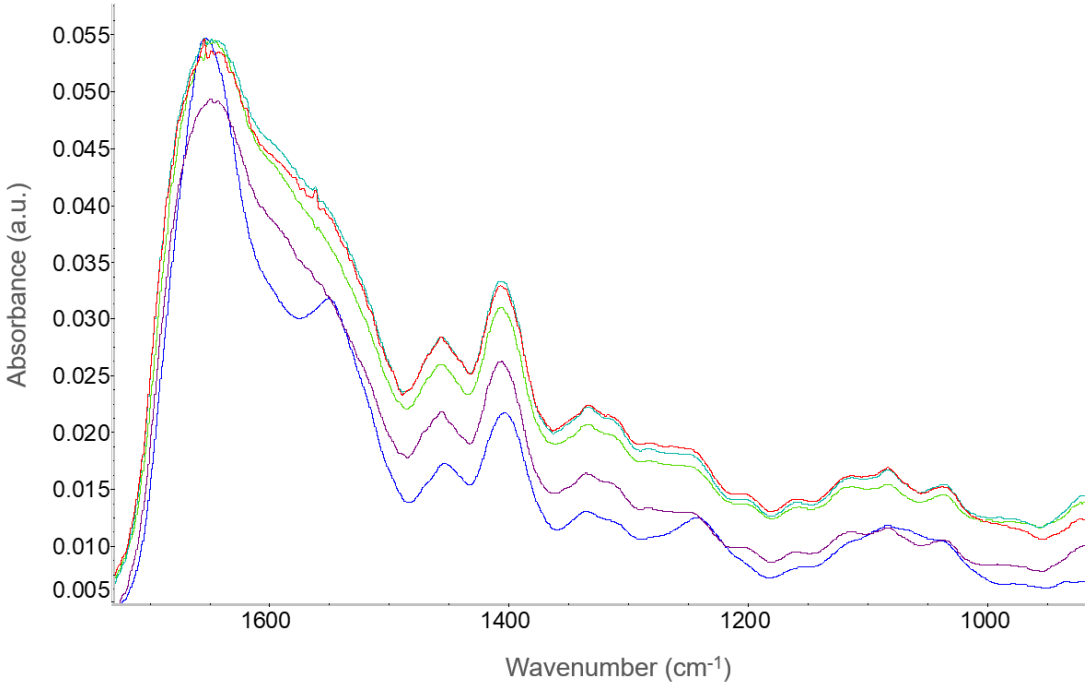

Figure 2.11 Representative FTIR spectra of planktonic *S. epidermidis* sample (blue) on a CaF_2 slide plotted against samples on CaF_2 incubated in culture medium for the following time points: 30 min (purple), 1 hr (green), 2 hrs (teal) and 4 hrs (red).

In an attempt to validate the significance of these findings a PCA test was conducted, the results of which show some overlapping when evaluating the change in amide I peak position (**Figure 2.12**). Broadly, the data sets for 30 minutes, 1 hour and 2-hour incubations appear to have separated out with the 4-hour data set overlapping the earlier timepoints. This MVA requires larger data sets to elucidate any useful information about the significance of the peak shifts.

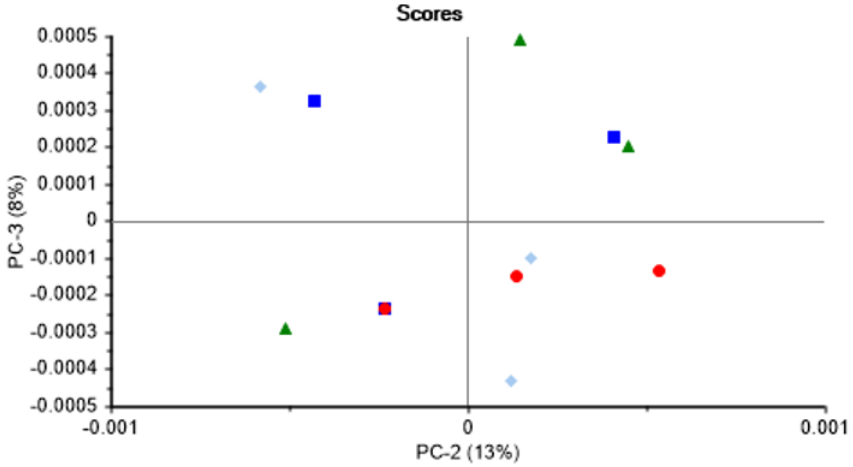

Figure 2.12 PCA 2D score plot contrasting the differences in biofilm data sets for samples incubated for: 30 min (square), 1 hr (circle), 2 hr (triangle) and 4 hr (rhombus).

2.4 Conclusions

In this work a preliminary, spectroscopic study of the mode to *S. epidermidis* RP62A biofilm formation was performed. By directly comparing both early and late stage biofilm development the real chemical changes associated with the existing accepted biofilm formation mechanism (presented in **Chapter 1**) have been put forward for consideration. The amide I and II region of the FTIR spectrum has been recognised as a spectral biomarker to define the biofilm phenotype. Across all work presented in this chapter, the peak shift of the amide I peak was the most obvious indicator for the formation of a biofilm. To strengthen this concept further repeats should be conducted to allow adequately sized data sets for a more comprehensive MVA than was permitted within the timescales of this project.

This work positions the application of FTIR as a viable, non-destructive and rapid tool for the clinical diagnosis of biofilm infections. To strengthen this concept, other biofilm forming microorganisms and multi-species biofilms have been investigated under the same protocol.

Chapter 3. Exploring Fungal and Mixed Species Biofilms with FTIR

3.1 Introduction

In this chapter, the method and findings presented in **Chapter 2** will be expanded to review a fungal biofilm model, alongside a fungal-bacterial biofilm model. The application of FTIR spectroscopy to monitor the evolution and development of a single biofilm has been evidenced. Whilst the foundational study presented in **Chapter 2** provided a guide to the regions of the relevant FTIR spectra and defined the biomarker peaks to identify the biofilm phenotype; the method needs to be applied to a wide range of microorganisms to establish realistic clinical relevance for spectroscopy in diagnostics. *Candida* infections are commonly associated with indwelling medical devices, making them extremely clinically relevant.[62,218] The most common way to diagnose a *Candida* infection is to remove the device, culture the microorganisms and study them microscopically. This is a time-consuming process that extends the time the patient is suffering. As a progression of the work outlined in **Chapter 2**, the logical next step to further validate a diagnostic vibrational spectroscopy method was to determine if the changes observed in one species are mirrored in other organisms. The spectral changes seen in a single *C. albicans* biofilm are reported across a 96-hour timespan, revealing the timepoint at which a biofilm develops and matures.

To further examine the novel application of FTIR for biofilm diagnosis, a mixed species biofilm was modelled. Multispecies infections are the most common and when bacteria and fungus are involved, the clinical outcome is worsened.[61] Fungi cells occupy over 100 times of the physical space compared to bacterial cells, and so can act as a surface for the bacteria to proliferate on.[58,60] The coexistence of *C. albicans* and *S. epidermidis* is common and is linked to the limited lifespan of vascular indwelling catheters.[61] This interkingdom interaction permits

the protection of the individual cells from antimicrobial therapies. Improving the efficiency of diagnosis could lead to enhanced clinical outcomes, therefore FTIR was applied to a *S. epidermidis*/*C. albicans* mixed species model. However, as presented in this chapter, the larger *C. albicans* cells dominate the FTIR signal, restricting the application of this method to single microorganism biofilm analysis.

3.2 Materials and Methods

3.2.1 Microorganisms

Candida albicans (GSK022, GSK107 and SC5314) were stored on beads at -80°C and revived as required by inoculating onto CBA plates and incubating for 24 hours at 37°C, in air. *Staphylococcus epidermidis* (ATCC 35984) was stored and revived as previously described (**Chapter 2, Section 2.2.1**).

3.2.2 Growth Methods

To establish biofilm development, a single fungal strain (*C. albicans* GSK107) was primarily cultured in Yeast extract Peptone Dextrose (YPD, Sigma Aldrich, UK) or for one experiment the culture media was Roswell Park Memorial Institute (RPMI, Sigma Aldrich, UK). A single colony was inoculated into the media (3 mL) and incubated for 24 hours at 37°C in air. Microbial density was measured and adjusted to $1.5x10^6$ CFU/mL by dilution with the same culture media. The microbial density was then further adjusted, in the same way, to $1.5x10^5$ CFU/mL which was then used to seed the biofilm growth system. The substrate, CaF_2 slides, was incubated at 37°C in air in the fungal suspension (20 mL) for between 4 and 96 hrs.

Initially the growth method implemented was exactly the same as the one used with *S. epidermidis*. But it was immediately identified that *Candida* did not grow up the CaF_2 slides (**Figure 3.1**). This was anticipated because *Candida* cells are naturally larger than bacterial

cells.[219] After 96 hr growth, the biomass had accumulated on the base of the growth chamber rather than on the slides.

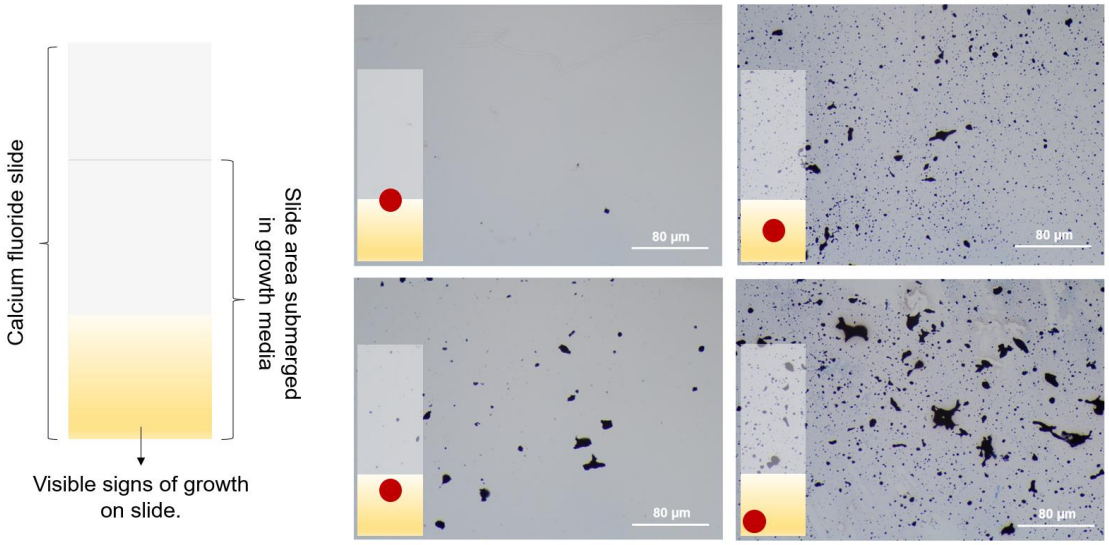

Figure 3.1 CV stain (method given in **Chapter 2**) of *C. albicans* on region of CaF_2 slide where there was a visible change after exposure to the growth media, following 24 hr incubation. Results indicate minimal growth, with the exception of the last 2-3 mm of the CaF_2 slide.

To solve this issue and permit horizontal growth, CaF_2 disks were evaluated but the same issue with spectral reflectance, as seen in **Chapter 2**, were experienced (**Appendix 3.1**). Therefore, new large glass petri dishes were acquired to allow up to 3 CaF_2 slides to be laid flat in a single *Candida* solution. Sample preparation for spectroscopy following the desired incubation period remained the same as previously described in **Chapter 2** (**Section 2.2.2**).

For the mixed species biofilm *S. epidermidis* (RP62A) was inoculated into NB media and cultured overnight at 37°C in air. The resulting bacterial suspension was then adjusted to $3x10^7$ CFU/mL by diluting the overnight broth with NB. *C. albicans* (GSK107) was inoculated into YPD broth and incubated at 37°C in air before adjusting the culture to $1.5 x10^5$ CFU/mL by diluting with YPD. Sterile YPD media (20 mL) was combined with the *C. albicans* culture (1 mL) and the *S. epidermidis* culture (1 mL) to yield the final model solution. CaF_2 slides were incubated horizontally in this mixed culture for 1 to 48 hours and semi-dried, as previously described, for analysis.

3.2.3 Analytical Methods

3.2.3.1 Standard Microorganism Characterisation

Microorganism samples for *S. epidermidis*, *C. albicans* and a mixed species culture were grown onto glass coverslips, following the same protocol as described above. The samples were produced and characterised with light microscopy by Mark Butcher and Prof. Gordon Ramage at Glasgow University. Briefly, to produce the stain mixture, calcofluor white (1.5 µL per 1 mL PBS, 1g/L, Fluka analytical) and Syto9 (1.5 µL per 1 mL PBS, 5 mM, Invitrogen) were combined. The dye mixture (35 µL) was added to each sample and another glass coverslip was placed on top. Samples were incubated in the dark for 30 minutes, after which the coverslip was removed and the samples washed with PBS (1 mL, three times). Next paraformaldehyde (4%, 50 µL) was added and the sample was covered with a coverslip to incubate in the dark for 15 minutes. Once ready to complete the imaging, the coverslip was removed and the sample mounted in the Invitrogen EVOS M5000 microscope using a x40 objective (calcofluor white (blue filter), Syto9 (green filter)).

3.2.3.2 FTIR Analysis

A desktop Summit PRO FTIR spectrometer (Nicolet, Thermo Scientific, UK) with iD1 transmission sampling apparatus was used for all analysis. All data was collected using OMNIC Paradigm™ software (Thermo Scientific, UK). Data acquisition was performed with 4cm^{-1} resolution, accumulating 64 scans over a spectral range of 4000-800 cm^{-1}. A blank copy of each substrate was taken as a background before each spectrum was acquired. All planktonic spectra were recorded by mixing a colony with PBS and drying onto a CaF_2 slide. Three locations were analysed on each sample to account for varying biomass distribution across the surface of the substrate. Each sample was repeated in triplicate.

3.3 Results and Discussion

3.3.1 Candida albicans

3.3.1.1 Planktonic Analysis

In this work, three strains of *C. albicans*, GSK107, GSK022 and SC5314, were available for analysis with FTIR. **Figure 3.2** provides an overlay of the FTIR spectra for each of these strains (full peak analysis table in **Appendix 3.2**). Firstly, as with *S. epidermidis*, the planktonic phenotype is indicated by the sharp lipid region (4000-2500 cm^{-1}), owing to the lack of hydration in the sample which could be explained by the lack of ECM surrounding the microbial cells. Individual cells are likely to have a comparatively lower water content, due to the absence of this surrounding fluid, meaning this region of the spectra does not suffer broadening from excessive O-H bonds in the sample. This is similar to the observations made for the bacterial species *S. epidermidis*, in **Chapter 2**. Between species of *Candida* definitive spectral differences would be expected in the occurrence and distribution of peaks, as seen throughout the literature.[125] Between strains of the *C. albicans* species, the differences in the FTIR spectra are subtle. While the peaks that occur within each spectrum remain the same, the primary difference is the specific peak position of the phospholipid region, where the FTIR signal originates from the PO_2 in the microbial cell polysaccharide membrane. The phospholipid peak falls at 1061, 1049 and 1076 cm^{-1} for strains GSK022, GSK107, SC5314, respectively. Generally, at the strain level, there are not any further significant peak positional shifts that were observed.

From the available clinical isolates, GSK107 was identified as the high-biofilm forming strain and GSK022 is a low biofilm former, as reported in a separate research project that was carried out by O'Donnell at Glasgow University.[220] *C. albicans* GSK107 was selected preferentially for all subsequent work, to efficiently produce biofilm samples.

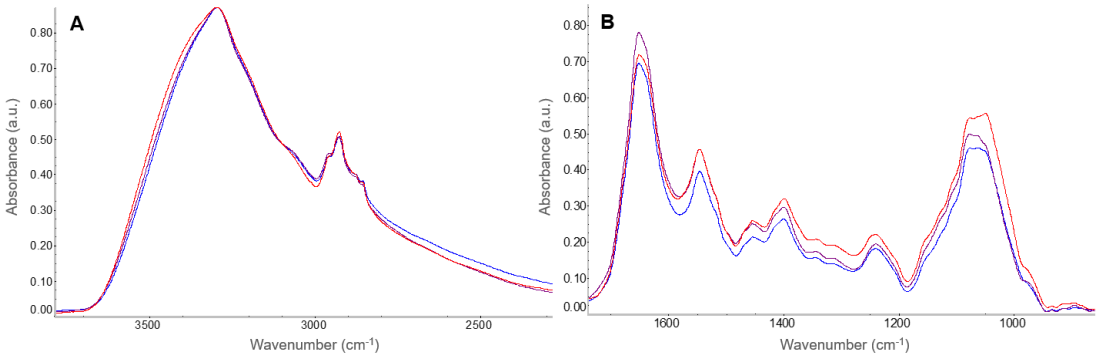

Figure 3.2 FTIR spectra for three strains of *C. albicans* (GSK022, GSK107 and SC5314). (**A**) Lipid region (4000-2500 cm^{-1}) with the primary water peak reported at 3295 cm^{-1} consistently for the three strains. (**B**) Fingerprint region (1700-400 cm^{-1}) where the phospholipid region is the main area of distinction between the three strains, peaking at 1061, 1049 and 1076 cm^{-1} for GSK022, GSK107 and SC5314, respectively.

3.3.1.2 Fungal Biofilm Monitoring

A horizontal growth protocol was established and utilised with CaF_2 slides for all biofilm development where *Candida* is involved. **Figure 3.3** shows *C. albicans* samples following 96 hours incubation, compared to the planktonic sample. The lipid region remains similar from planktonic to 96 hours growth with the water peak position moving from 3286 cm^{-1} (planktonic) to 3279 cm^{-1} (96 hr) and the key lipid peak varying slightly from 2925 cm^{-1} (planktonic) to 2929 cm^{-1} (96 hr). Unlike the immediate and distinct broadening of this region seen with *S. epidermidis*, the evolution of the lipids is more gradual in this *C. albicans* sample with only slight broadening of the peaks occurring at 72 and 96 hr incubation. This may indicate a different ECM composition which should be explored further, but is outside of the scope of this FTIR research study. The main area of focus in this work is the fingerprint region (1700-400 cm^{-1}) where a shift of the amide I region and subsequent change in phospholipid region, are observed. The amide I peak position shift for the planktonic to 96-hour sample is 1651, 1650, 1649, 1648 and 1644 cm^{-1}. The shift between the planktonic and 24-hour sample observed in the spectra is less than 2 cm^{-1} meaning it is reasonable to infer that the cells remain in the planktonic state at this timepoint. From the amide I and II peaks merging, a likely result of increasing sample hydration, it would be a sensible assumption that the ECM development is

established between 48 and 72 hours. In the phospholipid region there is a change in the peak definition from a dominant peak at 1048 cm^{-1} in the planktonic sample to two peaks at (1080 and 1049 cm^{-1}) at 24 hours, alluding to a chemical evolution, and potentially meaning at 24 hours there is not the same free-floating cells. Then at 48 hours the phospholipid peak region changes to a single peak at 1080 cm^{-1} where it remains up to 96 hours. These findings are in keeping with current literature on the development of fungal biofilms where *C. albicans* biofilm development is described with the early phase of reversible surface attachment (11 hrs), EPS production around irreversibly adhering cells (12-30 hrs) and maturation with a robust ECM (38-72 hrs).[24]

Figure 3.4 presents light microscopy images obtained by Mark Butcher at Glasgow University, in collaboration with this work. From the microscopy images, at 24 hours there is a large amount of *Candida* cells which all appear to be planktonic and in the hyphae stage of development. When yeast cells adhere to a surface they form long tails (hypha) which is required for biofilms to develop; this is referred to as the filamentous stage.[8,221] As seen in **Figure 3.4**, at 48 hours the cells have coagulated into clusters and by 72 hours these cells have developed and a denser surface layer is visible. This supports the suggestion from the FTIR analysis that the biofilm development and ECM establishment primarily occurs between 48 and 72 hours for *C. albicans* (GSK107) grown in YPD broth.

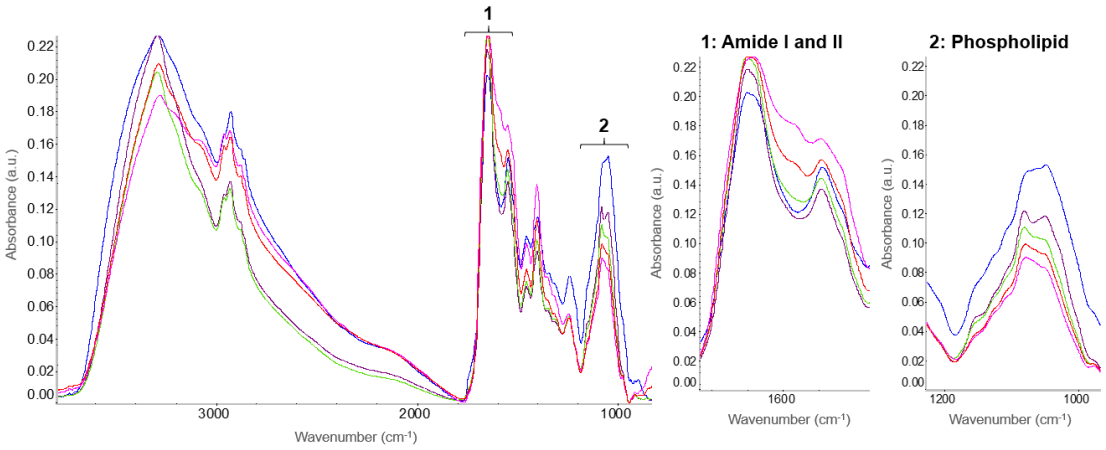

Figure 3.3 Whole representative spectra for planktonic, 24 hrs, 48 hrs, 72 hrs and 96 hrs *C. albicans* growth. The amide I and II regions (**1**) and the phospholipid region (**2**) have been expanded. Amide I shifts from 1651 cm^{-1} (planktonic) to 1644 cm^{-1} (mature biofilm), coincident with a phospholipid region change from 1048 to 1080 cm^{-1} (planktonic to biofilm).

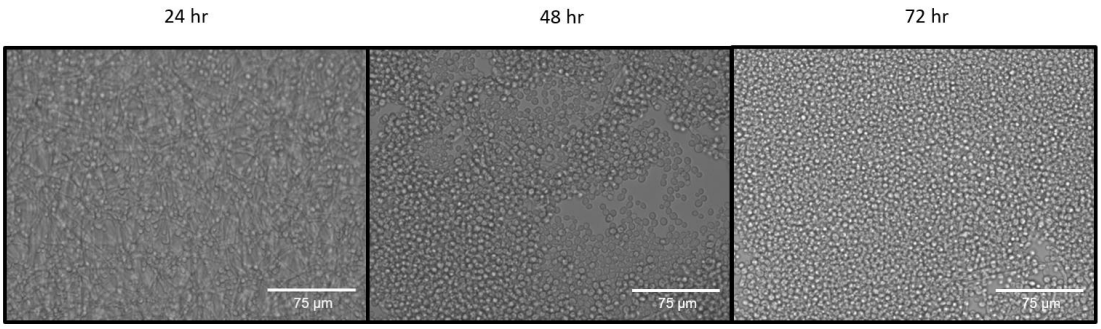

Figure 3.4 Light microscopy images captured (at Glasgow University) for *C. albicans* GSK107 grown in YPD broth for up to 72 hrs: images collected at 24, 48 and 72 hrs.

Before 24 hours of incubation spectral differences between a single *C. albicans* model were not expected. However, when samples were evaluated after 4 hours and 8 hours, a significant change was seen, as represented in **Figure 3.5**. The amide I region downshifts to 1631 cm^{-1} (4 hours) and 1633 cm^{-1} (8 hours) before moving back to 1650 cm^{-1} (24 hours). Within the phospholipid region, immediately two peaks are seen as reported at 24 hours. This spectral change occurs upon seeding of the broth. The lipid region is also broadened at 4 and 8 hours before returning to the sharper definition typically associated with planktonic sample spectra. The FTIR spectra are highlighting the changing dominance of O-H and N-H bonds within the samples; at 4 and 8 hours, the O-H is dominant, but at 24 hours this switches to N-H. This is also evidenced by the merging amide I and II regions which are only distinct at 24 hours. This originally suggested that there might be a vital compositional change that occurs with this species when seeding in the culture media. However, under further investigation it was found that this spectral change is caused by the YPD broth. **Figure 3.6** shows the standard planktonic spectrum (collected by dilution of cells in PBS), plotted against the planktonic cells diluted in YPD media. This spectrum reveals the appearance of two peaks in the phospholipid region at 1078 and 1034 cm^{-1}, alongside the amide I peak at 1637 cm^{-1}. This means that before 24 hours, the spectra reflect only the growth media and the signals do not relate to early composition changes within the microorganisms. As noted at 24 hours (**Figure 3.3**), the amide I peak returns to 1650 cm^{-1} which aligns with the peak position in the true planktonic sample (**Figure 3.6**: PBS). Therefore, it could be assumed that after 24 hours incubation the fungal cells have grown such that the broth is not visible within the FTIR spectrum.

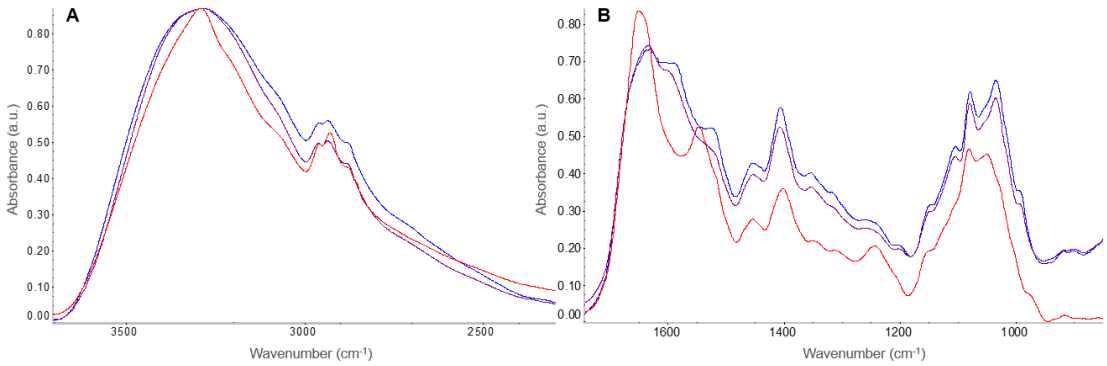

Figure 3.5 Overlay of FTIR spectra collected for *C. albicans* (GSK107) samples incubated in YPD for 4 hrs, 8 hrs and 24 hrs. (**A**) Lipid region (4000-2500 cm^{-1}). (**B**) Fingerprint region (1700-400 cm^{-1}). Amide I moves from 1632 to 1633 then 1650 cm^{-1} at 4, 8 and 24 hrs, respectively. Phospholipid region has 2 peaks at 1078 and 1033 cm^{-1} at all timepoints.

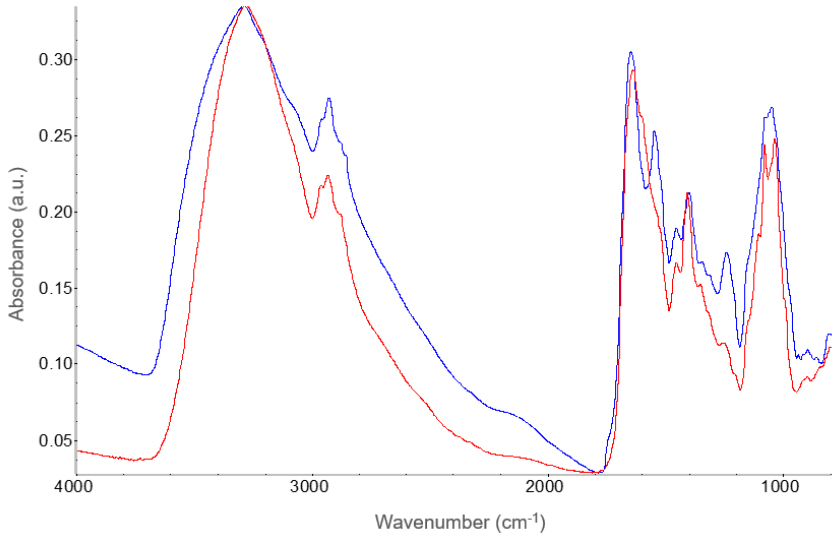

Figure 3.6 Overlay of FTIR spectra to investigate effect of changing dilution media for *C. albicans* planktonic cells. "True" planktonic sample (where cells were diluted in PBS) and "broth" planktonic sample (cells diluted in YPD broth). Amide I peak position is 1650 cm^{-1} in "true" sample, compared to 1637 cm^{-1} in the "broth" sample.

An attempt was made to explore the formation of the early filamentous stage by utilising RPMI medium. This media accelerates the development of the biofilm due to the lowered nutritional composition which places strain onto the microorganisms, encouraging biofilm formation.[222] It was hypothesised that by encouraging earlier surface attachment and collecting FTIR spectra between 30 minutes and 4 hours post incubation, the chemical signatures of the hyphae could

be detected. Unfortunately, this work could not progress due to the incompatibility of RPMI with FTIR spectroscopy, evident due to the large degree of spectral reflectance recorded (for these spectra see **Appendix 3.3**).

3.3.2 Staphylococcus and Candida Mixed Species Biofilms

Fungal and bacterial biofilms should exhibit chemical differences compared to their individual isolates. It is usually accepted that the planktonic fungal cells act as a surface for the bacteria to adhere to and develop upon.[60] **Figure 3.7** shows the FTIR spectra for a *C. albicans* and *S. epidermidis* mixed species sample incubated for 24 hours and 48 hours. At 24 hours the spectrum is generally comparable to the 24-hour *Candida* only spectrum as seen in the overlaid spectra given in **Figure 3.8**. The amide I peak position of the mixed species is 1651 cm^{-1} with a distinct amide II peak at 1551 cm^{-1}. Interestingly in the phospholipid region there is a single dominant peak at 1081 cm^{-1} rather than two peaks, as in *C. albicans* at 24 hours which most probably are an artefact of the YPD media. This observation of a single peak at 1081 cm^{-1} more closely mirrors the FTIR spectrum of a single *S. epidermidis* species biofilm where the phospholipid region shifted from 1069 to 1082 cm^{-1} upon biofilm formation. This potentially alludes to a *Staphylococcus* biofilm which has been detected with FTIR in the mixed species sample. At 48 hours (**Figure 3.7**) the amide I peak is shifted to 1649 cm^{-1} and there now appear to be two peaks in the phospholipid region (1077 and 1047 cm^{-1}) which is comparable to the 24-hour *Candida* spectrum. There is also a merge of the amide I and II regions signifying more O-H in the sample composition. However, the opposite is visible from the lipid region where more O-H is visible at 24 hours compared to 48 hours. This discrepancy could indicate that for these two timepoints the *S. epidermidis* biofilm is visible at 24 hours and then the early *C. albicans* surface adherence overwhelms the spectrum at 48 hours. It is important to acknowledge the added challenge of analysing the non-uniform co-development of two species on a surface; separate samples were analysed at each time point and this may mean that the ratio of species differs significantly, rendering results much less comparable than when analysing single species biofilms.

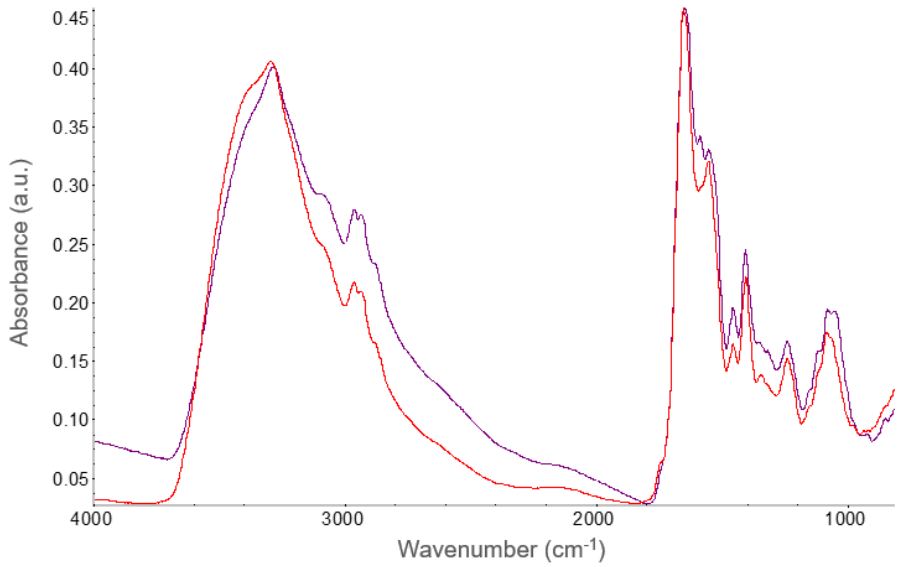

Figure 3.7 FTIR spectral collections for *S. epidermidis* and *C. albicans* mixed species biofilm samples analysed at 24 hrs and at 48 hrs post incubation, in YPD media. Amide I is shifted from 1651 cm^{-1} to 1649 cm^{-1} (24 hr to 48 hr).

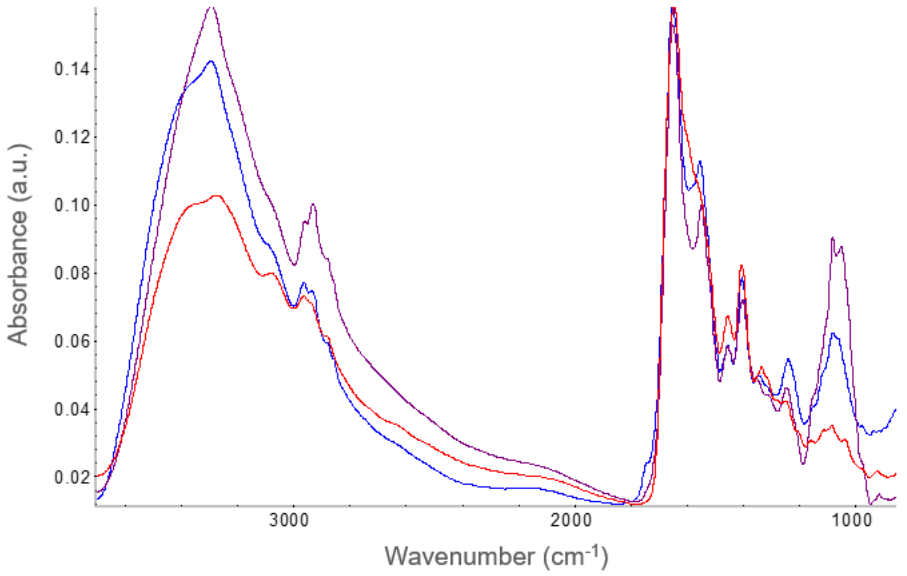

Figure 3.8 Overlay of FTIR spectra collected at 24 hr time point for a mixed species sample, *Candida* single species, *Staphylococcus* single species.

To supplement the understanding of the mixed species biofilm development, light microscopy images were once again collected by microbiologists at Glasgow University. **Figure 3.9** visualises the single *S. epidermidis*, single *C. albicans* and mixed species sample, after 24

hours of growth in the appropriate media. Within the mixed species sample there is a high degree of hyphae with only 2 primary regions where shadows may indicate *S. epidermidis* development. This disparity in cell density between the two species reaffirms the difficulty in defining the chemical signatures of the *S. epidermidis* in the FTIR analysis.

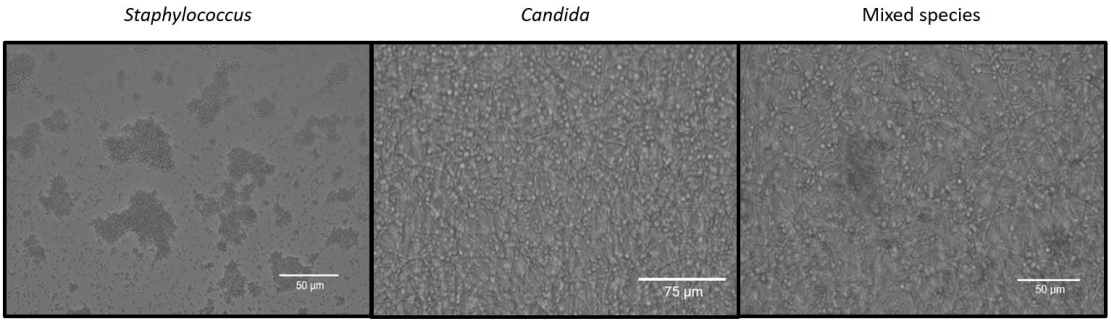

Figure 3.9 Light microscopy images for *S. epidermidis* RP62A, *C. albicans* GSK107 and a mixed species sample, following 24 hr incubation in the appropriate medium (NB for single *S. epidermidis*; YPD for single *C. albicans* and mixed species).

To evidence the notion that a *S. epidermidis* biofilm develops on the *C. albicans* base, earlier time points of mixed species samples were examined, whilst keeping in mind that YPD would potentially be a dominant feature. **Figure 3.10** presents the FTIR spectra for a mixed species biofilm at 4 and 8 hours. Under initial inspection these spectra appear very similar to the single *Candida* species sample at the same time points, in that only YPD media has been detected. But an exciting feature to highlight within these mixed species spectra is the amide I peak position which shifts from 1632 cm^{-1} at 4 hours to 1637 cm^{-1} at 8 hours. The amide I peak typically falls at 1647 cm^{-1} in single *S. epidermidis* biofilm samples whereas the *C. albicans* 8-hour sample maintained an amide I peak at 1633 cm^{-1}. Although it is a small shift in the mixed species sample, this movement to a higher wavenumber could indicate the underlying presence of the *S. epidermidis* biofilm. **Figure 3.11** displays the corresponding light microscopy images for the individual species and the mixed species samples after 4 hours incubation. The degree of filamentation in the *C. albicans* is limited within the mixed species sample and there are only small regions where the *S. epidermidis* biofilm can be seen.

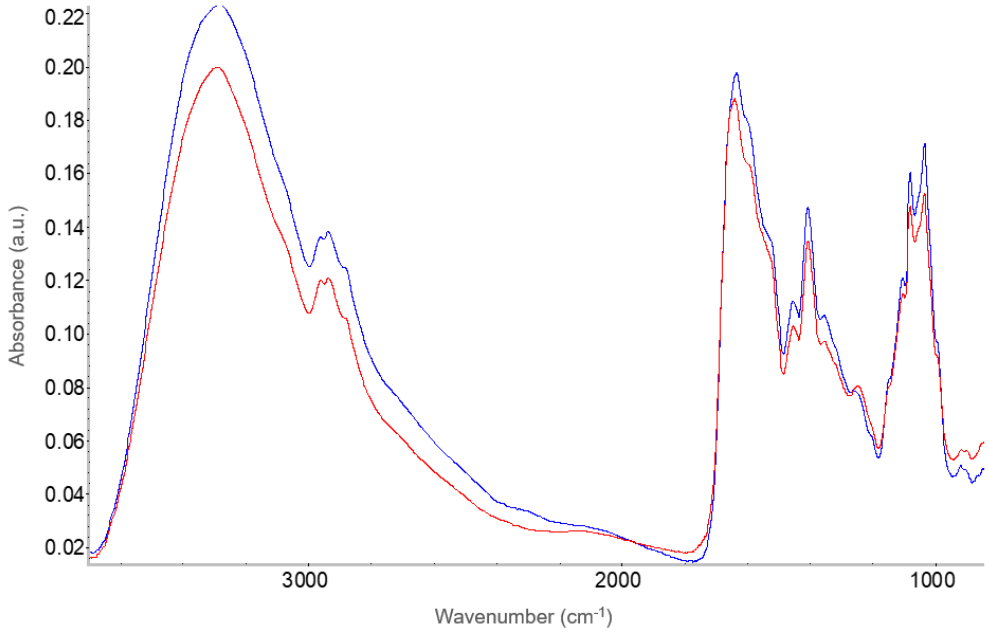

Figure 3.10 Overlaid FTIR spectra for mixed species (*S. epidermidis* and *C. albicans*) sample after 4 hrs and 8 hrs incubation. Amide I position is shifted from 1632 cm^{-1} (4 hrs) to 1637 cm^{-1} (8 hrs).

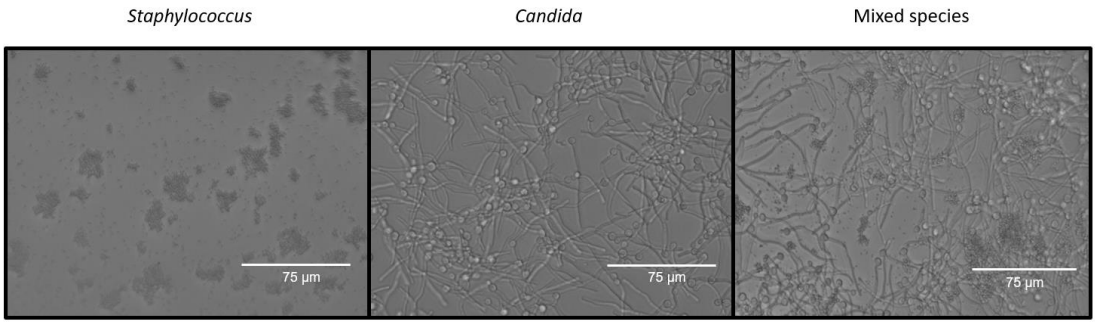

Figure 3.11 Light microscopy images for *S. epidermidis* RP62A, *C. albicans* GSK107 and a mixed species sample, following 4 hr incubation in the appropriate medium (NB for single *S. epidermidis*; YPD for single *C. albicans* and mixed species).

In a further effort to distinguish between the species in a mixed species sample, a lower *C. albicans* starting concentration was trialled. As seen in **Appendix 3.4**, the change in concentration did not significantly influence the resultant FTIR spectra.

3.4 Conclusions

Throughout this chapter the chemical signatures associated with fungal and mixed species biofilm development has been scrutinised with FTIR spectroscopy. The initial spectral recordings indicated that the ECM of the *Candida* samples differed greatly compared to the *Staphylococcus* samples (explored in **Chapter 2**); this was reflected in the high wavenumber, lipid region of the spectra leading to the speculation that the *Candida* species feature a lower amount of O-H bonds as the biofilm phenotype develops. For the single *C. albicans* GSK107 samples, the biofilm was visible and distinguishable in the FTIR spectra at 48 hours and this is supported by microscopy imaging results. Unfortunately, timepoints before 24 hours of incubation could not be evaluated with FTIR due to signals from the growth media which dominate the spectra. This highlighted the issue within implementation of FTIR for clinical diagnostics because competing signals will mask those coming from vital microorganisms in samples.

In general, when evaluating mixed species biofilm samples with FTIR the spectra were consistently overwhelmed by the larger fungal cells, even when starting with a lower concentration of *C. albicans*. This highlights the difficulty with FTIR in locating representative sections of a sample. It would be ideal to trial analysis with Raman spectroscopy. Mixed species samples might be too complex to solely rely on an FTIR spectroscopic analysis. By completing a Raman spectroscopy imaging analysis for a two- or three-dimensional slice, it would allow visualisation of how the two species interact.

Chapter 4. Producing and Interrogating Anti-Biofouling Surfaces

4.1 Introduction

In the preceding chapters, research focused on the biospectroscopy of biofilms for the advancement of understanding biofilm development and medical diagnostics. In this chapter, the second overarching aim of this thesis will be explored; what options exist for medical grade anti-biofouling coatings and how can these be engineered specifically to resist biofilm development. A key issue exists in the healthcare sector whereby essential blood contacting implantable materials, like CVCs, can result in infections, namely blood stream infections.[54] When these CRBSIs take the form of a biofilm infection, they become 1000 times more resistant to available treatment options, often resulting in a chronic infection.[64] Indwelling medical devices are formed from biocompatible metal and plastic materials which need to be changed frequently to prevent infection, incurring additional patient discomfort and substantial cost.[223,224] In the last 50 years novel coating techniques have been explored to minimise the protein and cell binding which leads to infection.[135,225] Coatings can be applied from solution (non-covalently) or covalently bound to the underlying material, using wet chemical grafting or by gaseous coating, as in PP.

In this chapter the focus is the development of PEO-like coatings which are known to reduce biomolecule adsorption due to the high C-O-C component.[138] PEO-like surfaces are highly hydrophilic and can prevent protein molecules from replacing pre-adsorbed water which makes them naturally non-biofouling.[226] To facilitate PP a reactor was designed and constructed to form coatings from ethanol and two crown ether monomers (15-crown-5 and 12-crown-4). In a collaborative effort with Liverpool university, the first successful polymerisation of 12-crown-4 without pulsing the plasma, will be shown. Alongside the development of novel PP coatings, the known HPG coating was investigated in a collaboration with Tekcyte® and the

University of South Australia (UniSA). Whilst HPG is known to have an exceptionally high C-O-C content, making it an ideal candidate for anti-biofouling applications, the chemical structure that results from the grafting is not completely understood. This work aimed to apply XPS to monitor various stages of the grafting, the characterisation of the substrate materials pre-, mid- and post-production are presented here.

4.2 Materials and Methods

4.2.1 Plasma Polymerisation

4.2.1.1 Purpose Built Reactor

At the start of the project a single barrel reactor was already available within the department (schematic drawing given in **Chapter 1**, **Figure 1.11**). This was used for the initial coating production whilst a larger system was designed for exclusive use in this work. A cruciform barrel plasma reactor (**Figure 4.1**) was designed and built to aid in producing PEO-like coatings. Due to the nature of PP reactors, the same parameters will not yield exactly the same coatings from reactor to reactor, there will always be slight variations. But when designing this reactor, every effort was taken to ensure it maintained the necessary and important features of the existing plasma reactor. This meant that the coatings produced should be comparable between the reactors. An important feature of the new reactor was the use of a cruciform glass barrel which provides more inlets into the chamber allowing the potential combination of multiple monomers, or the coupling of analysis with production, which would prevent exposing the coating to air before analysis. The reactor also featured a manual matching network for the generator.

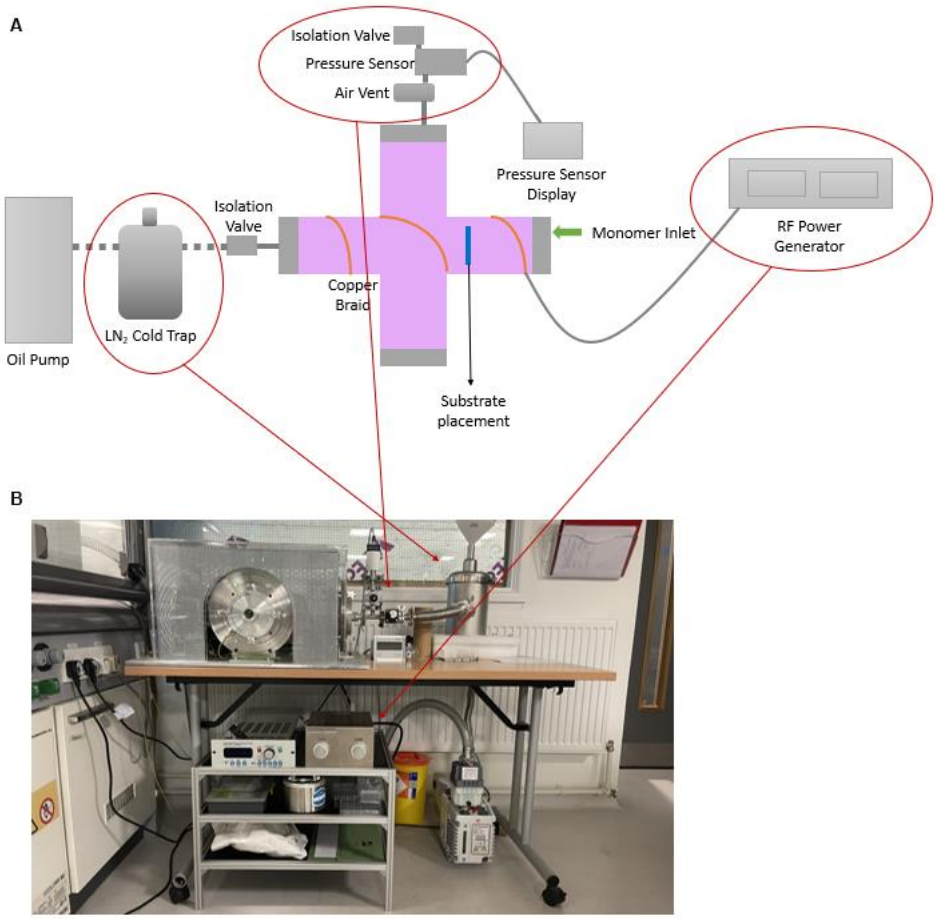

Figure 4.1 (**A**) The design for the cruciform plasma reactor; (**B**) A photograph of the constructed reactor in situ, with arrows corresponding to key elements of the original design.

4.2.1.2 Polymerisation Protocol

PP was carried out in a glass barrel reactor which underwent cleaning with acetone and isopropanol, before each experimental day. A vacuum pump maintained the barrel base pressure at 0.815 Pa. A needle valve was used to control the flow of monomer vapour into the chamber. A RF generator (13.56 MHz) was applied to deliver the power via an electrode connected to the barrel.

Monomer (5 mL) was loaded into a round bottom flask and connected to the chamber, freeze-thawing (3 times) to ensure it was degassed. In an initial step to validate a successful

plasma formation, the monomer valve was opened and a plasma ignited by slowly increasing RF power and the suitable plasma conditions (pressure/power) were established. Following turning RF power off, the monomer valve was closed and the chamber was brought to the base pressure (0.815 Pa) to ensure removal of residual monomer from the chamber before proceeding. At this point, the system was returned to atmospheric pressure to allow substrates to be loaded for PP coating to commence. Substrate material on a glass slide was placed at one end of the chamber, aligned with a marking on the barrel to ensure each slide was placed in the same position. The chamber was returned to the base pressure again. Monomer pressure was increased as required (see **section 4.2.1.4**), and once stabilised, RF power was increased to ignite a plasma. Each coating was produced by leaving the deposition to occur for a different length of time. Once the deposition time was finished, the power was turned off and the slide allowed to remain in the chamber for 1 minute with the monomer valve turned off and the system returned to base pressure. Finally, the chamber was brought up to atmosphere and the coated substrate was carefully removed to a sample holder.

4.2.1.3 Starting Materials to Produce PEO-like Coatings

This project focused on the production of PEO-like coatings. Therefore, the monomers selected for PP were ethanol, 15-crown-5 ether and 12-crown-4 ether (Sigma Aldrich, UK). The structure of the PP precursors are given in **Figure 4.2**. Due to the difficulty in vaporising the 12-crown-4 monomer in the glass PP reactor at Lancaster, this work was primarily progressed at the University of Liverpool. All coatings were polymerised on Si or Al (1x1 cm^2 approx.). Each substrate material was sonicated in isopropanol (5 minutes) and dried under a stream of N_2 to remove surface contamination before the deposition of a coating.

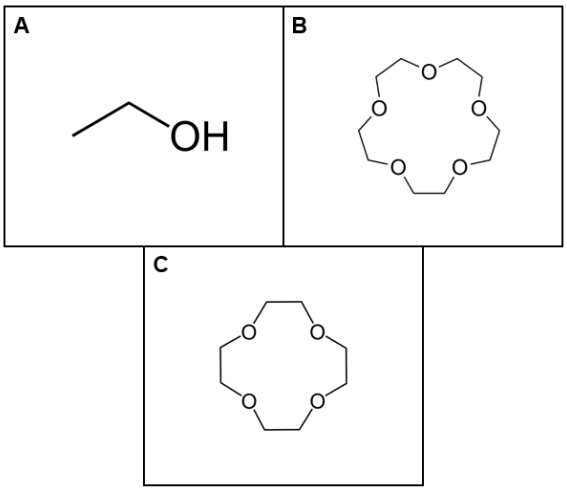

Figure 4.2 Chemical structure of each monomer used throughout this research project to produce non-fouling PEO-like coatings: (**A**) ethanol; (**B**) 15-crown-5; (**C**) 12-crown-4.

4.2.1.4 Optimising Plasma Parameters

Coatings were collected over a wide range of plasma parameters. The successful coatings presented throughout this chapter were produced using the conditions given in **Table 4.1**. For the crown ether samples there was a larger range of conditions trialled but only ones that yielded some functional retention are given.

Table 4.1 Plasma parameters trialled in the production of PP coatings for: ethanol (parameters **1**-**9**), 15-crown-5 (parameters **10**-**12**) and 12-crown-4 (parameters **13**-**14**).

Parameters	Pressure (Pa)	RF Power (W)	Time (min)	
1	1	10	15	ethanol
2	2.5	10	15	
3	5	10	15	
4	10	10	15	
5	20	10	15	
6	10	5	15	
7	10	10	15	
8	10	30	15	
9	10	15	45	
10	10	10	20	15-crown-5
11	33	80, 5	2, 5	
12	10	25	15	
13	10	5	15	12-crown-4
14	1	5	15	

Initial testing was conducted with ethanol (samples **1**-**9**) using continuous wave plasma. To replicate coating with 15-crown-5 (samples **10** and **11**) deposition methods began using the same plasma parameters explored for ethanol, matching power and pressure. This was followed by a method using high pressure (33 Pa) combined with high power (80W) for 2 minutes then maintaining the high pressure whilst dropping the power (5W) for 5 minutes. The

final attempt to PP 15-crown-5 (sample **12**) exploited pulsed plasma conditions. This incorporates plasma off times which theoretically allows diffusion of fragments to the surface which had previously been shown to improve ethylene oxide content. The 12-crown-4 PP coatings were produced with continuous wave by Stephane Simon and Prof. James Bradley at Liverpool University (sample **13**) and myself (sample **14**). Briefly, 12-crown-4 monomer was vaporised by wrapping heat tape, maintained at 100 ℃, around a monomer flask in a steel rig plasma reactor set up. **Figure 4.3** illustrates the configuration of the steel rig plasma reactor at Liverpool, including the position of the substrate for deposition.

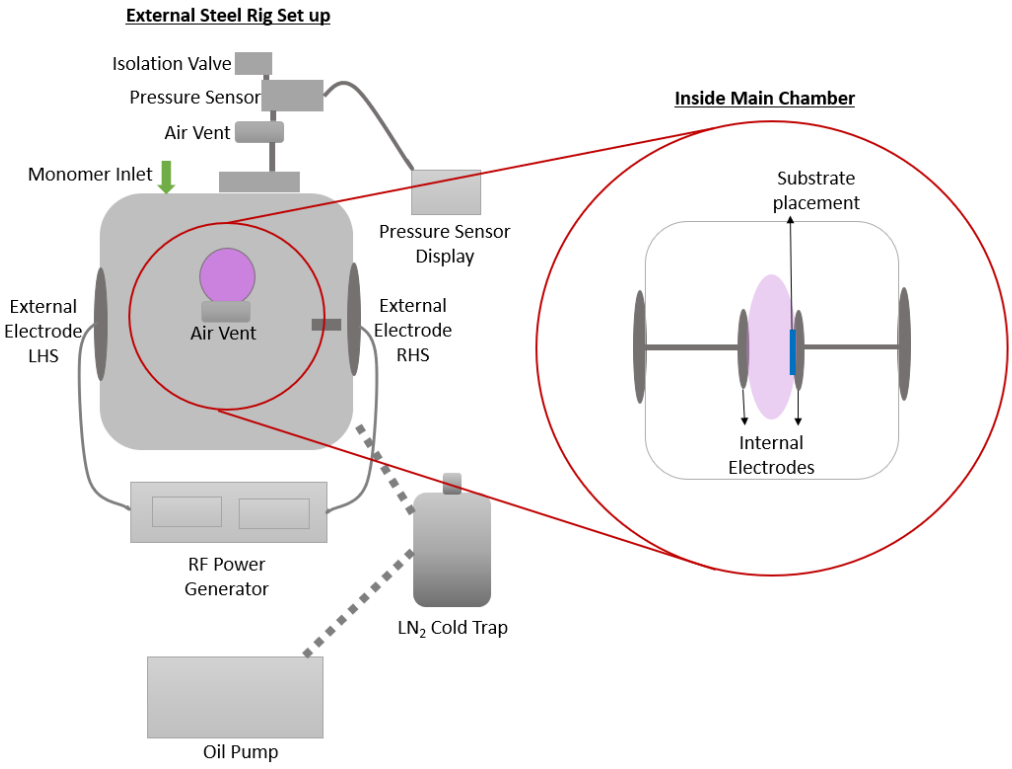

Figure 4.3 Steel chamber plasma reactor illustrating the use of two grounded electrode plates connected to an RF generator to permit the ignition of a plasma within the vacuum chamber.

4.2.2 Hyper-Branched Polyglycerol

An alternative class of PEO coatings is the surface grafted HPG. This is an industrial gold standard coating produced by TekCyte® and UniSA; this section of work is a collaboration where the existing PEO-like coating underwent extensive surface analysis at Lancaster as part of this project. HPG-grafted silicon (Si), titanium-silicon (TiSi), polystyrene (PS) and polytetrafluoroethylene (PTFE) (all fixed to 1x1 cm^2), and nitinol stents (fixed to 1x1x1 cm^3) were cleaned prior to HPG production. The TiSi used herein was produced by the ANFF-SA facility at UniSA. Briefly, Si wafer (15 cm diameter) was sputter coated with Ti to a thickness of 40 nm $^+/_-$ 5 nm. The disk was delivered to LU, pre-cut into 1 cm^2 pieces. Theoretically, this process uniformly coats the Si wafer with Ti. All substrates were gently agitated in 100% isopropanol (Thermo Fisher Scientific, UK) for 5 minutes. Substrates were then dried under a stream of N_2 and activated with air plasma in a plasma cleaner (Diener electronic plasma surface technology, Zepto). It is worth recognizing that this plasma cleaner was used by multiple users across a diverse range of research projects and subsequently, samples produced showed small signs of contamination which will be indicated where relevant.

Plasma activation was carried out under application of continuous RF power (100 W for 20 minutes), maintaining a 4 sccm flow rate. Following plasma treatment, the vacuum chamber was returned to atmospheric pressure and the substrates immediately immersed in glycidol (chemical structure provided in **Chapter 1, Figure 1.12**). Samples were left to polymerize in an oven at 80°C for 24 hours. Polymerization was terminated by quenching with ethanol then removing the unreacted monomer solution and washing for three sets of 5 minutes with ethanol. HPG-grafted substrates were dried under a stream of N_2 and stored under ambient conditions until use.

4.2.3 Surface Analysis

4.2.3.1 XPS and Depth Profiling

XPS was performed with a Kratos AXIS Supra spectrometer (Kratos Analytical Ltd, Manchester, UK), using monochromatic Al Kα radiation (hv = 1486.7 eV). Samples were mounted on sample holder using Kapton tape and an internal flood gun was used to reduce charging effects. Spectra were recorded using an acceleration voltage of 15 keV at a power of 225 W. Survey spectra were collected for 3 locations with a pass energy of 160 eV and an analysis area of 300 × 700 μm^2. High-resolution spectra were obtained in 3 locations per sample using a 20 eV pass energy and an analysis area of 300 × 700 μm^2. The emission current was set at 15 mA and all sweep times were set at 120 s, 0.1 eV step size and 5 sweeps. Data analysis was performed with CasaXPS software (version 2.3.22, Casa Software Ltd, Devon, UK). All binding energies were referenced to the low energy C 1s peak at 285.0 eV and all peak fitting was based on the standard binding energy values given by Beamson and Briggs, unless otherwise stated.[227] Core level envelopes were curve-fitted with the minimum number of mixed Gaussian–Lorentzian component profiles. Whilst the full width at half-maximum (FWHM) was constrained to match the reference peak, the Gaussian–Lorentzian mixing ratio (typically 30% Lorentzian and 70% Gaussian functions), positions and intensities of peaks were left unconstrained (unless otherwise stated) to result in the best fit.

XPS ion milling was performed, using an Ar GCIS with 2000^+ cluster size and 5 keV energy. The analysis area was the 100 µm slot and the emission current was set at 25 mA. Over a 4 mm raster, 100 etches were milled with pre-etch, etch and post-etch time each fixed at 10 s. Rotation mode was used throughout milling experiments. Core-line spectra (C 1s, O 1s, N 1s, Si 2p and Ti 2p) were collected, where relevant, with a 60s sweep time.

End group labelling was used to evaluate the percentage of carbon contributing to terminating groups in HPG. The labelling protocol was carried out by Laurine Martocq at LU, as part of her wider PhD study into end group labelling. Samples were placed inside a vacuum plasma reactor and pumped to the base pressure (0.005 Pa). Trifluoracetic anhydride (TFAA,

>5 mL) was pipetted into a round bottom flask which was attached at the monomer inlet of the plasma reactor. The inlet valve was opened and the TFAA was heated to 40°C in a water bath to increase the pressure inside the reactor chamber to 700 Pa. Samples remained in the chamber for 1 hour before closing the monomer inlet valve and maintaining system pumping for a further 30 minutes, to remove surplus TFAA. Samples removed and stored under vacuum until XPS analysis.

4.2.3.2 Atomic Force Microscopy

Atomic force microscopy (AFM) was used to conduct scratch testing on coated materials to accurately determine the coating thickness. This work was primarily carried out by Alessio Quadrelli at LU, using specialist ultra-low noise equipment in the IsoLab to maximise accuracy of the measurements. Briefly, AFM images were recorded with a Bruker Multimode 8 AFM, using the Nanoscope V controller in PeakForce mode. NuNano Scout 70 probes (nominal resonant frequency 70 kHz; 2 N/m cantilever stiffness; >10 nm probe radius) were used. To measure coating thickness, the sample was scratched in contact mode over a 500 x 500 nm area. A line depth profile of this area was then used to calculate coating thickness by finding the difference in height across the scratched area.

4.2.3.3 Water Contact Angle

WCA measurements were collected using an Ossila Contact Angle Goniometer system with a light source sample stage and camera which was connected to a laptop. Substrate placed on the stage, ensuring it was level, before turning the camera on as deionised water (5 µL) was pipetted onto the surface. The recording was then stopped and reviewed in Ossila software (Sheffield, UK) to calculate the contact angle.

4.2.3.4 FTIR

A Nicolet iS5OR FTIR spectrometer (Thermo Scientific, UK) was used in transmission to analyse an ethanol PP coating on Si substrate. All data was collected using OMNIC Paradigm software (Thermo Scientific, UK). Data acquisition was performed with 4 cm^{-1} resolution using 256 cycles. A section of blank Si was used as the background.

4.3 Results and Discussion

4.3.1 Basic PEO-like Coatings

PEO-like coatings are one of the most commonly applied biomaterials to reduce biofouling in medical environments.[138] Ethanol is a readily available monomer that has previously been explored as a pre-cursor to PP to produce a simple PEO-like coating.[168,169] Therefore, the first PP coatings produced in this work were formed from ethanol monomer, as a baseline to define the plasma parameters required to achieve optimal C-O retention. The overall aim for coatings produced was to resist biofilm formation on the surface by engineering samples that are hydrophilic with ethylene oxide repeating moiety. The amount of C-O determined by XPS acted as a guiding tool to indicate successful coatings. Various combinations of the plasma parameters (pressure and power) were evaluated (listed in **Table 4.1**) to increase the C-O moiety. For simplicity all preliminary ethanol coating work was conducted using continuous wave plasma on Si wafer with a 15-minute plasma on time in an attempt to maintain comparative coating thickness.

In general, each deposition condition applied resulted in a successful ethanol coating. The thickest coatings all resulted in a visibly blue change in appearance to the silicon wafer. The only coatings that were approximately less than 10 nm were the samples collected at 10 W reflected by the non-linear baseline in XPS results. By testing this range of plasma parameters, we can examine both the effects of pressure on the plasma polymer coating by

fixing the power and similarly the effect of power by fixing the pressure. From the literature, reducing monomer power and increasing pressure should produce surfaces with larger C-O functional retention.

XPS was used to interrogate the chemical environments within the ethanol plasma polymer surface and %C-O was utilised as a measure of the degree of ethylene oxide retention across the surface (note, %C-O includes contributions from not only the ethylene oxide repeat units, C-O-C, but also the terminating C-OH groups). The industrial gold standard coating that was used as a benchmark in this work was HPG which has an average C-O composition of 80% (detailed HPG analysis to follow in **Section 4.3.3**). The aim for all PP derived PEO-like coatings was to achieve at least 60% C-O composition.

Firstly, in the analysis of ethanol, a survey spectrum was recorded for each coated surface, in three locations, to provide a summary of the chemical elements present in the top 5-10 nm of the material (**Figure 4.4 (A)**). This wide scan analysis was followed by a high-resolution core line spectral collection of the relevant elements, in this instance C 1s and O 1s peaks, for each sample, at each of the three locations (**Figure 4.4 (B) and (C)**).

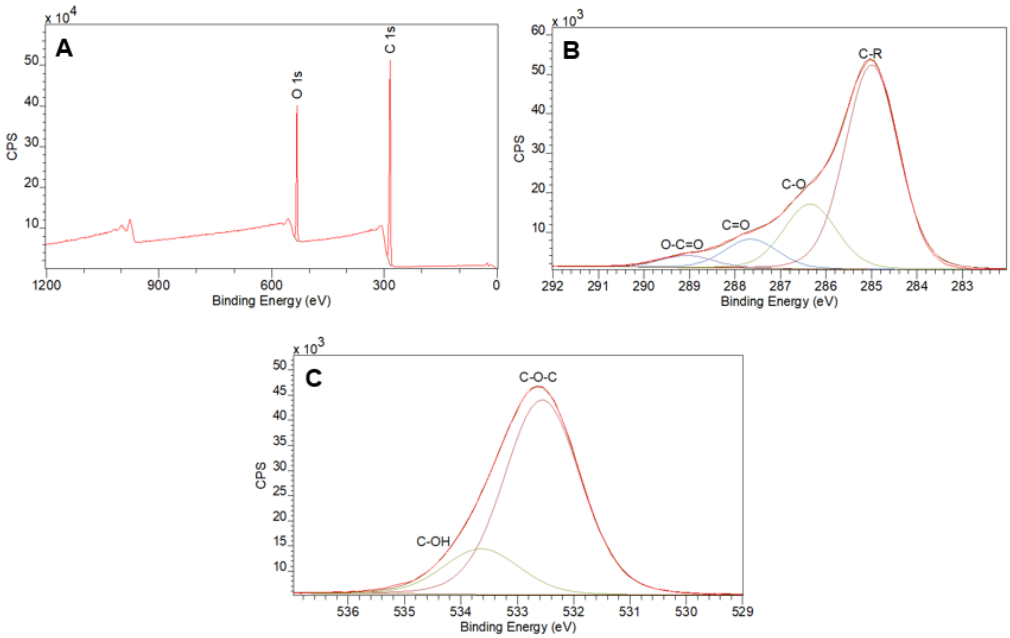

Figure 4.4 XPS spectra for an ethanol PP coating deposited at 10 Pa, 10 W. (**A**) *Representative survey scan*: O 1s 18.37%, C 1s 81.63%; (**B**) *C 1s*. C-R (285 eV, 65.92%), C-O (286.35 eV, 20.85%), C=O (287.65 eV, 9.35%), O-C=O (289.05 eV, 3.87%); (**C**) *O 1s*. C-O-C (532.56 eV, 81.07%), C-OH (533.64 eV, 18.93%).

As displayed in **Figure 4.4**, the only signals originating from the ethanol surface are C 1s, O 1s and the O_{KLL} auger peak at approximately 980 eV. For three locations surveyed per sample, the spectra yield similar results owing to the uniformity of the surface; this is also reflected in the core line C 1s and O 1s spectra. Importantly, in the wide scan spectrum (**Figure 4.4 (A)**), the background is linear indicating the coating thickness is greater than the XPS sampling depth (5-10 nm). As stated for the ethanol plasma polymer coatings, the C 1s core line spectrum was unlikely to differ greatly across the range of experimental conditions used (**Appendix 4.1**). Interestingly, the greatest changes were observed in samples where the monomer pressure remained below 5 Pa. These samples were the only ones where nitrogen was seen in the wide scan (at ~8%). Nitrogen incorporation could originate from leaks within the system or desorption of N from the walls of the plasma reactor barrel; both of these issues are heightened at lower monomer pressure.[228] This N contamination may explain the chemical environments which have shifted to higher binding energies, seen in both the C 1s and O 1s spectra for the 1 Pa

and 2.5 Pa samples. Nitrogen incorporation is recognised to cause issues with chemical shifts and peak fitting in XPS.[229] It is also worth stating that the highest %C-O retention seemingly comes from these samples (produced at 1 Pa and 2.5 Pa), however due to the incorporation of nitrogen (C-N peaks overlap with C-O at ~286 eV), these samples were excluded from the overall analysis of ethylene oxide retention. In order to determine the parameters at which the highest %C-O can be achieved, the percentage analysis of the C 1s spectra (fitted according to **Figure 4.4**) are given in **Table 4.2** (corresponding binding energies in **Appendix 4.2**). To supplement this, **Appendix 4.3** displays plots of the variable power (W) and variable pressure (Pa) against %C-O/%C-R. From this it is clear that increasing power routinely increases the amount of C-H on the surface, whilst the %C-O reduces from 24% to 19% when power is increased from 5 to 30 W. The correlation between variable pressure and %C-O/%C-R is less clear, initially increasing pressure reduces the surface C-O content but at the highest pressure (20 Pa), the %C-O is the best overall (28.55%). This increased ethylene oxide composition in the 20 Pa, 10 W sample is also reflected in the O 1s binding energies (**Appendix 4.4**) where the C-O-C environment is the largest compared to other samples. In general, a low power, high pressure system gives an optimum ethylene oxide retention; this regime is called the γ-regime, as discussed in **Chapter 1** (**Section 1.7.1**). Unfortunately, the C-O composition did not reach 60% for any pure ethanol coatings which is insufficient when looking towards coatings for biofilm prevention.

Table 4.2 Comparison of C 1s peak % area across all ethanol PP samples. [Samples produced at 1 and 2.5 Pa have been highlighted and excluded from overall analysis because of nitrogen incorporation]

Sample	FWHM	C-R	C-O	C=O	O-C=O	C-O/C-R
1 Pa 10 W	1.49	50.22	28.09 (+C-N)	15.73	5.96	0.559
2.5 Pa 10 W	1.45	50.72	26.61 (+C-N)	16.47	6.20	0.525
5 Pa 10 W	1.41	63.07	21.82	10.67	4.44	0.346
10 Pa 10 W	1.37	65.92	20.85	9.35	3.87	0.316
20 Pa 10 W	1.37	56.35	28.55	10.81	4.29	0.507
10 Pa 5 W	1.39	62.83	23.65	9.80	3.72	0.376
10 Pa 20 W	1.39	66.56	19.73	9.51	4.19	0.296
10 Pa 30 W	1.41	67.16	18.59	9.81	4.44	0.277

A limited evaluation of sample aging was conducted where each sample was analysed on the day of production and stored for further analysis 1 week after production (**Figure 4.5**). There was no pattern for the minor changes in the %C-O or C-O/C-R observed (**Appendix 4.5**). For example, the best sample produced at 20 Pa, 10 W had 28.55% C-O retention immediately after production and this reduced to 28.01% after 1 week in storage.

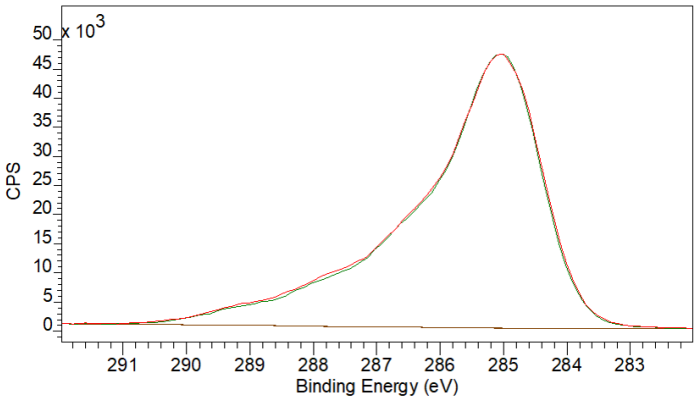

Figure 4.5 Overlaid C 1s core line spectra for a single ethanol PP coating (deposited at 10 Pa, 10 W) analysed on the day of production (not aged) and one week later (aged) revealing only slight loss of carbon peak definition.

In conjunction with the XPS analysis, FTIR was used to explore the ethanol features that had been retained in the polymer coating. This was performed on sample 9 (10 Pa, 15 W, 45 minutes) to ensure a thick coating layer was visible (**Figure 4.6**). To compare the chemical composition and bonding of the ethanol plasma polymer with pure ethanol the wavenumbers have been listed in **Table 4.3**. The peaks associated with the thin film coating, align with the signals produced by pure ethanol; the primary difference between sample 9 and a standard ethanol FTIR spectrum, was the presence of C=O stretches. This will conceivably be a result of the fragmentation that occurs during the plasma polymerisation process. As seen in the XPS analysis of ethanol PPs, C=O accounts for approximately 10% of the surface composition, and these bonding environments are likely to be the terminating groups for the polymer.

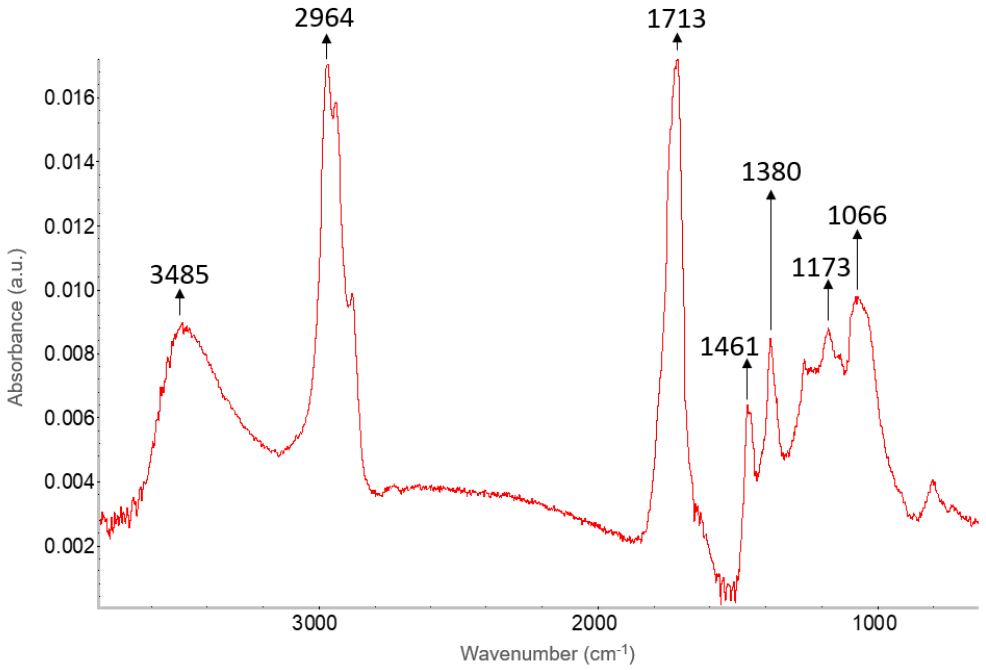

Figure 4.6 In transmission FTIR spectrum of ethanol PP coating (deposited at 10 Pa, 15 W for 45 minutes – sample **9** in **Table 4.1**).

Table 4.3 Comparison of key wavenumber regions from a standard ethanol FTIR spectrum and the spectrum of sample 9.

Expected ethanol peaks (cm^{-1})	**Actual ethanol PP peaks (cm^{-1})**	**Bond Motion**
1048	1066	C-O stretch, primary alcohol
1092	1173	C-O stretch, ester group
1384	1380	C-H/C-O in region
I	1461	Methylene group
I	1713	Strong C=O stretch
2980	2964	C-H alkane stretch
3366	3485	O-H alcohol stretch

4.3.2 Crown Ether Plasma Polymers

4.3.2.1 15-crown-5

Crown ethers are monomers that contain more C-O units than ethanol (for reference of monomer chemical structures see **Figure 4.2**). There have been previous investigations into the two smallest of these cyclic ethers for PP but the heavier 15-crown-5 does not appear to have been investigated due to difficulties experienced when attempting to vaporise the monomer.[172,173] While some progress in plasma polymerisation has been made with the smaller 12-crown-4 monomer, it is significantly more toxic, so the first stage in this work was to vaporise 15-crown-5. Initial attempts mirrored the parameters explored for ethanol (plasma parameters 1-8 in **Table 4.1**). Unfortunately, the 15-crown-5 could not be sufficiently vaporised, even with gentle monomer heating in a water bath (40 ℃). **Appendix 4.6** shows the result of the attempted polymerisation of 15-crown-5 at 10 Pa, 10 W (for 20 minutes) on Si.

To improve these coatings, the method utilised by the Ratner group was trialled. They were able to utilise a regime where a high pressure (33 Pa) was maintained with an initial high power (80 W) for 2 minutes which was reduced to a lower power (5 W) for 5 minutes.[173] By using these plasma parameters, this method yielded a coating with a 30% C-O retention, as reported in **Appendix 4.7**. This coating was also thinner than the XPS sampling depth (5-10 nm), which would reduce the long-term quality of the coating. Moreover, nitrogen has been incorporated into the coating and this will contribute to some of the signal attributed to C-O in the C 1s core line spectrum.

In a final effort to increase C-O retention from 15-crown-5, a pulsed plasma polymerisation regime was used, following the protocol demonstrated by the Timmons group.[172] Up to this point, only continuous wave plasma was used; in pulsed plasma methods the plasma is periodically turned off (pulse delay periods of 5-500 ms with a pulse width of 50 ms). Pulsed plasma theoretically allows time for the monomer fragments to diffuse towards the substrate for polymerisation to occur. A variety of pulsing conditions were explored whilst maintaining 10 Pa, 25 W (15 minutes total deposition time) but the C-O composition did not rise above 25% (**Appendix 4.8**).

4.3.2.2 12-crown-4

Vaporisation of the larger crown ether monomer was not successful, so to improve the EO content, the cyclic ether monomer was swapped to 12-crown-4. While an attempt was made with gentle monomer heating in a water bath held at 50℃, the smaller crown ether would not vaporise either. This monomer required heating to 100°C, to allow vaporization, with a heat tape around the plasma reactor. Due to the use of a glass reactor at Lancaster, heating was not practicable. In order to facilitate this work a collaboration was established with Liverpool University where all 12-crown-4 coatings were then produced by Stephane Simon in a steel rig reactor (**Figure 4.3**) which was compatible with heat tape at 100°C. Upon successful vaporisation, coatings were deposited onto Al and couriered to Lancaster for analysis. Al was the standard substrate in use at Liverpool university and as the PP process is independent of substrate, the use of Al will not have influenced the ability to produce a coating compared to Si. The Al photoemission peaks in the XPS spectrum do not overlap with peaks of interest from the coating, C 1s and O 1s, meaning that if coatings were thin enough to allow a visible substrate signal, there would be no issues with overlapping peaks.

The highest obtainable pressure for 12-crown-4 was 10 Pa, thus this was combined with a lower power of 5W so that the parameters fit within the γ-regime, previously identified to maximise EO retention (**Section 4.3.1**). **Figure 4.7** demonstrates a representative 12-crown-4 coating that was produced in this project at Liverpool University. In the best sample, the composition of C-O was 61% meaning ethylene oxide was the dominant chemical environment of the surface. It is also worth highlighting from the O 1s core line spectrum (**Figure 4.7 (C)**) that the dominant feature of the coating is the C-O-C environment with a small contribution in the O=C binding environment. This is in contrast to the ethanol plasma polymer coatings where the remaining O 1s character was from terminating C-OH environments. This indicates that the terminating groups of the 12-crown-4 coatings are primarily C=O groups.

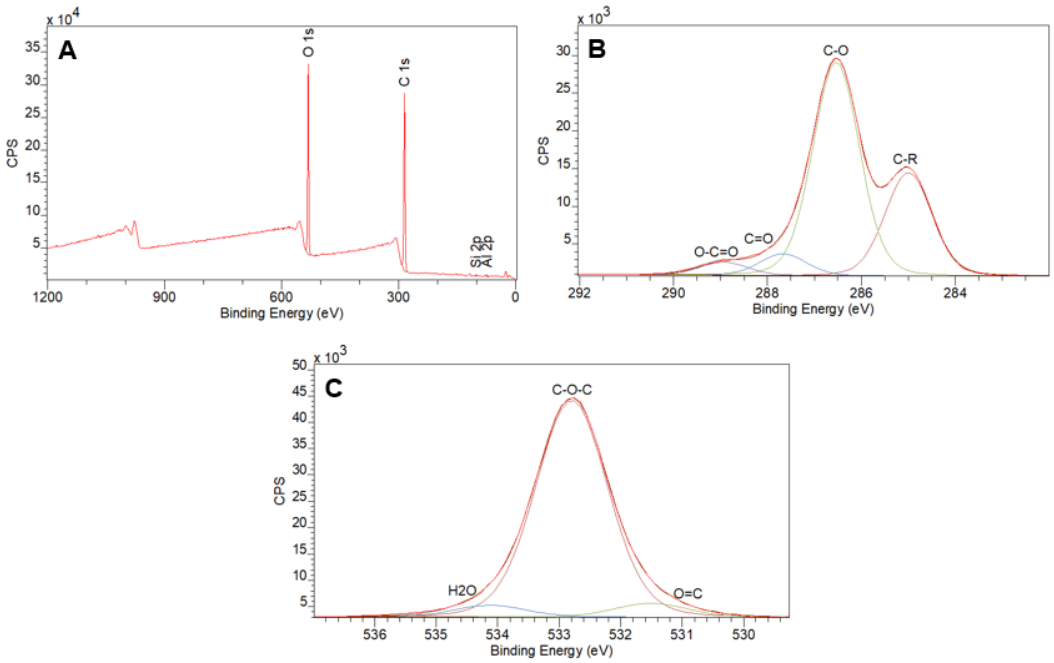

Figure 4.7 XPS spectra for representative 12-crown-4 PP coating (10 Pa, 5 W) produced on Al at Liverpool University and analysed at Lancaster. (**A**) *Compositional analysis*: O 1s 26.35%, C 1s 71.49%, Si 2p 0.66%, Al 2p 1.51%; (**B**) *C 1s*. C-R (285 eV, 29.41%), C-O (286.54 eV, 60.78%), C=O (287.67 eV, 6.11%), O-C=O (288.94 eV, 3.70%); (**C**) *O 1s*. O=C (531.51 eV, 5.76%), C-O-C (532.80 eV, 89.34%), H_2O (534.12 eV, 4.90%)*. [*peak at ~534 eV arises from chemisorbed water or weakly bound oxygen molecules within the structure, for ease these have been denoted H_2O through this thesis]

For the sample analysed in **Figure 4.7** the substrate was placed to the RHS of the electrode in the steel plasma reactor (see **Figure 4.3** for electrode positions within the reactor chamber). Due to the way the plasma sheath "hung" around the electrodes because of the use of the γ-regime (which brings the plasma close to the electrode), the substrate position during deposition may have be important. Different substrate placements on the electrode plates inside the chamber were investigated to see the effect on the coatings (**Figure 4.8**). But the %C-O remained between 55-65% for all samples (**Figure 4.7 (B)**, **Figure 4.8 (A)** and **(B)**); this would indicate that the substrate position on the electrode did not influence the ethylene oxide retention. As an additional experiment, the pressure was reduced to 1 Pa which was easier to maintain with less monomer wastage, however a coating of the same quality did not form denoted by the 25% C-O composition and dominant C-R binding environment exemplified in **Figure 4.8 (C)**.

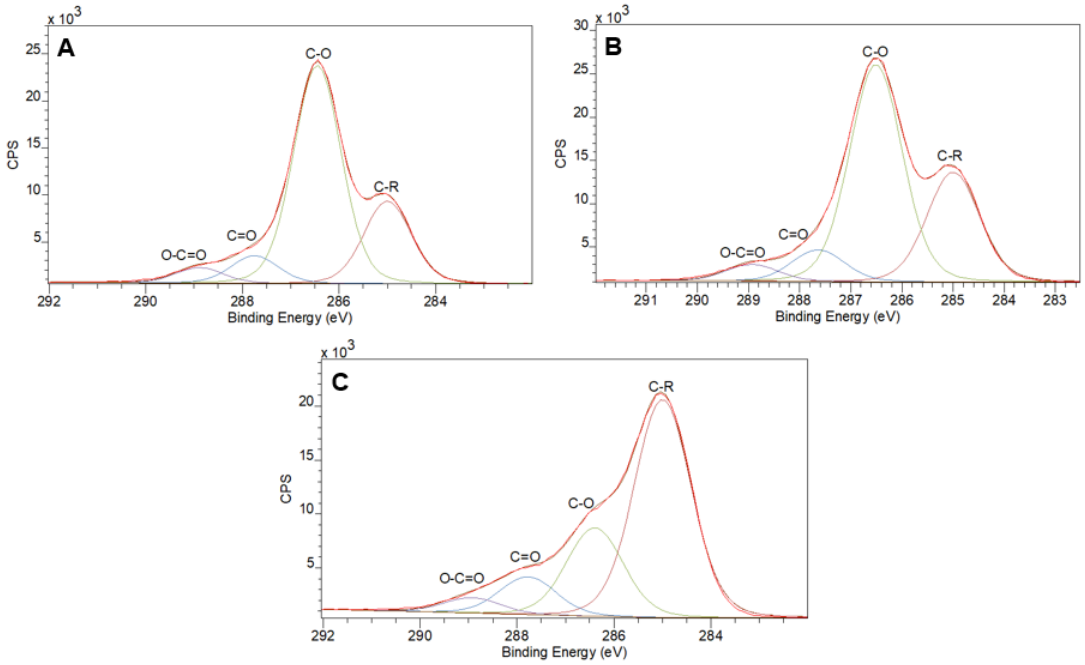

Figure 4.8 XPS C 1s core line spectra for three 12-crown-4 PP coatings produced at Liverpool University on Al at various reactor positions or pressures. (**A**) *10 Pa, 5 W, LHS*. C-R (285 eV, 24.00%), C-O (286.45 eV, 63.55%), C=O (287.75 eV, 7.97%), O-C=O (288.89 eV, 4.47%); (**B**) *10 Pa, 5 W, Top*. C-R (285 eV, 29.24%), C-O (286.51 eV, 57.91%), C=O (287.64 eV, 8.40%), O-C=O (288.93 eV, 4.45%); (**C**) *1 Pa, 10 W, RHS*. C-R (285 eV, 60.65%), C-O (286.39 eV, 24.60%), C=O (287.78 eV, 10.49%), O-C=O (288.93 eV, 4.26%).

The original aim of this PhD project was to produce non-biofouling plasma polymer coatings, using a custom-built plasma reactor. These aims were broadly accomplished. Firstly, a cruciform plasma reactor was designed and constructed as part of this work. Within this reactor PEO-like coatings were explored due to the already established idea that increasing ethylene oxide across a surface will reduce biofouling. This work built towards the use of 12-crown-4 to produce coatings with approximately 60% C-O retention. But whilst PP coatings were made, the conditions could not be optimised to approach the ethylene oxide moiety (80% C-O) which is regularly achieved by the industrial gold standard HPG. From discussions with the project HPG collaborators at TekCyte® and UniSA it quickly became clear that despite the high ethylene oxide retention, little was understood about the HPG coating material composition, particularly across a range of substrate materials. Therefore, the collaborators at TekCyte®

allowed use of their solvent phase HPG production method for research purposes. The remainder of this project focused on elucidating the material composition of HPG and understanding the coatings high anti-biofouling performance.

4.3.3 HPG

HPG is an exciting, industrially relevant PEO-like coating that has already shown promise for various anti-biofouling applications.[66,230,231] The collaborators for this study at UniSA had previously developed a plasma activation based graft-from approach to coat medically relevant materials with HPG.[232] This project builds upon the original work by rigorously monitoring the material development and formation. The excellent non-biofouling capabilities and prevention of biofilms that HPG exhibits will be demonstrated in **Chapter 5**. In order to fully understand and appreciate this, the coating composition must first be interrogated.

The substrates used most throughout this work to graft HPG are Si, TiSi, PS, PTFE and clinically relevant nitinol stents. Si was a good model in the first instance whilst the other materials highlight viable clinical application. The size of each substrate was fixed at 1 x 1 cm^2. All substrates have previously been reported to successfully allow HPG grafting and the production of a uniform coating.[188,189,232] Before exposing the substrate to glycidol (chemical structure in **Chapter 1**, **Figure 1.11**), the monomer required to produce the HPG coating, the surface must be activated which is achieved through plasma activation, as described in **section 4.2.2**. Following activation, a well reported, instant change to the surface energy, roughness and composition, will be observed.[233] Plasma activation works to “clean” carbon contamination from the surface, whilst introducing oxygen containing functional groups. This primes the surface, activating it, for reaction with the monomer. Air was selected because it has been shown to permit surface activation, promoting the formation of a reactive moiety on the substrate, increasing the likelihood of polymerisation on contact with glycidol, to produce the HPG coatings.[232] However, the new surface features that are introduced during activation, decay rapidly, highlighting the need for swift submersion of the substrate in the reaction monomer.[233] Before evaluating the HPG coating, the effect of plasma activation on each substrate has been monitored as a detailed examination of the grafting process had not been

previously undertaken. The time between plasma activation and placing the sample under vacuum in the XPS was kept to less than 1 minute in an effort to reduce the loss of surface properties.

4.3.3.1 Substrate Materials (Clean and Plasma Activated)

4.3.3.1.1 Silicon

Figure 4.9 displays the wide scan XPS spectra for a Si wafer before and after plasma activation. Initially evident after plasma activation is the removal of carbon contamination which prior to plasma treatment varied from location to location; carbon has been removed, to below 5%. The oxygen content has significantly increased, from 21.59% to 48.72%, coinciding with an incremental increase in nitrogen to 1.08%. This increase in O and N was expected because plasma activation primes the surface for bonding with reactive species. As previously stated, when the samples were removed from the plasma, the samples are quickly affixed to an XPS sampling bar and placed in the spectrometer, under vacuum. However, as soon as the samples are exposed, the air could quickly react with the activated surface, resulting in the increased O and N observed. While the samples can be mounted rapidly, the process of venting the plasma chamber, mounting samples and loading into the XPS takes several minutes. Some O and N may also come from the plasma.

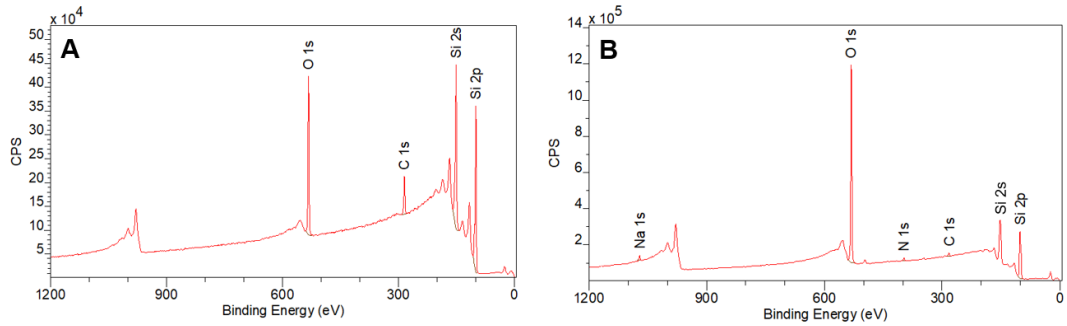

Figure 4.9 XPS wide scan spectra collected over three locations for (**A**) *clean Si wafer*: O 1s 21.59%, C 1s 13.61%, Si 2p 64.80%; (**B**) *Si wafer directly following 20 minutes plasma activation*: O 1s 48.72%, C 1s 1.94%, Si 2p 47.95%, N 1s 1.08%, Na 1s 0.31%.

Figure 4.10 presents the XPS core line spectra for the Si wafer before and after plasma activation. From the C 1s core line spectra the removal of carbon is evident in the counts reduction from 10^3 to 10^2 CPS. When a surface undergoes plasma activation carbon is etched, revealing an exposed and reactive surface. During this process, surface defects can be induced, as a result of ion damage to the existing surface which can cause a small percentage of carbon to remain, as observed.[233] In the O 1s spectra, the overall increase in surface oxidation is reflected by the CPS (from 55 x10^3 to 12 x10^4) whereas the binding energy remains in a similar position (centred at 532.55 eV). The standard value for Si-O-Si is 532.62 eV, which is in keeping with the result reported.[227] The Si 2p core line further exemplifies the increased surface oxygen content. The silicon core line spectra have been fitted to include the characteristic Si $2p^{1/2}$ and $2p^{3/2}$ spin orbit peaks at 100.32 eV and 99.73 eV, respectively, for clean Si substrate. The SiO_x peaks were also observed at 101.63 eV (where x=1) and 103.49 eV (where x=2). The SiO_x peaks are broad and not easily resolved due to existing surface oxidation.[234] Upon plasma activation, the Si $2p^{1/2}$ and $2p^{3/2}$ shift to 102.29 eV and 101.69 eV, respectively, coincident with the most significant effect of plasma activation which is the broadening and increased CPS of the SiO_x peaks at 104.15 eV. The ratio of SiO:Si increases from 0.22:1 in a clean sample to 1.72:1 in the plasma activated sample. It is most likely that this SiO activation, visible in the spectrum **Figure 4.10(F)**, is essential to react with glycidol and allow grafting of HPG. A potential explanation for the increase in the SiO:Si ratio is the addition

of binding environments such as HO-Si-OH, Si-O-OH and Si-O-O-Si which would facilitate radical glycidol grafting to initiate polymerisation.

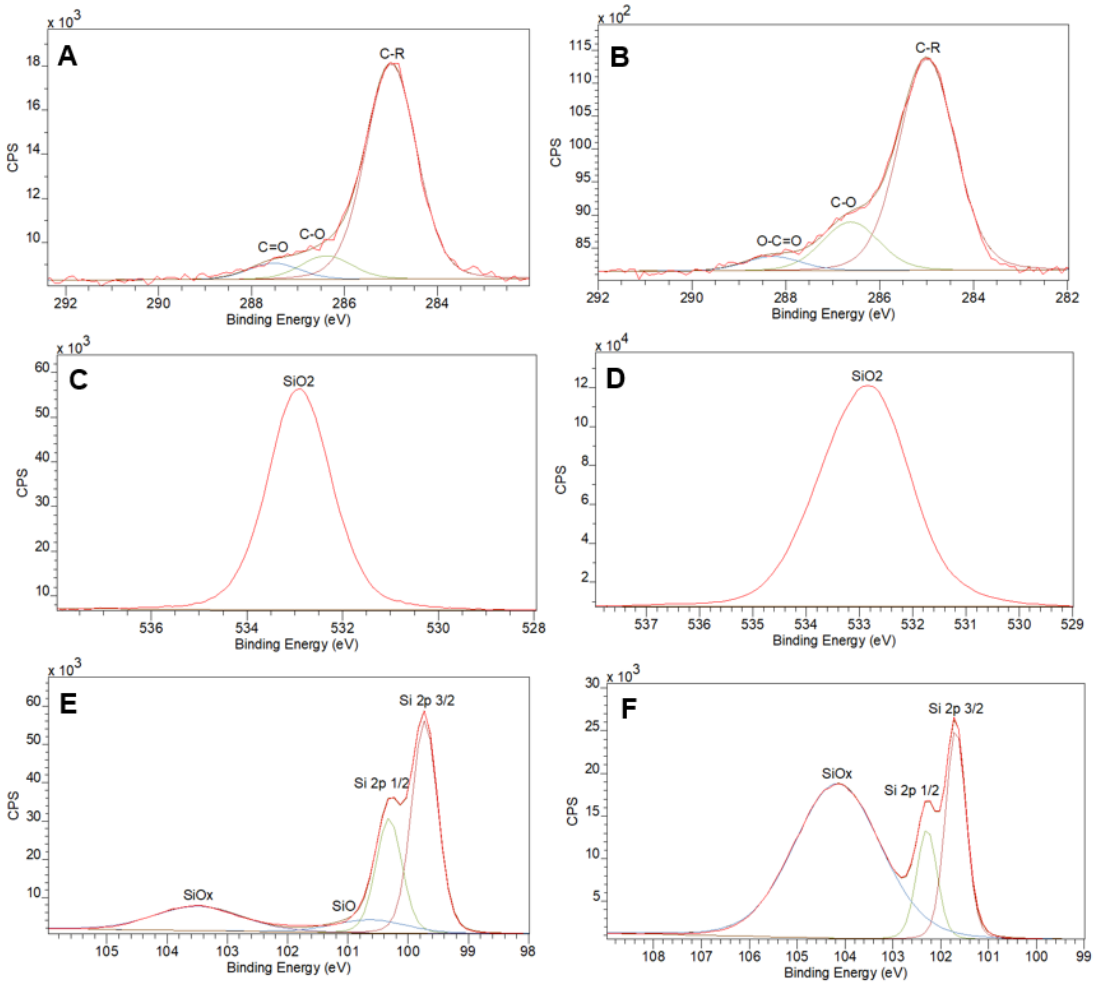

Figure 4.10 XPS core line spectra collected for Si after cleaning (**A, C, E**) and following 20 minutes plasma activation (**B, D, F**). (**A**) *Clean, C 1s*. C-R (285 eV, 84.45%), C-O (286.39 eV, 9.19%), C=O (287.52 eV, 6.37%); (**B**) *Plasma activated, C 1s*. C-R (285 eV, 77.06%), C-O (286.62 eV, 17.74%), O-C=O (288.28 eV, 5.20%); (**C**) *Clean, O 1s.* SiO_2 (532.87 eV); (**D**) *Plasma activated, O 1s*. SiO_2 (532.84 eV); (**E**) *Clean, Si 2p*. Si $2p^{3/2}$ (99.73 eV, 47.64%), Si $2p^{1/2}$ (100.32 eV, 25.71%), SiO (100.63 eV, 8.31%), SiOx (103.49, 18.34%); (**F**) *Plasma activated, Si 2p*. Si $2p^{3/2}$ (101.69 eV, 21.85%), Si $2p^{1/2}$ (102.29 eV, 11.36%), SiOx (104.15, 66.79%).[1]

[1] Spectra subject to charging which has shifted the SiO_x region, merging it with the Si 2p peaks. This was the only complete data set collected for a plasma activated Si sample, but the Si 2p spectrum is not representative of all other collections. This issue does not heavily affect the overall discussion.

4.3.3.1.2 Titanium-Silicon

TiSi had previously been selected as the standard substrate for analysing HPG, in the original study of this process carried out by the project collaborators at UniSA. TiSi was selected because it is a medically relevant surface. The O-O-Ti surface feature that remains after plasma activation is a potential reactive species to begin HPG formation.

Figure 4.11 displays the XPS measurements recorded for TiSi samples, clean and plasma activated. Immediately, the differences in the composition of the surface are evident. Firstly, whereas in the clean TiSi sample there are only C, O, Ti and N signals, after activation there are also visible Si and Na composition, a result of contamination from the plasma reactor. As noted in the methods (**Section 4.2.2**) the plasma cleaner used throughout this work was used across a wide range of research projects and Si/Na contamination was experienced by multiple users of the equipment, across a range of substrate materials. The small array of nitrogen environments present in the plasma activated sample have been highlighted in **Figure 4.11 (B)** because the existence of this on the surface will become significant in discussions presented in **Chapter 5**. Overall, plasma activation demonstrates the effective removal of carbon, revealing the increase in Ti content. The elemental oxygen composition, seen in the wide scans (**Figure 4.11 (A)** and **(B)**), increased to 64% from 40%. The O 1s core line spectra for the clean substrate has peaks that are akin to TiO_2 peaks as reported in previous studies.[235] Comparatively in the O 1s core line spectrum from the activated sample, there is the evolution of a third environment at 532.85 eV which based on previous literature could be the (Ti)-O-O-(Ti) environment, induced by plasma activation.[236]

The Ti $2p^{1/2}$ and Ti $2p^{3/2}$ peaks at 465 and 459 eV, respectively, remain unchanged aside from a x1.4 increase in counts after surface activation. It can be assumed that the titanium is fully oxidised before activation because the initial O:Ti ratio is 2.64:1 (expect 2:1 for TiO_2), increasing to 3.09:1 after activation, with little or no other elements present that would be expected to be bound with oxygen. This contributes to the conclusion that the reactive Ti-O-O-Ti moiety has been introduced.

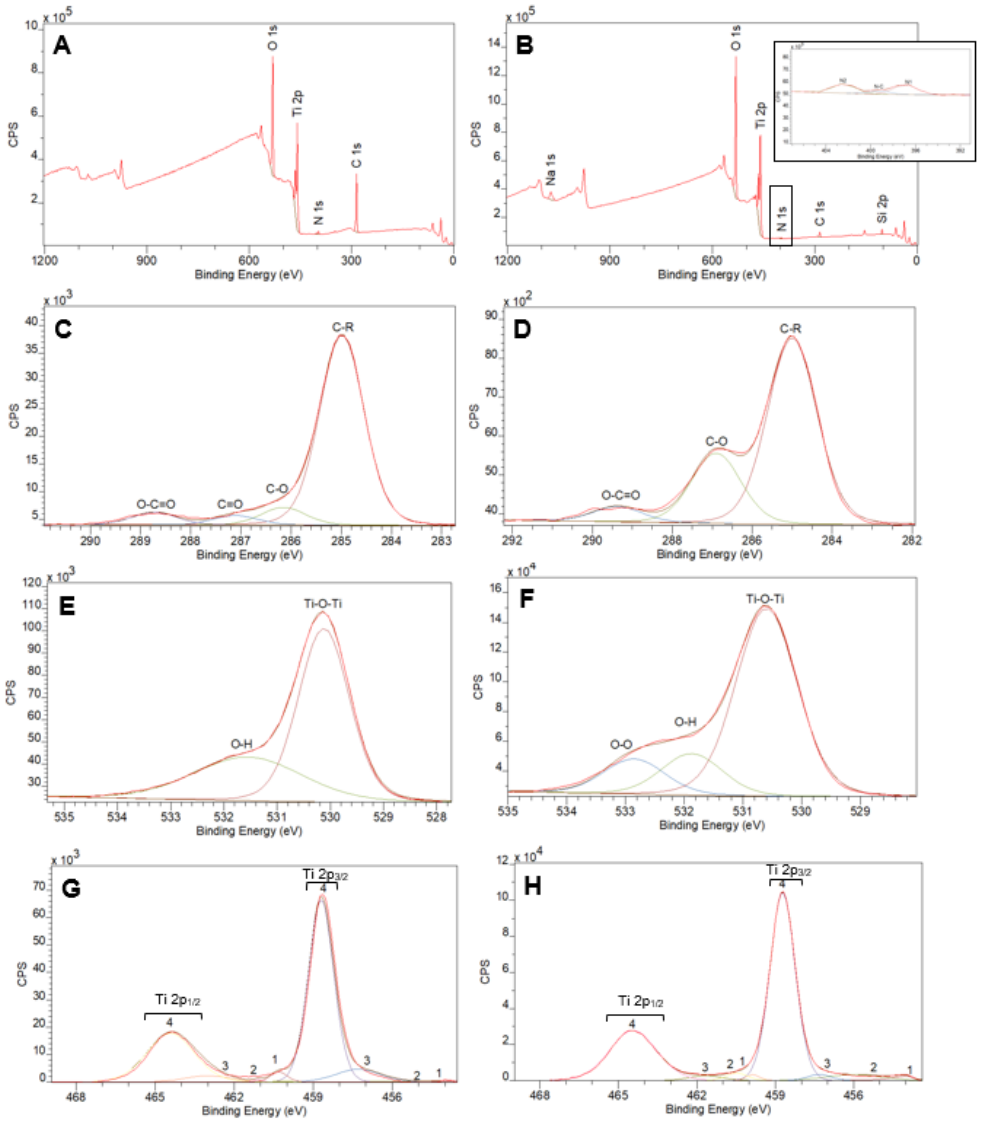

Figure 4.11 XPS wide scan and core line spectra collected on TiSi after cleaning (**A, C, E, G**) and following 20 minutes plasma activation (**B, D, F, H**). (**A**) *Clean*, O 1s 39.85%, C 1s 41.03%, Ti 2p 17.16%, N 1s 1.96%; (**B**) *Plasma activated*, O 1s 63.76%, C 1s 6.31%, Ti 2p 23.13%, N 1s 1.28%, Si 2p 5.52%; (**C**) *Clean, C 1s*. C-R (285 eV, 82.82%), C-O (286.15 eV, 7.66%), C=O (287.11 eV, 4.07%), O-C=O (288.72 eV, 5.45%); (**D**) *Plasma activated, C 1s*. C-R (285 eV, 68.56%), C-O (286.90 eV, 25.84%), O-C=O (289.37 eV, 5.59%); (**E**) *Clean, O 1s*. Ti-O-Ti (530.12 eV, 65.11%), O-H (531.55 eV, 34.89%); (**F**) *Plasma activated, O 1s*. Ti-O-Ti (530.60 eV, 70.96%), O-H (531.86 eV, 15.68%), Ti-O-O (532.85 eV, 13.36%); (**G**) *Clean, Ti 2p, where the transition states of the metal are denoted 1-4 (1 = Ti (0) metal, 2 = Ti (II), 3 = Ti (III), 4 = Ti (IV)).* Ti $2p^{3/2}$ (458.70 eV, 58.17%), Ti $2p^{1/2}$ (464.44 eV, 29.09%); (**H**) *Plasma activated, Ti 2p, where the transition states of the metal are denoted 1-4 (1 = Ti (0) metal, 2 = Ti (II), 3 = Ti (III), 4 = Ti (IV)).* Ti $2p^{3/2}$ (458.72 eV, 59,82%), Ti $2p^{1/2}$ (464.44 eV, 29.91%).

Interestingly, after plasma activation an Si 2p environment was revealed (**Figure 4.12**). The Si 2p core line spectrum displays a singlet peak, rather than the expected doublets. Si-Si metalloid peaks generally arise between 99.7-101.7 eV whilst SiO_x peaks are located between 101-104 eV.[237] There is a singular SiO environment in this sample. The Ti layer of this material should be 40 nm which is far greater than the XPS sampling depth and while plasma treatment is designed to remove carbon contamination, significant etching (e.g. 30-35 nm) of Ti is extremely unlikely. From cross-referencing results with colleagues using the same equipment, it was found that Si contamination occurred from the plasma cleaner.

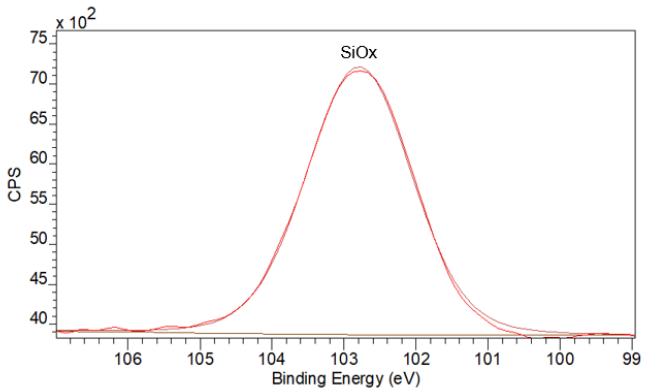

Figure 4.12 XPS Si 2p core line spectrum collected on TiSi after 20 minutes plasma activation (102.79 eV).

4.3.3.1.3 Polystyrene

PS was explored as a substrate for HPG grafting in an earlier study which prompted this work.[232] Polystyrene was spin-coated onto a Si wafer before undergoing standard analysis and plasma activated XPS measurements. It was found that after the standard 20-minute plasma activation period, the PS was simply removed from the Si substrate. The process was repeated, applying a smaller activation time (10 minutes) and the same result was observed, see **Appendix 4.9**. The plasma activation process removes all carbon, leaving only the Si substrate, as reflected in the XPS spectra.

To evaluate further a solid PS sample was required. However, the 20-minute plasma activation time led to the complete destruction of the sample. A shorter activation time was therefore attempted, to obtain a suitably activated sample. **Figure 4.13** displays the wide scan XPS spectra for PS before and after 5 minutes of plasma activation. Through plasma activation (**Figure 4.13(B)**) the carbon content on the surface experienced a 16% reduction, whilst the oxygen content has increased 6-fold, relative to the clean substrate (**Figure 4.13 (A)**). Despite a reduction in the activation time (to 5 minutes) the sample was still damaged, reducing the size to approximately 0.5 x 0.5 cm^2, from 1 x 1 cm^2. This is a result of the plasma cleaner sample plate, which heats up during plasma on time, causing the shrinkage of solid PS samples. After plasma activating the surface, the core line C 1s spectrum demonstrates the effect of introducing oxygen to the PS structure, that has been observed in previous studies.[238] Four distinct carbon-oxygen environment peaks have been added, when compared to the pre-activation spectrum which displays a single dominant C-R environment. Notably, the π-π* satellite peak, at approximately 292 eV, has been partially destroyed.

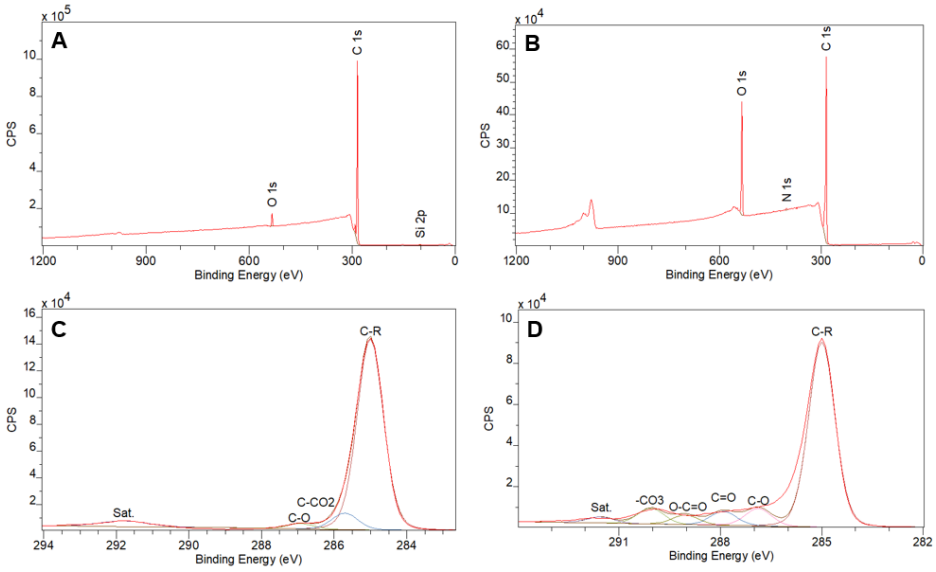

Figure 4.13 XPS wide scan and core line spectra collected for PS after cleaning (**A, C**) and 20 minutes plasma activation (**B, D**). (**A**) *Clean,* O 1s 2.98%, C 1s 96.69%, Si 2p 0.33%; (**B**) *Plasma activated*, O 1s 18.43%, C 1s 81.05%, N 1s 0.51%; (**C**) *Clean, C 1s*. C-R (285 eV, 85.52%), C-CO_2 (285.70 eV, 7.42%), C-O (286.92 eV, 2.39%), sat. (291.80 eV, 4.66%); (**D**) *Plasma activated, C 1s*. C-R (285 eV, 74.68%), C-O (286.88 eV, 7.07%), C=O (287.91 eV, 5.66%), O-C=O (289.03 eV, 3.84%), -CO_3 (290.06 eV, 6.31%), satellite (291.56 eV, 2.45%).

4.3.3.1.4 Polytetrafluoroethylene

Under XPS analysis clean PTFE has a prominent C 1s signal at 292 eV, consistent with the CF_2 environment. A trace signal was found at 285 eV indicating low H-C contamination. The wide scan spectrum displays <0.5% surface oxygen, indicating limited surface oxidation, **Figure 4.14**. Plasma activation of PTFE only results in a small increase to the surface oxidation from 0.49% to 3.14%. Peak fitting of the C 1s spectrum for the plasma activated PTFE reveals an increase in C environments, clearly identifiable between 285 eV and 292 eV; these are anticipated with the introduction of oxygen binding environments (such as C-O, C=O, etc.), as well as potential damage to the CF_2 backbone structure, resulting in a broad range of carbon-fluorine-oxygen environments. The presence of fluorine within a surface is known to shift all of the chemical bonding environments to higher binding energies that would normally be associated with different functionalities.[239] These peaks are labelled as 1-4 in **Figure 4.14 (D)**; it is likely that 1 = C-R, 2 = C-O, 3 = C=O/CF, 4 = CF-CF_n. The O 1s binding energies have not been peak fitted due to chemical shifting as a result of F.

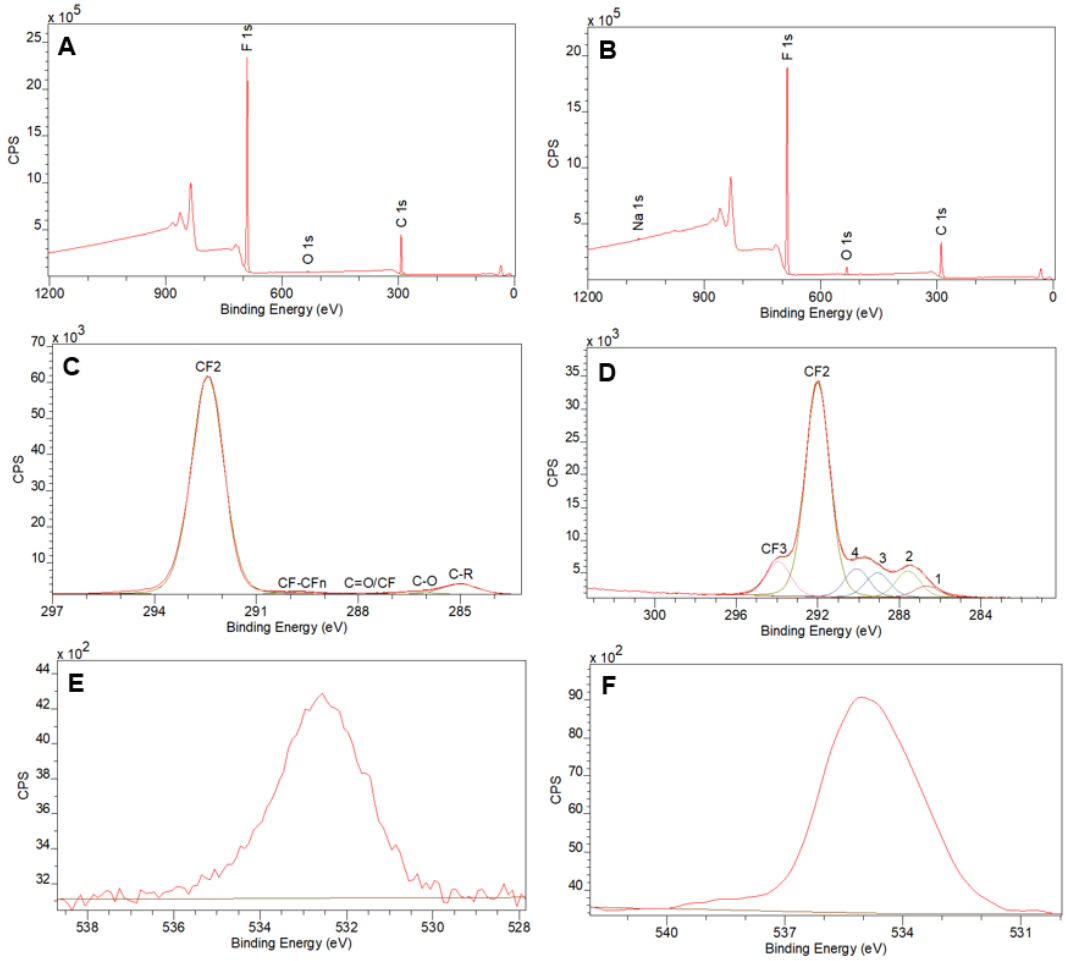

Figure 4.14 XPS wide scan and core line spectra collected on PTFE after cleaning (**A, C, E**) and following 20 minutes plasma activation (**B, D, F**). (**A**) *Clean*, O 1s 0.49%, C 1s 38.64%, F 1s 60.87%; (**B**) *Plasma activated*, O 1s 3.14%, C 1s 40.87%, F 1s 55.74%, Na 1s 0.25%; (**C**) *Clean, C 1s*. C-R (285 eV, 4.87%), C-O (286.39, 1.23%), C=O/CF (287.91 eV, 0.54%), CF-CFn (289.71 eV, 1.11%), CF_2 (292.44 eV, 92.25%); (**D**) *Plasma activated, C 1s*. 1 (286.69 eV, 3.44%), 2 (287.58 eV, 7.76%), 3 (289.08 eV, 7.19%), 4 (290.09 eV, 8.44%), CF_2 (292.02 eV, 63.16), CF_3 (293.94 eV, 10.11%); (**E**) *Clean, O1s* (532.56 eV); (**F**) *Plasma activated, O1s* (535.15 eV).

4.3.3.1.5 Nitinol Stents

Nitinol stents were trialled throughout this study as a clinically relevant substrate. Due to the small size of these stents (strut size approximately 150 µm), challenges were presented in terms of surface analysis. In order to collect spectra from the stent, the spectral collection area

was limited to 110 µm aperture and a line of measurements at small intervals were collected. Unfortunately, the clean and plasma activated nitinol sample XPS spectra (**Appendix 4.10**) closely resemble the spectrum of Kapton tape on which all samples are affixed (**Appendix 4.11**). Plasma activation should increase surface oxygen and it would be reasonable to assume this has occurred but due to the sampling difficulties this is not completely obvious within the XPS spectra.

4.3.3.2 XPS analysis of HPG Coatings

All substrate materials studied during plasma treatment exhibited an increase surface O content and (as shown later) O environments (peroxide) that would be required to promote HPG grafting. Once a substrate has undergone plasma activation to make the surface reactive for polymerisation, it should be immediately submerged in liquid glycidol. Following incubation at 80℃ for 24 hours, ethanol is added to the sample vials to quench the reaction. Samples then undergo further cleaning with ethanol to remove self-polymerised monomer from the surface, leaving an ultra-thin, uniform HPG coating. Although the method to produce this coating is well documented, there is a lack of surface analysis available in the literature, particularly across multiple substrates within the same study.

4.3.3.2.1 Grafting on Si

HPG was first grafted onto Si and analysed with XPS (**Figure 4.15**). In the wide scan of the surface, the rising baseline of the spectrum (from 100 eV) and the appearance of Si 2p peaks is typical of thin coatings, less than the XPS sampling depth (5-10 nm).[200] This is in contrast to the linear baseline observed for the thicker ethanol PP coatings (e.g. **Figure 4.4**). Zn 2p is also seen sporadically in the survey scans across all HPG samples; this is plausibly a contaminant from the grafting containers which were used repeatedly in this study. The characteristic high C-O-C content indicates the successful formation of HPG, in the C 1s core line spectrum.

Generally, in this project, using the plasma graft-from protocol of HPG coating, samples result with 75-90% C-O surface composition. The formation of HPG is also accompanied by a downward shift of the O 1s centroid binding energy. Following plasma activation, a single O 1s environment was observed at 532.84 eV, whereas after grafting two oxygen environments are seen. The larger peak at 532.78 eV primarily originates from C-O-C, alluding to the HPG coating, and the smaller peak at 531.28 eV relates to O=C, the terminating group.[240,241]

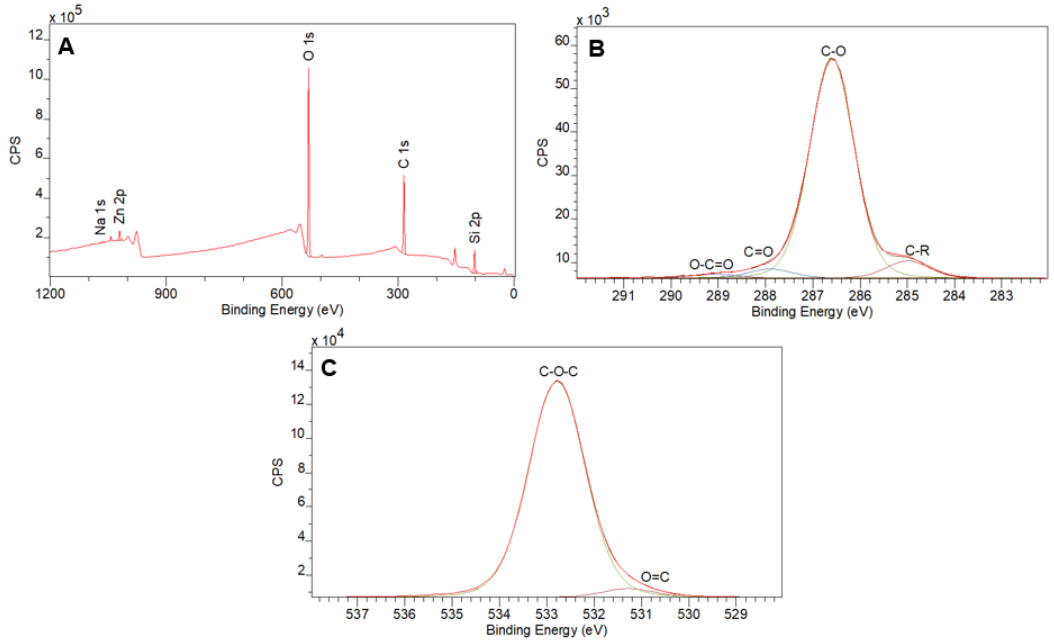

Figure 4.15 XPS spectra of HPG grafted onto Si substrate. (**A**) *Wide scan*, O 1s 40.90%, C 1s 43.92%, Si 2p 14.80%, Na 1s 0.08%, Zn 2p 0.30%; (**B**) *C 1s**. C-R (285 eV, 6.91%), C-O (286.59 eV, 87.97%), C=O (287.90 eV, 3.63%), O-C=O (289.04 eV, 1.49%); (**C**) *O 1s*. O=C (531.28 eV, 3.51%), C-O-C (532.78 eV, 96.49%).[2] [*constrained peak positions to aid fit analysis, C=O peak position held at 285+2.9 eV]

A study of life-time for plasma aged samples was conducted. Whereas in usual proceedings, plasma activated samples were immediately submerged in glycidol, the time between activation

[2] Large peak at 532.78 eV not purely related to the coating, C-O-Si and Si-O-Si environments incorporated within this peak.

and submersion was delayed to explore the effect of this on the HPG coating. After only a 4-hour delay between surface activation and submersion in the reactive material, the coating was altered. **Appendix 4.12** displays the resultant HPG coating where the carbon content is decreased to 35% (from 44% in **Figure 4.15**), coincident with the C-O content reducing to 39% (from 88% in **Figure 4.15**). The Si 2p signal in the wide scan has also increased to 26% (**Appendix 4.12**) from 15% (**Figure 4.15**), suggesting that a thinner HPG coating was grafted because of reduced reactivity. Given the time delay, it is also possible that the substrate became contaminated before reaction with glycidol, and it is this contamination that is primarily visible in the XPS spectra. This study emphasises the importance of a rapid immersion step, following surface activation.

4.3.3.2.2 Grafting on TiSi

Figure 4.16 displays HPG grafted onto the clinically relevant substrate, TiSi. The characteristic 84% C-O content in the C 1s core line spectra immediately indicates the formation of the HPG coating. The O 1s core line spectra in **Figure 4.16** is markedly different to those seen in **Figure 4.11**, with Ti-O-Ti and Ti-O-C binding energies alongside the C-O-C environment at 532.67 eV. Therefore, this peak could also be used as a marker for successful HPG formation.

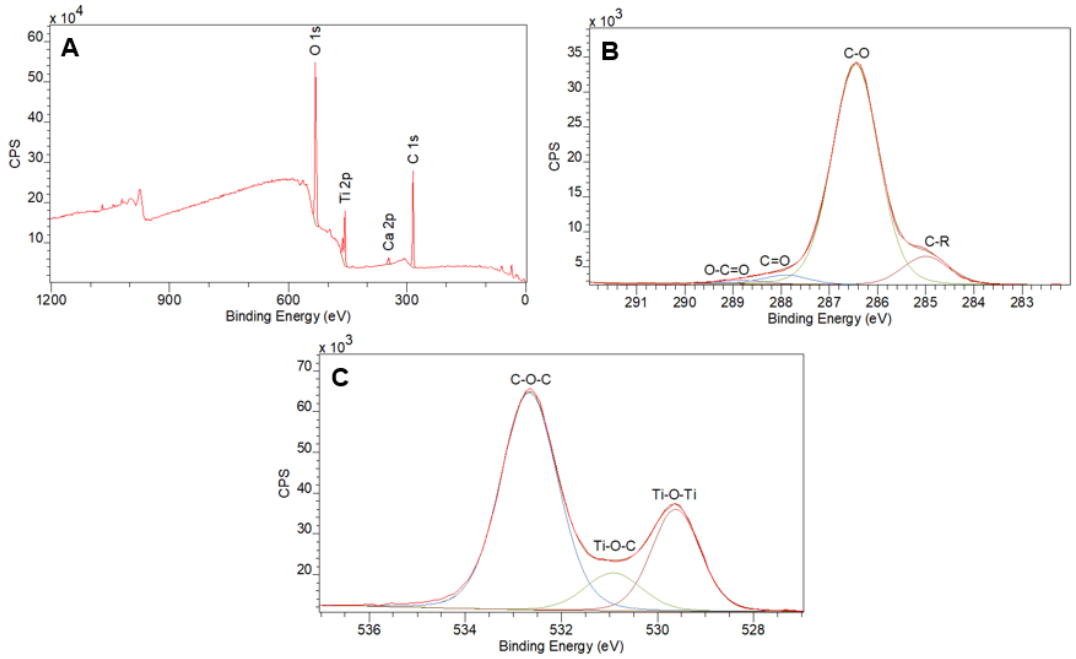

Figure 4.16 XPS spectra of HPG grafted onto TiSi substrate. (**A**) *Wide scan*, O 1s 45.49%, C 1s 47.72%, Ti 2p 5.86%, Ca 2p 0.94%; (**B**) *C 1s**. C-R (285 eV, 10.89%), C-O (286.46 eV, 84.32%), C=O (287.90 eV, 3.47%), O-C=O (288.80 eV, 1.32%); (**C**) *O 1s*. Ti-O-Ti (529.62 eV, 25.36%), Ti-O-C (530.92 eV, 11.05%), C-O-C (532.67 eV, 63.59%). [*constrained peak positions to aid fit analysis, C=O peak position held at 285+2.9 eV]

4.3.3.2.3 Grafting on PS

Solid PS did undergo composition changes when plasma activated as seen in the C 1s binding energy displayed in **Figure 4.13**. However, to prevent sample destruction it was necessary to reduce the activation time from 20 minutes to 5 minutes (**Section 4.3.3.1.3**). After incubating the PS sample in glycidol, HPG did not form a coating on the surface, as reported **in Figure 4.17**. The wide scan is visibly comparative to the clean PS. From the C 1s spectrum (**Figure 4.17 (B)**) there is no C-O content, which leads to the conclusion that HPG has not formed on this surface. This could be as a result of the reduced plasma activation time. Alternatively, it could result from the damage sustained to the PS structure, seen in **Figure 4.13**. Since

conducting this experiment, further literature has been sourced which demonstrates the detrimental effect of liquid glycidol on polystyrene, in which the polymer structure swells to incorporate the monomer, rather than forming a single coating on the active surface.[232] A vapour based method to coat polystyrene has been developed by collaborators at UniSA, outside of the scope of this thesis which may provide a solution to this issue.

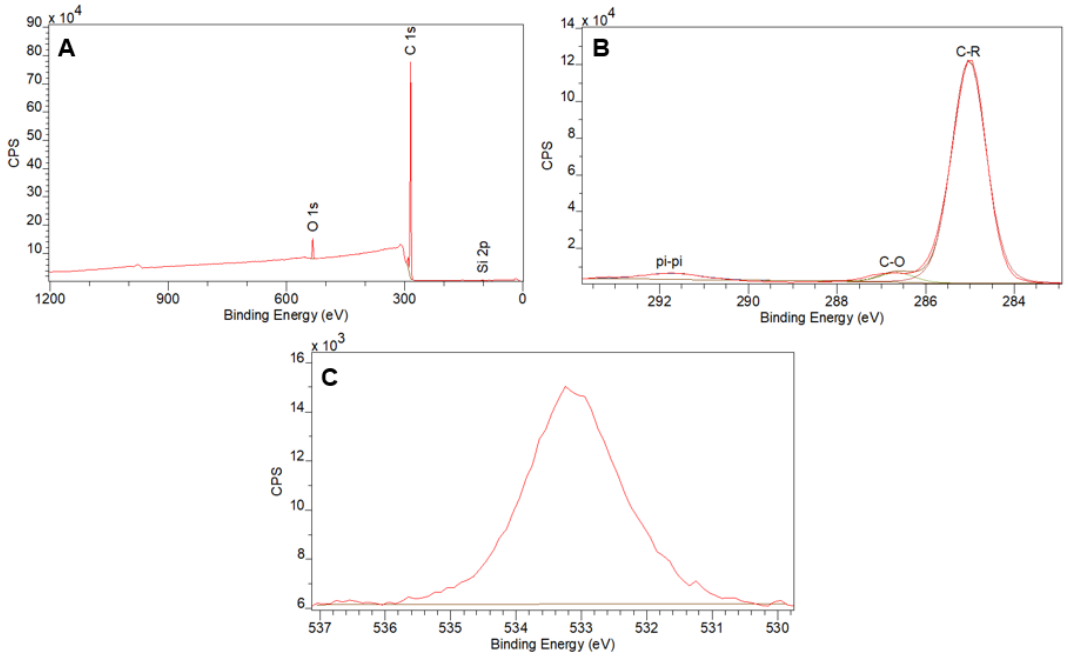

Figure 4.17 XPS spectra of unsuccessful HPG formation on solid PS following 5-minutes of plasma activation and exposure to glycidol for 24 hours. (**A**) *Wide scan*, O 1s 3.98%, C 1s 95.82%, Si 2p 0.19%; (**B**) *C 1s*. C-R (285 eV, 91.85%), C-O (286.62 eV, 3.99%), pi-pi* (291.70 eV, 4.15%); (**C**) *O 1s* (533.25 eV).

4.3.3.2.4 Grafting on PTFE

PTFE is a clinically relevant polymer material used to make catheters. The XPS spectra recorded for HPG coated PTFE appear quite different to the other substrates described but still show clear signs of a HPG coating. **Figure 4.18** provides the C 1s core line spectrum where a strong signal from the CF_2 group remains, alongside the newly dominant signal introduced by

the HPG at 286.51 eV indicative of the C-O-C moiety. The thinness of the HPG coating (shown in **section 4.3.3.3.2**) accounts for the presence of the CF_2 signal that is observable in the XPS spectra, through the HPG coating. WCA measurements were made on PTFE (109°) and on HPG coated PTFE (44°) (**section 4.3.3.3.3**) which illustrates the enhanced hydrophilicity of the surface, strengthening the conclusion that HPG has formed.

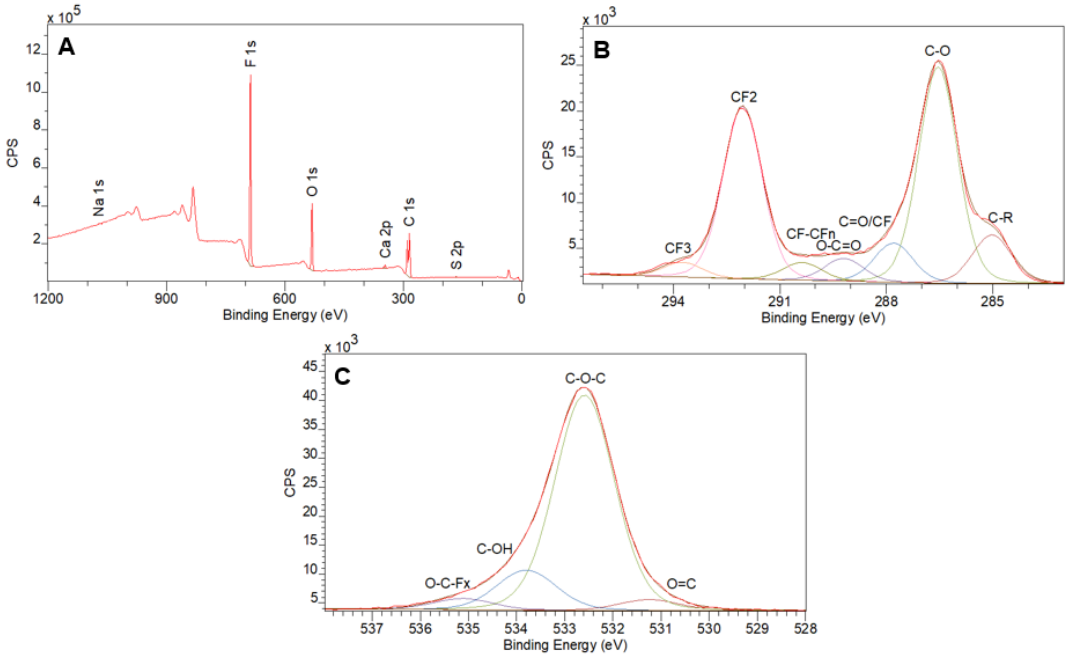

Figure 4.18 XPS spectra of HPG grafted onto PTFE substrate. (**A**) *Wide scan*, O 1s 16.15%, C 1s 50.64%, F 1s 32.33%, Na 1s 0.07%, S 2p 0.32%, Ca 2p 0.49%; (**B**) *C 1s.* C-R (285 eV, 9.12%), C-O (286.51 eV, 40.75%), C=O/CF (287.77 eV, 7.37%), O-C=O (289.17 eV, 4.29%), CF-CFn (290.34 eV, 3.34%), CF_2 (292.05 eV, 32.32%), CF_3 (293.74 eV, 2.75%); (**C**) *O 1s*. O=C (531.25 eV, 3.89%), C-O-C (532.59 eV, 77.73%), C-OH (533.80 eV, 14.37%), O-C-F_x (535.12 eV, 4.01%).

4.3.3.2.5 Grafting on Nitinol Stent

The surface analysis of HPG coated onto a nitinol stent, was harder to conduct due to the size of the wire mesh, as discussed in **section 4.3.3.1.5**. From the XPS, an increase in C-O-C content was reported to rise from 14.73% in clean, uncoated substrate to 41.97% on the HPG

coated substrate, (**Figure 4.19**). However, it is probable that the C-O-C retention is significantly higher, and this low result is due to the challenge of sampling the thin wire mesh which means background signals from the supporting Kapton tape are included. The O 1s is peak fitted with two binding environments at 532.72 eV (C-O-C) and 530.79 eV (Ti-O-C) consistent with the formation of an HPG coating.

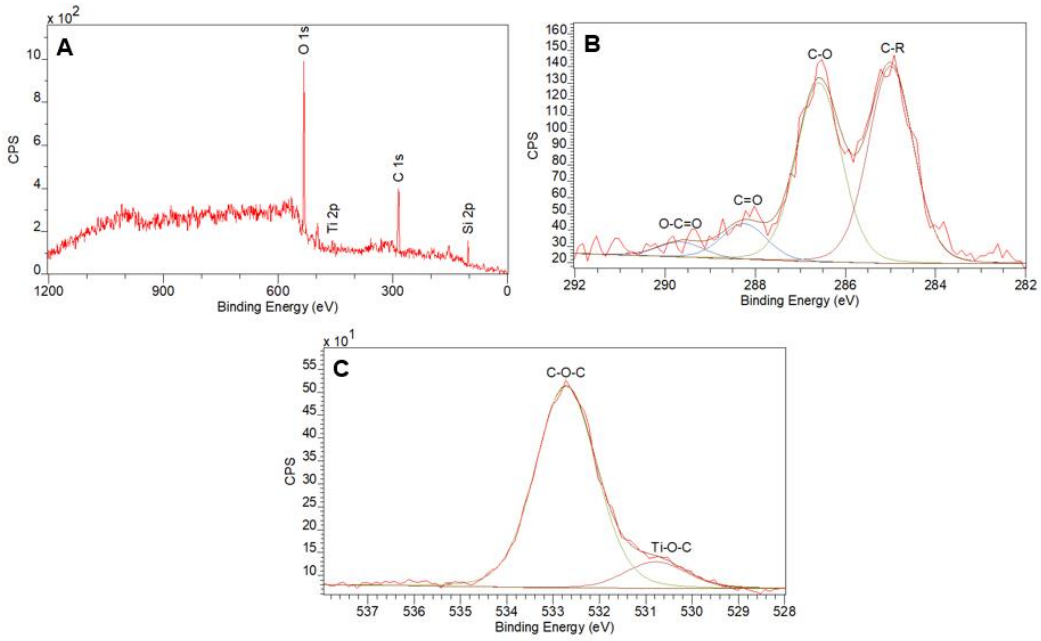

Figure 4.19 XPS spectra of HPG grafted onto a nitinol stent. (**A**) *Wide scan*, O 1s 34.82%, C 1s 47.44%, Si 2p 14.05%, Ti 2p 3.70%; (**B**) *C 1s*. C-R (285 eV, 46.16%), C-O (286.59 eV, 41.97%), C=O (288.25 eV, 8.36%), O-C=O (289.55 eV, 3.52%); (**C**) *O 1s*. Ti-O-C (530.79 eV, 11.54%), C-O-C (532.72 eV, 88.46%).

4.3.3.3 Further HPG analysis

4.3.3.3.1 TFAA Labelling

Additional analyses were performed on HPG coated TiSi, in an attempt to further understand the thickness and composition of the coating. Firstly, labelling was performed by employing TFAA, allowing derivatisation of end groups (primarily -OH but also C=O and O-C=O) which

are known to react with TFAA to form -O-C(=O)-CF_3, **Figure 4.20 (A)**.[242] The labelling process was performed by Laurine Martocq at LU, who had been working on end group labelling for a range of PP coatings as part of her PhD. By using XPS to measure fluorine concentration in the wide scan spectrum or CF_3 percentage composition in the C 1s core line spectrum, the number of terminating groups that are in the HPG coating can be estimated.

Figure 4.20 displays the XPS measurements for a representative HPG sample following TFAA derivatisation. The intensity under the CF_3 peak relative to the C-O peak gives the percentage of labelled end groups. From 3 samples, 50% of the C content is related to C-O; this equates to 5 in every 10 carbons. Derivatization introduces CH contamination, which is not uncommon. From the CF_3 and CO peak compositions the amount of carbon atoms that are end groups is approximately 6% as calculated by using CF_3 / (C-O + C=O + O-C=O).[243] It follows that each C-O-C chain is approximately 15-16 carbons long and from protein adsorption data, presented later, it is speculated that these chains are packed in a regular and tight pattern across the substrate surface.

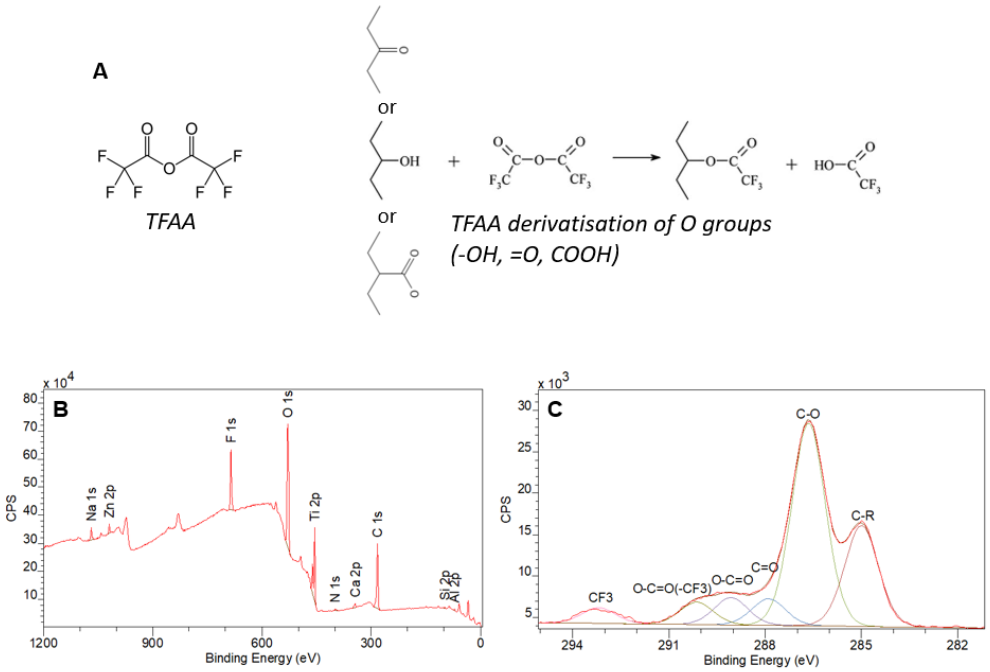

Figure 4.20 XPS spectra of HPG grafted onto TiSi substrate after labelling end groups with TFAA (performed by Laurine Martocq). (**A**) Chemical structure of TFAA and mechanism for derivatisation reaction of TFAA with a –OH and =O end group molecules; (**B**) *Wide scan spectrum for HPG grafted on TiSi after TFAA labelling experiment*, O 1s 38.30%, C 1s 38.95%, N 1s 0.56%, F 1s 11.52%, Na 1s 1.62%, Ti 2p 6.52%, Zn 2p 0.31%, Ca 2p 0.45%, Si 2p 0.50%, Al 2p 1.28%; (**C**) *HPG grafted on TiSi after TFAA labelling experiment, C 1s*. C-R (285 eV, 25.55%), C-O (286.65 eV, 51.24%), C=O (287.89 eV, 6.72%), O-C=O (289.06 eV, 6.90%), O-C=O(-CF_3) (290.14 eV, 5.65%), CF_3 (293.19 eV, 3.93%).

4.3.3.3.2 AFM

The thickness of HPG coatings produced via the plasma graft-from protocol had not previously been defined on TiSi. AFM was used to perform a scratch test to indicate sample thickness. AFM scratch testing works by raster scanning an AFM tip with a high force, removing softer layers and forming a scratched area. Once material is removed, a much gentler force is applied to the AFM probe for a scan over a large area surrounding the scratch. This image can be used to generate a step height profile across the scratch area and the immediately surrounding, undamaged surface. The line profile resulting from a scratch test on HPG on TiSi should therefore include a step which when measured will be equivalent to the thickness of the sample;

a preliminary result is given in **Appendix 4.13**. Typically, the line profile should display two peaks, the separation of which can be measured to provide an approximate sample thickness. However, this line profile demonstrated a single peak, alluding to an extremely thin coating (1-2 nm) where a definite thickness could not be calculated. Further AFM was performed using a more sophisticated instrument by Alessio Quadrelli at LU in the ultra-low noise "IsoLab" facility using an AFM that was set up for imaging molecular layers. **Figure 4.21 (A)** and **(B)** firstly provide evidence of the complete change in roughness between plasma activated and HPG coated TiSi which suggests a pinhole free coating has been grafted. The scratch test (**Figure 4.21 (C)**) showed that while the lower bound estimate of coating thickness was 1.27 nm (for a representative sample), the coating may be very strongly bound to the TiSi preventing total removal as the initial morphology of plasma activated TiSi was not revealed at the bottom of the scratched area. This thickness analysis provides further evidence that the HPG coating is thinner than the sampling depth of the XPS (5-10 nm) supporting suggestions that the substrate is often visible beneath the coating (as mentioned throughout **section 4.3.3.2**).

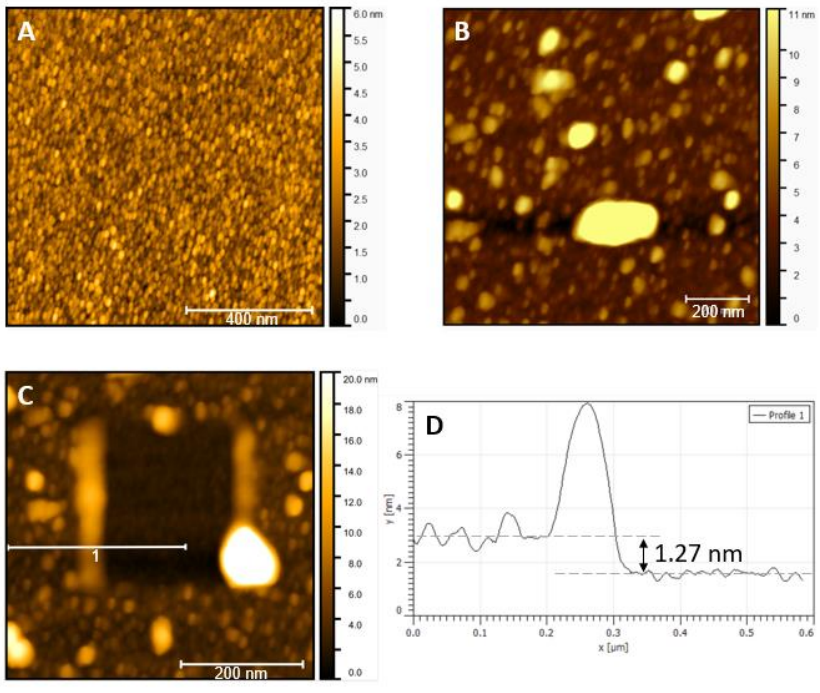

Figure 4.21 AFM scratch test on TiSi samples performed by Alessio Quadrelli. (**A**) Topographical image of plasma activated TiSi; (**B**) Topographical image of HPG grafted onto TiSi; (**C**) Topographical image of HPG on TiSi showing the scratch test area (denoted **1**); (**D**) Line profile illustrating coating has a lower bound thickness of 1.27 nm.

4.3.3.3.3 Water Contact Angle

HPG is a hydrophilic coating. This has been demonstrated in WCA measurements, as displayed in **Appendix 4.14**. WCA is a quick experiment where samples are placed in front of a camera which records whilst a single water droplet is deposited onto the surface. Using a still image of the droplet in contact with the surface, the contact angle can be calculated, providing evidence of hydrophilic or hydrophobic characteristics. The WCA for HPG on TiSi, Si and PTFE are summarised in **Table 4.4**. As an example, the WCA on coated TiSi is 31.49˚which reduces from 76.39˚on the clean, uncoated pre-activation substrate. In all cases, the WCA of the HPG coating is clearly lower than that of the pre-activation clean, substrate and definitively hydrophilic. The differences seen from substrate to substrate was unanticipated and suggests there are other factors involved like surface roughness. From external work by the project collaborators at TekCyte®, the solvent based grafting method was found to produce low quality HPG coatings on all plastics, including PTFE. Therefore, it is plausible that this high WCA (44˚) is a result of a surface which is not pin-hole free. TekCyte® have developed a vapour-based approach to graft HPG to plastics, which avoids this issue.

The WCA for the ethanol PP coating (production discussed in **section 4.3.1**) is provided alongside the HPG coating. As a contrasting example, in **Chapter 5** ethanol PP coatings will be utilised to demonstrate the effect of increased ethylene oxide retention and subsequent hydrophilicity, on the non-biofouling performance of the surfaces.

Table 4.4 WCA measurements for three key coated and uncoated substrate materials indicates the increase hydrophilicity of the PEO-coated surfaces.

		Contact	**Angle (◦)**
	Substrate	**HPG**	**EtOH PP**
Si	54	19	49
TiSi	76	31	/
PTFE	109	44	/

4.3.3.3.4 XPS Ion Milling

XPS ion milling allows depth profiling of materials by alternating steps of ion beam-etching and XPS analysis. This technique was used to evaluate a HPG coating from the air-interface, through the coating to the substrate-interface. Ion milling uses a GCIS to remove layers of material with minimal damage to the underlying polymer.[205] Reaching the substrate (TiSi) is evidenced by comparing the significant removal of carbon reflected in the wide scan spectra recorded before and after ion milling (**Figure 4.22 (A) and (B)**). Notably, an N 1s peak (with three binding environments) is recorded on the underlying substrate, as seen in the XPS analysis of plasma activated TiSi (**Figure 4.11**); this will become relevant in **Chapter 5**, as protein adsorption to the surface is explored. Over a 1000s etch time, the core line spectra for C 1s, O 1s and Si 2p were collected in 10 s etch steps. The removal of HPG coating was defined as the time at which %C-O composition plateaued, found to occur just above 20% of the total C 1s signal (**Figure 4.22 (D)**). For HPG on Si substrate this occurred at 300 s (**Appendix 4.15**). **Figure 4.22** reports the similar result of complete coating removal on TiSi, a more clinically relevant substrate. After 340 s the C 1s composition remains unchanged until 1000 s which suggests that the gentle ion cluster method employed, is only able to remove HPG and does not affect the underlying TiSi. The approximate etch rate for HPG on TiSi is 0.004 nms^{-1}. The O 1s spectrum binding energy shifts, as the ion mill progresses through the HPG, between 532.50 and 532.72 eV, without a discernible pattern.

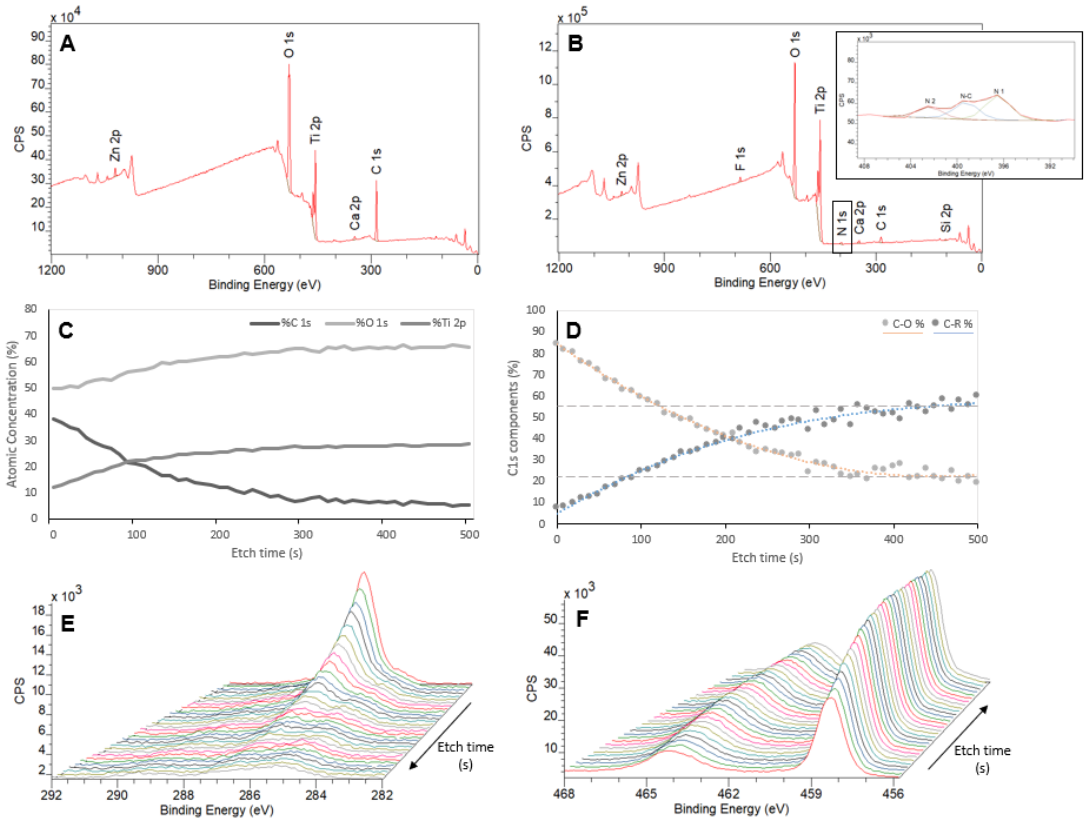

Figure 4.22 Depth profile XPS results for HPG on TiSi, ion milled for 1000s. (**A**) *Wide scan recorded before the sample was milled*, O 1s 52.60%, C 1s 35.53%, Ti 2p 11.00%, Zn 0.25%, Ca 2p 0.62%; (**B**) *Wide scan recorded after the sample was milled*, O 1s 57.93%, C 1s 9.08%, Ti 2p 27.48%, F 1s 1.53%, N 1s 2.13%, Ca 2p 0.79%, Zn 2p 0.18%, Si 2p 0.89%; (**C**) Atomic composition (%) plotted by etch time (s); (**D**) C 1s component plot against etch time (s), where plateau of %C-O at ~20% signals removal of HPG coating; (**E**) 3D plot of C 1s spectra from 0 s etch to 300 s; (**F**) 3D plot of Ti 2p spectra from 0 s to 300 s, showing the underlying substrate material that is uncovered during etching.

4.4 Conclusions

Within this chapter, HPG is used as a benchmark non-biofouling PEO-coating. Although the coating is widely researched and production methods are well established (for detail see **Chapter 1**), work presented in this chapter details the first rigorous surface analysis of HPG on both metallic and plastic substrate materials. The ultrathin, sub 5 nm, coating can successfully be grafted onto Si, TiSi, PTFE, and nitinol stents, as well as Al foil and glass as will be noted in **Chapter 5**. These PEO coatings have an ideal C-O composition of up to 90% and are benefitted

by extreme hydrophilicity. Alongside HPG investigations the development of a new PEO coating formed from 12-crown-4 in a plasma polymerisation method was progressed in a collaborative project with Liverpool University. The optimised 12-crown-4 coatings are able to maintain a dominant C-O composition of 60%, approaching the ethylene oxide content seen in HPG coatings. Future work should be in the progression and further optimisation of 12-crown-4 coatings to increase the %C-O and reduce the harsh experimental conditions; extreme heating of the monomer is currently required.

The next stage of this research is to explore the realistic viability of the surfaces presented through this chapter, to reduce biomolecule adsorption and ideally prevent biofilm development.

Chapter 5. Monitoring the Viability of Anti-Biofouling Surfaces to Prevent/Delay Biofilm Development

5.1 Introduction

Following the material analysis of novel coatings (detailed in **Chapter 4**) aimed at reliably resisting biofouling on medical devices, the realistic viability of the coatings towards this aim should be explored. All blood contacting materials have the potential to experience infection and particularly CRBSIs are an increasing threat.[54] A common route to infection in CVCs is via innocuous strains of bacteria at the skin barrier, like *Staphylococcus epidermidis*, that upon entering the blood stream result in device colonization and in severe cases, the evolution of biofilms.[57] In clinical practice, the occurrence of a CVC infection will worsen patient prognosis, reducing treatment options and increasing length of hospital stay. The prelude to the occurrence of infection, is the initial adsorption of proteins, which form a conditioning layer on the surface attracting microbial colonisation.[196] It is reasonable to assume that if this initial non-specific protein binding can be prevented, then the surface will be resistant to the subsequent microbial colonisation.[232,244] Although it is generally accepted that non-fouling properties can be induced by removing the protein molecule's ability to have a hydrophobic interaction with a surface (i.e. ethylene oxide surfaces), there is a lack of surface analysis in the literature to illustrate this.[226]

In this chapter, the results from non-biofouling testing begins with the attachment of key proteins that absorb to a surface before microbial attachment. Proteins like albumin, fibrinogen and fibronectin are essential in the conditioning of a surface towards microorganism colonisation. By first exposing a surface to the individual proteins you can gage the likelihood

that the surface will resist microbial attachment.[245,246] These preliminary anti-biofouling tests gave a realistic idea of which coatings should be tested against real bacteria. This chapter reveals the original finding that high ethylene oxide content surfaces retain reversible protein attachment at the surface and do not permit absorption into the coating structure which causes irreversible protein binding. In the subsequent biofilm study the novel analytical method outlined in **Chapter 2** was used to accurately monitor initial bacterial attachment and biofilm development on coated and uncoated materials. The biomass on the surface after incubation was also calculated as a standard check of degree of colonisation. HPG has been definitively proven to prevent biofilm colonisation of a rapidly proliferating *S. epidermidis* bacterial strain.

5.2 Materials and Methods

5.2.1 Protein Adsorption

5.2.1.1 Experimental Procedure

Coated and uncoated samples were placed in a 24-well plate. Samples were pre-hydrated in PBS (0.01 M, 1 mL), for 30 minutes. Albumin and fibrinogen (2 mg/mL) added, individually, to each sample and incubated statically for 1 hour at room temperature. Two protein tests were used to interrogate reversible and irreversible protein attachment (summarized in **Table 5.1**). In the initial test to evaluate reversibly bound protein, the samples were washed three times with PBS (1 mL) following incubation, to remove non-adherent material. In the subsequent testing, to determine the degree of irreversibly bound protein, after protein incubation samples were incubated for a further 72 hours in sodium dodecyl sulphate (SDS) solution, to denature proteins, permitting the complete removal of all reversibly bound material. The irreversibility test samples were then washed three times with PBS (1 mL).

Table 5.1 Summary of the key the processes involved to produce samples with reversible ("initial") and irreversible ("retained") protein adsorption.

"Initial" Protein Test	"Retained" Protein Test
3,600 s protein exposure	3,600 s protein exposure
PBS wash (three times)	PBS wash (three times)
XPS analysis	SDS incubation (72 hrs)
	PBS wash (three times)
	XPS analysis

5.2.1.2 Measuring Adsorbed Protein

To determine the amount of adsorbed protein on the sample surface, XPS measurements were collected. Nitrogen was used as the marker for adsorbed protein because none of the uncoated surfaces or coated materials contained nitrogen before protein exposure. Therefore, the total N 1s counts (CPS) were used as a correlation for the relative amounts of protein adsorbing to each surface. Small experimental errors in set-up in day-to-day usage of the XPS (for example the power to X-ray source may be calibrated slightly differently), can lead to significant changes in the counts between experiments. Therefore, day-to-day it is ideal to have a standard measurement to normalize relevant data points. To allow direct comparison between results the N 1s counts were normalized to the total Au counts measured on a gold standard (Au on mica), before each collection.

XPS was performed on a Kratos AXIS Supra spectrometer (Kratos Analytical Ltd, Manchester, UK) with monochromatic Al Kα radiation (hv = 1486.7 eV) and an internal flood gun. Samples were mounted with Kapton tape on plain dual height sample bar. An acceleration voltage of 15 keV at a power of 225 W was used to record the spectra. Survey spectra were

collected over a 300 × 700 μm^2 analysis area with a pass energy of 160 eV and core-line spectra were collected from the same area using a 20 eV pass energy (sweep time 120 s, 0.1 eV step size, 5 sweeps). Both survey and core line spectra were obtained for 3 locations per sample.

To probe the depth of absorption of the proteins in the surface, XPS ion milling was performed using the Axis Supra spectrometer, by applying an Ar source with 2000^+ cluster size and 5 keV energy. The analysis area was the 100 µm slot and the emission current was set at 25 mA. Each sample was analysed over a 4 mm area in rotating mode, with 100 etches and the pre-etch, etch and post-etch times were fixed at 10 s. Core-line spectra (C 1s, O 1s, N 1s, Si 2p and Ti 2p) were collected, where relevant, with a 60s sweep time.

All XPS data analysis was performed with the CasaXPS software (version 2.3.22, Casa Software Ltd, Devon, UK). Binding energies were referenced to the low energy C 1s peak (C-R) at 285.0 eV. Core line spectra were curve-fitted with the minimum number of mixed Gaussian–Lorentzian component profiles. Whilst the FWHM was constrained to match the reference peak, the Gaussian–Lorentzian mixing ratio (typically 30% Lorentzian and 70% Gaussian functions), positions and intensities of peaks were left unconstrained to result in the best fit.

5.2.2 Bacterial Exposure

5.2.2.1 Sample Preparation

To evaluate the degree of non-biofouling of each surface, bacterial exposure tests were conducted using *S. epidermidis* RP62A (ATCC 35984). Bacterial storage and revival procedure detailed in **Chapter 2**. The bacterial exposure test was carried out by incubating the coated and uncoated samples in the inoculant solution ($3x10^7$ CFU/mL, 1 mL) for 4 hours. Samples were washed once with growth media to remove loosely adhering cells.

5.2.2.2 Standard Biomass Quantification

Following incubation, a Miles and Misra serial dilution protocol was performed to quantify the biomass on the surface. Briefly, each sample is submerged in PBS (1 mL) in a test tube which is sonicated for 5 minutes to remove biomass from the surface; the resultant solution was retained. PBS (180 µL) was then added to 8 wells in a 96-well plate. The solution from sonication (20 µL) was then added to the first of these wells, becoming the -1 dilution (as depicted in **Figure 5.1:A**). The solution in the '-1' well is mixed by drawing up and expelling solution, then 20 µL are removed and pipetted into the '-2' well. This process continues until the '-8' well after which 20 µL is removed so that all wells contain 200 µL in total. A CBA plate is sectioned and labelled as shown in **Figure 5.1:B** and a 20 µL drop from each well is pipetted into the relevant sections. The agar plates are incubated overnight and the resultant colonies are counted (**Figure 5.1:C**). To calculate the CFU/mL for each sample, the number of colonies and dilution factor is divided by the proportional drop size and multiplied by the original solution volume to give the CFU/mL. Three CBA plates were produced per sample and the results averaged.

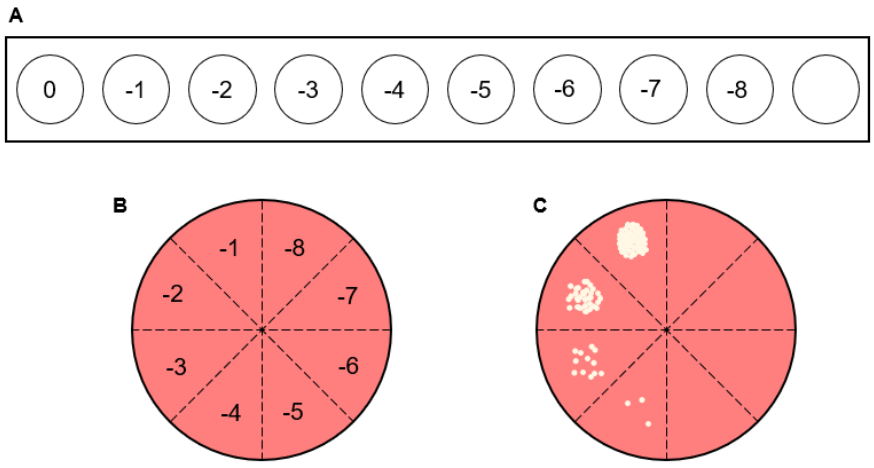

Figure 5.1 (**A**) Depiction of a well plate indicating that each solution is 1 log more dilute than the previous; (**B**) A CBA plate was labelled to correspond to each dilution in the 96-well plate; (**C**) After incubation the growth of individual colonies was counted to calculate the starting biomass concentration.

5.2.2.3 Fluorescence Microscopy

This characterisation was performed under the guidance of microbiologists at Glasgow University (Jontana Allkja, Mark Butcher and Prof. Gordon Ramage). Samples (HPG on glass slides) were incubated in bacterial culture media and biofilm formation was facilitated as described above. Following 4-hour incubation samples were removed from culture media and washed with PBS (1 mL). To produce the staining mixture, calcofluor white (1.5 µL per 1 mL PBS, 1g/L, Fluka analytical), propidium iodine (1.5 µL per 1 mL PBS, 0.1 mg/mL, Life technologies) and Syto9 (1.5 µL per 1 mL PBS, 5 mM, Invitrogen) were combined. Dye mixture (35 µL) was added to each sample and covered with a glass coverslip. Samples incubated in the dark for 30 minutes after which the coverslips were removed and the cells were washed with PBS (1 mL, three times). Then 4% paraformaldehyde (50 µL) was added to each sample, before covering with a coverslip and incubating in the dark for 15 minutes. Once ready to complete the imaging, coverslips were removed and the samples mounted in a new 6-well plate on a drop of BacLight mounting medium (Invitrogen). Image collection with Invitrogen EVOS M5000 microscope using a x40 objective (calcofluor white (blue filter), Syto9 (green filter) and propidium iodide (red filter)).

5.2.2.4 FTIR Analysis

A novel application of FTIR was also applied to define whether a biofilm had formed on the sample and control surfaces. The exact details of this protocol are given in **Chapter 2** (**section 2.2.5**). Briefly, following incubation to grow bacteria, samples were partially dried before FTIR analysis. A desktop Summit PRO FTIR spectrometer (Nicolet, Thermo Scientific, UK) with iD1 transmission sampling apparatus was used for all analysis. Data was collected using OMNIC Paradigm™ software (Thermo Scientific, UK). Data acquisition was performed at 4cm^{-1} resolution, accumulating 64 scans over a spectral range of 4000-800 cm^{-1}. Each sample was repeated in triplicate. Data analysis was conducted using OMNIC software in the first instance.

Each spectrum was processed in the same way, completing normalization followed by a base line correction.

5.3 Results and Discussion

5.3.1 Simple Protein Testing

5.3.1.1 Protein Adsorption Test

In order to test surfaces against biofouling, the first step is to evaluate the adsorption of key proteins; conceivably if a surface can resist protein adsorption, it follows that there is a higher chance of preventing microbial colonisation. Protein testing was conducted using an adapted method presented by the Timmons group where originally non-biofouling surfaces were exposed to (125)I-labelled albumin and fibrinogen, individually, and the radioactivity of the final sample was used as a measure of the amount of protein absorbed.[172] In the work presented in this chapter, XPS was employed to monitor the uptake of the proteins. Each surface that was examined does not contain nitrogen prior to protein exposure, and proteins naturally contain nitrogen. Therefore, following a protein test, any nitrogen signal observed in the resultant XPS signal can be assumed to originate from protein that is bound to the surface of the sample.

The protein test protocol briefly involves submerging a sample in PBS to pre-load with water because hydrophilic surfaces can prevent biofouling by stopping the displacement of water molecules with proteins.[226] A standard amount of protein solution is then added to the sample and allowed to adsorb, before removing the solution and washing in PBS. This gives a sample with reversibly attached protein. When beginning this experimental work, the first tasks were to determine the most appropriate adsorption time and the best measure of nitrogen to use as an equivalent for protein, %N or N counts and either the wide or N 1s core line spectra could be utilised. The determination of adsorption time was completed using an ethanol PP coating on Si. From the work presented in **Chapter 4**, the optimal ethanol PP parameters in terms of ethylene oxide retention were 20 Pa, 10 W (where C-O composition was 29%). But all

of the ethanol PP coatings had a similar %C-O, between 18-29%. For the protein test work, the thicker 10 Pa, 30 W coating (C-O of 19%) was selected for numerous reasons, not least due to the improved ability to maintain plasma conditions to allow effective deposition of a coating. Firstly, the ethanol coating was partially soluble in solution and was therefore removed upon contact with PBS. This was reflected in subsequent XPS analysis, as the baseline became inclined following protein exposure, insinuating a coating thickness of less than 10 nm (**Appendix 5.1**). This test was conducted on both the 20 Pa/10 W and 10 Pa/30 W ethanol PP coating and reproducibly the 20 Pa/10 W coating was removed during protein testing, such that the underlying substrate signals (Si 2p) were visible. The thickest ethanol PP coating was produced at 10 Pa/30 W (85 nm). To further investigate the issue of coating instability in solution, AFM was performed on two samples by Alessio Quadrelli and used to reveal a reduction in surface thickness from 85 nm to 58 nm (**Appendix 5.2**). Despite the coating reduction observed across all ethanol PP samples, the 10 Pa/30 W coating only reduced to a minimum of 50 nm which meant the substrate would not be detected in XPS analysis; hence the 10 Pa/30 W ethanol coating was used in the protein testing as a representative ethanol PP coating, despite the lower %C-O retention.

Figure 5.2 displays a representative survey scan, C 1s and N 1s core line spectra collected for a 10 Pa/30 W ethanol PP coating after exposure to albumin for 1000s. The N composition is increased to 3.23% (739.13 CPS), from 0% in the surface before the experiment. The N 1s core line spectrum reveals 2 binding environments: N-C, the protein marker (at 400.08 eV) and a second peak, denoted N2 which seems to originate from the underlying material (at 401.82 eV). The effect of not pre-adsorbing water to the coating before the protein test was noted with the N counts moving from 1244.67 CPS (non-hydrated) to 781.38 CPS (hydrated) (**Appendix 5.3**). If the samples are not suitably loaded with water prior to testing, the dry sample will naturally draw in water from solution which would also force the uptake of protein, skewing the results.

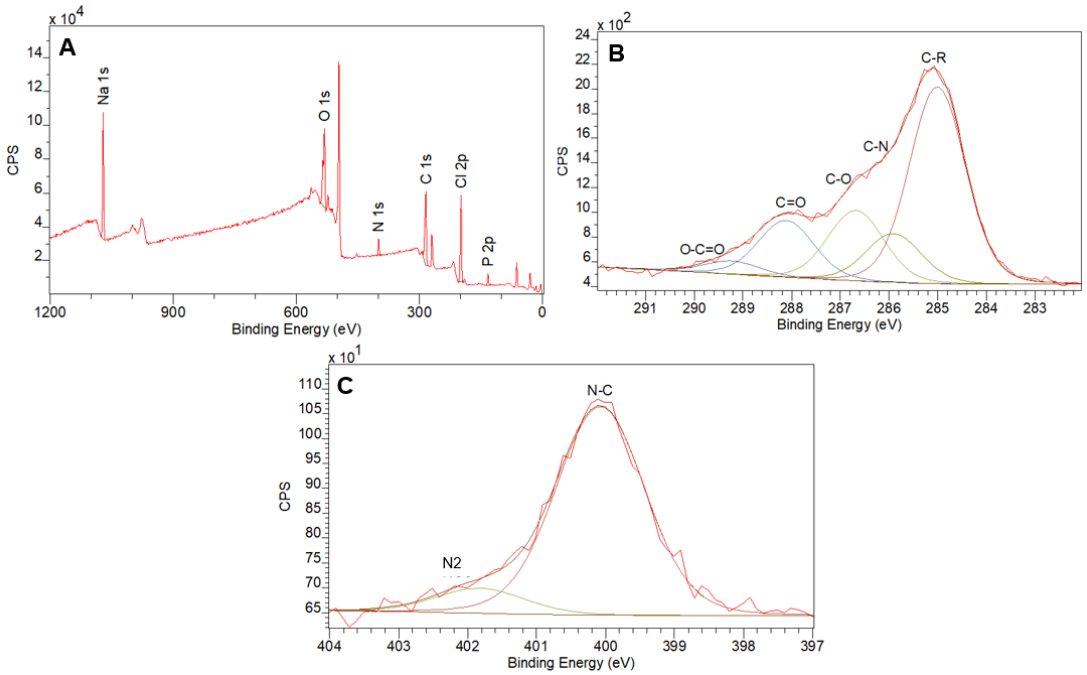

Figure 5.2 XPS analysis of an ethanol PP coating (deposited at 10 Pa, 30 W) after exposure to albumin for 1000 s. (**A**) *Wide scan*, O 1s 23.41%, C 1s 44.75%, N 1s 3.23% (counts 739.13 CPS), Na 1s 8.78%, Cl 2p 16.14%, P 2p 3.69%; (**B**) *C 1s.* C-R (285 eV, 51.00%), C-N (285.91 eV, 12.65%), C-O (286.68 eV, 18.23%), C=O (288.11 eV, 14.70%), O-C=O (289.13 eV, 3.42%); (**C**) *N 1s*. N-C (400.08 eV, 89.35%), N2 (401.82 eV, 10.65%).

To optimise the time that the surface was exposed to the protein, a range of adsorption times were trialled, from 10 s to 10,000 s. A calibration curve is presented in **Figure 5.3**. The N counts rapidly increased over the initial adsorption period before peaking at 3600 s, after which this maximum N counts was not exceeded. Therefore, in all protein adsorption tests for the remainder of this project, the adsorption time was fixed at 3600 s.

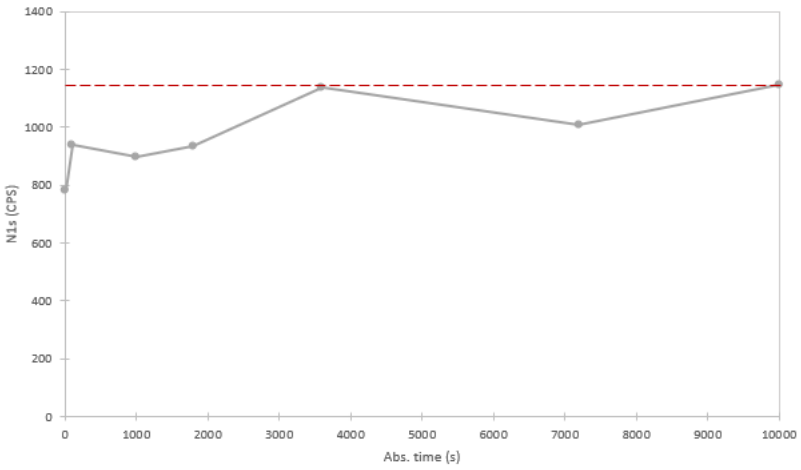

Figure 5.3 Calibration curve to optimise protein adsorption time using an ethanol PP coating (10 Pa/ 30 W) which plots N 1s counts as a measure of adsorbed protein after 10 – 1000 s of exposure.

The use of XPS in this way does result in one key issue in the small variation in set up day-to-day. This prevents the comparison of results collected on different days; this was not an issue for the results given in **Figure 5.3**, as all spectral collections were made in a single day. To circumvent this problem, an Au standard was analysed once on each experimental collection day and then ratioed with the N counts to provide comparable, normalised values. **Figure 5.4** demonstrates an example of this process: the Au 4f peak has a total 356595.2 counts compared to a N 1s peak in the coating with 3406.63 counts, giving a N/Au of 0.00955. It is the N/Au values that is used as the measure of adsorbed protein and can be compared between materials to evaluate the uptake of protein.

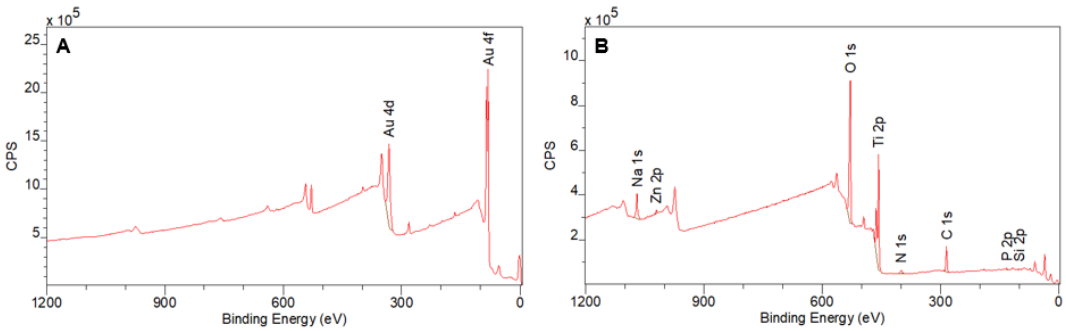

Figure 5.4 Wide scan spectra from XPS analysis of: (**A**) *Au on mica standard*, Au 4f (356595.2 CPS); (**B**) *HPG on Si, following albumin exposure*, N 1s (3406.63 CPS). N/Au = 0.00955.

Along with ethanol PP coatings, the substrate materials referenced throughout **Chapter 4** (Si, TiSi, PS, PTFE and Al), and HPG were tested against protein adsorption. Unfortunately, due to limited availability of 12-crown-4 PP coated samples, this coating was not tested against biofouling in this project. Unlike ethanol PP coatings, HPG does not wash away after submersion in PBS at room temperature which was established because the C-O composition remained above 80% (**Appendix 5.4**). **Table 5.2** displays the average uptake of albumin and fibrinogen, individually, on HPG, ethanol PP, TiSi, Si, Al foil and PTFE (for corresponding representative spectra for the albumin exposure see **Appendix 5.5**). HPG was the most successful at resisting reversible protein adsorption of both albumin and fibrinogen. Compared to the blank substrate (TiSi) albumin adsorption was reduced by x2 and fibrinogen was reduced by x1.4. Interestingly, fibrinogen was reversibly adsorbed more readily to all surfaces than the larger albumin molecules. The highest degree of overall protein adsorption was in PTFE which is a clinically relevant substrate material that is omnipresent within healthcare environments. PTFE is routinely used for implants and medical devices namely catheters, due to the materials ideal biocompatibility.[247] However, the implantable materials are disadvantaged by microbial colonisation.[57] This point was proven in the protein test which reiterates the need for coatings on medical devices to prevent infection.

Table 5.2 Protein exposure test conducted on various coated and uncoated samples, using albumin and fibrinogen. Values given are the N 1s counts (CPS) normalised to the Au 4f counts (CPS) collected on a Au standard before each experiment. For each condition 3 samples were produced with 3 analysis locations collected per sample; the values are the average of these 9 measurements.

Sample	Albumin	Fibrinogen
HPG (on TiSi)	0.0090	0.0185
EtOH PP (on Si)	0.0152	0.0315
TiSi	0.0197	0.0257
Si	0.0211	0.0342
Al foil	0.0216	0.0593
PTFE	0.0240	0.0665

Up to this point, testing focused on reversible attachment of the proteins on the samples meaning that only gentle washing was employed to remove non-adherent cells. To further probe the non-biofouling capabilities of the samples, a more rigorous washing protocol was used. SDS solution washing removes any reversibly bound protein by denaturing it so that a PBS wash will remove reversibly bound cells from the surface. This leaves only permanently and irreversibly bound protein. It is probable that a surface with irreversibly attaching protein is more likely to experience increased biofouling in natural environments. **Figure 5.5** shows the result that only three samples (ethanol PP coating, TiSi and Al foil) experienced this irreversible albumin attachment; all materials were tested, where 0 CPS is recorded (without error bars), this indicates the result for HPG, Si and PTFE. It could be speculated that all materials that allow the proteins to penetrate the surface are formed from a material coated onto another material which possibly provides stability to facilitate an irreversible bond. Whilst the TiSi is not strictly a coating, the Ti is sputtered on top of Si and may leave areas where protein can penetrate within the Ti structure. Remarkably, of the three “coated” materials (ethanol PP, TiSi and HPG) only HPG resists irreversible protein binding, reinforcing the assumption that the high

ethylene oxide content surface should resist microbial attachment. Surprisingly, the Al foil also allowed irreversible binding despite the material remaining uncoated. This could be a result of a dirty surface which is trapping the proteins. The Al foil is hard to clean thoroughly so surviving carbon may allow protein attachment. The result that PTFE did not permit any retained protein adsorption was unexpected. This test should be repeated to further validate results.

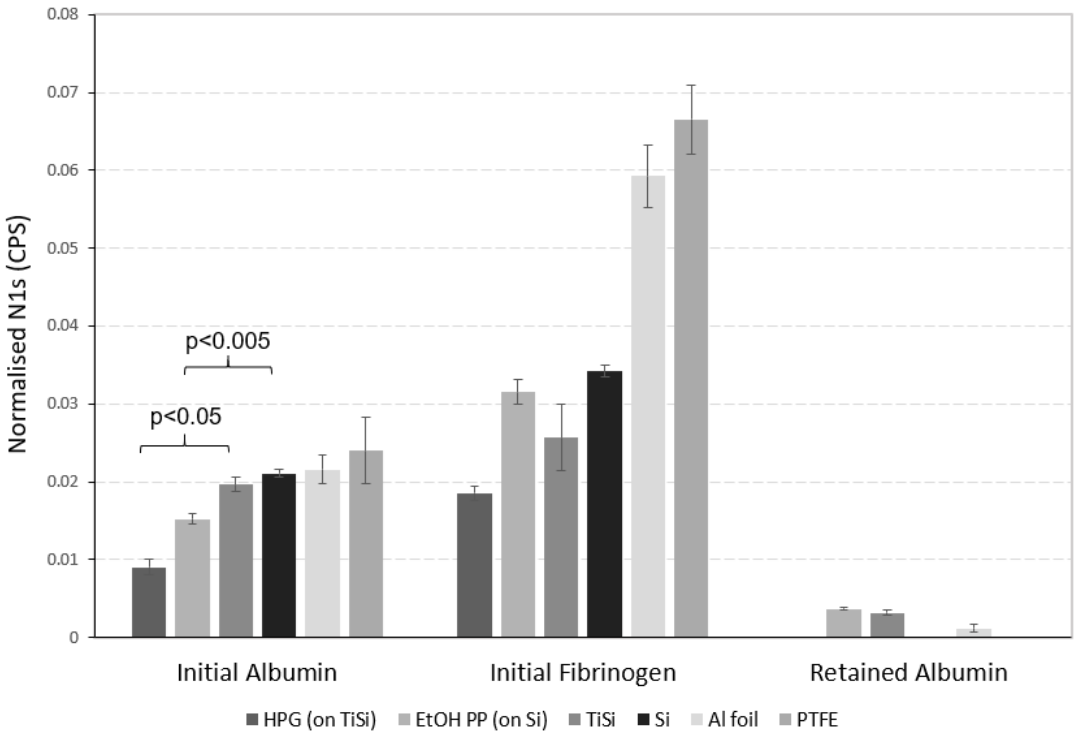

Figure 5.5 Protein adsorption test, initial (reversible) and retained (irreversible), on coated and uncoated substrates with albumin and fibrinogen. For HPG and ethanol PP coatings the results were significant as compared to the blank substrate.

5.3.1.2 Monitoring Protein Penetration within HPG

In the case of reversibly bound protein, an interesting question that was raised is whether the protein is held at the coating surface, or whether it penetrates into the coating. To investigate these possibilities, XPS ion milling was employed to etch the reversibly bound protein on HPG and a representative ethanol PP coating (10 Pa/30 W). By etching the material in layers and collecting XPS spectra, the position of the N 1s signal within the coating could be established. To this end, ion milling was conducted over a 1000 s etch time, following HPG exposure to albumin; this etch time allows complete removal of all N (protein) and C (protein /coating). For each etch a C 1s, O 1s and N 1s core line spectrum was collected (**Figure 5.6**). From the wide scan spectra collected before and after milling, the N 1s region has been expanded. Even after milling (**Figure 5.6 (B)**), three N 1s binding environments are observed. This mirrors the spectra collected for the plasma activated TiSi (**Figure 4.11**) and during the milling of HPG on TiSi before protein testing (**Figure 4.22**). This observation indicates that a low level of N is incorporated in the substrate regardless of the protein test.

The N 1s signal rapidly changes over the first 100 s of etching (**Figure 5.6 (C)**). From the three peaks that are observed, only the dominant N-C environment (400 eV) is related to the protein. The other 2 peaks relate to N incorporation in the substrate material which is visible in the XPS spectra because the HPG is thinner than the XPS sampling depth.[248] From 0 to 50 s, in the N 1s spectrum the %N-C signal reduces by over 50%, and continues to reduce until 100 s etch time which denotes the removal of the protein. The N 1s signal does not completely decay to 0% because of this underlying substrate N presence.

Shown in **Figure 5.6** and consistent with data presented in **Chapter 4** (**Figure 4.22**) an etch time of 340 s is required to remove the HPG layer equating to an approximate etch rate of 0.004 nms^{-1}, when considering the lower bound coating thickness estimate (1.27 nm). In the depth profile (**Figure 5.6 (D)**) and overlaid C1s core-line spectra (**Figure 5.6 (F)**), the C-R component observed at 0 s, is 32.84% making it larger than the reported % composition in the HPG without adsorbed protein (from **Chapter 4**: **%**C-R was 4.58%). This reflects the contribution of the adsorbed protein to this signal alongside any surface contamination obtained

during the protein test. As visualised in the N 1s and C 1s depth profiles (**Figure 5.6 (C)** and **(D)**), the etch rate of N-C (amide) and C-O (HPG) are different. A potential explanation is that the HPG coating is preventing proteins from moving within the coating towards the substrate. This is a significant finding because whilst the ability of HPG to resist proteins is well known, the reason for its success was not evidenced in the literature.

The same experiment was carried out on an 80 nm ethanol PP coating (10 Pa/30 W), by depth profiling a sample following exposure to albumin. **Figure 5.7** shows that the protein (N-C at 400.19 eV) is etched until it plateaus at 600 s and the ethanol (C-O at 286.39 eV) continues etching up to 1500 s, without completely removing the coating (as evidenced by C 1s peak in **Figure 5.7 (B)**). In this case, the protein initially drops sharply for the first 50 s before etching at the same rate as the coating over the remaining etch time, 1500 s. For clarity, the ion mill of an ethanol PP coating prior to protein testing is given in **Appendix 5.6**, which shows that a 900 s etch time is reproducibly required to remove the bulk of the coating, seen in the rising background of the XPS spectra which equates to the underlying silicon becoming more visible as the etch progresses. The N-C milling at a similar rate to the ethanol coating, indicates that the protein has migrated into the coating structure. This strengthens the conclusion that HPG can resist protein attachment because it prevents the protein molecules moving within the bulk material of the coating; protein is held at the substrate-air interface in HPG.

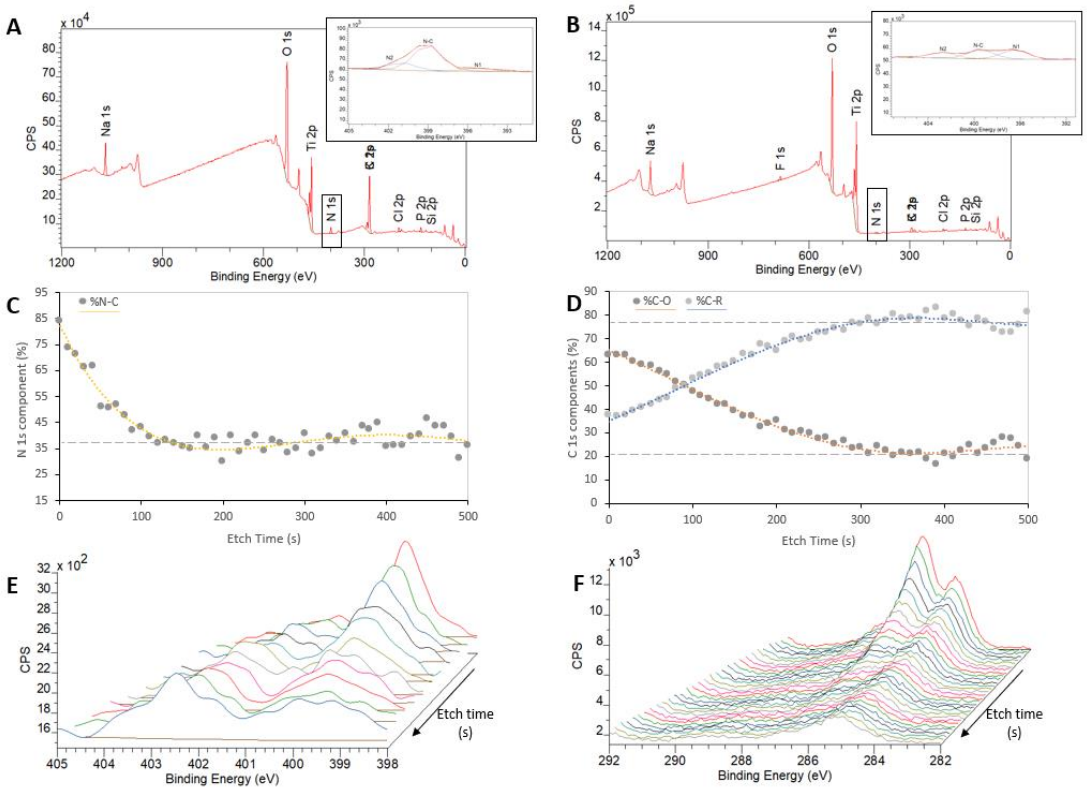

Figure 5.6 Depth profile XPS results for HPG on TiSi after albumin exposure, ion milled for 1000 s. (**A**) Wide survey scan spectrum recorded before the sample was milled[3]; (**B**) Wide survey scan spectrum recorded after all etching had finished, after 1000 s total etching time*; (**C**) %N-C and %O-N-O plotted by etch time (s) to show the point that N-C reduces, indicating total removal of protein, is between 50 and 100 s; (**D**) C 1s component plot against etch time (s), showing that HPG coating is removed after 300 s; (**E**) 3D plot of N 1s over 100 s etch time, smoothing applied (Savitzky-Golay, quadratic, width 7); (**F**) 3D plot of C 1s spectra collected over 300 s etch time.

[3] In the wide scan spectra, the C 1s and K 2p labels are overlapped due to the close proximity of the two binding environments

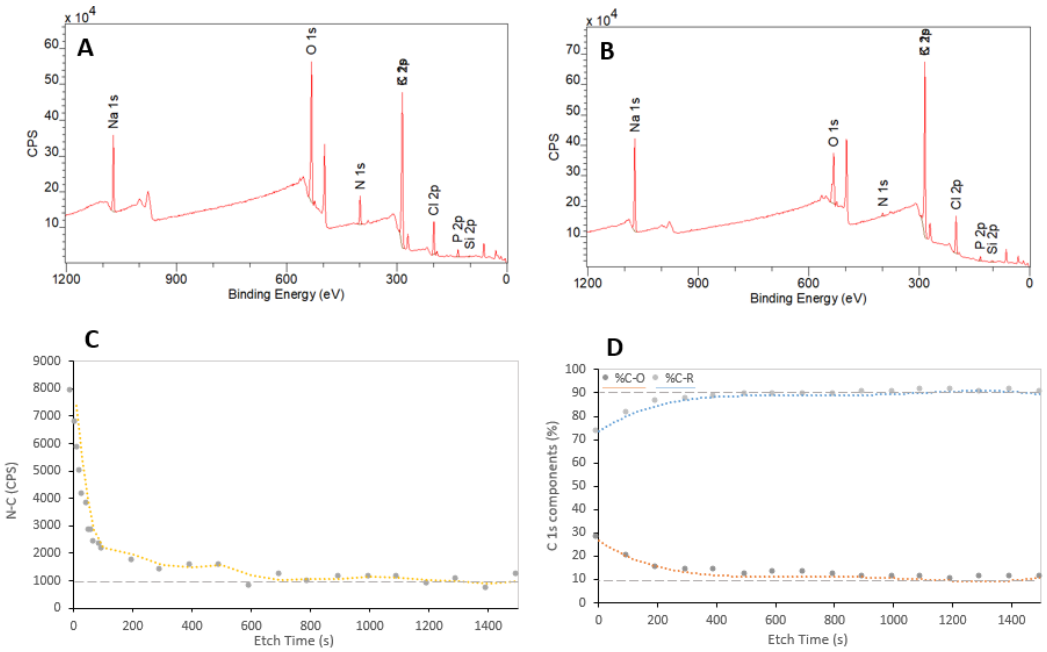

Figure 5.7 Depth profile XPS results for ethanol PP on Si after albumin exposure, ion milled for 1500 s. (**A**) Wide survey recorded before milling; (**B**) Wide survey collected after milling which shows the removal of N to <1%; (**C**) Plot of the reduction in total area of single N-C peak, as sample is milled for 1500 s; (**D**) C 1s component plot against etch time (s), showing that the removal of the bulk of coating from the Si.

5.3.2 Coatings to Delay Biofilm Development

HPG was the only coating examined that reliably resisted irreversible protein adsorption and therefore it was the only coating tested in the bacterial study. Whilst standard microbiological tests can determine degrees of colonisation, these tests often fail to accurately determine whether a biofilm has formed. The existence of a biofilm on medical equipment is common but needs to be avoided. HPG was tested by using the novel FTIR biofilm phenotyping protocol that was introduced in **Chapter 2**. For ease this biofilm work was carried out using the same single bacterial strain, *S. epidermidis* RP62A, which rapidly forms a biofilm within 4 hours.

Through the coating investigation for HPG, the easiest substrate to work with across XPS and AFM was Si due to the atomically flat nature of the substrate that only contributed additional Si 2p signals, simplifying analysis. Therefore, initial bacterial tests involved exposing the HPG coated Si to *S. epidermidis* for 24 hours, under the same growth conditions used in **Chapter 2**.

Following the test, samples were washed once with nutrient broth, to remove non-adherent cells. The samples were then allowed to semi-dry before analysis with FTIR. Unfortunately, it was found that silicon was incompatible with FTIR and results were not comparable to the earlier biofilm study. **Figure 5.8** shows an example of the spectra with a high degree of spectral reflectance (effecting signals below 1000 cm^{-1}) and the peak positions have shifted dramatically from the anticipated positions. For instance, the phospholipid region is *S. epidermidis* RP62A was reported to peak at 1068.6 cm^{-1} (planktonic cells) or at 1082.6 cm^{-1} (biofilms). However, for the sample grown onto HPG on Si, the phospholipid region peaks at 1107 cm^{-1} with a completely distorted region shape. Positively, the amide I region peaks at 1655 cm^{-1}, indicative of planktonic cells. However, this result cannot be accepted due to the discussed reflectance issues at the lower wavenumbers. These results were inconclusive and did not reliably demonstrate whether a biofilm was there on either the coated or uncoated samples. Fortunately, following FTIR analysis, samples were immediately placed in PBS and sonicated to remove biomass from the surface, allowing a standard characterisation, Miles and Misra, protocol to quantify the colony forming units (CFUs) on the surface. After 24-hour incubation, HPG samples more often showed very similar CFUs to the uncoated Si substrate. Out of three experiments, only 1 demonstrated a lower level of colonization on the coated substrate compared to uncoated suggesting that by 24 hours a biofilm is at least in the early phase of development on the HPG.

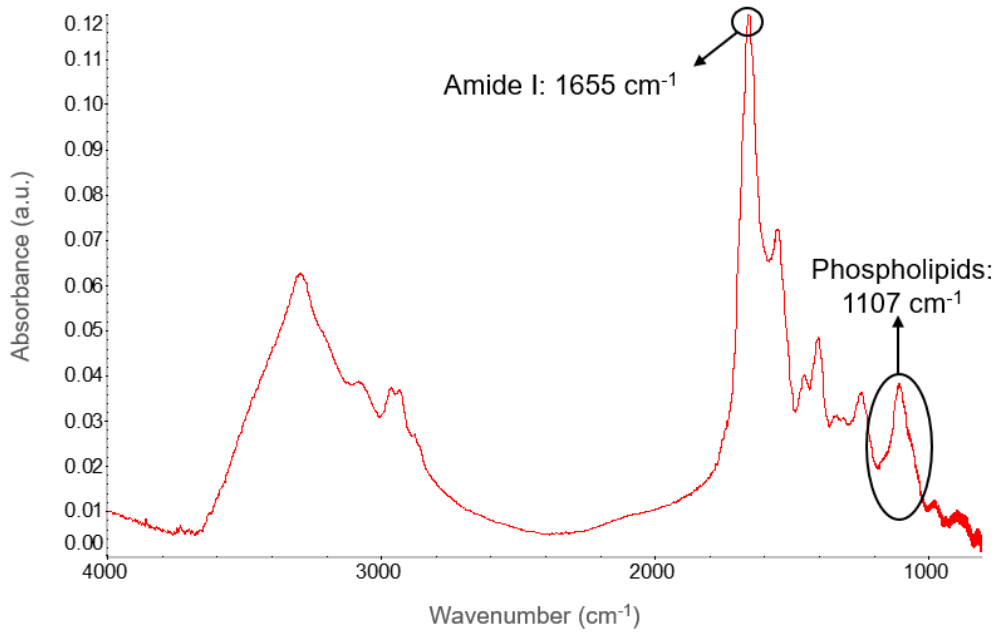

Figure 5.8 FTIR spectrum for a sample of HPG coated Si after 24 hrs incubation in *S. epidermidis*. Amide I and phospholipid regions are emphasised to reveal the spectral distortions caused by using Si.

To improve this experiment, two variables needed to change. Firstly, the substrate material was altered. Aluminium was selected as a useful substrate that allowed a uniform HPG coating (XPS evidence in **Appendix 5.7**), whilst being more compatible with FTIR. As described in **Chapter 2**, Al is a useful substrate that can be applied with ATR-FTIR, allowing a more accurate collection of peaks. The issue with using aluminium in earlier work (reported in **section 2.3.2.2**), was that the sample comes into contact with the sampling apparatus, preventing re-incubation and re-analysis of the same samples. This is not an issue within this experiment. The second experimental parameter that required alteration was the incubation time; 24 hours was likely too optimistic an incubation time to see a meaningful difference between HPG coated and uncoated samples, given the strain used is a rapid biofilm former that completely matures within 4 hours. Therefore, in this next set of results, the substrate was aluminium and all experiments used a 4-hour incubation time only. Immediately from the Miles and Misra, **Table 5.3**, the difference in colonisation on the coated and uncoated surfaces, is clear, with HPG showing 2 log less biomass than uncoated Al foil.

Table 5.3 Quantification of biomass on uncoated and HPG coated Al foil reveal the sub-biofilm CFU seen consistently in HPG samples.

Sample	CFU
Al foil	**1.2 x10^{7}**
HPG	**8 x10^{5}**

Figure 5.9 shows the result from the FTIR analysis of uncoated and coated samples (Al substrate), after 4-hour bacterial exposure. In summary, FTIR is used here to monitor the progression from planktonic cells to a biofilm because it can be used to evaluate the protein composition of a sample as evidenced throughout **Chapter 2** and **3**. For *S. epidermidis*, the key protein region (amide I) is centred at 1634 cm^{-1} for planktonic samples, when analysed on foil substrate. On 4h incubation of an uncoated sample, a peak shift to 1644 cm^{-1} was recorded signifying a chemical change coincident with the phenotypic switch (for evidence of this peak shift and the relationship to the biofilm development see **section 2.3.2.3**). Importantly, on the HPG coated sample, the protein peak position does not shift, indicating that a biofilm has not formed across the surface.

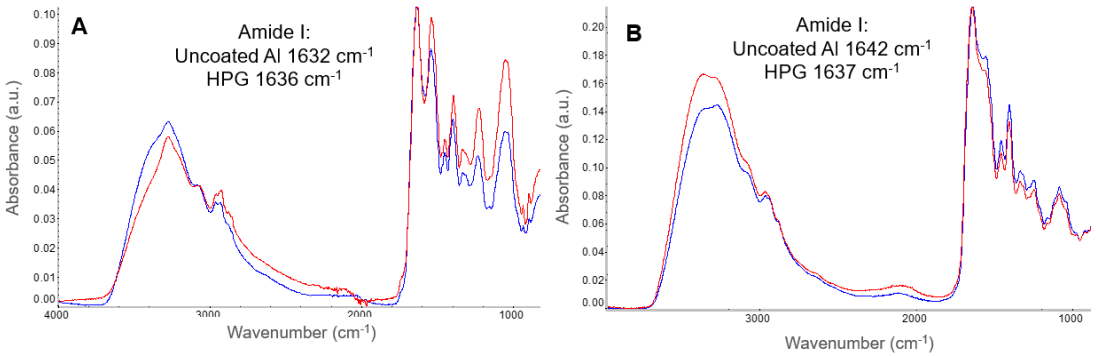

Figure 5.9. FTIR spectrum for a sample of HPG coated Al and uncoated Al after exposure to *S. epidermidis* RP62A. (**A**) Planktonic sample dried onto each substrate; (**B**) Samples partially dried after 4 hr incubation to allow biofilm formation. [red indicates uncoated sample and blue indicates HPG sample]

For further confirmation of the reduced colonisation on HPG fluorescence microscopy was carried out, using live dead staining, by myself and collaborators at the University of Glasgow. For this work, HPG was grafted onto glass coverslips (XPS proof of successful HPG grafting on glass in **Appendix 5.8**). After 4 hours, results clearly demonstrate extremely low colonisation of the coated surface compared to the uncoated glass coverslip, **Figure 5.10**. From these microscopy results, many researchers would conclude that the coating prevents biofilm formation. But while standard microbiological characterisation can demonstrate low bacterial attachment it is unable to define the biofilm phenotype.[77] From the novel application of FTIR, evidence of no biofilm growth was provided more quickly with less pre-processing allowing the sample to remain intact for further testing (i.e. Miles and Misra). This highlights the usefulness of the FTIR technique for applications within coatings research.

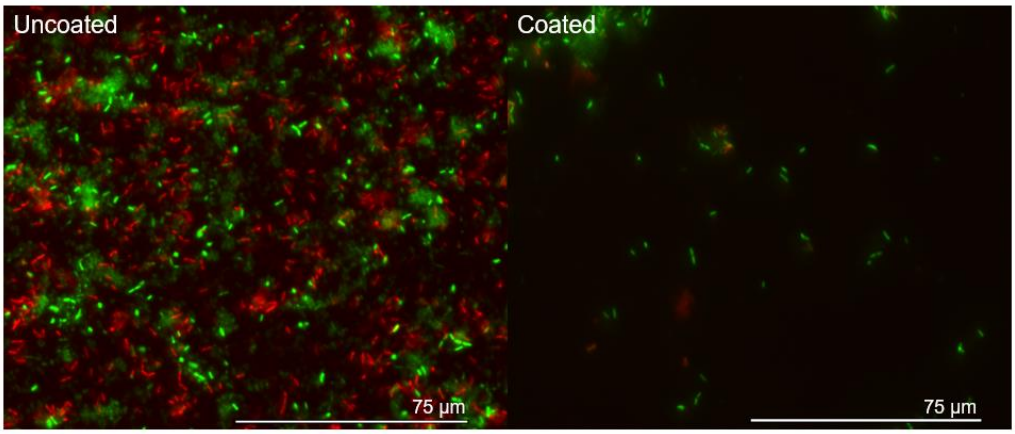

Figure 5.10 Fluorescence microscopy live dead stain following 4-hour incubation of samples in *S. epidermidis* highlights exceptionally low colonisation of HPG coated glass compared to the uncoated control sample.

5.4 Conclusions

In this chapter, XPS was used to monitor protein uptake in different materials (coated and uncoated). By monitoring N counts, which are equivalent to the amount of protein adsorbing to the surface, the results in this chapter show that PEO-like coatings reduce protein adsorption compared to the blank substrate materials. In particular the industrial standard HPG coating

extensively analysed in **Chapter 4**, was evidenced as the only coating to resist irreversible protein attachment. Further to this, in a novel depth profiling experiment, it became clear that HPG unlike other coatings, will hold proteins at the top of the surface, increasing the likelihood of positive non-biofouling capabilities. By extending the biofouling tests to include real bacterial exposure and combining the novel FTIR application that was developed in **Chapter 2**, the low colonisation and vitally, the lack of biofilm formation on HPG coated material has been exemplified.

Chapter 6. Conclusions and Future Work

6.1 Research Objectives

The aims of this research project were two-fold. Firstly, it was expected that spectroscopy could be utilised to monitor the growth of live biofilm samples. This was chiefly achieved by using FTIR spectroscopy to contribute to the chemical understanding of biofilm formation by identifying the key biomarker region (peaks located 1700-1500 cm^{-1}). The second overarching aim related to preventative strategies for medical devices coatings. This was accomplished in the development of new plasma-derived polymer coatings, alongside the rigorous testing of various non-biofouling coatings against microbial colonisation.

6.2 Conclusions

All of the initial objectives set out at the start of this thesis have been demonstrated. Firstly, **Chapter 2** presents evidence to support the use of FTIR as a non-destructive and rapid diagnostic tool for identifying the biofilm phenotype. The biomarker peaks, amide I and II (1700-1500 cm^{-1}), were revealed as important identifying features, signifying the chemical change induced by biofilm development, speculatively resulting from the production of an extracellular matrix. The difference was clear; biofilm samples display an FTIR spectrum with merged amide peaks at a shifted wavenumber position, compared to planktonic sample spectra which have distinct amide regions. The biomarker identification was supported by chemometric analysis. This novel application of FTIR to determine the maturity of a live biofilm was a foundational study, and the results could point to the clinical application of FTIR as a tool for detecting biofilm in infection samples.

Chapter 3 further explored the notion that FTIR could be a useful clinical tool to improve the speed of infection diagnosis, greatly impacting patient care and aiding in the minimisation of unnecessary antimicrobial usage. This chapter first provides evidence that the same biomarker region identified for biofilms in an *S. epidermidis* model, can be used with the fungal biofilm model, *C. albicans*. The maturity of the fungal biofilm was identifiable in the FTIR spectra recorded for samples across 96 hours of incubation. In an attempt to extend this preliminary study to multispecies biofilms, a *S. epidermidis* and *C. albicans* model was monitored with FTIR. Unfortunately, attempting to study the mixed species biofilm with FTIR revealed the inability to distinguish between the biofilm features of multiple organisms of varying sizes, within a single sample. This could limit the application of FTIR for clinical diagnostics. Further work should be completed to explore multispecies biofilm development, spectroscopically, as outlined in **Section 6.3**.

Chapter 4 detailed the iterative development, in collaboration with Liverpool University, of a novel PEO-like plasma polymer coating. This coating was formed from a crown ether starting material, specifically 12-crown-4, and boasted a 60% C-O-C surface composition. Alongside the development of a new non-fouling coating, the material composition of an industrially relevant PEO-like coating, hyperbranched polyglycerol, was explored. HPG production was already established at TekCyte® (and UniSA) to produce a coating that regularly achieved 90% C-O-C surface retention. Throughout this chapter the production process towards HPG grafting was dissected and rigorously explored for the first time, allowing the conclusion that a uniform and durable coating can be grafted onto a wide range of substrate materials, including clinically relevant nitinol stents.

In **Chapter 5** an application of XPS was utilised to quantify protein adsorption to the supposedly non-biofouling surfaces outlined in **Chapter 4**. Through protein adsorption testing it was ascertained that the coating with the highest %C-O-C composition, HPG, displayed the highest resistance to reversible protein adsorption and was the only material tested to resist irreversible adsorption. This work also uniquely exposes that HPG is capable of preventing protein molecules from moving within the coating structure. Whereas, other 'non-biofouling' coatings can minimise adsorption, protein is evidenced to move into the coating, potentially contributing to a higher degree of irreversible protein adsorption. In a final effort to affirm the

clinical potential of HPG for implantable medical devices, biofilm development on the coating was monitored and showed that compared to the uncoated substrate, HPG delayed biofilm formation. This was proven through multiple types of standard microbiological characterisation, as well as by using the application of FTIR outlined in **Chapter 2** to define the biofilm phenotype. Whilst the clinical application of FTIR to diagnose biofilm infection may be limited, the technique was excellent for the rapid evaluation of non-fouling coatings. This method could easily be adopted in future research for the facile evaluation of new non-fouling coatings to evidence their viability.

6.3 Future Work

Vibrational spectroscopy has been outlined as a suitable method to monitor the progression of live biofilm samples. The limiting factor for the application of FTIR in clinical diagnosis of biofilm infection is the ability to distinguish biomarkers in multi species models. Further work should be completed to explore the interactions of multiple species and perhaps for diagnosis purposes, sample preparation should be considered to remove excess background signals. For the improvement of this work in terms of expanding biofilm understanding, focus should move to the implementation of Raman spectroscopy, as oppose to FTIR. Raman spectroscopy affords the opportunity to collect spectra whilst incubating the samples. Furthermore, two and three-dimensional imaging would permit specific chemical analysis of slices from within a growing biofilm, which could circumvent the issue of variable cell sizes between species. This could also allow a more specific investigation into the origin of the chemical compositional changes associated with biofilm development: are the biomarker peak alterations a result of the evolution of an extra-cellular matrix, or are they a result of DNA changes within the cells as a result of the phenotypic switch from planktonic to biofilm forming cells. Revealing this would in turn allow a more targeted approach to preventing the beginning of pathogenic biofilms.

In terms of progressing the advancement of preventative strategies for minimising biofilm progression in medical implantable devices, further work should explore both the novel crown ether plasma polymer coating and the established HPG coating. In the first instance, the

crown ether coating is already approaching the industrial standard with an ethylene oxide retention of 60% (compared to 90% in HPG). Currently the method to produce the crown ether coating involves harsh experimental conditions with the use of heat tape maintained at 100 ℃ that is required in order to maintain the optimal plasma pressure. If the monomer vaporisation could be achieved via a less energy intensive method, this would enhance the viability of the process as an industrial competitor. The process of PP is advantaged by the speed of material coating (approximately 20 minutes for the coatings presented in this thesis) compared to the 24-hour period required to coat surfaces with HPG. Following optimisation of the PP coating production method, the surfaces should be examined against protein adsorption, followed by microbial exposure. If research continues to build on the facile application of plasma polymer coatings to medical equipment, the process could enhance infection prevention measures, not only in the healthcare sector but across all sectors where biofilms pose an issue.

For the existing PEO-like coating, HPG, additional work should initially include a wider study with FTIR to determine the maximum amount of time for which a biofilm can be delayed (under extreme experimental conditions). This should then be progressed to focus on testing the surface against clinically relevant mixed species biofilms. By collecting this additional data there would be substantial evidence to support the implementation of HPG as a non-fouling coating on medical devices, and due to the breadth of materials which can be coated with HPG, the material would be ready to undergo clinical trial.

References

1 H. C. Flemming, T. R. Neu and D. J. Wozniak, *J. Bacteriol.*, 2007, **189**, 7945–7947.

2 Y. Xu, Y. Dhaouadi, P. Stoodley, D. Ren, U. States, U. States, U. States, N. Biofilm, I. Centre, U. Kingdom, U. States and U. States, *Curr. Opin. Biotechnol.*, 2020, **64**, 79–84.

3 C. Molina-Santiago, A. de Vicente and D. Romero, *Comput. Struct. Biotechnol. J.*, 2021, **19**, 2796–2805.

4 T. M. Wassenaar, *Bacteria: The Benign, the Bad and the Beautiful*, John Wiley & Sons Ltd, 2012.

5 C. De la Fuente-Núñez, F. Reffuveille, L. Fernández and R. E. W. Hancock, *Curr. Opin. Microbiol.*, 2013, **16**, 580–589.

6 A. Fleming, *Nov. Price*, 1945, **11**, 83-93.

7 Gram-positive and Gram-negative bacteria, https://www.antibioticresearch.org.uk/about-antibiotic-resistance/bacterial-infections/types-of-bacteria/, (accessed 26 February 2021).

8 R. Pereira, R. O. dos Santos Fontenelle, E. H. S. de Brito and S. M. de Morais, *J. Appl. Microbiol.*, 2021, **131**, 11–22.

9 C. Spampinato and D. Leonardi, *Biomed Res. Int.*, 2013, **2013**, 204237.

10 G. M. Abebe, *Int. J. Microbiol.*, 2020, **2020**, 1705814.

11 D. Lindsay and A. von Holy, *J. Hosp. Infect.*, 2006, **64**, 313–325.

12 S. Srivastava and A. Bhargava, *Biotechnol. Lett.*, 2016, **38**, 1–22.

13 N. Rabin, Y. Zheng, C. Opoku-Temeng, Y. Du, E. Bonsu and H. O. Sintim, *Future Med. Chem.*, 2015, **7**, 493–512.

14 J. W. Costerton, G. G. Geesey and K. J. Cheng, *Sci. Am.*, 1978, **238**, 86–95.

15 R. M. Donlan and J. W. Costerton, *Clin. Microbiol. Rev.*, 2002, **15**, 167–193.

16 R. M. Donlan, *Emerg. Infec. Dis.*, 2002, **8**, 881–890.

17 J. N. Anderl, M. J. Franklin and P. S. Stewart, *Antimicrob. Agents Chemother.*, 2000, **44**, 1818–1824.

18 K. Sauer, P. Stoodley, D. M. Goeres, L. Hall-Stoodley, M. Burmølle, P. S. Stewart and T. Bjarnsholt, *Nat. Rev. Microbiol.*, 2022, **20**, 608–620.

19 T. Das, P. K. Sharma, H. J. Busscher, H. C. Van Der Mei and B. P. Krom, *Appl. Environ. Microbiol.*, 2010, **76**, 3405–3408.

20 W. M. Dunne, *Clin. Microbiol. Rev.*, 2002, **15**, 155–166.

21 K. Sauer, A. K. Camper, G. D. Ehrlich, J. W. Costerton and D. G. Davies, *J. Bacteriol.*, 2002, **184**, 1140–1154.

22 M. Otto, *Annu. Rev. Med.*, 2013, **64**, 175–188.

23 J. Palmer, S. Flint and J. Brooks, *J. Ind. Microbiol. Biotechnol.*, 2007, **34**, 577–588.

24 M. Cavalheiro and M. C. Teixeira, *Front. Med.*, 2018, **5**(28), 1-15.

25 W. Yin, Y. Wang, L. Liu and J. He, *Int. J. Mol. Sci.*, 2019, **20**, 3423.

26 R. Roy, M. Tiwari, G. Donelli and V. Tiwari, *Virulence*, 2018, **9**, 522–554.

27 M. Kostakioti, M. Hadjifrangiskou and S. J. Hultgren, *Cold Spring Harb. Perspect. Med.*, 2013, **3**, 1–24.

28 T. R. Garrett, M. Bhakoo and Z. Zhang, *Prog. Nat. Sci.*, 2008, **18**, 1049–1056.

29 W. G. Characklis and K. C. Marshal, *Biofilms*, John Wiley & Sons Ltd, New York, 1990.

30 J. S. Madsen, M. Burmølle, L. H. Hansen and S. J. Sørensen, *FEMS Immunol. Med. Microbiol.*, 2012, **65**, 183–195.

31 M. N. Hajiagha and H. S. Kafil, *Infect. Genet. Evol.*, 2023, **112**, 105459.

32 J. G. Leid, C. J. Willson, M. E. Shirtliff, D. J. Hassett, M. R. Parsek and A. K. Jeffers, *J. Immunol.*, 2005, **175**, 7512–7518.

33 R. Singh, P. Ray, A. Das and M. Sharma, *J. Antimicrob. Chemother.*, 2010, **65**, 1955–1958.

34 V. J. Savage, I. Chopra and A. J. O'Neill, *Antimicrob. Agents Chemother.*, 2013, **57**, 1968–1970.

35 R. Boudjemaa, R. Briandet, M. Revest, C. Jacqueline, J. Caillon, M. P. Fontaine-Aupart and K. Steenkeste, *Antimicrob. Agents Chemother.*, 2016, **60**, 4983–4990.

36 R. Singh, S. Sahore, P. Kaur, A. Rani and P. Ray, *Pathog. Dis.*, 2016, **74**, 1–6.

37 M. J. Ashby, J. E. Neale, S. J. Knott and I. A. Critchley, *J. Antimicrob. Chemother.*, 1994, **33**, 443–452.

38 R. Singh, P. Ray, A. Das and M. Sharma, *J. Med. Microbiol.*, 2009, **58**, 1067–1073.

39 D. Fleming and K. Rumbaugh, *Microorganisms*, 2017, **5**(2), 15.

40 N. M. Oliveira, E. Martinez-Garcia, J. Xavier, W. M. Durham, R. Kolter, W. Kim and K. R. Foster, *PLoS Biol.*, 2015, **13**, 1–23.

41 H. C. Flemming, *Water Res.*, 2020, **173**, 115576.

42 G. Brackman and T. Coenye, *Curr. Pharm. Des.*, 2014, **21**, 5–11.

43 M. K. Kim, A. Zhao, A. Wang, Z. Z. Brown, T. W. Muir, H. A. Stone and B. L. Bassler, *Nat. Microbiol.*, 2017, **2**, 17080.

44 C. Solano, M. Echeverz and I. Lasa, *Curr. Opin. Microbiol.*, 2014, **18**, 96–104.

45 R. C. MacLean and A. S. Millan, *Science (80-.).*, 2019, **365**, 1082–1083.

46 A. H. Holmes, L. S. P. Moore, A. Sundsfjord, M. Steinbakk, S. Regmi, A. Karkey, P. J. Guerin and L. J. V. Piddock, *Lancet*, 2016, **387**, 176–187.

47 J. Botelho and H. Schulenburg, *Trends Microbiol.*, 2021, **29**(1), 8-18.

48 J. Davies, *Microbiol. Mol. Biol. Rev.*, 2010, **74**, 417–433.

49 J. O' Neill, *Antimicrobial Resistance: Tackling a crisis for the health and wealth of nations The Review on Antimicrobial Resistance Chaired*, 2014.

50 J. O' Neill, *Tackling drug-resistant infections globally: Final report and recommendations*, 2016.

51 A. P. Roberts, P. Mullany and M. Wilson, *Methods Enzymol.*, 2001, **336**, 60–65.

52 J. W. Beaber and B. Hockhut, *Nature*, 2004, **427**, 72–74.

53 M. Hausner and S. Wuertz, *Appl. Environ. Microbiol.*, 1999, **65**, 3710–3713.

54 T. Singh, A. L. Hook, J. Luckett, M. F. Maitz, C. Sperling, C. Werner, M. C. Davies, D. J. Irvine, P. Williams and M. R. Alexander, *Biomaterials*, 2020, **260**, 120312.

55 A. Yousif, M. Jamal and I. Raad, *Adv. Exp. Med. Biol.*, 2015, **830**, 157–179.

56 National Biofilm Innovation Centre, biofilms.ac.uk/international-biofilm-markets/, (accessed April 2022).

57 M. van Kerckhoven, A. Hotterbeekx, E. Lanckacker, P. Moons, C. Lammens, M. Kerstens, M. Ieven and P. Deputte, *J. Microbiol. Methods*, 2016, **127**, 95–101.

58 B. Short, A. Bakri, A. Baz, C. Williams, J. Brown and G. Ramage, *Curr. Clin. Microbiol. Reports*, 2023, **10**, 9–16.

59 M. B. Atiencia-Carrera, F. S. Cabezas-Mera, E. Tejera and A. Machado, *PLoS One*, 2022, **17**, 1–23.

60 G. Seneviratne, J. S. Zavahir, W. M. M. S. Bandara and M. L. M. A. W. Weerasekara,

World J. Microbiol. Biotechnol., 2008, **24**, 739–743.

61 M. Pammi, R. Liang, J. Hicks, T. A. Mistretta and J. Versalovic, *BMC Microbiol.*, 2013, **13**, 1.

62 C. B. Costa-Orlandi, J. C. O. Sardi, N. S. Pitangui, H. C. de Oliveira, L. Scorzoni, M. C. Galeane, K. P. Medina-Alarcón, W. C. M. A. Melo, M. Y. Marcelino, J. D. Braz, A. M. Fusco-Almeida and M. J. S. Mendes-Giannini, *J. Fungi*, 2017, **3**, 1–24.

63 B. Adam, G. S. Baillie and L. J. Douglas, *J. Med. Microbiol.*, 2002, **51**, 344–349.

64 C. Potera, *Environ. Heal. Perspect.*, 2010, **118**, A288.

65 A. L. S. Burzava, M. Jasieniak, M. P. Cockshell, N. H. Voelcker, C. S. Bonder, C. S. Bonder, H. J. Griesser and E. Moore, *ACS Appl. Bio Mater.*, 2020, **3**, 3718–3730.

66 K. Hoger, T. Becherer, W. Qiang, R. Haag, W. Friess and S. Kuchler, *Eur J Pharm Biopharm*, 2013, **85**, 756–764.

67 N. B. S. Silva, L. A. Marques and D. D. B. Röder, *J. Appl. Microbiol.*, 2021, **131**, 2148–2160.

68 C. Wilson, R. Lukowicz, S. Merchant, H. Valquier-Flynn, J. Caballero, J. Sandoval and M. Okuom, *Res Rev J Eng Technol.*, 2017, **6**, 1–42.

69 A. P. S. Munro, C. J. Highmore, J. S. Webb and S. N. Faust, *Curr. Opin. Infect. Dis.*, 2019, **32**, 505–509.

70 H. Frickmann, A. E. Zautner, A. Moter, J. Kikhney, R. M. Hagen, H. Stender and S. Poppert, *Crit. Rev. Microbiol.*, 2017, **43**, 263–293.

71 A. Hassan, J. Usman, F. Kaleem, M. Omair, A. Khalid and M. Iqbal, *Brazilian J. Infect. Dis.*, 2011, **15**, 305–311.

72 T. J. Marrie, J. Nelligan and J. W. Costerton, *Circulation*., 1982, **66**(6), 1339-1341.

73 K. Standar, B. Kreikemeyer, S. Redanz, W. L. Münter, M. Laue and A. Podbielski, *PLoS One*, 2010, **5**, 1–14.

74 Y. Shen, S. Stojicic and M. Haapasalo, *J. Endod.*, 2010, **36**, 1820–1823.

75 M. Rosenberg, N. F. Azevedo and A. Ivask, *Sci. Rep.*, 2019, **9**, 1–12.

76 J. H. Priester, A. M. Horst, L. C. Van De Werfhorst, J. L. Saleta, L. A. K. Mertes and P. A. Holden, *J. Microbiol. Methods*, 2007, **68**, 577–587.

77 K. Harika, V. Shenoy, N. Narasimhaswamy and K. Chawla, *J. Glob. Infect. Dis.*, 2020, **12**, 129–134.

78 J. R. Lawrence, D. R. Korber, B. D. Hoyle, J. W. Costerton and D. E. Caldwell, *J.*

Bacteriol., 1991, **173**, 6558–6567.

79 S. P. Gorman, W. M. Mawhinney, C. G. Adair and M. Issouckis, *J. Med. Microbiol.*, 1993, **38**, 411–417.

80 B. Little, P. Wagner, R. Ray, R. Pope and R. Scheetz, *J Ind. Microbiol.*, 1991, **8**, 213–222.

81 D. L. Williams and R. D. Bloebaum, *Microsc. Microanal.*, 2010, **16**, 143–152.

82 S. Sugimoto, K. I. Okuda, R. Miyakawa, M. Sato, K. I. Arita-Morioka, A. Chiba, K. Yamanaka, T. Ogura, Y. Mizunoe and C. Sato, *Sci. Rep.*, 2016, **6**, 1–13.

83 N. Høiby, T. Bjarnsholt, C. Moser, G. L. Bassi, T. Coenye, G. Donelli, L. Hall-Stoodley, V. Holá, C. Imbert, K. Kirketerp-Møller, D. Lebeaux, A. Oliver, A. J. Ullmann, C. Williams, ESCMID Study Group for Biofilms (ESGB) and Consulting External Expert Werner Zimmerli, *Clin. Microbiol. Infect.*, 2015, **21**, S1–S25.

84 L. Nistico, L. Hall-Stoodley and P. Stoodley, in *Microbial Biofilms: Methods in Molecular Biology*, ed. G. Donelli, Humana Press, New York, NY, 2014, pp. 105–126.

85 S. Stöckel, J. Kirchhoff, U. Neugebauer, P. Rösch and J. Popp, *J. Raman Spectrosc.*, 2016, **47**, 89–109.

86 E. Smith and G. Dent, *Modern Raman Spectroscopy - A Practical Approach*, 2005, vol. 5.

87 A. Rohman, A. Windarsih, E. Lukitaningsih, M. Rafi, K. Betania and N. A. Fadzillah, *Biomed. Spectrosc. Imaging*, 2020, **8**, 55–71.

88 A. Ghosh, S. Raha, S. Dey, K. Chatterjee, A. Roy Chowdhury and A. Barui, *Analyst*, 2019, **144**, 1309–1325.

89 P. Larkin, *Infrared and Raman spectroscopy: Principals and spectral interpretation*, Elsevier, 2011.

90 C. V. Raman and K. S. Krishnan, *Nature*, 1928, **121**, 501–502.

91 Lord Rayleigh, *London, Edinburgh Dublin Philos. Mag. J. Sci.*, 1871, **41**, 447.

92 V. Charwat, K. Schütze, W. Holnthoner, A. Lavrentieva, R. Gangnus, P. Hofbauer, C. Hoffmann, B. Angres and C. Kasper, *J. Biotechnol.*, 2015, **205**, 70–81.

93 P. D. Maker and R. W. Terhune, *Phys. Rev. Online Arch.*, 1965, **137**, A801–A818.

94 H. J. Butler, L. Ashton, B. Bird, G. Cinque, K. Curtis, J. Dorney, K. Esmonde-White, N. J. Fullwood, B. Gardner, P. L. Martin-Hirsch, M. J. Walsh, M. R. McAinsh, N. Stone and F. L. Martin, *Nat. Protoc.*, 2016, **11**, 664–687.

95 M. Fleischmann, P. J. Hendra and A. J. McQuillan, *Chem. Phys. Lett.*, 1974, **26**, 163–166.

96 G. J. Puppels, F. F. M. De Mul, C. Otto, J. Greve, M. Robert-Nicoud, D. J. Arndt-Jovin and T. M. Jovin, *Nature*, 1990, **347**, 301–303.

97 L. Ashton, K. A. Hollywood and R. Goodacre, *Analyst*, 2015, **140**, 1852–1858.

98 D. I. Ellis, D. P. Cowcher, L.Ashton, S. O'Hagan and R. Goodacre, *Analyst*, 2013, **138**, 3871–3884.

99 A. Zoladek, F. Pascut, P. Patel and I. Notingher, *Spectroscopy*, 2010, **24**, 131–136.

100 M. Delhaye and P. Dhamelincourt, *J. Raman Spectrosc.*, 1975, **3**, 33–43.

101 R. Smith, K. L. Wright and L. Ashton, *Analyst*, 2016, **141**, 3590–3600.

102 S. Schlücker, M. D. Schaeberle, S. W. Huffman and I. W. Levin, *Anal. Chem.*, 2003, **75**, 4312–4318.

103 S. J. Baldock, A. C. S. Talari, R. Smith, K. L. Wright and L. Ashton, *J. Raman Spectrosc.*, 2019, **50**, 371–379.

104 I. Notingher, *Sensors*, 2007, **7**, 1343–1358.

105 I. Notingher, S. Verrier, H. Romanska, A. E. Bishop, J. M. Polak and L. L. Hench, *Spectroscopy*, 2002, **16**, 43–51.

106 G. B. Jung, S. W. Nam, S. Choi, G.-J. Lee and H.-K. Park, *Biomed. Opt. Express*, 2014, **5**, 3238.

107 A. P. Lister, C. J. Highmore, N. Hanrahan, J. Read, A. P. S. Munro, S. Tan, R. N. Allan, S. N. Faust, J. S. Webb and S. Mahajan, *Anal. Chem.*, 2022, **94**, 669–677.

108 B. Virdis, F. Harnisch, D. J. Batstone, K. Rabaey and B. C. Donose, *Energy Environ. Sci.*, 2012, **5**, 7017–7024.

109 N. P. Ivleva, P. Kubryk and R. Niessner, *Anal. Bioanal. Chem.*, 2017, **409**, 4353–4375.

110 T. Smith-Palmer, S. Lin, I. Oguejiofor, T. Leng, A. Pustam, J. Yang, L. L. Graham, R. C. Wyeth, C. D. Bishop, M. E. Demont and D. Pink, *Appl. Spectrosc.*, 2016, **70**, 289–301.

111 J. Feng, C. De La Fuente-Núñez, M. J. Trimble, J. Xu, R. E. W. Hancock and X. Lu, *Chem. Commun.*, 2015, **51**, 8966–8969.

112 A. Alvarez-Ordóñez, D. J. M. Mouwen, M. López and M. Prieto, *J. Microbiol. Methods*, 2011, **84**, 369–378.

113 J. J. Ojeda and M. Dittrich, in *Microbial Systems Biology. Methods in Molecular*

Biology., ed. A. Navid, Humana Press, Totowa, NJ, 2012.

114 Â. Novais, A. R. Freitas, C. Rodrigues and L. Peixe, *Eur. J. Clin. Microbiol. Infect. Dis.*, 2019, **38**, 427–448.

115 A. A. Ismail, F. R. van de Voort and J. Sedman, in *Instrumental Methods in Food Analysis*, eds. J. R. . Pare and J. M. R. Belanger, Elsevier Science, 1997, pp. 93–139.

116 C. Berthomieu and R. Hienerwadel, *Photosynth. Res.*, 2009, **101**, 157–170.

117 C. Petibois and B. Desbat, *Trends Biotechnol.*, 2010, **28**, 495–500.

118 D. Naumann, D. Helm and H. Labischinski, *Nature*, 1991, **351**, 81–82.

119 J. Schmitt and H. C. Flemming, *Int. Biodeterior. Biodegrad.*, 1998, **41**, 1–11.

120 Y. Burgula, D. Khali, S. Kim, S. S. Krishnan, M. A. Cousin, J. P. Gore, B. L. Reuhs and L. J. Mauer, *J. Rapid Methods Autom. Microbiol.*, 2007, **15**, 146–175.

121 D. E. Nivens, D. E. Ohman, J. Williams and M. J. Franklin, *J. Bacteriol.*, 2001, **183**, 1047–1057.

122 H. Y. N. Holman, R. Miles, Z. Hao, E. Wozei, L. M. Anderson and H. Yang, *Anal. Chem.*, 2009, **81**, 8564–8570.

123 M. N. Ariafar, N. Iğci, M. Akçelik and N. Akçelik, *Arch. Microbiol.*, 2019, **201**, 1233–1248.

124 F. Quilès, P. Polyakov, F. Humbert and G. Francius, *Biomacromolecules*, 2012, **13**, 2118–2127.

125 M. Essendoubi, D. Toubas, M. Bouzaggou, J. M. Pinon, M. Manfait and G. D. Sockalingum, *Biochim. Biophys. Acta - Gen. Subj.*, 2005, **1724**, 239–247.

126 D. Serra, A. Bosch, D. M. Russo, M. E. Rodríguez, Á. Zorreguieta, J. Schmitt, D. Naumann and O. Yantorno, *Anal. Bioanal. Chem.*, 2007, **387**, 1759–1767.

127 T. Frost, in *Encyclopedia of spectroscopy and spectrometry*, eds. J. C. Lindon, G. E. Tranter and D. W. Koppenaal, Academic Press, Third., 2017, pp. 811–815.

128 R. Gautam, S. Vanga, F. Ariese and S. Umapathy, *EPJ Tech. Instrum.*, 2015, **2**(8), 1-38.

129 M. Esteban, C. Arino and J. M. Diaz-Cruz, in *Comprehensive Chemometrics*, eds. S. D. Brown, R. Tauler and B. Walczak, Elsevier, 2009, pp. 425–458.

130 L. Mariey, J. P. Signolle, C. Amiel and J. Travert, *Vib. Spectrosc.*, 2001, **26**, 151–159.

131 N. M. R. de Brito and F. R. Lourenço, *Brazilian J. Pharm. Sci.*, 2021, **57**, 1–11.

132 A. Tata, F. Marzoli, M. Cordovana, A. Tiengo, C. Zacometti, A. Massaro, L. Barco, S. Belluco and R. Piro, *Front. Microbiol.*, 2023, **14**, 1–8.

133 L. Tessaro, Y. Mutz, J. C. de Andrade, A. Aquino, N. K. R. Belem, F. G. S. Silva and C. A. Conte-Junior, *Spectrochim. Acta - Part A Mol. Biomol. Spectrosc.*, 2023, **285**, 121883.

134 N. Beshchasna, M. Saqib, H. Kraskiewicz, L. Wasyluk, O. Kuzmin and O. Duta, *Pharmaceutics*, 2020, **12**, 349.

135 Z. K. Zander and M. L. Becker, *ACS Macro. Lett.*, 2018, **7**, 16–25.

136 B. Mendrek, N. Oleszko-Torbus, T. Teper and A. Kowalczuk, *Prog. Polym. Sci.*, 2023, **139**, 101657.

137 S. Lowe, N. O'Brien-Simpson and L. Connal, *Polym. Chem.*, 2015, **6**, 198.

138 C. Y. Lee, S. M. Hu, J. Christy, F. Y. Chou, T. C. Ramli and H. Y. Chen, *Adv. Mater. Interfaces*, 2023, **10**(10), 2202286.

139 P. Y. J. Yeh, R. K. Kainthan, Y. Zou, M. Chiao and J. N. Kizhakkedathu, *Langmuir*, 2008, **24**, 4907–4916.

140 D. Terada, S. Sotoma, Y. Harada, R. Igarashi and M. Shirakawa, *Bioconjug. Chem.*, 2018, **29**, 2786–2792.

141 H. Yasuda and Y. Iriyama, in *Comprehensive Polymer Science and Supplements*, 1989.

142 S. Lata, S. Chakravorty, T. Mitra, P. K. Pradhan, S. Mohanty, P. Patel, E. Jha, P. K. Panda, S. K. Verma and M. Suar, *Mater. Today Bio*, 2022, **13**, 100200.

143 K. S. Siow, L. Britcher, S. Kumar and H. J. Griesser, *Plasma Process. Polym.*, 2006, **3**, 392–418.

144 M. Shen and A. T. Bell, in *Plasma polymerisation*, eds. M. Shen and A. T. Bell, American Chemical Society, 1979, pp. 1–33.

145 B. R. Coad, P. Favia, K. Vasilev and H. J. Griesser, *Plasma Process. Polym.*, 2022, **19**(11), 2200121.

146 A. Michelmore, J. D. Whittle, J. W. Bradley and R. D. Short, *Front. Chem. Sci. Eng.*, 2016, **10**, 441–458.

147 D. Thiry, S. Konstantinidis, J. Cornil and R. Snyders, *Thin Solid Films*, 2016, **606**, 19–44.

148 T. Williams and M. W. Hayes, *Nature*, 1966, **209**, 769.

149 S. Zane and A. Kargari, in *Emerging Technologies for Sustainable Deslination Handbook*, 2018.

150 A. Michelmore, D. A. Steele, J. D. Whittle, J. W. Bradley and R. D. Short, *RSC Adv.*, 2013, **3**, 13540–13557.

151 J. D. Whittle, R. D. Short, D. A. Steele, J. W. Bradley, P. M. Bryant, F. Jan, H. Biederman, A. A. Serov, A. Choukurov, A. L. Hook, W. A. Ciridon, G. Ceccone, D. Hegemann, E. Körner and A. Michelmore, *Plasma Process. Polym.*, 2013, **10**, 767–778.

152 T. D. Michl, B. R. Coad, A. Hüsler, J. D. P. Valentin, K. Vasilev and H. J. Griesser, *Plasma Process. Polym.*, 2016, **13**, 654–662.

153 A. Asad, D. Sameoto and M. Sadrzadeh, in *Micro and Nano Technologies*, Elsevier, 2020, pp. 1–28.

154 S. Saboohi, M. Jasieniak, B. R. Coad, H. J. Griesser, R. D. Short and A. Michelmore, *J. Phys. Chem. B*, 2015, **119**, 15359–15369.

155 M. J. Barnes, A. J. Robson, J. Naderi, R. D. Short and J. W. Bradley, *Biointerphases*, 2020, **15**, 061007.

156 I. Sulemankhil, J. G. Ganopolsky, C. A. Dieni, A. F. Dan, M. L. Jones and S. Prakash, *Antimicrob. Agents Chemother.*, 2012, **56**, 6095–6103.

157 N. Barraud, D. J. Hassett, S. H. Hwang, S. A. Rice, S. Kjelleberg and J. S. Webb, *J. Bacteriol.*, 2006, **188**, 7344–7353.

158 A. Ghaffari, C. C. Miller, B. McMullin and A. Ghahary, *Nitric Oxide - Biol. Chem.*, 2006, **14**, 21–29.

159 L. Plate and M. A. Marletta, *Trends Biochem. Sci.*, 2013, **38**, 566–575.

160 D. MacDougald and S. A. Rice, *Nat. Rev. Microbiol.*, 2011, **10**, 39–50.

161 C. De La Fuente-Núñez, F. Reffuveille, K. E. Fairfull-Smith and R. E. W. Hancock, *Antimicrob. Agents Chemother.*, 2013, **57**, 4877–4881.

162 F. C. Fang, *J. Clin. Invest.*, 1997, **99**, 2818–2825.

163 B. Akhavan, T. D. Michl, C. Giles, K. Ho, L. Martin, O. Sharifahmadian, S. G. Wise, B. R. Coad, N. Kumar, H. J. Griesser and M. M. Bilek, *Appl. Mater. Today*, 2018, **12**, 72–84.

164 T. D. Michl, D. T. T. Tran, H. F. Kuckling, A. Zhalgasbaikyzy, B. Ivanovská, L. E. González García, R. M. Visalakshan and K. Vasilev, *RSC Adv.*, 2020, **10**, 7368–7376.

165 P. H. Li and P. K. Chu, in *Thin Film Coatings for Biomaterials and Biomedical*

Applications, 2016.

166 K. Vasilev, N. Poulter, P. Martinek and H. J. Griesser, *ACS Appl. Mater. Interfaces*, 2011, **3**, 4831–4836.

167 K. Vasilev, S. S. Griesser and H. J. Griesser, *Plasma Process. Polym.*, 2011, **8**, 1010–1023.

168 H. D. Hazrati, J. D. Whittle and K. Vasilev, *Plasma Process. Polym.*, 2014, **11**, 149–157.

169 B. R. Coad, K. Vasilev, K. R. Diener, J. D. Hayball, R. D. Short and H. J. Griesser, *Langmuir*, 2012, **28**, 2710–2717.

170 G. P. Lopez, B. D. Ratner, C. D. Tidwell, C. L. Haycox, R. J. Rapoza and T. A. Horbett, *J. Biomed. Mater. Res. A*, 1992, **26**, 415–439.

171 D. Beyer, W. Knoll, H. Ringsdorf, J. Wang, R. B. Timmons and P. Sluka, *J. Biomed. Mater. Res.*, 1997, **36**, 181–189.

172 Y. J. Wu, A. J. Griggs, J. S. Jen, S. Manolache, F. S. Denes and R. B. Timmons, *Plasmas Polym.*, 2001, **6**, 123–144.

173 E. E. Johnston, J. D. Bryers and B. D. Ratner, *Langmuir*, 2005, **21**, 870–881.

174 Y. H. Kim and O. W. Webster, *J. Am. Chem. Soc.*, 1990, **112**, 4593–4594.

175 S. Abbina, S. Vappala, P. Kumar, E. M. J. Siren, C. C. La, U. Abbasi, D. E. Brooks and J. N. Kizhakkedathu, *J. Mater. Chem. B*, 2017, **5**, 9249–9277.

176 M. Ramezani Farani, M. Azarian, H. Heydari Sheikh Hossein, Z. Abdolvahabi, Z. Mohammadi Abgarmi, A. Moradi, S. M. Mousavi, M. Ashrafizadeh, P. Makvandi, M. R. Saeb and N. Rabiee, *ACS Appl. Bio Mater.*, 2022, **5**, 1305–1318.

177 J. Xie, S. Qi, Q. Ran and L. Dong, *Materials (Basel).*, 2022, **15**, 1–16.

178 Y. Deng, J. K. Saucier-Sawyer, C. J. Hoimes, J. Zhang, Y. E. Seo, J. W. Andrejecsk and W. M. Saltzman, *Biomaterials*, 2014, **35**, 6595–6602.

179 D. Wilms, S. E. Stiriba and H. Frey, *Acc. Chem. Res.*, 2010, **43**, 129–141.

180 A. Zill, A. L. Rutz, R. E. Kohman, A. M. Alkilany, C. J. Murphy, H. Kong and S. C. Zimmerman, *Chem. Commun.*, 2011, **47**, 1279–1281.

181 Q. Wei, S. Krysiak, K. Achazi, T. Becherer, P. L. M. Noeske, F. Paulus, H. Liebe, I. Grunwald, J. Dernedde, A. Hartwig, T. Hugel and R. Haag, *Colloids Surfaces B Biointerfaces*, 2014, **122**, 684–692.

182 A. Sunder, R. Hanselmann, H. Frey and R. Mülhaupt, *Macromolecules*, 1999, **32**,

4240–4246.

183 M. Khan and W. T. S. Huck, *Macromolecules*, 2003, **36**, 5088–5093.

184 G. Perumal, S. Pappuru, M. Doble, D. Chakraborty, S. Shajahan and M. Abu Haija, *ACS Omega*, 2023, **8**(2), 2377-2388.

185 T. Becherer, C. Grunwald, V. Engelschalt, G. Multhaup, T. Risse and R. Haag, *Anal. Chim. Acta*, 2015, **867**, 47–55.

186 D. Pranantyo, L. Q. Xu, K. G. Neoh, E. T. Kang and S. L. M. Teo, *Ind. Eng. Chem. Res.*, 2016, **55**, 1890–1901.

187 M. Weinhart, T. Becherer, N. Schnurbusch, K. Schwibbert, H. J. Kunte and R. Haag, *Adv. Eng. Mater.*, 2011, **13**, 501–510.

188 A. Boulares-Pender, A. Prager, S. Reichelt, C. Elsner and M. R. Buchmeister, *J. Appl. Polym. Sci.*, 2011, **121**, 2543–2550.

189 T. Weber, M. Bechthold, T. Winkler, J. Dauselt and A. Terfort, *Colloids Surfaces B Biointerfaces*, 2013, **111**, 360–366.

190 T. Weber, Y. Gies and A. Terfort, *Langmuir*, 2012, **28**, 15916–15921.

191 Y. He, S. Xing, P. Jiang, Y. Zhao and L. Chen, *Biomacromolecules*, 2022, **23**, 4924–4933.

192 E. M. Hetrick and M. H. Schoenfisch, *Chem. Soc. Rev.*, 2006, **35**, 780–789.

193 K. Bazaka, M. V. Jacob, W. Chrzanowski and K. Ostrikov, *RSC Adv.*, 2015, **5**, 48739–48759.

194 G. Regev-Shoshani, M. Ko, C. Miller and Y. Av-Gay, *Antimicrob. Agents Chemother.*, 2010, **54**, 273–279.

195 E. Moore, B. Delalat, R. Vasani, G. McPhee, H. Thissen and N. H. Voelcker, *ACS Appl. Mater. Interfaces*, 2014, **6**, 15243–15252.

196 C. Siegers, M. Biesalski and R. Haag, *Chem. - A Eur. J.*, 2004, **10**, 2831–2838.

197 M. Shen, L. Martinson, M. S. Wagner, D. G. Castner, B. D. Ratner and T. A. Horbett, *J. Biomater. Sci. Polym. Ed.*, 2002, **13**, 367–390.

198 K. Siegbahn, *J. Electron Spectros. Relat. Phenomena*, 1985, **36**, 113–129.

199 D. T. Clark and D. Shuttleworth, *J. Polym. Sci.*, 1978, **16**, 1093.

200 D. Briggs and M. P. Seah, *Practical Surface Analysis by Auger and XPS*, John Wiley & Sons Ltd, Chichester, 1983.

201 S. Tougaard, in *Encyclopedia of Analytical Science*, eds. P. Worsfold, A. Townshend and C. Poole, Elsevier, Second., 2005, pp. 446–456.

202 F. A. Stevie and C. L. Donley, *J. Vac. Sci. Technol. A Vacuum, Surfaces, Film.*, 2020, **38**, 063204.

203 D. Briggs, in *Surface analysis of polymers by XPS and static SIMS*, eds. D. R. Clark, S. Sunesh and I. M. Word, Cambridge University Press, 1998.

204 D. M. Mattox, in *Handbook of Physical Vapour Distribution (PVD) Processing*, William Andrew Publishing, Second edi., 2010, pp. 25–72.

205 J. L. S. Lee, S. Ninomiya, J. Matsuo, I. S. Gilmore, M. P. Seah and A. G. Shard, *Anal. Chem.*, 2010, **82**, 98–105.

206 M. A. Isaacs, J. Davies-Jones, P. R. Davies, S. Guan, R. Lee, D. J. Morgan and R. Palgrave, *Mater. Chem. Front.*, 2021, **5**, 7931–7963.

207 I. Yamada, J. Matsuo, N. Toyoda and A. Kirkpatrick, *Mater. Sci. Eng. R*, 2001, **34**, 231–295.

208 K. Ichiki, S. Ninomiya, Y. Nakata, Y. Honda, T. Seki, T. Aoki and J. Matsuo, *Appl. Surf. Sci.*, 2008, **255**, 1148–1150.

209 K. . Kim, W. Baitinger, J. Amy and N. Winograd, *J Electron Spectrosc. Relat. Phenom.*, 1974, **5**, 351–367.

210 J. Malherbe, S. Hofmann and J. Sanz, *Appl. Surf. Sci.*, 1986, **27**, 335–365.

211 E. F. Smith, J. D. P. Counsell, J. Bailey, J. S. Sharp, M. R. Alexander, A. G. Shard and D. J. Scurr, *Surf. Interface Anal.*, 2017, **49**, 953–959.

212 Y. Q. Zhang, S. X. Ren, H. L. Li, Y. X. Wang, G. Fu, J. Yang, Z. Q. Qin, Y. G. Miao, W. Y. Wang, R. S. Chen, Y. Shen, Z. Chen, Z. H. Yuan, G. P. Zhao, D. Qu, A. Danchin and Y. M. Wen, *Mol. Microbiol.*, 2003, **49**, 1577–1593.

213 L. Cui, H. J. Butler, P. L. Martin-Hirsch and F. L. Martin, *Anal. Methods*, 2016, **8**, 481–487.

214 X. Guo, L. Liu, J. Wu, J. Fan and Y. Wu, *RSC Adv.*, 2018, **8**, 4214–4220.

215 N. M. Amiali, M. R. Mulvey, J. Sedman, M. Louie, A. E. Simor and A. A. Ismail, *J. Microbiol. Methods*, 2007, **68**, 236–242.

216 M. Wenning and S. Scherer, *Appl. Microbiol. Biotechnol.*, 2013, **97**, 7111–7120.

217 P. Bassan, H. J. Byrne, F. Bonnier, J. Lee, P. Dumas and P. Gardner, *Analyst*, 2009, **134**, 1586–1593.

218 E. M. Kojic and R. O. Darouiche, *Clin. Microbiol. Rev.*, 2004, **17**, 255–267.

219 N. V. Kollu and D. R. Lajeunesse, *ACS Omega*, 2021, **6**, 1361–1369.

220 L. E. O'Donnell, H. K. A. Alalwan, R. Kean, G. Calvert, C. J. Nile, D. F. Lappin, D. Robertson, C. Williams, G. Ramage and L. Sherry, *J. Med. Microbiol.*, 2017, **66**, 54–60.

221 D. Kadosh and A. D. Johnson, *Mol. Biol. Cell*, 2005, **16**, 2903–2912.

222 Y. Tan, M. Leonhard, S. Ma and B. Schneider-Stickler, *J. Microbiol. Methods*, 2016, **130**, 123–128.

223 H. Toor, S. Farr, P. Savla, S. Kashyap, S. Wang and D. E. Miulli, *Cureus*, 2022, **14**, 1–7.

224 M. Cámara, W. Green, C. E. MacPhee, P. D. Rakowska, R. Raval, M. C. Richardson, J. Slater-Jefferies, K. Steventon and J. S. Webb, *npj Biofilms Microbiomes*, 2022, **8**, 1–8.

225 B. Mendrek, N. Oleszko-Torbus, P. Teper and A. Kowalczuk, *Prog. Polym. Sci.*, 2023, **139**, 101657.

226 L. Yu, C. Schlaich, Y. Hou, J. Zhang, P. L. M. Noeske and R. Haag, *Chem. - A Eur. J.*, 2018, **24**, 7742–7748.

227 G. Beamson and D. Briggs, *High Resolut. XPS Org. Polym. - Sci. ESCA300 DataBase*.

228 A. Holländer and S. Kröpke, *Surf. Coatings Technol.*, 2011, **205**, S480–S483.

229 K. Artyushkova, *J. Vac. Sci. Technol. A Vacuum, Surfaces, Film.*, 2020, **38**(3), 031002.

230 P. R. Chen, T. C. Wang, S. T. Chen, H. Y. Chen and W. B. Tsai, *Langmuir*, 2017, **33**, 14657–14662.

231 R. K. Kainthan, J. Janzen, E. Levin, D. V. Devine and D. E. Brooks, *Biomacromolecules*, 2006, **7**, 703–709.

232 A. L. S. Burzava, M. Jasieniak, M. P. Cockshell, N. H. Voelcker, C. S. Bonder, C. S. Bonder, H. J. Griesser and E. Moore, *ACS Appl. Bio Mater.*, 2020, **3**, 3718–3730.

233 E. Ortiz-Ortega, S. Hosseini, S. O. Martinez-Chapa and M. J. Madou, *Appl. Surf. Sci.*, 2021, **565**, 150362.

234 B. Stegemann, D. Sixtensson, T. Lußky, A. Schoepke, I. Didschuns, B. Rech and M. Schmidt, *Nanotechnology*, 2008, **19**(42), 424020.

235 L. Yang, Y. Peng, Y. Yang, J. Liu, Z. Li, Y. Ma, Z. Zhang, Y. Wei, S. Li, Z. Huang and

N. V. Long, *ACS Appl. Nano Mater.*, 2018, **1**, 4516–4527.

236 X. Kong, C. Zeng, X. Wang, J. Huang, C. Li, J. Fei, J. Li and Q. Feng, *Sci. Rep.*, 2016, **6**, 1–8.

237 L. Q. Zhu, L. D. Zhang and Q. Fang, *Appl. Phys. Lett.*, 2007, **91**, 2–5.

238 N. Recek, M. Mozetic, M. Jaganjac, L. Milkovic, N. Zarkovic and A. Vesel, *Int. J. Polym. Mater. Polym. Biomater.*, 2014, **63**, 685–691.

239 G. Nanse, E. Papirer, P. Fioux, F. Moguet and A. Tressaud, *Carbon N. Y.*, 1997, **35**, 175–194.

240 D. Briggs and G. Beamson, *Anal. Chem.*, 1993, **65**, 1517–1523.

241 M. Rjeb, A. Labzour, A. Rjeb, S. Sayouri, M. C. El Idrissi, S. Massey, A. Adnot, D. Roy and C. M. Society, *Moroccan J. Condens. Matter*, 2004, **5**, 168–172.

242 F. Pippig, S. Sarghini, A. Holländer, S. Paulussen and H. Terrvn, *Surf. Interface Anal.*, 2009, **41**, 421–429.

243 J. C. Ruiz, S. Taheri, A. Michelmore, D. E. Robinson, R. D. Short, K. Vasilev and R. Förch, *Plasma Process. Polym.*, 2014, **11**, 888–896.

244 A. Thomas, S. S. Muller and H. Frey, *Biomacromolecules*, 2014, **15**, 1935–1954.

245 J. van de Wouw and J. A. Joles, *Clin. Kid. J*, 2022, **15**, 624–634.

246 T. A. Horbett, *J. Biomed. Mater. Res. A*, 2018, **106**, 2777–2788.

247 Y. Roina, F. Auber, D. Hocquet and G. Herlem, *J. Biomed. Mater. Res. - Part B Appl. Biomater.*, 2022, **110**, 302–320.

248 R. Asahi, T. Morikawa, T. Ohwaki, K. Aoki and Y. Taga, *Science (80-.).*, 2001, **293**, 269–271.

Appendices

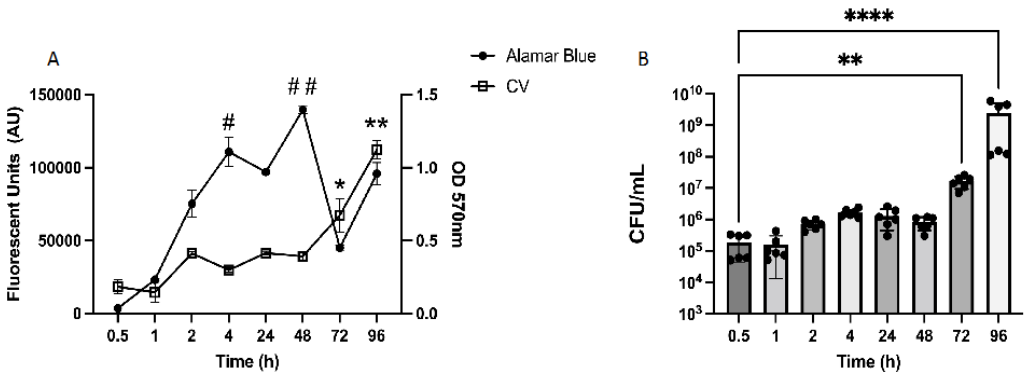

Appendix 2.1 *S. epidermidis* RP62A biofilms grown onto coverslips for time periods up to 96 hr in NB and monitored with traditional microbiology characterisation. (**A**) biofilm viability (black circles) measured by fluorescence of Alamar blue and biomass (white squares) determined from CV staining. (**B**) Quantification of biofilms by colony counting (CFU). Error bars represent the standard deviation from the mean. Hash symbols relate to viability data and asterix symbols relate to biomass quantification (#, * where p<0.05; ##, ** where P<0.01).

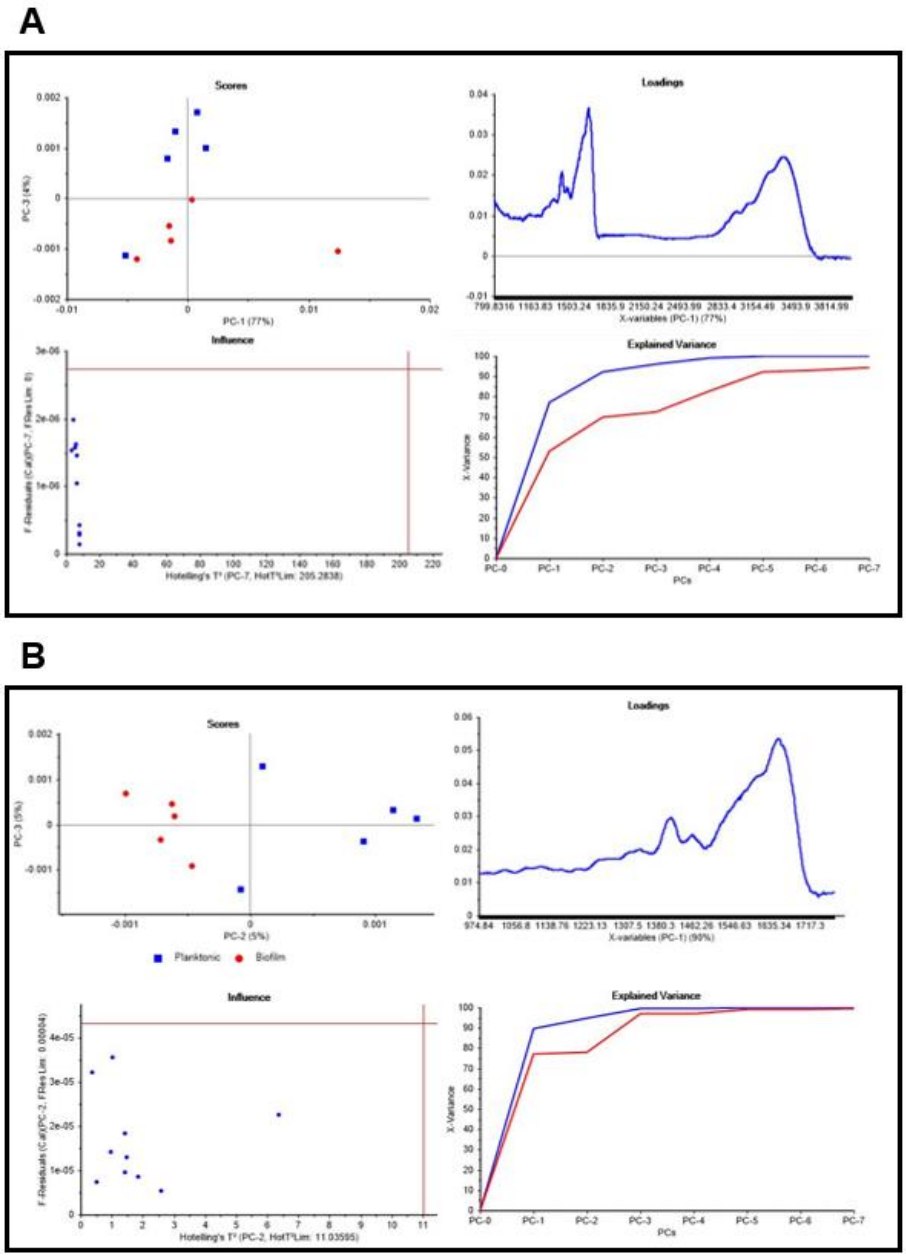

Appendix 2.2 Supplementary findings from principal component analysis evaluating the significance of spectral differences between planktonic and biofilm cells. Score plot indicates separation of data. A loadings plot is produced for each principal component and indicates the spectral feature for each point of difference. Influence plot determines which data points, if any, are outliers (shown by points lying outside of the red marked area). Explained variance shows the maximum number of principal components that can be used to prove difference, above the maximum point there is negligible change. (**A**) Whole spectrum, 4000 to 400 cm^{-1}; (**B**) Fingerprint region restricted to 1778 to 980 cm^{-1}.

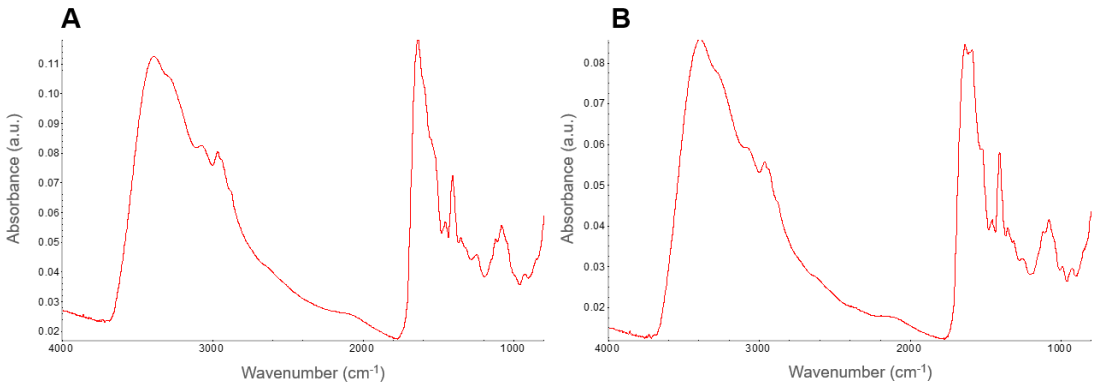

Appendix 2.3 FTIR spectra collected for *S. epidermidis* RP62A incubated for 24 hrs on CaF_2 slide. (**A**) Bacteria seeded and grown in TSB. Amide I peak position 1636.4 cm^{-1}; phospholipid peak at 1078.5 cm^{-1}. (**B**) Bacterial growth in BHI. Amide I peak position 1633.1 cm^{-1}; phospholipid peak at 1078.6 cm^{-1}.

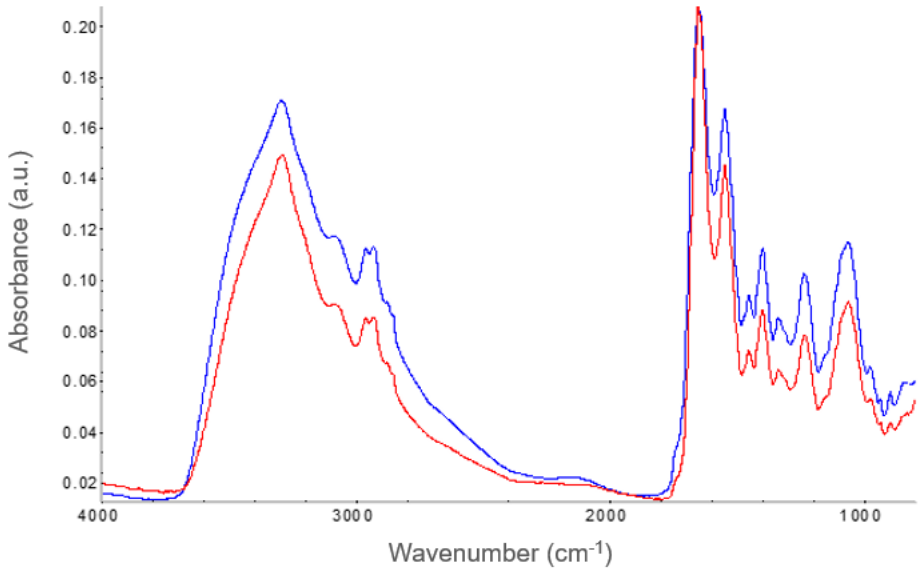

Appendix 2.4 Overlaid FTIR spectra of *S. epidermidis* ATCC 12228 planktonic cells (blue) and 72 hr incubated sample (red), originating from the same colony. Amide I peak position does not shift significantly (1651 cm^{-1} in the planktonic sample and 1652 cm^{-1} in the incubated sample) nor do the amide I and II regions merge following incubation.

Appendix 2.5 Amide I peak position (cm^{-1}) in FTIR following analysis of early biofilm development. The results for 3 experiments are given to demonstrate reproducibility of the data.

	Exp. 1	Exp. 2	Exp. 3
Planktonic	1652	1651	1650
30 minutes	1648	1648	1645
1 hour	1647	1647	1645
2 hours	1646	1645	1644
4 hours	1644	1642	1644

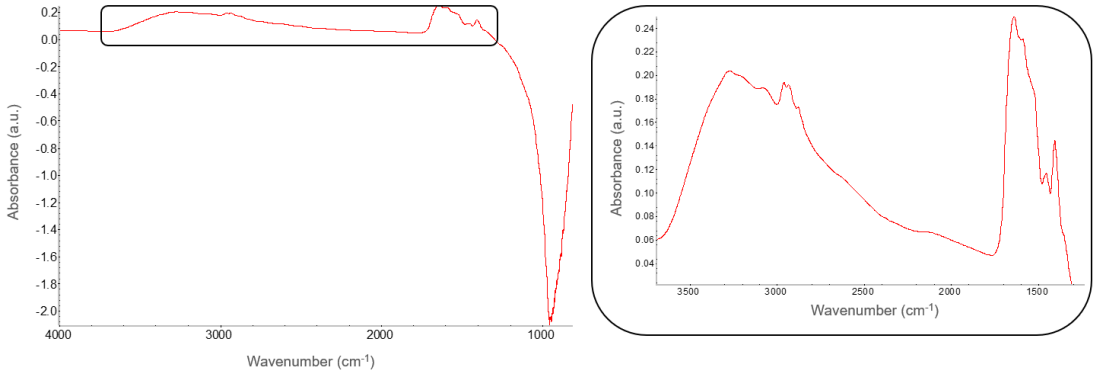

Appendix 3.1 FTIR spectra recorded for *C. albicans* cell growth on CaF_2 disks which revealed extreme distortion below 1500 cm^{-1} as a result of the substrate thickness.

Appendix 3.2 Full peak analysis (cm^{-1}) for three strains of *C. albicans*, relating to spectra presented in **Figure 3.2**.

Peak assignment (cm^{-1})	GSK022	GSK107	SC5314
Water	3294	3296	3295
Lipids	2926	2926	2926
Amide I	1652	1651	1652
δ_{as} (CH_3), δ_{as} (CH_2), proteins and lipids.	1546	1546	1546
δ_s (CH_3), δ_s (CH_2), proteins and lipids.	1453	1454	1454
Amide III	1399	1399	1399
ν_5 (PO_2^-), DNA, RNA, phospholipids	1061	1049	1076

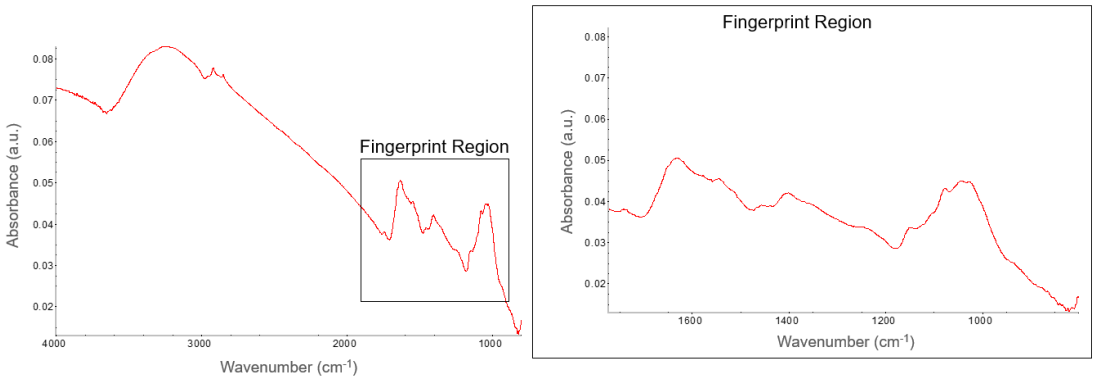

Appendix 3.3 FTIR spectrum produced when a single *C. albicans* species was grown in RPMI media, instead of YPD. The alternative broth overwhelmed the FTIR spectrum and prevented analysis of the peaks originating from the microorganisms.

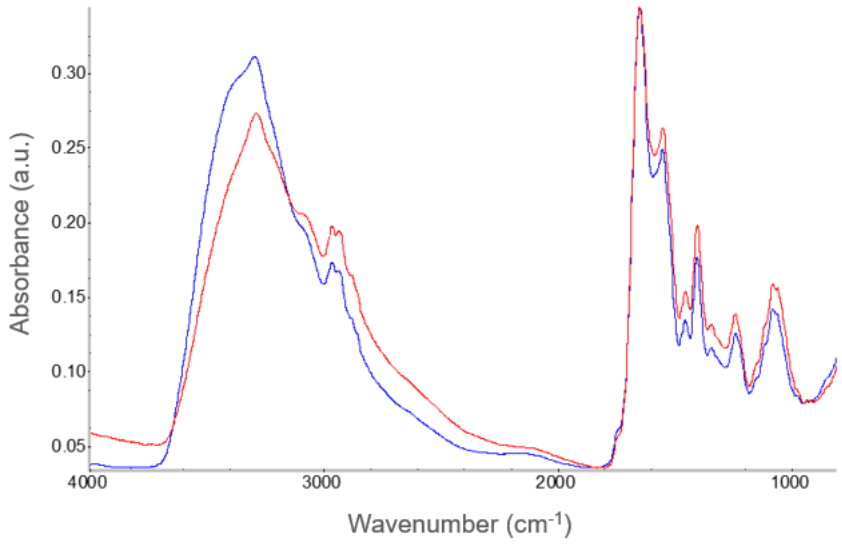

Appendix 3.4 FTIR spectra recorded after 24 hr incubation of mixed species biofilm samples (*S. epidermidis* and *C. albicans*) with two different *Candida* starting concentrations: 10^4 CFU/mL and 10^5 CFU/mL.

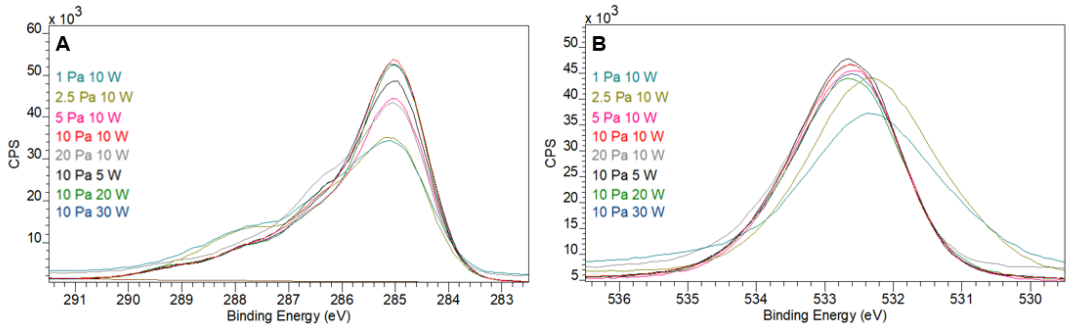

Appendix 4.1 Overlaid high-resolution spectra collected for 8 samples (listed as parameters 1-8 in **Table 4.1**). (**A**) C 1s; (**B**) O 1s.

Appendix 4.2 Binding energies (eV) of C 1s key bonding environments for ethanol PP coatings produced at a range of plasma parameters (C-R standardised at 285 eV).

Sample	C-O	C=O	O-C=O
1 Pa 10 W *	286.24	287.69	288.86
2.5 Pa 10 W *	286.26	287.71	288.81
5 Pa 10 W	286.33	287.68	289.05
10 Pa 10 W	286.35	287.65	289.05
20 Pa 10 W	286.29	287.59	289.03
10 Pa 5 W	286.34	287.68	289.07
10 Pa 20 W	286.37	287.68	289.06
10 Pa 30 W	286.32	287.63	289.04

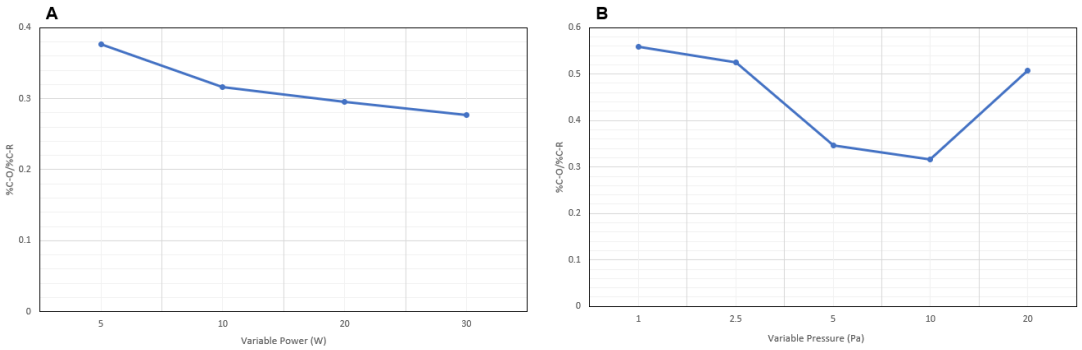

Appendix 4.3 (A) Plot of %C-O/%C-R against variable power for ethanol PP samples produced at 10 Pa. **(B)** Plot of %C-O/%C-R against variable pressure for ethanol PP samples produced at 10 W.

Appendix 4.4 O1s binding environments for ethanol PP coatings produced at a range of plasma parameters, except 1 and 2.5 Pa samples where incorporation of N has skewed the O 1s binding environments.

	C-O-C		C-OH	
Sample	**BE (eV)**	**At.%**	**BE (eV)**	**At.%**
5 Pa 10 W	532.53	80.72	533.60	19.28
10 Pa 10 W	532.56	81.07	533.64	18.93
20 Pa 10 W	532.58	81.18	533.74	18.82
10 Pa 5 W	532.56	80.96	533.64	19.04
10 Pa 20 W	532.52	79.03	533.61	20.97
10 Pa 30 W	532.50	76.88	533.58	23.12

Appendix 4.5 Percentage composition of the C 1s bonding environments for all ethanol PP coatings produced across a variety of plasma parameters. C-O/C-R indicates usefulness of ethylene oxide retention. C-O-C is found in the O 1s core line spectra.

Sample	C-R	C-O	C=O	O-C=O	C-O/C-R	C-O-C
1 Pa 10 W	49.11	27.38	16.32	7.20	0.558	-
2.5 Pa 10 W	50.35	25.92	16.98	6.74	0.515	-
5 Pa 10 W	61.89	21.91	11.19	5.01	0.354	79.21
10 Pa 10 W	64.82	20.91	9.98	4.29	0.323	80.34
20 Pa 10 W	55.71	28.01	11.53	4.75	0.503	80.03
10 Pa 5 W	60.90	23.89	10.82	4.39	0.392	79.95
10 Pa 20 W	65.69	19.71	10.13	4.47	0.300	77.73
10 Pa 30 W	66.39	18.46	10.27	4.88	0.278	76.83

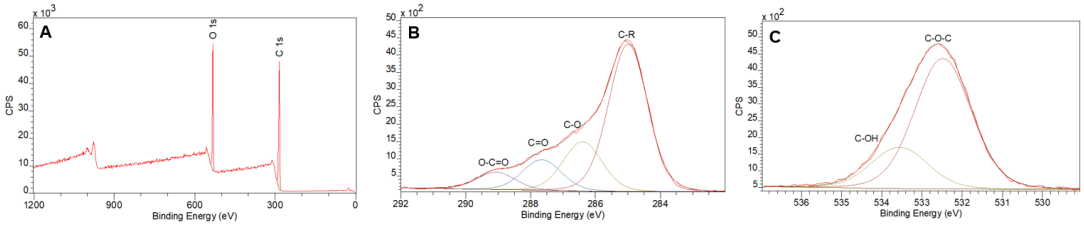

Appendix 4.6 XPS analysis of a 15-crown-5 PP coating produced at 10 Pa, 10 W (20-min deposition time) on Si. (**A**) *Whole compositional analysis*: O 1s 22.86%, C 1s 77.14%; (**B**) *C 1s*. C-R (285 eV, 60.22%), C-O (286.40 eV, 20.16%), C=O (287.65 eV, 12.55%), O-C=O (289.07 eV, 7.07%); (**C**) *O 1s*. C-O-C (532,48 eV, 75.90%), C-OH (533.56 eV, 24.10%).

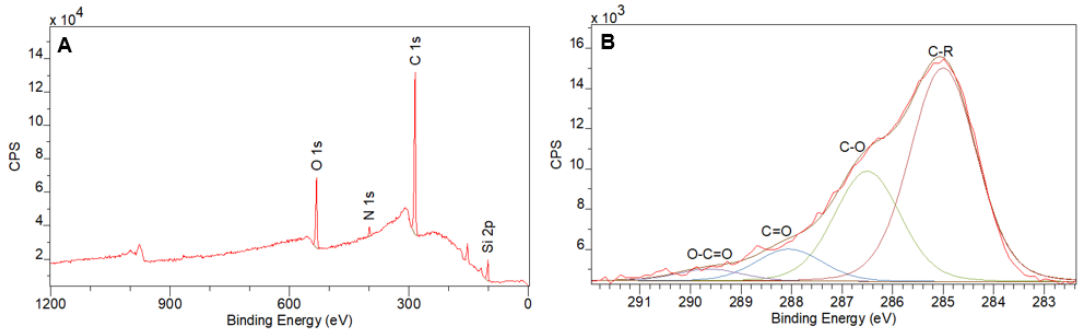

Appendix 4.7 XPS analysis of 15-crown-5 deposited under Ratner parameters (33 Pa, 80 W (2 min) then 5 W (5 min)). (**A**) *Wide scan*: O 1s 13.05%, C 1s 76.46%, N 1s 1.78%, Si 2p 8.71%. (**B**) *C 1s*. C-R (285 eV, 58.12%), C-O (286.50 eV, 29.98%), C=O (288.04 eV, 8.71%), O-C=O (289.63 eV, 3.19%).

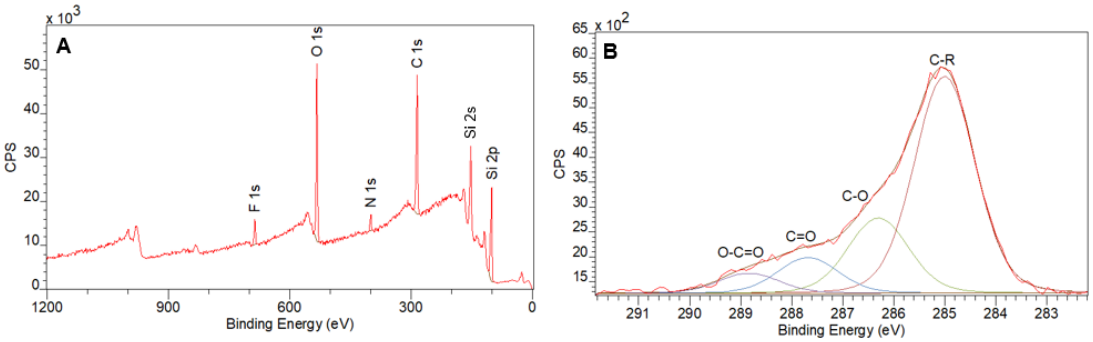

Appendix 4.8 XPS analysis of 15-crown-5 PP coating attempted under pulsed plasma conditions using plasma parameters: 10 Pa, 25 W, pulse width 50 ms, pulse delay 5 ms, total deposition time 15 minutes. (**A**) *Wide scan spectrum*: O 1s 19.24%, C 1s 43.60%, N 1s 2.50%, F 1s 1.91%, Si 2p 32.75%. (**B**) *C 1s*. C-R (285 eV, 62.39%), C-O (286.30 eV, 21.61%), C=O (287.68 eV, 10.24%), O-C=O (288.63 eV, 5.76%).

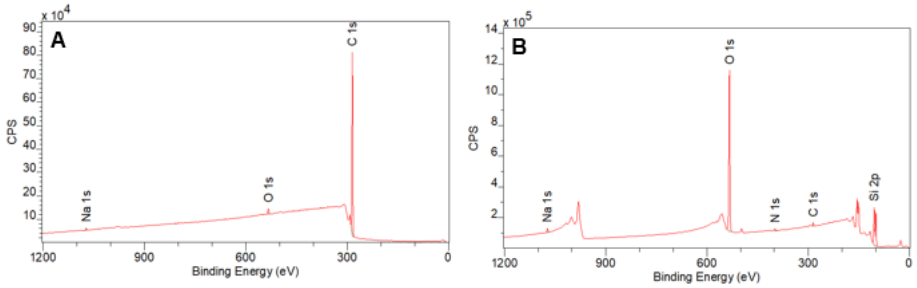

Appendix 4.9 (**A**) Clean PS on Si wafer, O1s 1.56%, C1s 98.18%, Na1s 0.26%; (**B**) Plasma activated PS on Si wafer, O1s 46.29%, C1s 2.26%, Na1s 0.56%, Si2p 49.95%, N1s 0.93%.

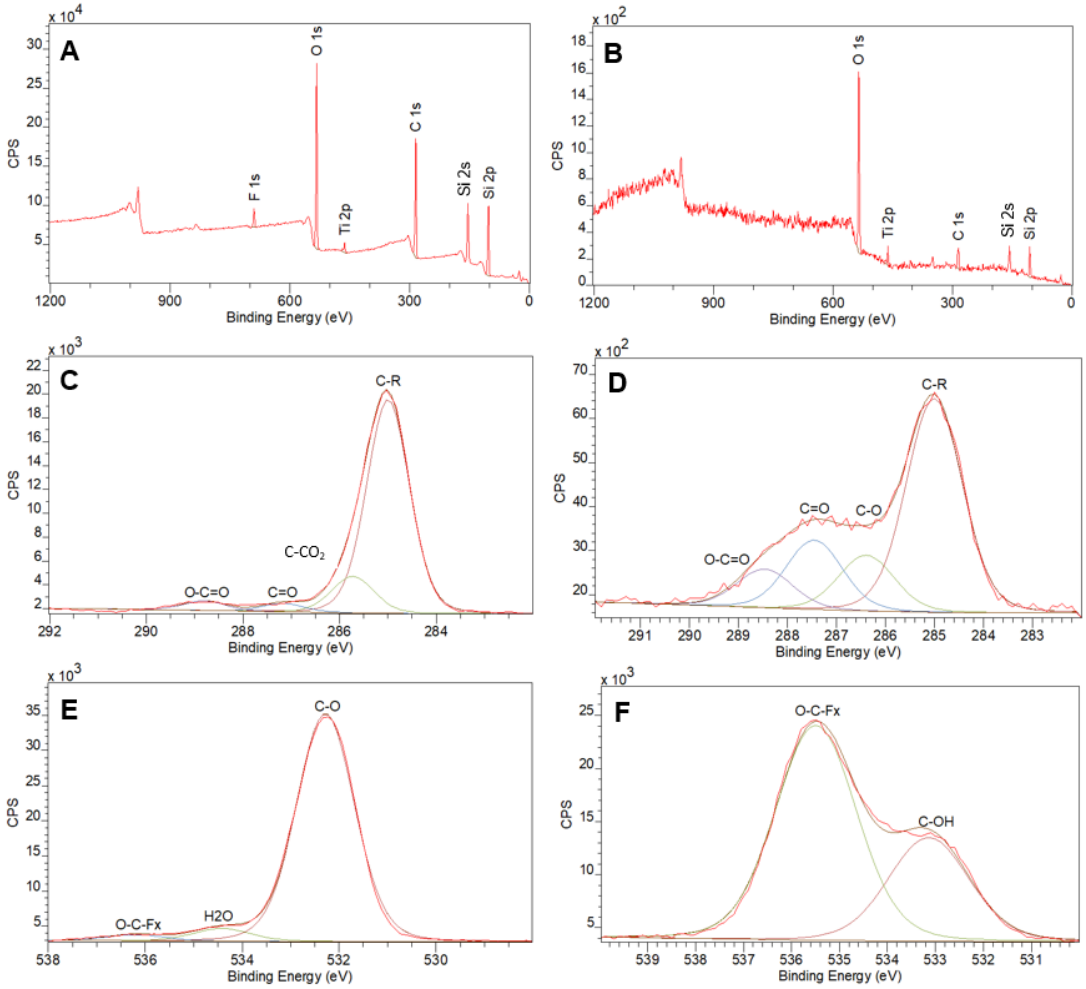

Appendix 4.10 XPS wide scan and core line spectra collected on nitinol stents after cleaning (**A, C, E**) and following 20 minutes plasma activation (**B, D, F**). (**A**) *Clean*, O 1s 23.75%, C 1s 40.73%, F 1s 2.10%., Ti 2p 4.49%, Si 2p 28.93%; (**B**) *Plasma activated*, O 1s 50.24%, C 1s 18.45%, Ti 2p 12.23%, Si 2p 19.07%; (**C**) *Clean, C 1s*. C-R (285 eV, 79.79%), C-CO_2 (285.73 eV, 13.56%), C=O (287.17 eV, 3.11%), O-C=O (288.79 eV, 3.54%); (**D**) *Plasma activated, C 1s*. C-R (285 eV, 56.68%), C-O (286.39 eV, 14.73%), C=O (287.45 eV, 18.35%), O-C=O (288.47 eV, 10.23%); (**E**) *Clean, O 1s*. C-O (532.28 eV, 92.45%), H_2O (534.43 eV, 5.05%), O-C-F_x (536.21 eV, 2.50%); (**F**) *Plasma activated, O 1s*. C-OH (533.15 eV, 32.48%), O-C-F_x (535.50 eV, 67.52%).

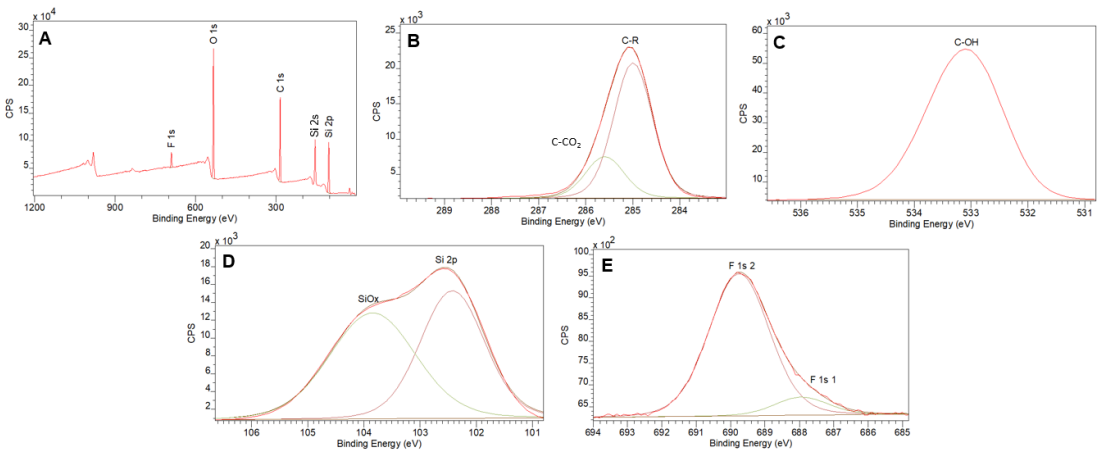

Appendix 4.11 XPS spectra of Kapton tape (on which all samples are affixed to when sampling in XPS). (**A**) *Wide scan,* O 1s 26.33%, C 1s 38.06%, Si 2p 33.19%, F 1s 2.42%; (**B**) *C 1s*. C-R (285 eV, 76.48%), C-CO_2 (285.59 eV, 23.52%); (**C**) *O 1s*. C-OH (533.11 eV); (**D**) *Si 2p*. Si 2p (102.43 eV, 47.28%), SiOx (103.84 eV, 52.72%); (**E**) *F 1s*. 1 (687.94 eV, 10.17%), 2 (689.75 eV, 89.83%).

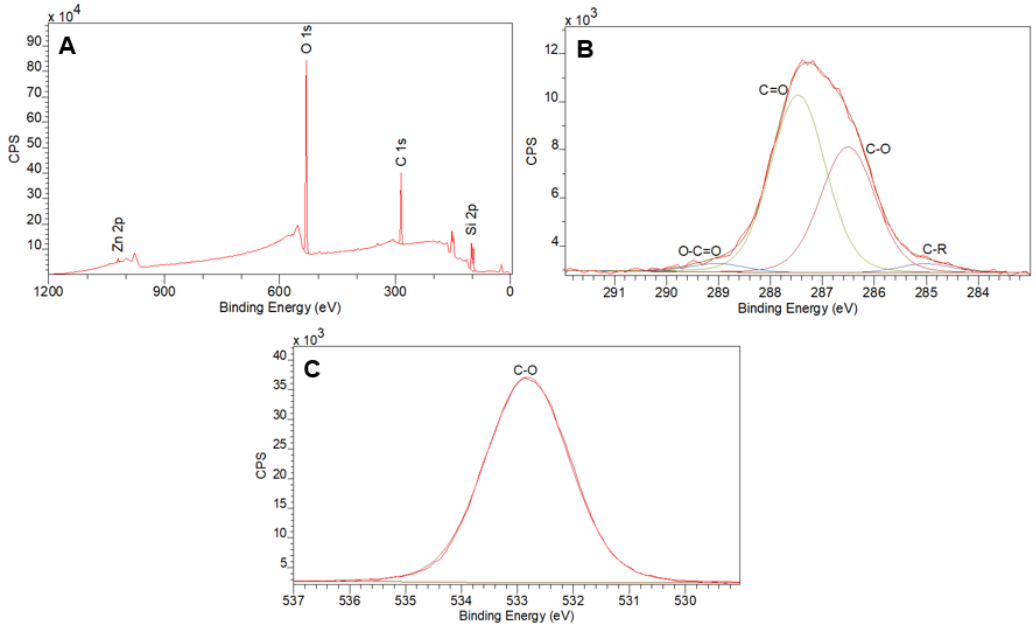

Appendix 4.12 HPG growth after allowing 4 hr delay between plasma activation and starting the grafting process. (**A**) *Wide scan*, O 1s 39.25%, C 1s 34.66%, Si 2p 26.01%, Zn 2p 0.08%; (**B**) *C 1s*. C-R (285 eV, 2.82%), C-O (286.50 eV, 39.28%), C=O (287.46 eV, 55.28%), O-C=O (289.01 eV, 2.62%); (**C**) *O 1s*. C-O (532.83 eV, 100%).

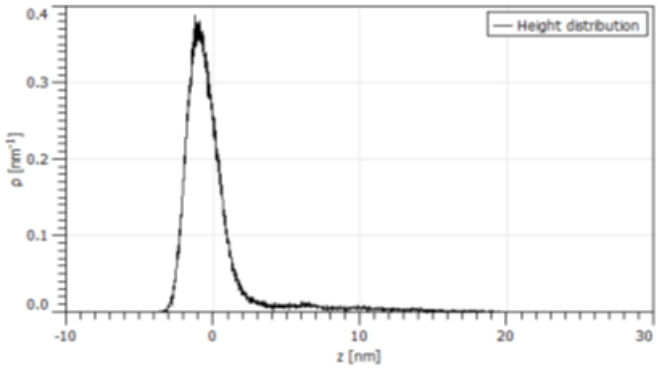

Appendix 4.13 Line profile collected from preliminary AFM scratch test carried out on HPG grafted onto TiSi. Line profile does not provide a lower bound coating thickness.

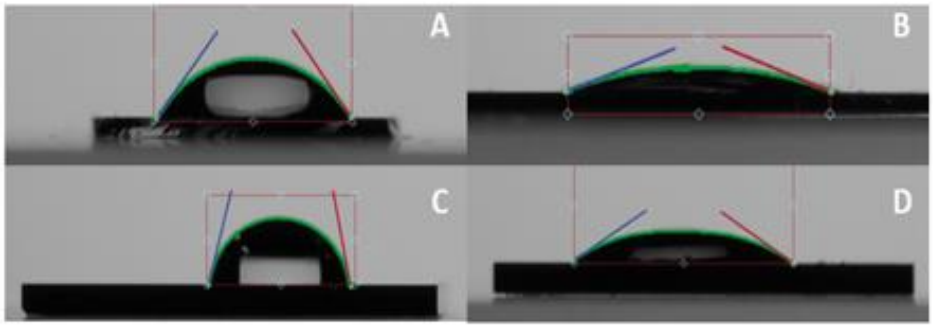

Appendix 4.14 Examples of contact angle measurement determination. (**A**) Clean Si substrate, average CA = 53.85˚; (**B**) HPG coated Si, average CA = 19.47˚ (**C**) Clean TiSi substrate, average CA = 76.39˚; (**D**) HPG coated TiSi, average CA = 31.49˚.

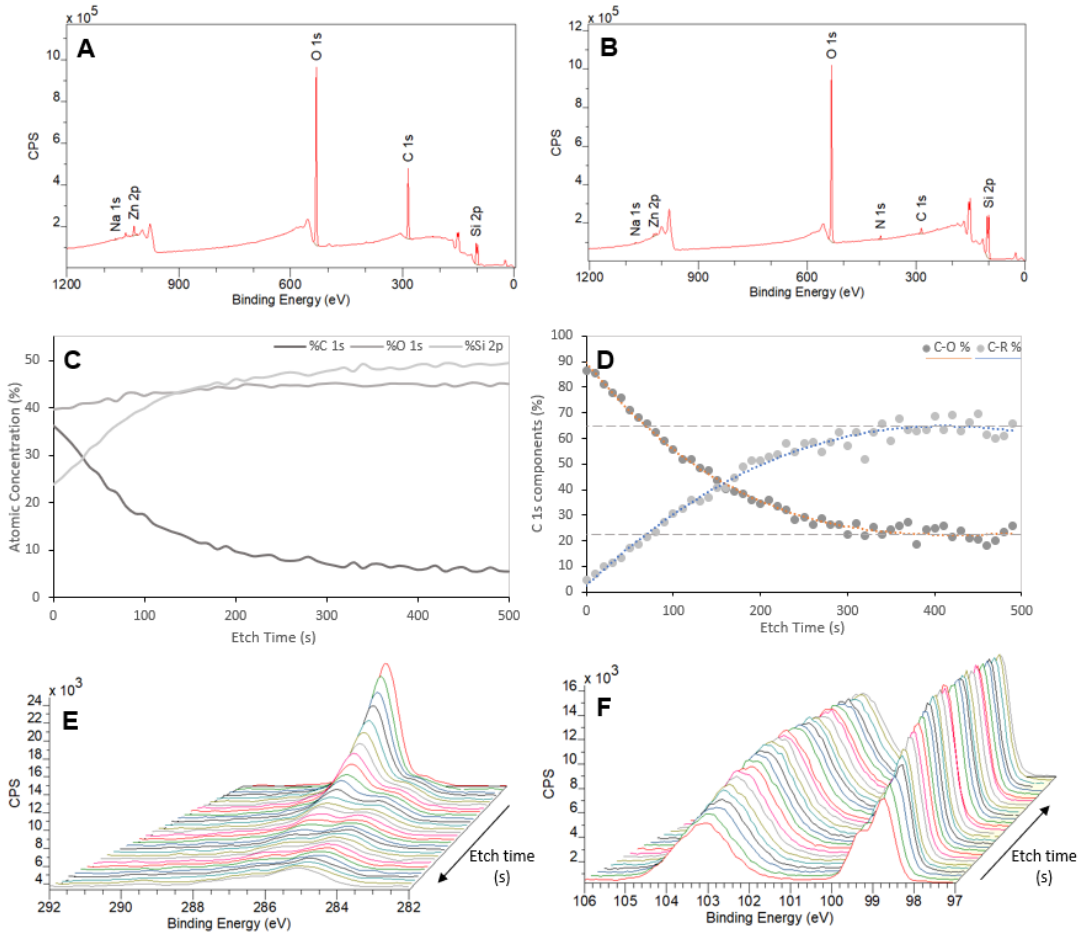

Appendix 4.15 Depth profile XPS results for HPG on Si, ion milled for 1000s. (**A**) *Wide scan recorded before the sample was milled*, O 1s 39.16%, C 1s 37.80%, Si 2p 22.62%, Zn 2p 0.34%, Na 1s 0.09%; (**B**) *Wide scan recorded after the sample was milled*, O 1s 41.39%, C 1s 4.13%, N 1s 1.11%, Si 2p 53.10%, Na 1s 0.10%, Zn 2p 0.18%; (**C**) Atomic composition (%) plotted by etch time (s); (**D**) C 1s component plot against etch time (s), where plateau of %C-O at 20% signals removal of HPG coating; (**E**) 3D plot of C 1s spectra from 0 s etch to 300 s; (**F**) 3D plot of Si 2p spectra from 0 s to 300 s, showing the increasing SiO_x component that is revealed as the substrate is uncovered.

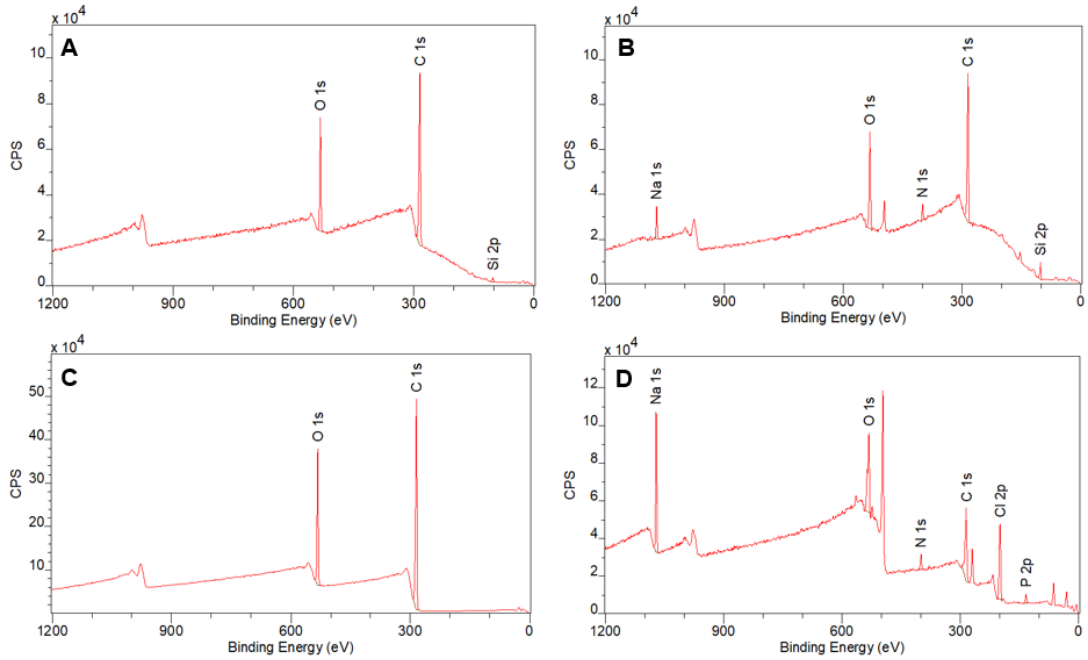

Appendix 5.1 XPS wide scan spectra collected on ethanol PP coatings with different ethylene oxide content. (**A**) *20 Pa, 5 W no protein*, O 1s 17.06%, C 1s 80.68%, Si 2p 2.26%; (**B**) *20 Pa, 5 W protein*, O 1s 17.65%, C 1s 69.79%, N 1s 3.45%, Na 1s 2.02%, Si 2p 7.09%; (**C**) *10 Pa, 30 W no protein*, O 1s 18.94%, C 1s 81.06%; (**D**) *10 Pa, 30 W protein*, O 1s 20.29, C 1s 47.51, N 1s 3.71, Na 1s 9.07, Cl 2p 16.26, P 2p 3.16. [Note: %N1s are not directly comparable because the results were collected on different days]

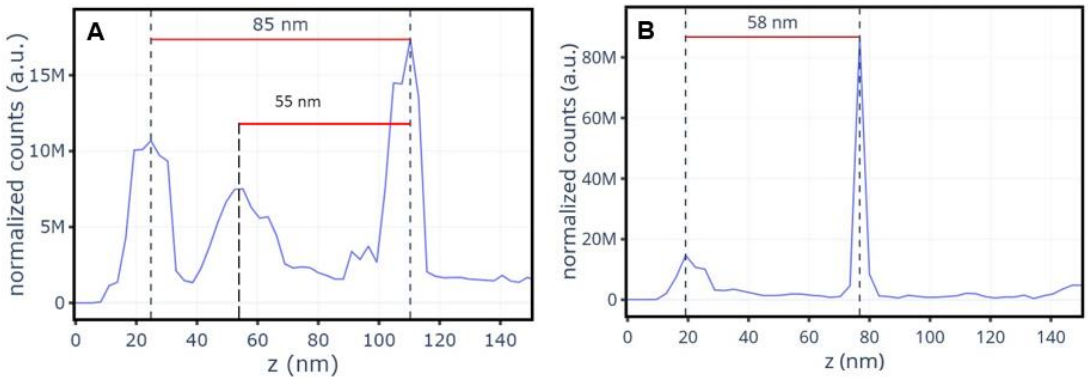

Appendix 5.2 (**A**) AFM scratch test performed by Alessio Quadrelli, on ethanol PP coating (10 Pa/30 W), no protein. Roughness (-500,500 pm) made it hard to distinguish between the PP and Si. RMS9Sq 316.9 pm. Coating thickness 85 nm, with hard to scratch sections that are 55 nm; (**B**) AFM scratch test on ethanol PP coating, protein. Rough surface (-3,3 nm), visually different from pristine ethanol PP. Coating thickness 58 nm and can be easily scratched back to Si.

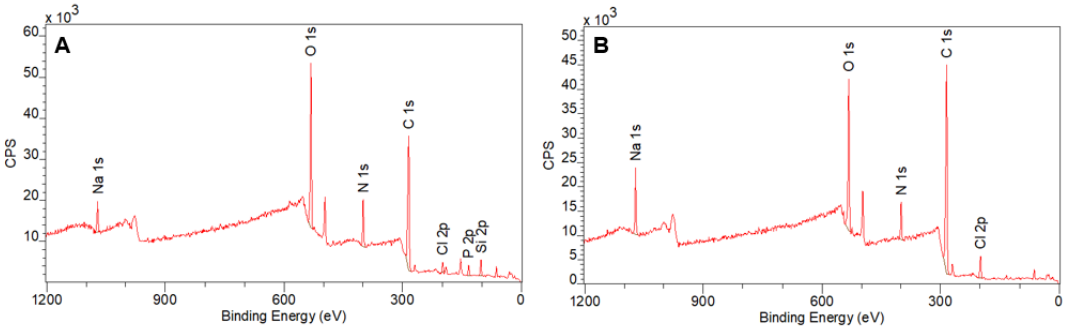

Appendix 5.3 Effect of pre-hydrating an ethanol PP coating (10 Pa, 30 W) before exposure to albumin for 1000 s. (**A**) *Not pre-hydrated*. O 1s 22.57, C 1s 57.68, N 1s 9.05, Na 1s 1.85, Cl 2p 1.04, P 2p 2.39, Si 2p 5.40. N counts: 1244.67; (**B**) *Pre-hydrated*. O 1s 18.50, C 1s 70.51, N 1s 5.69, Na 1s 2.64, Cl 2p 2.66. N counts: 781.38.

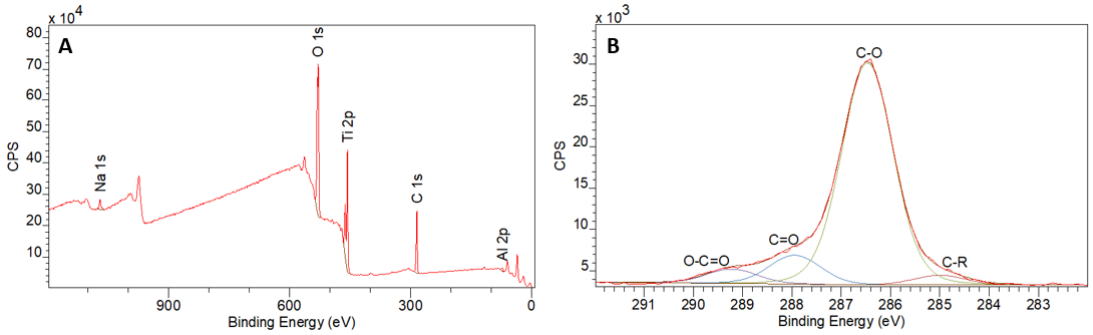

Appendix 5.4 HPG on TiSi wash test completed by following protein test protocol without using protein (i.e. 90-minute total incubation in PBS at room temperature). (**A**) *Wide scan*, O 1s 50.06, C 1s 32.23, Na 1s 1.45, Ti 2p 12.29, Al 2p 3.98; (**B**) *C 1s*. C-R (285 eV, 3.50%), C-O (286.47 eV, 80.77%), C=O (287.94 eV, 10.52%), O-C=O (289.22 eV, 5.21%).

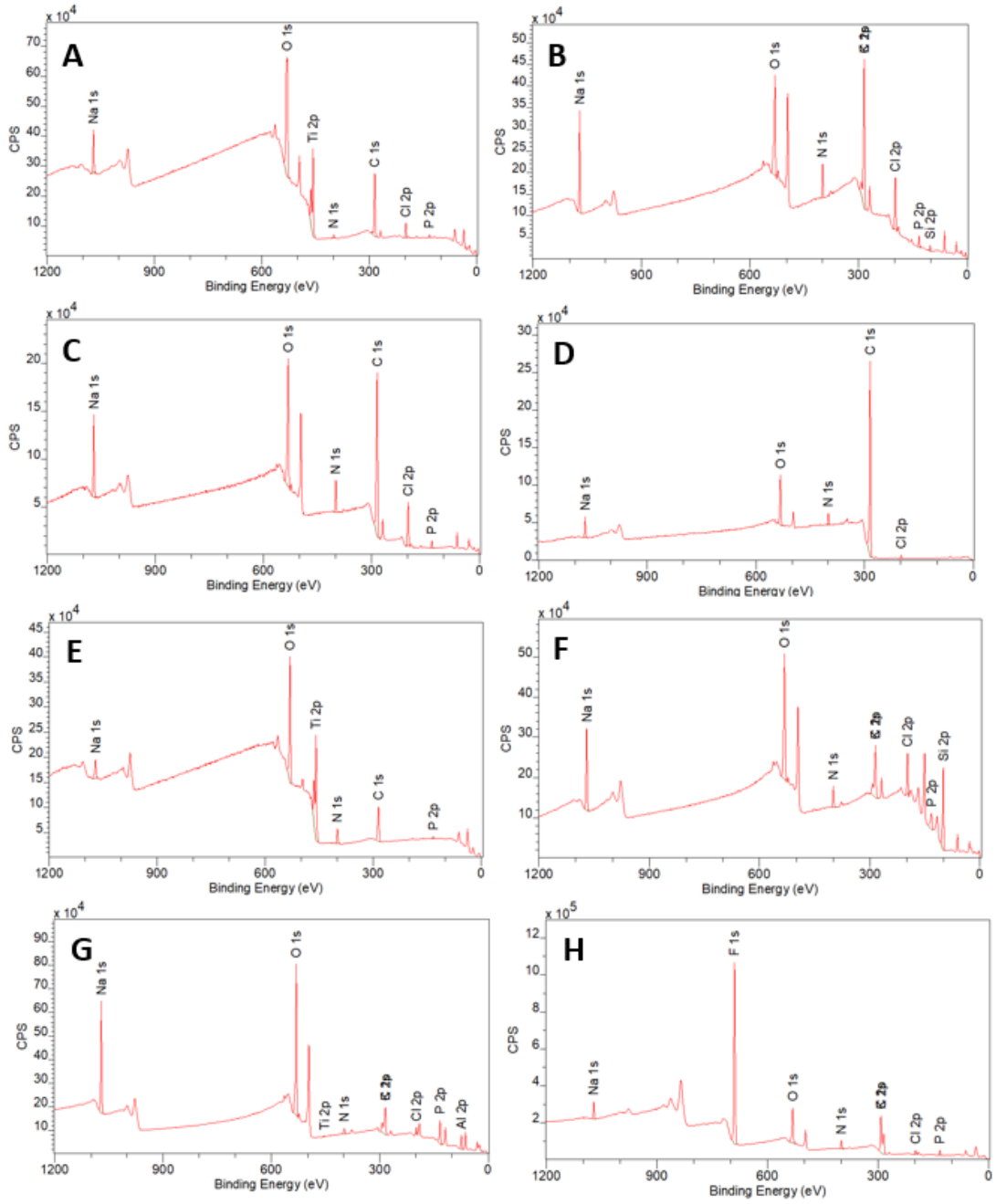

Appendix 5.5 Reversible adsorption of albumin monitored by the uptake of nitrogen into different coated and uncoated materials. (**A**) *HPG,* N counts: 99488.9, N/Au: 0.0319; (**B**) *PS on Si*, N counts: 220287.8, N/Au: 0.0982; (**C**) *Ethanol PP (10 Pa/30 W),* N counts: 77675.4, N/Au: 0.0625; (**D**) *PS*, N counts: 62949.6, N/Au: 0.0506; (**E**) *TiSi*, N counts: 57542.7, N/Au: 0.0571; (**F**) *Si*, N counts: 179630.1, N/Au: 0.107; (**G**) *Al foil*, N counts: 108647.5, N/Au: 0.904; (**H**) *PTFE*, N counts: 82946.5, N/Au: 0.0690.

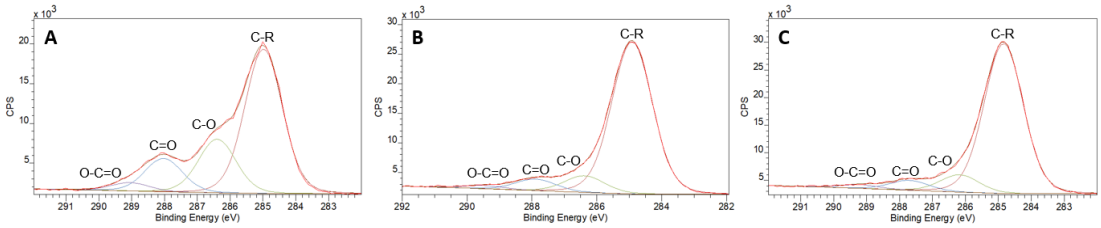

Appendix 5.6 Ethanol PP coating (10 Pa/30 W) ion milled for 1500 s, C 1s spectra reveal decay of C-O composition. (**A**) 0 s etch time; (**B**) 900 s etch time; (**C**) 1500 s etch time.

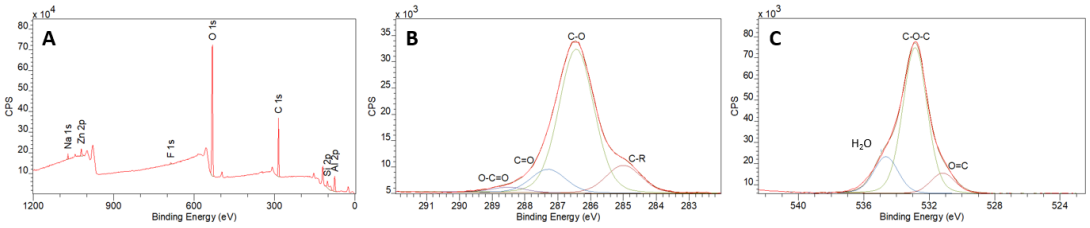

Appendix 5.7 Evidence of HPG coating on Al foil. (**A**) *Wide scan*, O 1s 35.58%, C 1s 30.92%, Si 2p 14.03%, Al 2p 18.42%, Na 1s 0.38%, Zn 2p 0.27%, F 1s 0.41%; (**B**) *C 1s*. C-R (285 eV, 13.88%), C-O (286.43 eV, 71.75%), C=O (287.30 eV, 11.73%), O-C=O (288.50 eV, 2.64%); (**C**) *O 1s.* O=C (531.15 eV, 10.07%), C-O-C (532.87 eV, 71.95%), H_2O (534.65 eV, 17.98%).

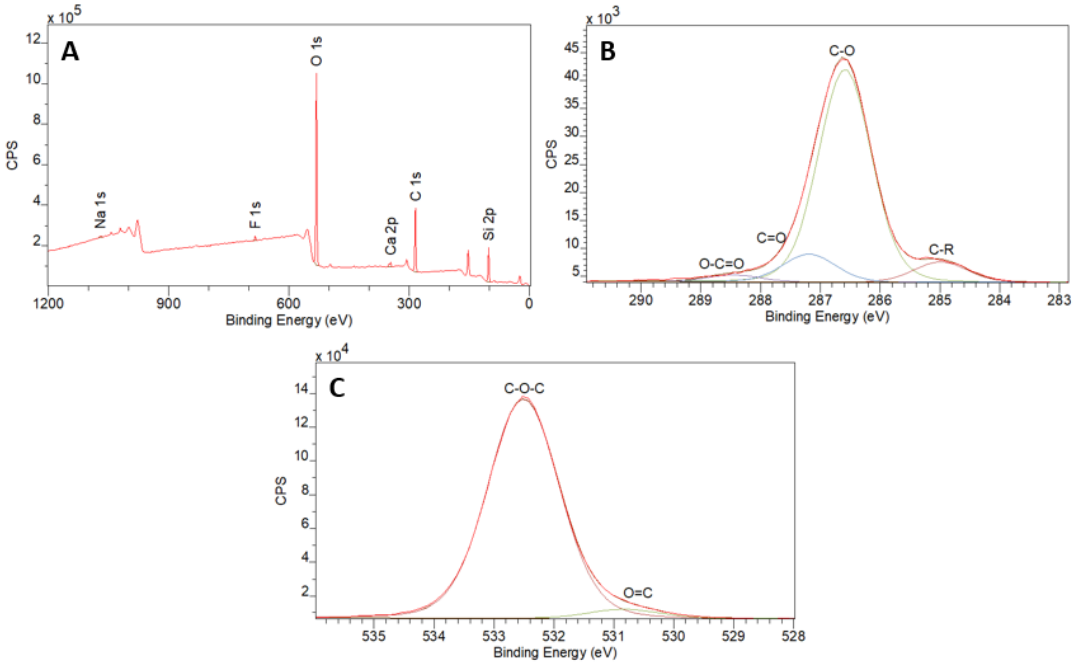

Appendix 5.8 Evidence of HPG coating on a glass coverslip. (**A**) *Wide scan*, O 1s 43.72%, C 1s 34.87%, Si 2p 19.58%, Na 1s 0.17%, Ca 2p 0.92%, F 1s 0.74%; (**B**) *C 1s*. C-R (285 eV, 7.66%), C-O (286.60 eV, 79.36%), C=O (287.20 eV, 10.41%), O-C=O (288.46 eV, 2.57%); (**C**) *O 1s*. O=C (530.83 eV, 4.01%), C-O-C (532.51 eV, 95.99%).